PhD Title:

Mooring lines analysis and design for wave energy converters

Gianmaria Giannini BSc, MSc

Department of Naval Architecture, Ocean and Marine Engineering
University of Strathclyde, Glasgow

August 1, 2018

Abstract

Soon, wave energy converters will be anchored in several offshore locations for extended periods of time, where high wave energy exist. These devices moored in such areas experience continuous dynamic loads exerted mainly by colliding waves. Therefore, their mooring system is a fundamental component, which influences overall performance characteristics through its dynamic behaviour. The mooring component of wave power devices has been typically analysed and designed by using a simplified static and quasi-static based approach and thus independent from the design of the floating structure dynamics. Given the peculiarities of mooring system design and analysis for wave energy devices, no particular available tools are suitable for analysing and design the mooring component as an integral active part of the entire moored system. All commercial software and codes available are in fact developed by having in mind different mooring requirements. Through this project, opportunities to improve entire moored system design were investigated. This study aimed to consider the potential option of designing mooring component as an integral dynamic part of the whole wave energy converter system. An overview of relevant existing studies is delineated, and a generic methodology, aiming at analysis and design moored wave energy system based on a fully dynamic approach, is proposed. For showing on how this can be applied, a particular focus on an Earth-reacting type of wave energy devices is made. Thus, a numerical code capable of analysing the dynamics, and predict performances of specific single tethered Earth-reacting wave energy converters, was developed. Through this code moored devices of any shape under regular or irregular seas' loads can be

analysed. Both frequency-domain and time-domain mathematical formulations of the system considered are resolved by the proposed method. By using the comparison of numerical predictions with experimental data, the numerical code was validated for the specific cases of both, a half submerged and a fully submerged, spherical floaters. The accuracy of the proposed method was quantified. Results showed that the numerical method proposed is accurate, computationally efficient and well validated by the extensive experimental data, which was beside acquired during this project. Following the validation of the numerical tool, this last was used in two case studies. The outcome of these studies indicated that by using the proposed method, the trade-off between floater's immersion depth and mooring load peaks could be examined so that the optimal system design can be identified. The main advantage of the developed tool, compared to existing codes, is that this is tailored to the specific case of analysis and design for Earth-reacting wave energy converters. The new generic methodology proposed showed to be useful and suitable for analysing and design wave energy converters by including the mooring system as an integral component.

This thesis is the result of the author's original research. It has been composed by the author and has not been previously submitted for examination which has led to the award of a degree.

Date: August 1, 2018.

Acknowledgments

First of all, I would like to express the best gratitude to my advisors of study Prof. Sandy Day, David Clelland and Dr Narakorn Srinil for their extended support and guidance during all time of the project.

I would like to thank Charles Keay, Grant Dunning for the help provided at our university laboratories, and I thank Prof. Tomoki Ikoma, Prof. Panagiotis Kaklis, and Dr Giuseppe Mortola, for the support and advice provided. A special thank goes to Prof. Ermina Begovic of University of Naples Federico II for her availability. I further thank Mrs Thelma and Mrs Susan for always comforting and helping me with administrative matters. Then I would like to acknowledge all colleagues that have been interacting with me during these years, in particular, I thank Gonzalo, Luigi, Dr Hossein. I would like to further acknowledge Dr Pedro Vicente and Prof. António Falcão for their support at IST in Portugal. I thank, Michele Martini, Marinella Passerella, Carlos Perez Collazo and the all others members of committee and participants of 2014 and 2015 INORE symposiums, held in Spain and afterwards in Italy, for a considerable time passed together.

My gratitude goes as well to my family who always motivated me. I would like to thank my mother for all the love and teachings she ever has given me. I am grateful to my father in particular for often being an enthusiast listener of my research progress. I would like to thank my brother who always has been supportive.

I would like to further thank all friends here in Glasgow, in between Abi, Avaro, Luis,

Rachel, Victor. At last but not least, I appreciate a lot Irina who helped me to improve the grammar and punctuation of this dissertation.

Contents

List of Figures

List of Figures

List of Tables

List of abbreviations

BEM . . . . . Boundary Element Method

DoF . . . . . Degree of freedom

n. / no. . . . . Number

PTO . . . . . Power-take-off

PA . . . . . Point absorber

RCW . . . . . Relative capture width (Pizer, 1994)

RPV . . . . . Rated Power Value

WEC . . . . . Wave energy converter

TD . . . . . Time-domain

List of symbols

$A_{i,j}$ Added mass coefficients (kg)

a Wave amplitude (m or mm)

$B_{i,j}$ Radiation damping coefficients (Ns/m)(=kg/s)

C_{pto} Damping constant of power-take-off mechanism (Ns/m)

ΔL Mooring line axial displacement (= ℓ). Intended to be the extension the mooring line due to the elongation of the spring (m)

η Free surface elevation (m or mm)

$expC$ Exponent of floater vertical component of the velocity (=1 for linear PTO force or =2 for quadratic PTO force)(dimensionless)

F_e Excitation force coefficients (dimensionless)

F_w Excitation force (N)

F_m Mooring force (N)

F_p Mooring line pretension (N)

f Frequency (Hz)

ϕ Mooring force (N)

Φ Velocity potential (function)

H_s Significant wave height (m)

k Wave number $= \omega^2/g$ (for deep water linear theory) (1/m)

K_s Stiffness of mooring line (N/m)

L Mooring line length (m)

ℓ Mooring line axial displacement ($= \Delta L$) (m)

m Mass of floater (kg)

n Numerical simulation step

ω Angular frequency (rad/s)

P_F Power factor, indicating theoretical device efficiency (capture width ratio) (dimensionless)

kr Dimensionless wave number (radius x wave number)

r Radius (m)

t Time (s)

T_p Wave period (or, in irregular sea, is characteristic wave period) (s)

V_w Volume of the water displaced by the floater in calm condition (m^3)

Chapter 1

Introduction

Along most of the countries facing oceans, it exists an enormous wave energy resource that can be harnessed. Although nowadays the energy which is being extracted and converted into a form of useful energy is almost nil. This is due to a series of factors which are: difficult bureaucracy, political will, social commitment and reliable technology development. While the first three factors are under the direct control of bureaucrats, politicians and citizens, the third factor is the one on which engineers, scientists and technologists have to focus on. To further develop wave energy projects at a commercial level a series of technological challenges exist. The study exposed in this thesis focuses on of methods for analysing and design mooring lines for wave energy converters (WECs).

Due to the nature of wave energy technology, it is of fundamental importance to overcome technical challenges. Among the principals of these challenges, there is the one concerning mooring design and analysis. This last is one of the essential research subjects which need to be addressed so that the wave energy technology can reach a level of maturity regarding commercialisation. Differently that for conventional floating structures, the mooring system for wave energy applications has significant costs with which the developer would have to deal. Reducing such costs may not only permit of max-

imising profit but in some cases would be a requisite for allowing a particular project to be economically viable. To minimise such costs is required to analyse and identify potential best mooring designs, in the most accurate way. Due to the characteristics of WECs, existing analysis methods are not in all cases applicable.

Most convenient wave energy resources are located near coastal countries, at relatively high latitudes, at relatively deep ocean sites where the most of the wave energy is present. At these locations the wave power is the highest, meaning that the moored wave energy converters (WECs), deployed to absorbing such power, experience severe structural loads. In particular, these loads are primarily due to waves acting on the floating body part of the WEC, and these loads are then transmitted to the mooring system. As a consequence, this last is an essential component needed for permitting the WEC operation, if this fails the WEC would drift away determining substantial safety issues and economic losses. The mooring component has to counteract loads which are of magnitudes and characteristics similar to environmental forces acting on the floating WEC. Despite this, as the mooring loads are determined by the combination of both environmental loads and loads due to WEC dynamics, it is not an easy task to accurately estimate and predict these loads. The problem of quantifying such mooring loads it is an old one, and it has always existed in the traditional offshore industries for station keeping of ships and offshore structures moored for oil and gas exploitation. However, substantial differences between the problem of mooring WECs and the problem of mooring vessels and conventional offshore platforms exist. On the one hand some of the existing knowledge, can in some ways, be transferred to the new problem of mooring WECs. On the other hand, due to the peculiar characteristics of WECs, a new methodological approach is needed.

In general mooring systems for ships and conventional structures, were designed in the past by putting in practice simplistic static or quasi-static design approaches which assumed the floating structure almost stationary. Due to the nature of WECs, applying these approaches may not entirely give good design results. Luckily there already exist other approaches that take into account fluid and structure interaction dynamics; these

are more suitable to be used for mooring analysis and design for WECs. Despite this, dynamics based methods for the traditional type of methods are in general complex and only applicable to particular cases. Even if these methods may be applicable in some cases, these are often complex to be implemented. In the available commercial software for analysing and design mooring systems for floating structures are implemented these traditional methods. No existing software was build with the primary aim of analysis and design mooring systems for WECs. As a consequence, there is a need for practical new methods based on fully dynamic approaches which should be suited to the particular requirements of the WECs. Focusing on this thought, by this project a methodology is proposed and is applied via a numerical tool for the specific case of Earth-reacting WECs.

The above arguments together with the points listed below represent the primary motivation of this research project.

- There is a need to identifying new mooring system requirements for WECs and differences with traditional applications.
- There is a need for identifying which conventional theories can be of interest for mooring analysis and design for WECs.
- Wave energy compared to other renewable energy technologies is costly; thus it is crucial to optimise the overall system for increasing power absorption performances and reducing the overall repayment period. Efforts toward finding the optimal design of the mooring system have to be made.
- To predict system performances so that financial risk can be diminished and well quantified. Taking into account the mooring system in the entire system analysis is essential.
- To develop a code that can be used for the specific case of WECs studies. In fact, it is often difficult to model WECs systems in existing commercial codes. Commercial codes in all cases were developed for analysing traditional structures.

Due to radical differences between these structures and WECs, it may be suitable to start building new codes from scratch. Otherwise, it may be more difficult to adapt existing codes for modelling moored WECs taking into account all new mooring requirements.

- To validate the proposed methods with empirical evidence. Due to the peculiar new problem that needs to be solved, it is essential to prove experimentally the validity of numerical methods and limitations implemented.

- To provide to others empirical data that can be used to validate other numerical studies on generic moored WECs.

1.1 Structure of thesis and objectives

Due to the motivation mentioned above and in order to address specific project objectives reported next, this thesis is structured in six main chapters, these cover: the review on the topic (Chapter 2); the Earth-reacting wave energy converter numerical tool (Chapter 3); the experimental work carried out on scale models of point absorbers wave energy converters (Chapter 4); the verification and validation of the numerical code (Chapter 5); the case studies (Chapter 6); and the summery and conclusions (Chapter 7).

From the understanding acquired by reviewing the literature (Chapter 2), it was found that there is a need to delineate a new methodology for analysing and design mooring systems for wave energy converters (WECs). The conventional approach for designing a mooring system for conventional floating structures is not suitable for WECs. Common practice concerns designing and analysing the mooring system as an added component, in contrast, for the nature of the WECs it is more suitable to integrate the mooring system design process into the design of the WEC itself. As a consequence, taking into consideration new mooring requirements, WECs' characteristics and other indispensable aspects later discussed, the flowchart illustrated in Figure 1.1 was delineated. This

flow chart represents the proposed methodology for designing and analysing moored WECs. In practice, a numerical tool can be defined were input factors, represented by the geometry, the hydrodynamic parameters, the mooring system, the PTO and the environmental loads, are evaluated. The solution is found by solving a central equation of motion so that outputs concerning the estimated energy production and estimated forces can be obtained. One main extra step is required. This concern a validation task which may also include verification actions. Other two steps may be included, these concerns fatigue analysis, extreme loads analysis. Depending on the quality of the outputs, some optimisation procedures, with the aim of optimising the inputs, have to be done. Thus, the calculations for solving the equation of motion are re-run. The process is repeated until the quality of outputs is satisfactory. The validation step once it has been performed does not need to be repeated in every cycle of the analysis.

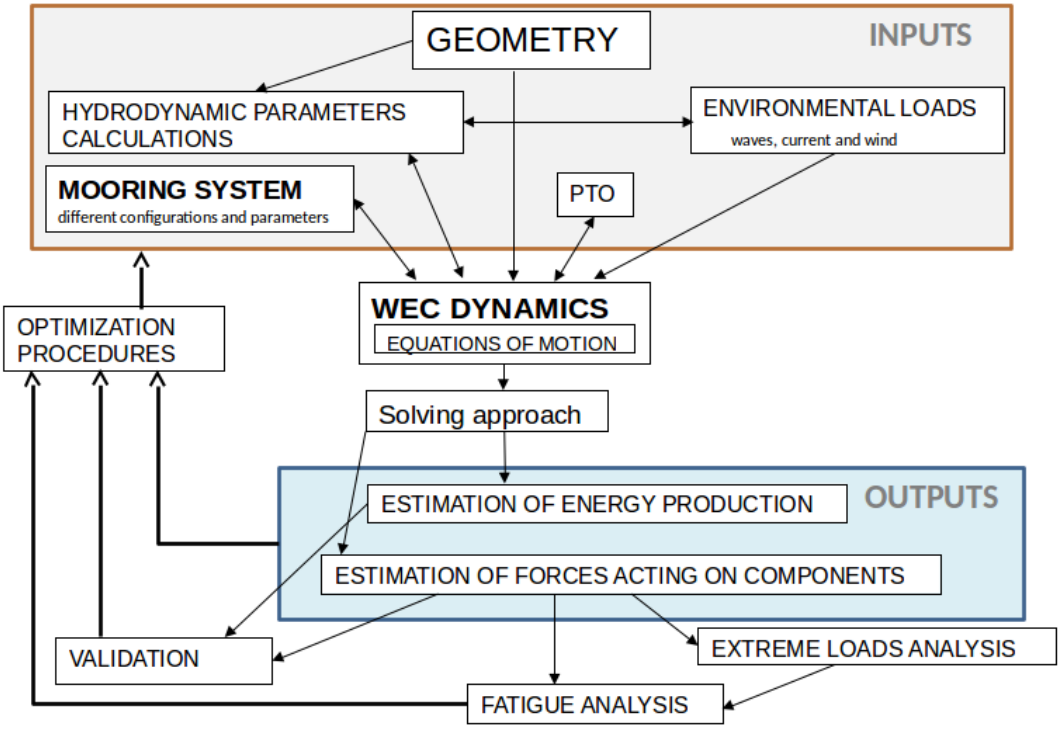

Figure 1.1: WEC and mooring system integrated design/analysis methodology proposed.

In order to show a possible way of application of the proposed methodology, this is applied to the specific case of taut moored point absorber WEC. It was chosen this type of WEC as this represents a well developed WEC concept. As it will be introduced in Section 2.3.1 there are various WEC projects of this type which reached a proper stage of commercial development. Meaning that this type of WEC technology is shown to be one of the most successful types compared to other types. Another main advantage, over other technologies, is that taut moored PA WECs can be packed close to each other; thus the energy extraction from a limited sea area can be maximised. For these reasons, a numerical tool for this specific type of WEcs was developed, verified, validated and used for giving an example of how the optimal system design can be investigated and identified.

Given the above reasons, the work presented in this thesis concerns numerical and experimental studies on analysis and design of mooring systems for WECs focusing on Earth-reacting taut moored devices. Supposing that the proposed methodology, summarised in Figure 1.1, can be a valid solution for design and analysis moored WECs, the following main PhD objectives were defined:

1. To explore the existing literature on the topic of interest both, from a broader perspective and with a specific focus on a particular type of WECs. *This objective is addressed in Chapter 2.*

2. To develop a numerical tool for practical simulating Earth-reacting wave energy converters of generic geometry. *This objective is addressed in Chapter 3.*

3. To develop different experimental set-ups and methods and to accurately simulate the considered generic Earth-reacting device at hydrodynamics laboratories. *This objective is addressed in Chapter 4.*

4. To obtain reliable and repeatable empirical results. *This objective is addressed in Chapter 4*

5. To verify and validate the numerical methods proposed. *This objective is ad-*

dressed in Chapter 5.

6. To show how the proposed numerical tool could be used to investigate the best parameters for optimum system design. *This objective is addressed in Chapter 6.*

These are the primary objectives of the PhD project. Objective 1 it was set for understanding the research topic and for gathering all vital information which may be of help for the understanding the area of study. While Objectives no.2 and no.6 are delineated to prove the validity of the proposed methodology itself, Objectives no.3, no.4 and no.5 relate to the validation of the numerical calculations. The latter is an important step required to put into practice the proposed methodology (Figure 1.1).

As a plus, from information gathered from the literature review, it was found to be important to delineate other extra objectives. These objectives relate merely to the contributions of this study regarding the experimental study:

- To investigate empirically: the motion response, the axial mooring line displacement, the mooring loads and the power absorption, for the considered device.
- To quantify the uncertainties of the experimental results of the different conducted experiments.

Both of these two additional objectives are addressed in Chapter 4.

To the best author's knowledge, for such device in consideration, there are no extensive published empirical data. For this reason, the first extra objective was set. Differently, the second extra objective was set to obtain supportive evidence towards the accomplishment of main Objectives 4 and 5.

Chapter 2

Mooring systems analysis and design for wave energy converters

In this chapter is addressed the objective of exploring the existing literature on the topic of interest both, from a wider perspective and with a specific focus on a particular type of WECs. At first in Section 2.1 a background on the general topics of wave power, on the mooring systems requirements and on traditional analysis techniques are discussed. Will follow a generic literature review section (Sec. 2.2), which is independent of the type of WEC and focuses on previous studies concerning mooring analysis of moored WECs. A set of valuable references to existing studies describing methods and theory for WECs mooring systems analysis are reported. The reason why this section was included is that due to the great rising number of different wave energy devices and the variety of the possible mooring problems, it is not feasible to delineate general design methods and procedures for designing and analysing for all different type of moored WECs. Thus, the main aim of the first part of this chapter is to provide a broad overview on the subject independently from the type of wave power technology and type of mooring system. Successively, in Section 2.3 a narrowed literature review on the specific case of Earth-reacting WECs is exposed. In fact, specific focus on this type of devices, which concern tight mooring configurations will be made in later

chapters, thus it was of particular importance to dedicate an entire section to only this type of WECs. Recent commercial projects concerning these specifics WECs are briefly described and specific arguments concerning numerical and empirical methods of interest are reviewed.

2.1 Background

2.1.1 Wave power

The coastal World's wave power resource is shown in Figure 2.1. This last, provided by Mørk et al. (2010), indicates annual average net power. It can be said that there is enough power in waves to provide energy to all world population (Ross, 1995). Considering these factors and given the high cost of existing wave energy devices, first offshore wave power farms will be located in nearshore sites at locations with depths less than 200 meters. In contrast, at higher depths, the mooring systems may be too expensive to be justified for the initial investment. In Figure 2.2 by green, yellow and orange colours are indicated suitable areas where possible future wave energy farms could be located.[1] As can be seen in this figure North Europe because of available depths and wave energy potential is a particularly suitable geographical area.

[1]The depths data was obtained from the Marine Geoscience Data System of Columbia University and was filtered as per Figure 2.2.

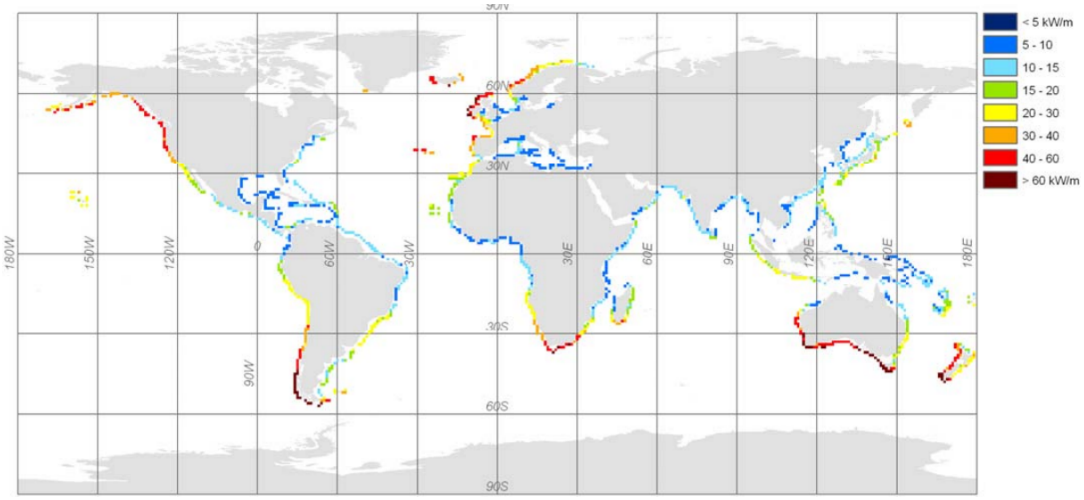

Figure 2.1: World coastal annual average net wave power resource (Mørk et al., 2010).

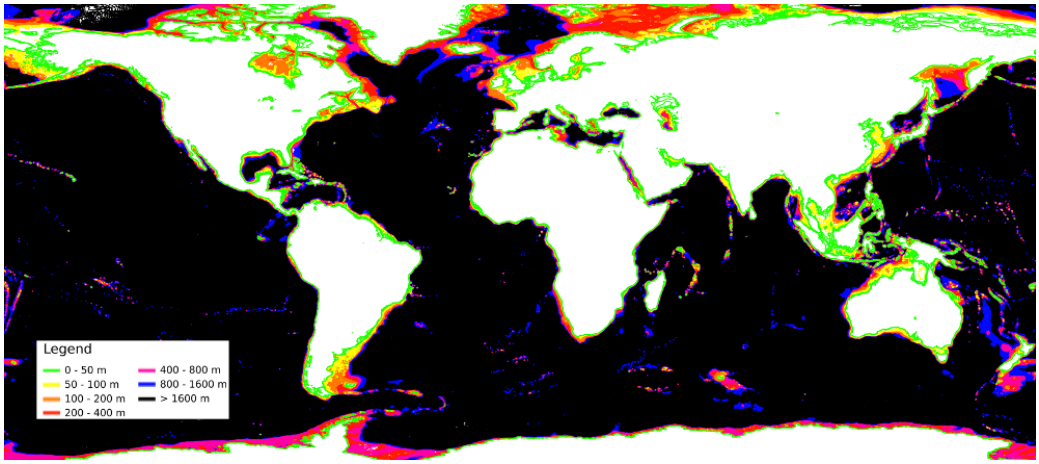

Figure 2.2: World's oceans bathymetry: contour lines for different ranges of depths.

General reviews on the whole theme of wave energy technology were produced by Falnes (2002) and Falcão (2010). Few books were written on the entire subject. In between, Falnes (2002) focused on the topic from a mathematical viewpoint, differently Cruz (2008) proposed a broad picture of wave energy prospectives and related theory by categorising different topics of interest.

First known attempts of extracting energy from ocean waves were made in 1799 when a first patent was registered, sequentially inventions started to accumulate. Among the primary precursors of the modern wave energy research of the last century, there

are Masuda, Xianguang, and Xiangf (1993), Salter (1974) (Ross, 1995). Through a scientific approach, they invented the first modern wave energy devices. Many others followed. The number of invented wave energy devices is consistent and, depending on the applicability of a particular invention and financial support that was available, each of these reached a determined stage of development. Nowadays, very few projects succeed to get at a commercial stage of progress.

In particular, intense research on wave energy was done starting in the late sixties. After there was an interruption, this corresponding to an oil price fall. In this period until about the early eighties, only academical theoretical research was progressing. Sequentially, during lasts decades, various studies, at specific intervals in time, were produced worldwide. The reason for these is related to the need of inventing new concepts so to obtain best power extraction capability, reliability, and economic feasibility. In fact, due to a series of matters such as the harsh environment, unpredicted phenomena, non-technical issues, the developments of wave energy devices, were often terminated before reaching the commercial stage of development.

While the world's wave energy resource is enormous, the wave energy technology is still very little used; this is due to mainly feasibility issues and due to high technology costs. For what concern practical matters, many of the episodes reported in the literature, concern the technical failure of particular components. The mooring system and the power take-off (PTO) are the most critical components. However while studies on the PTO are numerous, research on mooring system design and analysis for WECs is limited.

Diversely, studies on mooring systems for traditional floating structures are many; nevertheless, the application of existing knowledge to the case of wave power devices is not straightforward. Since past centuries a large number of studies have been carried out, these mainly relating to research on station keeping of vessels and traditional floating structures used within the oil and gas industry. As mentioned, there are very few published works concerning mooring systems for wave energy converters (WECs). The

design approach of wave energy converters was almost entirely focusing on dynamic models of a particular wave power technology concept, where the mooring system was treated as an added component. Existing methodologies, for conventional floating structures, were most of the times applied. Though in the case of WECs, different mooring system requirements exist. The reason for this is that due to the existence of different purposes of why a WEC is constructed and utilised, i.e. extracting and converting mechanical energy held by ocean waves into electricity possibly at a competitive and feasible price.

2.1.2 Station keeping requirements and categories of devices

There are various ways of classifying offshore wave energy devices, and each type of WEC has different mooring requirements. In the context of mooring systems analysis, we can categorise WECs between self-reacting, Earth-reacting, and semi-Earth-reacting (hybrid) types. Self-reacting devices are those which need mooring lines for passively and exclusively maintain the WEC in position. For this category, the primary aim of the mooring system is to keep the floating device into an area defined by a particular perimeter in a way that the device's energy extraction performance is not reduced. The required station keeping system for this type of devices can be referred as a passive mooring system. In other words, a self-reacting WEC requires a mooring system merely for conventional station keeping purpose. In this case, the mooring system is typically not considered an integral component of the entire wave energy capture system. On the contrary, Earth-reacting devices for their operation require a reactive type of mooring system that can entirely be considered an inclusive component of the power-take-off (PTO) system. Diversely, in the semi-Earth-reacting category it can be allocated every WEC that requires a mooring system which it is not essential to the PTO mechanism for operation, but in this case, the mooring system is an active component, meaning that its design affects power extraction performances to some extent.

The main mooring system requirement shared by all three defined WECs categories

relates to the keeping of the device into a defined area. Thus, permitting that each WEC is not drifting away, interfere or collide to close devices due to environmental forces acting on the moored system. For environmental forces, we refer to the action of wind, currents, and waves. These forces are cyclical stochastic loads, which can be numerically modelled as a combination of multiple sinusoidal components of different phases and amplitudes. While for average weather conditions environmental loads tend to be more regular, for severe conditions these tend to be increasingly more stochastic. The environmental forces can be categorized between low and high frequencies loads. For high-frequency loads, it is, in general, referred to first order wave frequency loads. Instead, low-frequency loads are generally referred to those associated with: wind, marine currents and second order wave drift forces. For normal weather and sea conditions, the magnitude of loads due to the wind and marine currents is considerably less than those relative to waves. Thus, considering the scope of this thesis, only loads due to waves were treated during this project.

In general, the mooring system is a critical component which needs to be very reliable so that the overall business risk can be reduced. While for conventional floating structures the mooring system can be considered as a relatively minor cost (3-5 % of overall structure cost), for a WEC this can be a significant cost (up to 15% of total cost) (FitzGerald, 2009).

Mooring system design requirements for conventional floating structures are still valid for wave energy converters; indeed, for these new type of devices, additional requirements must also be considered. For the conventional type of floating structures, main technical requirements concern the creation of a mooring system that has to be: affordable and reliable; made to resist for relatively long operative periods; and designed to sustain high repeated loads, in particular, when critical extreme environmental conditions exist. For the WECs the following additional topics must be considered for defining the full list of mooring system requirements:

- The optimal power performance design (optimum mooring system dynamic re-

sponse and optimum mooring compliance);

- Relatively long system life (over 30 years);
- Minimum maintenance for reducing costs for operation;
- Access for maintenance of mooring systems for single devices deployed in arrays.

The second and third topics represent requirements which concern substantial reduction of the overall financial cost. In fact for making a wave energy power project viable in economic terms, and considering that the return period for wave energy farms compared to other renewable technologies usually is extended, the project life should be lengthened as much as possible. The mooring system should be designed so that this would last as long as economically feasible before its replacement is needed. At the same time, for what concern maintenance operations and replacements of single mooring system components, the best mooring design would be the one which requires the least maintenance, so that overall cost for producing energy is reduced.

As a plus, independently on WEC technology mooring systems special requirements concern allowing tidal height excursion and installation/removal operations.

2.1.3 Type of mooring systems for wave energy converters

Mooring systems can be of different types. For a full list of the conventional types of systems reference to Barltrop (1998) is made. In general, we can distinguish between rigid, tethers and catenary mooring (slack type) systems. While rigid mooring, due to their cost, can be used for WECs deployed in relatively shallow waters (ca. less than 30 m), tethers and catenaries types of mooring are more convenient for relatively deeper waters. Putting apart rigid mooring systems that are very design specific, tethers and catenaries based systems can be of various types. For single or multiple mooring lines systems a combination of weights and floaters can be used. Elastic or almost inelastic mooring lines can be chosen for particular WEC type.

In Figure 2.3 is reported an overview on the possible application of types of mooring depending, installation depth, type of WEC technology and device weight. With colours are indicated the suitability for the particular type of WEC technology. Light blue, grey and orange are used to indicate suitable mooring systems for respectively Earth-reacting, self-reacting, or both types of WECs. This figure was defined based on information provided by FitzGerald (2009).

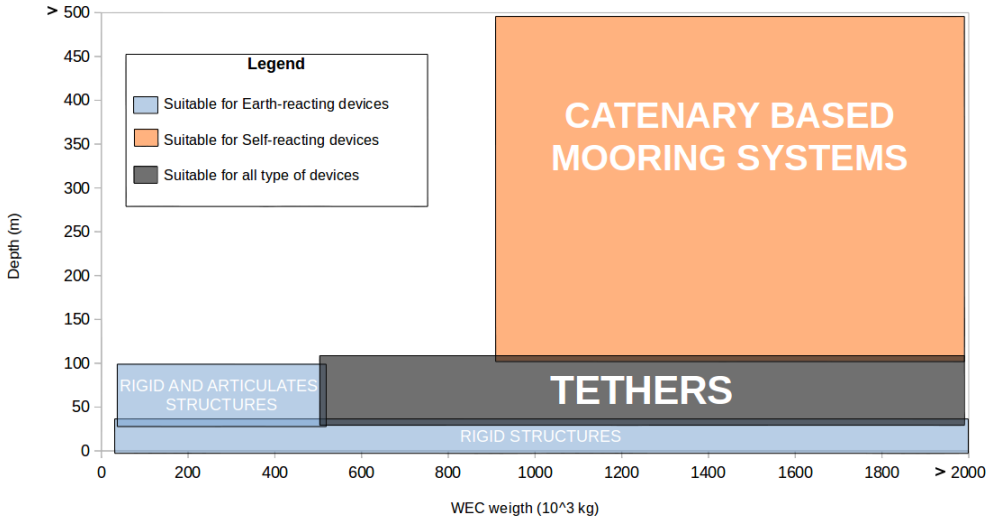

Figure 2.3: Scheme showing indicative usage of different mooring systems depending on water depth and WEC weight. This was constructed by information provided by FitzGerald (2009)

.

In fact, depending on a specific WEC a particular type of mooring system would suit more than another. In general especially for self-reacting WECs, common mooring systems used in conventional floating structures may not be the best option to adopt. For instance, a simple single mooring line chain would not be suitable to secure a motion dependent WEC. Precisely, for a self-reacting WEC the extra length of the mooring line needed to reliable secure on station the device, may dictate high downward mooring force and this may negatively affect the entire system power performances. As a consequence, other more advanced mooring system solutions can be considered, and the complexity of the design analysis may rise significantly.

Five possible basic mooring lines types are represented in Figure 2.4. The first type of mooring line (Type A) is a single tether. Tether mooring systems compared to other types permit of anchoring a floating device into a more constrained area. This system can be a valuable solution when its required to install as many devices as possible into a limited sea area. In fact, with this type of mooring, the devices can be moored near to each other so that more devices can be deployed and the extraction of wave energy from a limited sea area could be incremented. Despite this, for tether mooring systems is required that the floater holds extra buoyancy so that a mooring pretension can be implemented. In this way snatch loads, happening when the tension of the mooring line varies from zero to large values, are avoided. As the pretension is considerable large, tether systems also require particular anchors that need to counteract the vertical loads. As a consequence, gravity based, drag-embedded or simple pile anchors, which usually are more convenient for large devices moored with a single tether, can be impractical. The typical solution is to use plate anchors, but the cost involved is higher.

In general, traditional floating structures having tethers as mooring systems are referred as Tension Leg Platforms (TLP). In order to implement the pretension, the TLP are designed so that a considerable part of the hull is underwater. Due to the dimensions of TLP this is possible. in fact given the TLP design and the pretension implemented, even when most extreme waves collide, no snatch loads usually occur. However, concerning these floating structures, the WECs are generally of smaller size and their draft is limited thus for implementing tethers design some differences exist. Taking into account these reasons and given WECs's dynamics, for implementing tethers, is required to add, to the mooring line, extra elastic elements. These elements, e.g. a spring component, are needed so to allow floater motion. The pretension, in this case, allows an initial extension of these components determining a useful range for axial mooring displacement.

The second sketch Type B of Figure 2.4 illustrates a simple catenary mooring line. This type of mooring is normally constituted by a chain which assumes a curve, referred to as catenary. The shape is defined by its weight and the horizontal pull of the floating

structure. The chain alone, in this case, exerts a mooring restoring force. It has the advantage to be very simple. Instead, the main disadvantages are that, due to the weight of the chain, the floating device is pulled downwards and that the chain for certain length touches the sea-floor. As a consequence, this may significantly affect power performance, and it may have a consistent environmental impact on the seabed Environment. This type of mooring is further discussed in Section 2.1.4.

Types C, D and E of Figure 2.4 relate to configurations normally more suitable for Self-reacting WECs, these include floaters and weights elements. The main advantage is that by using these configurations, the mooring line peaks tension may be substantially reduced. This reduction is possible thanks to the fact that peak loads are dissipated by hydrodynamic forces acting on these extra floaters and weights components, as these last moves into the water. Depending on the design, different mooring restoring force can be obtained. For these configurations, the first segment, usually constituted by a chain attached to the anchor, does not touch the seabed. As a consequence, the chain and the Environment are more preserved. Furthermore, such configurations permit segmenting the mooring line with different mooring line materials. Thus, to a certain extent, the cost may be reduced. Despite this, extra costs may exist due to long lines. Besides, as more critical mooring components are added, the overall mooring reliability may decrease, e.g. as when extra shackles for connecting segments are added.

The main advantage of configurations indicated by Types C and D to the simple catenary mooring (Type B), is that the extra floater element due to its buoyancy it counteracts the vertical downward load due to chain weight. Despite this, the extra floater as it floats (Type C) may dissipate some of the wave power from an upstream position, thus affecting the power capturing performances of the device. In contrast in Type D, the floater is submerged, so that in this case the device is not covered by this floater element, thus preserving part of the power in waves which would in case of Type C been missed. Instead, Type E compared to Type D varies by an extra weight element. With this last configuration, more compliance can be given to a moored WEC, in this way radically reducing loads at the anchor. Despite this, the space required for mooring

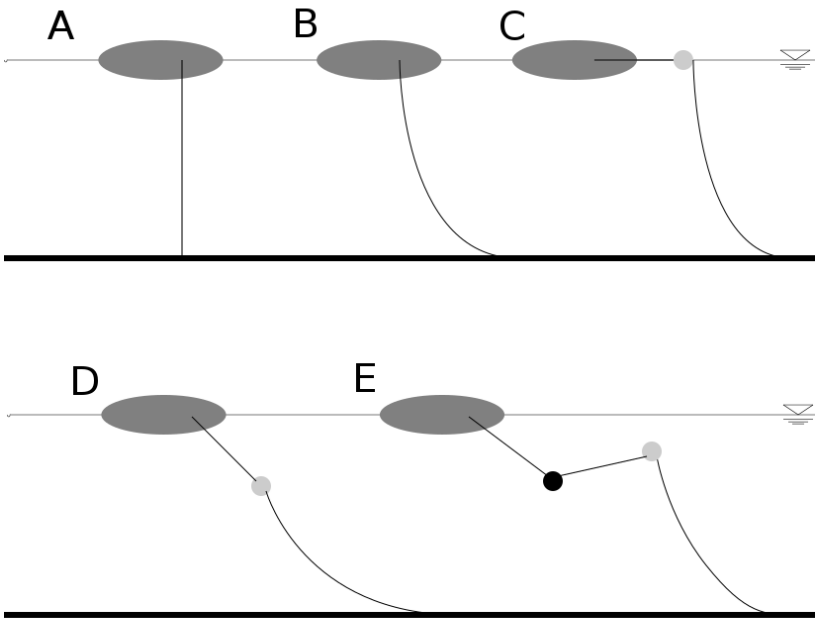

Figure 2.4: Common types of single line mooring systems suitable for WECs. Gray and black circles represents floaters and weights

and the cost would substantially increase.

2.1.4 Conventional theory review

In this section a brief discussion on fundamental mooring analysis theories used for standard floating structures is present. More extended literature review on the specific topics of mooring analysis and design for different WECs types and taut mooring line configurations can be found respectively, in Sections 2.2 and 2.3.

First traditional step in the design process of a mooring system are static calculations. In this case the floating structure is assumed to be stationary. For instance considering a single catenary mooring line (as represented in Figure 2.4 Type B), the shape and design parameters can be initially estimated by static calculations. Ignoring hydrodynamic forces acting on a slack chain and assuming the chain is inelastic, we can derive the

following equations. These represent the static equilibrium configuration of a single line (Chakrabarti, 2005; Journee and Massie, 2001).

$$s = \left(\frac{T_H}{w}\right) sinh\left(\frac{wx}{T_H}\right) \tag{2.1}$$

$$T = \frac{w(s^2 + d^2)}{2d} \tag{2.2}$$

$$T_v = ws \tag{2.3}$$

$$T_H = Tcos\phi_w \tag{2.4}$$

where, s is the length of suspended line, w is the submerged line weight per unit length, x is the horizontal displacement of the moored device, d is the water depth, T_v is the vertical component of the line tension (at the top end), T_H is horizontal component of the line tension (constant along the line) and ϕ_w is the angle between a tangent line, at any point, and the horizon.

In order that the catenary mooring line is operating effectively, this need to be long enough. For the simple case of a single catenary line (e.g. chain) the vertical component of the tension at the lower end needs to be zero. In fact, for anchoring issues, counteracting the horizontal pull instead of the vertical pull is more convenient. This solution is possible by using a catenary mooring. With the increase of environmental forces acting on the floating WEC, the catenary mooring line shape will be less curved, until the chain is all lifted. This latter case has to be avoided otherwise load at anchor may drastically increase. As a consequence, the anchor's stability may be compromised causing mooring failure and drift. For having a reliable design, the length (s) and weight (w) of the catenary line need to be increased. For this reason, the horizontal distance, between the anchor point and the floating structure, usually is in the range of 5 to 20 times larger than the water depth (Chakrabarti, 2005). Despite this, the available areas for wave farm are limited, thus having such long catenary lines may not be the best solution for optimally mooring many devices close to each other. Other solutions may permit of moor more devices in such limited areas.

Previous equations assume that the catenary line is inelastic and this may be a limiting factor. Either for precisely considering elongation or for entirely design a new slack elastic mooring line, further mathematical terms should also be taken into account. In the simple case of a single chain, the length of the slack mooring line become $L = L_0 + \Delta L_0$, where L_0 is the initial cable length and ΔL_0 is the increment in length due to increased tension during operation. The static solution for single or multiple elastic lines can be found by discretisation of the line and by using numerical procedures, such as the *Regula Falsi* (Journee and Massie, 2001).

Another method consists in applying the quasi-static approach; this assumes that the floating structure is slowly moving, only horizontal displacement is considered. As for the static analysis, in this case, all dynamic effects of floating structure mass, structural damping and hydrodynamic damping are neglected. This approach leads to acceptable results for shallow water cases and when the motion of the floating structure is limited (Mavrakos et al., 1996). Assumptions related to this approach may normally be justified for large floating structures when fatigue analysis need to be performed, only for normal sea conditions.

The next step relates typically to analyse the moored structure by a dynamic approach. In general, the advantage is that the methodology entirely captures the mooring system and the floating structure dynamics. In this case, all dynamic effects of structure mass, added mass, structural damping, hydrodynamic damping and structure-fluid interactions can be included in the analysis.

When a dynamic approach is implemented, the mooring system can be modelled in different ways. For fully estimate coupled dynamics of the WEC-mooring system complex time-domain based methods and mathematical formulations, taking into account multiple DoFs, were developed by many authors. For instance, reference is made to Ran, Kim, and Zheng (1999) who compared their coupled dynamics approach to quasi-static results; to work carried out by Idris, Leonard, and Yim (1997) related to the analysis of a tethered buoy systems; and to the model proposed by Pascoal et al. (2005) for

coupled motion analysis of a structure and its mooring system. More in details, for high sea-states and high depths, due to drag forces induced by waves and currents on mooring lines, the dynamic tension may increase considerably and results obtained by a quasi-static model are generally not sufficiently accurate. A method was invented by Van Den Boom (1985) which consist of the discretisation of a mooring line by seeing it as multiple elements each constituted by concentrated mass and an ideal spring with no weight. As shown in Figure 2.5 N elements ideally discretise the mooring line. A spring and mass form each element and eventually by an extra spring and a damper. Elements of the line which are permanently or temporarily in contact with seabed also comprehend a bottom spring and damper which are needed to simulate the effect of bottom friction. In brief, the method consent of applying a constraint of dynamic equilibrium to each mooring line element and consequently a set of equation of motions can be formulated. Successively a time-domain solution scheme, usually using finite difference methods, can be adopted for integrating the equations of motion. By increasing the number of elements used for discretisation more precise line dynamics results can be computed. Despite this, for improving line dynamics results, thus increasing results precision, the following further aspects are also fundamental to consider: accurate evaluation of the dynamics of the floating structure, estimation of environmental forces, also including viscous effects on floating structure and mooring system. More recent work based approaches, based on the discretisation of mooring lines, was done by Raman-Nair and Baddour (2002) and Hall and Goupe (2015). Similarly, Lau, Ji, and Ng (1990), Ran, Kim, and Zheng (1999), Aamo and Fossen (2000), Yang et al. (2012), and Gutirrez-Romeo et al. (2016) studied and developed methodologies focusing on the finite element method.

However, these methods were usually developed and applied for designing complex mooring systems for large traditional floating structures to be moored in deep waters, so with substantially different requirements concerning WECs. In general, these methods may provide precise results, but are in general quite complicated to implement.

In the case of WECs due to their characteristics dynamic based methods compared to

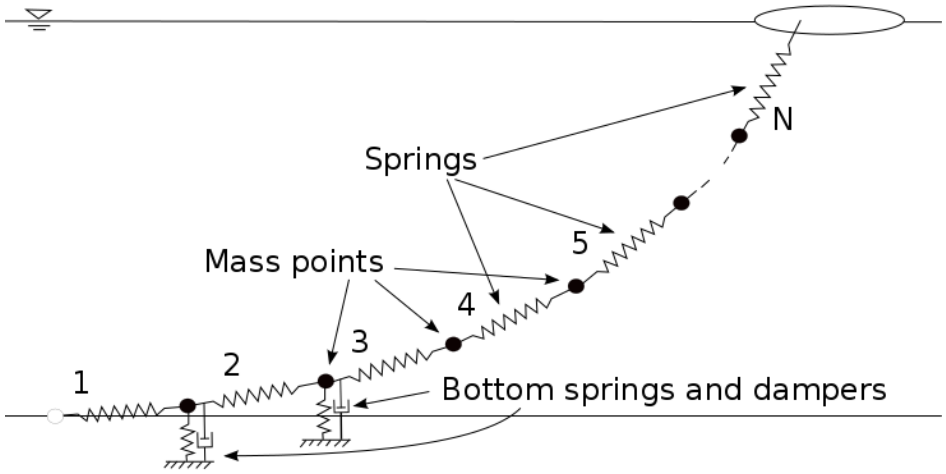

Figure 2.5: Discretization of mooring line by N elements (Van Den Boom, 1985).

other mentioned methods are more appropriate. In the next subsection is explained why fully dynamic methods are more suitable to be used for moored WECs analysis.

2.1.5 Advantages of fully dynamic methods

Due to WECs' peculiar characteristics concerning traditional structures, fully dynamic approaches for analysing moored systems are far better suited. In fact, WECs are in general small structures, and their mass usually is much less than the one of conventional structures. Besides, most of WECs for operation require mooring compliance. Meaning that the motion of WECs is relatively much more compared to traditional cases. Thus, in order to quantify the mooring loads, it is essential to take into account also the floating device dynamics. In contrast, if static or quasi-static methodologies are implemented these may lead to results which would be not very representative of the problem analysed.

A further point concerns that, given to the nature of WECs, concerning the mission of absorbing wave power, during the design process it is essential to estimate the power absorption in the most realistic sea model. Fully dynamic codes allow modelling the

device in a way which is more representative of the real life. These codes permit of including the dynamics of the floating WEC into the numerical simulation, as a consequence the effect of the mooring restoring force over the power performance prediction can be correctly included. Without using dynamic approaches, power absorption estimation may be incorrect.

When dynamic approaches are implemented, more effects can be taken into consideration. In this way, results are more accurate. For instance, the transient effect of the mooring restoring force can be analysed only with fully dynamic codes. Similarly, when dynamic approaches are implemented, usually, it is possible to include the effect on dynamics due to nonlinear power-take-off (PTO) systems.

For the specific case of Earth-reacting WECs, it is even more important to use fully dynamic approaches. The first reason for this is that the mooring system for such WECs is an active component. As an active component, this last can be analysed as an integral part of the device. Solving the equation of motion of the entire system including the mooring component is essential for obtaining predictions related to floater displacements, structural forces, power absorption and mooring loads.

As in later chapters, particular focus will be made on Earth-reacting WECs, in later Section 2.3, studies and methods concerning fully dynamics methods to be applied on this type of devices, are more in-depth treated.

2.2 General literature review

In this section, a general literature review concerning the broad topic of analysis and design methodologies for mooring system of wave energy converters is presented. Previous work concerning all types of WECs is briefly reviewed. In contrast, a specific literature review only on Earth-reacting type of WECs and on taut line studies is described in Section 2.3.

2.2.1 Self-reacting and semi-Earth-reacting wave energy converters

For what concern studies on mooring systems for self-reacting and semi-Earth-reacting WECs, often combinations of catenaries, floaters, sinkers, and tethers were considered.

Few researchers approached the theme by aiming at finding general solutions, providing guidelines and proposing methodologies for analysing and design mooring systems. Harris, Johanning, and Wolfram (2004) presented a discussion on which mooring system configuration can be more suitable depending on the type of wave energy technology considered. Similarly, Johanning, Smith, and Wolfram (2006) proposed a preliminary mooring design methodology for different types of offshore WECs. Again, Johanning, Smith, and Bullen (2007) focused on the damping effect of the mooring system affecting WEC performances and found that by implementing a quasi-static approach, good results can rarely be obtained. In a more general way, Fitzgerald and Bergdahl (2008) presented a method for the assessment and analysis of mooring configuration for a generic WEC. Diversely, Bachynscki, Young, and Yeung (2012) through a frequency-domain analysis, taking into account irregular wave loads and wave statistics, studied a cylindrical moored WEC; and Gilloteaux and Ringwood (2009) studied, through time-domain analysis, the effects of wave directionality on a generic point absorber connected to a catenary mooring system formed of four lines.

2.2.2 Experimental studies

Many experimental studies on WECs were undertaken, these most of the times did not include the mooring component. The reason for this concerns complexities in manufacturing the mooring component at laboratory scales. As a consequence, the mooring component if present was usually simplified. In fact, when the effect of the mooring system was taken into account, most of the times, this was done by using springs or elastics, which merely kept the WEC in position.

Only a limited number of studies were focusing on empirical work specifically on moor-

ing systems for WECs. Johanning, Smith, and Bullen (2007) conducted numerical simulation and performed water tank experiments at 1:10 scale. Differently, at real-scale, Vickers and Johanning (2009) performed experiments for assessing single chains to be used for a WEC-mooring system. Krivtsov, Linfoot, and Harris (2012) empirically studied the effect of the shape and size of a mooring cable by looking at forces exerted by this component to the WEC. More recently, Harnois et al. (2015) validated a numerical tool including a compliant mooring system made of multiple sections and lines.

For a specific review on experimental studies on taut moored devices refer to Section 2.3.4.

2.2.3 Mooring systems for specific wave energy converter designs

Almost all early research on wave power focused on wave power hydrodynamics and PTO technologies. However, very few published studies exist which also deal with the mooring system. One of the few exception concern work related to the Edinburgh Duck. This device concept was extensively developed in both, empirical and theoretical ways. For the Edinburgh Duck invented by Steven Salter, various optimisation methods and mooring configurations were studied. In particular extensive work was carried out from the seventies to the eighties, during the Edinburgh Wave Power Research Program, and in the nineties aiming at systematically improving the Duck WEC (EWPP, 1987; EWPP, 1984; Young and Pollok, 1985). Initially, the PTO was actuated only by the pitching motion; thus the Duck may have been considered an Earth-reacting type of WEC. Later, by introducing the gyroscopic PTO, the device became of self-reacting type and progressively more complex options were explored by Young and Pollok (1985). Extracting energy from different degrees of freedom by including added stiffness to peculiar DoFs and complex control was further investigated by Pizer (1994). An extensive mooring study was also performed for an Edinburgh Duck to be deployed with a spine mooring configuration (EWPP, 1986). The experience gained from studies on

the Edinburgh Duck demonstrates that advanced control of motion can lead to excellent results regarding efficiency. Compliance and stiffness determined by the mooring lines affecting the entire coupled WEC-station keeping system are key factors.

With recent new interest in wave power, mainly in the private sector, various researchers focused on mooring systems design and analysis during wave power projects of particular WEC. Fonseca et al. (2009) studied a mooring system with synthetic ropes for a double-body device named Flow WEC. During the same period, Fitzgerald and Bergdahl (2009) analysed a rigidly moored articulated tower WEC in shallow waters. Later Muliawan et al. (2011) analysed the effects of different mooring lines and PTOs configurations on the Wavebobs WEC performances. Differently, Elwood et al. (2011) estimated energy production of a taut moored dual-body WEC using a model created with the Orcaflex (Orcina Ltd.) software and performed water tank experiments. Parmeggiani, Kofoed, and Friis-Madsen (2011) studied mooring loads for the Wave Dragon WEC, which is a semi-Earth-reacting type of device. Different types of mooring systems for a oscillating water column (OWC) type of offshore WEC called Seabreath were analysed by Martinelli, Roul, and Cortellazzo (2012) who proposed a mooring design method and performed experimental tests.

2.2.4 Arrays of moored wave energy converters

Single stand-alone devices can provide limited power and studies have confirmed that increasing size of an offshore floating WEC is not always beneficial. Independently of the type, in almost all cases multiple devices can extract more energy for a less capital cost. Thus, a well-designed mooring system for arrays of particular WEC may in a first-place enable the considered technology to be economically viable rather than make the overall cost to be reduced. Furthermore, an optimal mooring system can allow the entire structure to be advantageous in financial terms especially for deep ocean sites (refer to Figure 2.2 for world's oceans bathymetry). Nevertheless is almost inexistent the number of studies on arrays of WECs and mooring systems for multiple devices

configurations. In between the few exemptions there is the work of Vicente et al. (2009), who from a theoretical perspective studied the interactions between, firstly three and after seven, point absorber WECs, by formulating and solving the problem written in a frequency-domain formulation; and there is the study of Gao and Moan (2009) who investigated the topic concerning WECs arrays by performing a set of experimental tests.

2.2.5 Design for extreme conditions survival

Other authors focused on mooring lines analysis aiming at evaluating extreme environmental loads. In particular, Gao and Moan (2009), by concentrating on survivability issues, studied mooring systems for multiple WECs in an array configuration. Parmeggiani, Kofoed, and Friis-Madsen (2011) studied extreme mooring loads for the Wave Dragon WEC for implementing a survivability mode strategy. Through a set of experimental tests Hann, Greaves, and Raby (2015) focused on snatch loads due to wave groups acting on a point absorber WEC moored by a single tether.

2.2.6 Reliability and efficiency

Fatigue analysis and efficiency are two critical aspects of WECs design. Usually the more a WEC is efficient regarding power extraction performances, the more WEC's components are under fatigue. In order to limit the cost of energy production and to make this cost competitive with other renewable energy technologies, WECs to have to be designed to sustain life at sea of at least c.a. 30 years. This lifetime usually is more than the designed lifetime for conventional floating structures.

Fatigue and system failures prediction

Available methodologies and standards for mooring systems design, of conventional floating structures, concern the use of high factors of safety. In most cases, these high

factors were applied due to risks concerning human life losses and due to probable environmental disasters. Both risks existing because of the possibility of accidents which may be caused by a failure of the mooring system. In the case of WECs, these factors may not be suitable to be applied. The main reasons for this are that WECs are unmanned and that the risk of an environmental disaster is negligible. In fact, WECs when functioning does not require operators on board, technicians need to access WECs usually only for maintenance during safe weather conditions. Thus no significant direct risk to humans on board WECs exists if the mooring system fails. Besides, even if a failure generally occurs the marine Environment may be very little impacted. For instance, while the environmental impact due to an oil spill incident usually is an enormous disaster, the impact on the Environment due to a failure of a WECs, in comparison, is of little concern. As a consequence with respect to traditional structures, substantial differences and minor risks have to be taken into account. In the case of mooring failure a WEC would drift away this would determine safety concerns for marine traffic. To partially overcome this possible issue, practical solutions can be implemented. For example: to immediately alarm competent people so that they can soon intervene, and to track drifting devices with available technology. In other words, it is maybe worth finding new safety factors to be applied, new fatigue prediction methods and new standards to be developed.

Compared to traditional structure it remains essential to predict fatigue of WECs' components. The main reasons for this concern the estimation of financial uncertainties and other different relatively minor safety risks. Main WEC critical components which would produce substantial economic losses are the PTO and mooring systems. Thus long and short terms fatigue predictions for these components are still essential. The WEC's design life is typically set around 30 years which compared to traditional floating structures is a long operating period at sea. Besides, due to the new characteristics of WECs, mainly concerning their dynamics, it would be sensible to develop new fatigue predicting methods more suitable to analyse WECs and their mooring systems.

In this area of study Thies, Smith, and Johanning (2012) applied the Bayesian statistical

framework for identifying magnitudes and types of significant uncertainties of generic moored marine renewable energy devices. Afterwards Thies et al. (2014) defined an approach for the prediction of the fatigue life of mooring lines when data from sea trials are available.

New materials and mooring components

Given the peculiar mooring system requirements of WECs, recent research focused on new materials. In general, mooring lines can be made of steel, synthetic ropes and organic fibres (Weller et al., 2013). Few materials for manufacturing mooring lines for offshore marine renewable energy devices were investigated by Ridge, Banfield, and Mackay (2010) and Weller et al. (2015) who evaluate mooring lines made of synthetic fibre ropes. They performed fatigue tests, measured strength, and stiffness for various types of cables. Cost comparisons were presented, and they concluded that nylon ropes could be an enabling technology rather than just another economically feasible option.

Novel types of mooring cables were recently developed. Gordelier et al. (2015), introduced the 'Exeter mooring' made with an elastomeric core. Similarly, Thies, Johanning, and McEvoy (2014), present a mooring component with an elastomeric part and peculiar thermoplastics compressive elements.

Dynamic positioning

Regardless of the WEC technology, it is reasonable to design an active dynamic controlled (slow motion) type of mooring system (Harris, Johanning, and Wolfram, 2004). For instance, a new type of active mooring system which changes mooring cable properties (damping and stiffness) to desired values was developed by Luxmoore et al. (2016).

In general, it is proposed that for WECs station keeping system design, three existing concepts are worth to be investigated. The first (Figure 2.6 Type A), concerns the strategy of tuning the mooring length of an Earth-reacting WEC so that this is

submerged at variable depths. Consequently, the environmental forces acting on the floating structure are reduced, mooring line loads are limited, and energy extraction is increased. For example, if lowered at a certain depth, a point absorber WEC can continue operating even when extreme sea states occur. In fact, during extreme sea states, the mooring line tension dramatically varies in short time frames and presents the highest possible peaks. In the worst case snatch, loads can happen. These lasts represent sudden extreme variations of the mooring load. In the case of taut moored WECs, snatch loading may occur when lines go slack or when end-stops terminate the axial mooring displacement. During snatch loads, in particular, mooring components experience dynamic loads amplified up to several times the usually applied tension. By implementing the mentioned concept (Type A) peaks of the mooring tension can be reduced and thus snatch loads can be avoided. Furthermore, the mooring system can be tuned for ensuring optimal operation during different tidal heights. On the other hand, if the floater is submerged below the free surface, a significant disadvantage is that the floating structure should withstand high external pressures, similar to submarines. Also, extra expensive components such as winches need to be included. Thus significant extra costs needed to strength floater's structure and for other components, do exist. The use of active winches in some cases may be justified but, apart from the fact of introducing extra critical components, the implementation of these would add further complexities to the entire system. Active winches for their operation, even if operated at low speed, would require suitable power source available on WECs. Besides, these components would require extra maintenance. For self-reacting WECs, another active controlled mooring systems can be considered (Figure 2.6 Type B). This concept regards the strategy of automatically elongating or shortening one or multiple slack mooring lines by keeping the device in surface. In this case, during extreme weather conditions, the mooring cable can be extended and therefore loads at anchors and fairleads are reduced. A third concept (Figure 2.6 Type C) concerns the increment of energy extraction (for wave direction dependent WECs - both Earth and self-reacting devices) by tuning the mooring system so that the WEC is optimally facing incoming waves. Mainly, due to the interference of current and wind, particular WECs designs

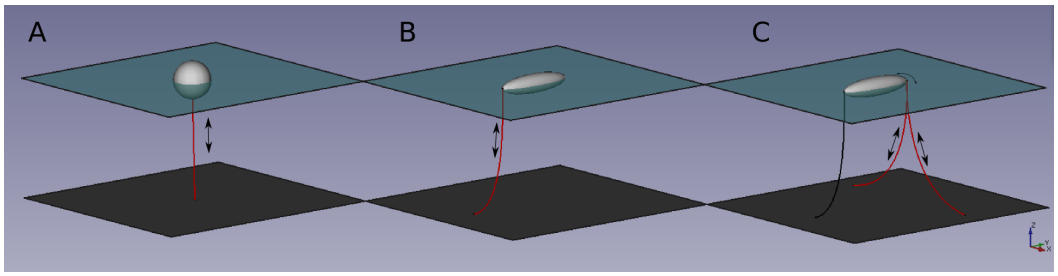

Figure 2.6: Active mooring system concepts. In red are shown the lines which varies length automatically.

may not optimally orientate to the dominant direction of incoming waves which allows these systems to obtain the designed absorption efficiency. For this purpose, in the case of using active mooring systems, some mooring lines are shortened and other elongated by an automatically controlled winch, implying the WEC to be oriented so that annual energy extraction could be maximized.

The extra costs involved for extra components needed for dynamic positioning in some cases may be justified. The reasons of this are: the possible increment of system efficiency; the possibility of keeping the device in operation also during severe sea state during which otherwise the device would be set on idle; and possible reduction on maintenance costs concerning standard mooring components if the implementation of dynamic positioning systems would give benefits in terms of reducing fatigue. Thus the amortisation period of the entire system cost, when these extra components are added, may in some cases be reduced.

2.3 Specific literature review

In this thesis in next Chapters 3 to 6 particular focus on an Earth-reacting point absorber is given, thus this section is dedicated to the review of WECs theory concerning such type. A specific review, on only theoretical and experimental matters related to the studied taut moored Earth-reacting device, is presented here. In this section is also exposed all relevant information needed as background requisites for approaching later

chapters.

2.3.1 Commercial Earth-reacting devices: recent projects

At present, there are various existing Earth-reacting WECs projects under development. Here next are briefly described four taut moored Earth-reacting WECs which are between the most developed at a commercial stage. These are named: the Seabased, the Ceto, the BOLT Lifesaver and the CorPower. The WECs discussed are illustrated in Figure 2.7.

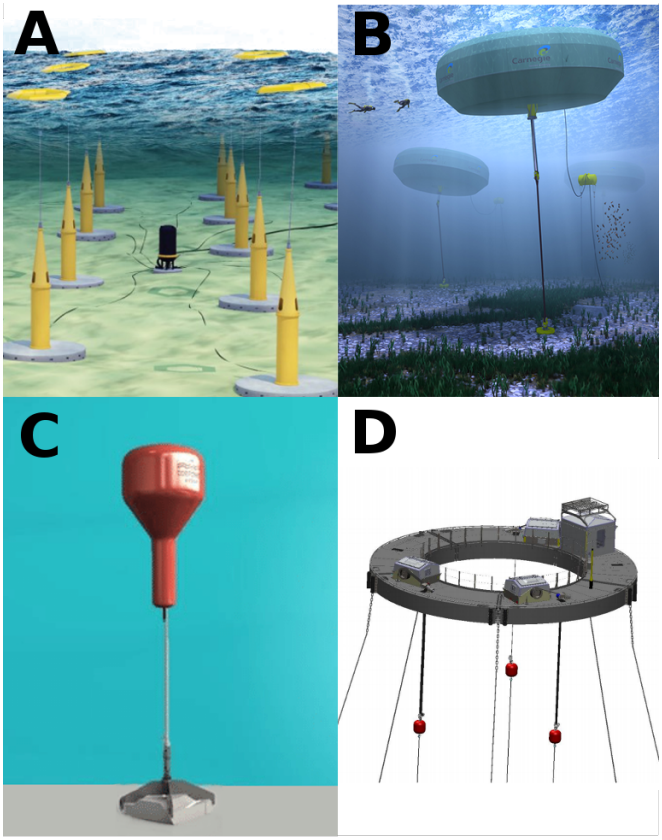

Figure 2.7: The Seabased (A), the Ceto (B), the CorPower (C) and the BOLT Lifesaver (D) WECs

The *Seabased* is a bottom-referenced heaving buoy WEC, the Seabased industry AB company developing this device is based in Sweden and, at present, has active projects

in different worldwide locations. The Sea-based device is shown by Letter A in Figure 2.7. This consist of an axisymmetric floating structure connected at its centre through a mooring line to a fixed unit which stands on the sea floor. The fixed unit is formed by a steel hull where inside is located the power-take-off (PTO) system. The PTO consist of a linear generator which is activated by the mooring line thanks to the pull of the moving floating structure.

Similarly, the *Ceto* device is a bottom-referenced submerged heaving buoy WEC. The buoy, in this case, is fully submerged, as illustrated by Letter B in Figure 2.7. This WEC is currently in development in Australia by Carnegie Clean Energy Limited. It works similarly as the Seabased device, but in this case, the PTO system is hydraulic. Also for this device, the floater is connected to a fixed unit by a taut line. The hydraulic system is located in the floater. As hydraulic pumps are activated by the movement of the floater, wave energy is converted in mechanical energy in form of high-pressure fluids. Depending on the type of Ceto device the extracted mechanical energy is converted into electricity through turbines or this form of energy is used for desalinisation of seawater.

The third WEC indicated in Figure 2.7 by the Letter C is the *CorPower* device. The concept, in this case, is similar to the previous WECs. The floater also, as previously, is connected to the sea floor through a taut mooring line. The PTO system, in this case, is a mechanical drivetrain with a pneumatic element. The linear heaving motion is converted into rotation by the PTO system. This PTO system, also, includes a phase controller, this is needed for improving the WEC performances.

Slightly different is the *BOLT Lifesaver* point absorber WEC developed by Fred. Olsen BOLT Sea Power in Norway. This WEC, as indicated by the Letter C in Figure 2.7, is formed by a circular floating structure where over this all machinery is allocated. This device is connected to multiple tethers. While most of the tethers are needed only for mooring the structure, three tethers are connected to three independent PTO rotatory systems. These systems operate independently, meaning that if one fails the others are not compromised.

2.3.2 Theoretical work on Earth-reacting devices

In general, for the case of Earth-reacting devices, designed to be deployed in intermediate deep waters, tethers mooring lines are usually a requisite. Advantages of using this type of mooring system are mainly that this may be the most cost-effective solution and that this allows for installing multiple devices in a limited area compared to other mooring options. Only moored Earth-reacting WECs are discussed here; however, do exist other types of Earth-reacting devices which are rigidly connected to the seabed. These lasts are not treated in this thesis. Here next only recent studies on moored Earth-reacting point absorber WECs will be briefly summarised.

In order to analyse the Earth-reacting WEC-mooring system dynamics, mathematical models were often developed where the mooring component was normally considered as an integral part of the WEC. All these devices are similar in the way are activated, i.e. thanks to the reaction given by taut lines fixed to seafloor.

Cruz and Sarmento (2005) analysed a submerged dimension-changing moored sphere, firstly by frequency-domain analysis and after through a time-domain formulation. By comparing the two types of analysis, they found that the frequency-domain calculations were leading to acceptable results only for cases where small period waves were considered.

Mavrakos and Katsaounis (2005) developed a mathematical model of a generic tightly moored point absorber including a hydraulic mechanism as PTO. The hydraulic PTO, in this case, pressurises a fluid into a reservoir which is used as an accumulator. Then the fluid at high pressure flowing out from the reservoir drives an electric generator at a constant speed. The floater considered was cylindrical and was moored by a single tether. A time-domain analysis, taking into account five degrees of freedom and the cable tension unknown, was carried out. Wave exciting forces were formulated by examining frequency-dependent first-order wave loads. Also, viscous forces calculations were included in the mathematical model, but it was discussed that these were negligible.

An analogous model was then implemented by Mavrakos, Katsaounis, and Apostolidis (2009), for assessing different floaters geometry.

Similarly, Vicente, Falcão, and Justino (2013) studied another tightly moored single-body point absorber (PA) by frequency-domain and time-domain analysis. The same theoretical PA was after taken into consideration by Spanos et al. (2016), who emphasise the difficulty of modelling such a system in two DoFs and developed a statistical linearisation technique to analyse the system for extended time frames. Particular focus on this device is given in later chapters of this thesis.

2.3.3 Dynamic based methods

As previously discussed fully dynamic methods are more suitable for numerically analyse and design moored WECs. These can be categorized into two main types: potential flow and computational fluid dynamics (CFD) based methods. This distinction manly concern the way hydrodynamic forces acting on the WEC device are calculated. All available modelling methods are those which were developed from studies on modelling traditional floating structures and vessels hydrodynamics. These two types of approaches are consistently diverse. Due to the type of physical problem in question, i.e. modelling an Earth-reacting WEC, the potential flow approach was assumed to be the most suitable to be used for this project. Thus, in this thesis, only the potential flow approach is discussed. The reason of this is that the potential flow approach for the problem considered is considered reliable for normal operating conditions and demands limited computational cost. However, CFD methods may be better suited for investigating other essential phenomena such as extreme loading conditions due to nonlinear hydrodynamic effects, nonlinear hydrodynamics of complex structures and viscous forces. The CFD methods concern of solving the Navier-Stokes equations, where all nonlinear hydrodynamics effects can be captured.

In order to put in practice a dynamic based method the equation of motion of the entire moored system has to be identified. This equation is derived from Newton's law and

can be defined as Equation 2.5 (Wilson, 2003).

$$[\mathbf{M}_{i,j}(\omega) + \mathbf{A}_{i,j}(\omega)]\ddot{\mathbf{x}}_j + [\mathbf{B}_{i,j}(\omega)]\dot{\mathbf{x}}_j + [\mathbf{K}_{i,j}]\mathbf{x}_j + \mathbf{F}_{pto_j}(\omega) + \mathbf{F}_{m_j}(\omega) = \mathbf{F}_{e_j}(\omega) \quad (2.5)$$

Depending on the degrees of freedom (DoF) to take into consideration and on system symmetries, Equation 2.5 can be subdivided in some j coupled or uncoupled differential equations. For a vessel, normally 6 DoFs are considered, in this case, three differential equations concern translational (surge sway and heave) motions, and other three equations concern rotational (roll, pitch and yaw) motions. However, depending on the case less or more DoFs can be studied. $\mathbf{x}_j$ is the coordinate vector, and one or two over dots denote respectively the velocity and acceleration vectors. In order to study the motion of a floating structure Equation 2.5 needs to be solved for finding these last vectors. While $\mathbf{M}_{i,j}$, $\mathbf{B}_{i,j}$ and $\mathbf{K}_{i,j}$ are, respectively the mass, damping and stiffness matrices, which are normally constant over time. The mass matrix $\mathbf{M}_{i,j}$ and $\mathbf{A}_{i,j}$ are the mass of the floating structure and the added mass matrices. The added mass is needed for taking into account the inertia to be added to the system, thus to include forces acting on the structure due to the induced acceleration and deceleration of the surrounding volume of water. The damping matrix $\mathbf{B}_{i,j}$ represents the radiation damping. The radiation damping exists due to the waves which are generated by the movement of the floating structure. The stiffness matrix $\mathbf{K}_{i,j}$ includes the hydrostatic stiffness. The PTO system forces are indicated by the term $\mathbf{F}_{pto_j}$, depending on the type of device these can concern multiple DoFs. In the $\mathbf{F}_{e_j}$ can be grouped all mooring system restoring and damping forces. $\mathbf{F}_{e_j}$ represent all environmental forces due to waves, current and wind.

The Equation 2.5 represent a complex fluid-structure interaction problem. The main difficulty in solving such equation is related to the aspect of modelling the hydrodynamic forces acting on the floating structure. These forces depend on also the motion of the floating structure. Different solutions methods exist. The complexity of these

solutions increases when severe sea states have to be better modelled and when the higher accuracy is required. For normal sea conditions, a solution based on solving the hydrodynamic forces over the mean wetted hull surface is possible. For this solution in a first instance, the hydrodynamic forces are calculated by solving the radiation and diffraction potentials for the free-floating structure. For solving these potentials, the boundary element method is implemented. In this way, the essential hydrodynamic coefficients are obtained. These coefficients are then applied to the equation of motion so that hydrodynamic forces can be evaluated. Thus the boundary element method implementation is an important step. This step is often performed by using specific available codes. In later Subection 2.3.3 the Nemoh code, used during this project, is described.

Optimally, Equation 2.5 can be solved in time-domain where impulse-response functions can be included to simulate the more realistic behaviour of the WEC motion and, in this way, better predict mooring loads. Otherwise, this equation can be solved in the frequency domain, therefore results describing the WEC -mooring system at a resonance condition can be obtained. However, in this latter case, the transient loads due to the mooring system cannot be studied. In fact, when the frequency-domain approach is implemented, the motions of the device and the loads acting on this are assuming to be varying as a simple single sinusoidal pattern. Thus, when the frequency-domain analysis is applied, usually, only the effect of first order wave loads can be evaluated. However, in particular for mooring system analysis, second-order wave loads are required to be taken into consideration. These last determine complex floater oscillations which cannot be analysed by the frequency-domain approach only.

Potential flow approach and Nemoh

For implementing a dynamic based method, as previously discussed, it is required to evaluate hydrodynamic forces. Within this project, this task is performed in part with the aid of a boundary element method. This method is based on the potential flow

approach.

For the potential flow approach, the flow is assumed to be irrotational and incompressible. The flow is described by a velocity potential defined as $\Phi(\mathbf{X}, t)$, and this can be found by solving the Laplace equation (Eq. 2.6).

$$\nabla^2 \Phi = 0 \tag{2.6}$$

Finding an exact solution of the Laplace equation can be a very difficult task. Assuming waves are linear, the linear wave theory can be used for defining kinematic and dynamic boundary conditions. In practice, various relations have to be derived for taking into account the boundaries of the fluid under study. These boundaries are the seabed, the free surface interface and the surface of the floating body.

Once the velocity potential is solved, the hydrodynamic forces can be estimated. The total hydrodynamic force acting on a floating body is the sum of wave radiation, wave diffraction and Froude-Krylov components. The wave radiation force can be defined as Equation 2.7.

$$\mathbf{F}_R = \mathbf{A}\ddot{\mathbf{X}} + \mathbf{B}\ddot{\mathbf{X}} \tag{2.7}$$

where $\mathbf{A}$ and $\mathbf{B}$ are respectively, the added-mass and added-damping or radiation damping coefficients. While $\mathbf{A}\ddot{\mathbf{X}}$ represent the inertia to be added to the system for taking into account the surrounding water moving with the floating body, the wave radiation force $\mathbf{B}\ddot{\mathbf{X}}$ represent hydrodynamic forces acting on the body due to generated waves by the movement of the body. Both $\mathbf{A}$ and $\mathbf{B}$ coefficients depends on the floating body geometry.

The total wave excitation force is composed of the Froude-Krylov force and wave diffraction force. This total force can be found by solving Equation 2.8.

$$\mathbf{F}_e = \mathbf{F}_{FK} + \mathbf{F}_{DF} = \int_{S_W} \frac{\partial(\Phi_I + \Phi_D)}{\partial t} \mathbf{n} ds \tag{2.8}$$

Where Φ_I+ and Φ_D are the incident wave velocity potential, and the diffraction velocity potential. The integral in Equation 2.8 needs to be solved for the wetted surface of the body which is indicated by S_W.

Many studies exist on solving the velocity potentials for basic geometries with analytical methods. For instance: Newman (1963) by using Haskind relations calculated wave forces acting on fixed ellipsoidal shapes; Hulme (1982) estimated wave forces acting on a floating hemisphere oscillating in waves; similarly, Wang (1986) and Swaroop (2004) calculated forces and motion concerning submerged spherical bodies in waves. These studies concern only some elementary shapes such as cylinders or spheres. Despite this, these studies at times are beneficial, as the results provided can be used for initially validating numerical calculations.

For solving the potential flow for more complex geometries and for multiple bodies the boundary element method (BEM) can be used. This method was developed for conventional floating structures and vessels over many years. It concerns solving the flow velocity potential through a numerical approach.

In Chapter 3, the added mass and the radiation damping coefficients and the diffraction forces were calculated by using the Nemoh code which is based on the boundary element method. This code was developed at the Ecole Centrale de Nantes for more than thirty years (Babarit, 2014). The Nemoh code is an upgraded version of the AquaDyn code initially developed by Delhommeau (1987). The Nemoh code is capable of solving the diffraction-radiation problem which concerns floating structures (with no forward speed) interacting with water waves, to the first order solution (of a boundary value problem). The main peculiar characteristics of this code compared to other similar codes (e.g. WAMIT, Diodore, DIFFRACT, Hydrostar, Aquaplus) are that this is particularly suitable for wave power applications and that, at present, this is unique

because it has been released under the terms of an open source license (Babarit, 2014).

Following the potential flow assumption, in the Nemoh code, the fluid is modelled by assuming that: this is irrotational; the continuity equation is valid, and the only considered external forces are due to the presence of gravity.

In mathematical form, these assumptions can be described as following:

Inviscid fluid: $\nu = 0$
Meaning that the viscosity of the fluid is assumed nill.

Irrotational fluid: $\nabla \times \vec{V}$
Meaning that it is assumed that all elements of the fluid do not rotate with respect to a specified coordinate system.

Incompressible fluid: $\nabla \vec{V} = 0$
Meaning that the water density is kept constant and the fluid volume is conserved.

The velocity is given by a velocity potential: $V = \nabla \Phi$
Meaning that a scalar potential can describe velocity of fluid particles.

The pressure can be obtained from the Bernoulli equation:
$p + \rho g z + \frac{1}{2}(\nabla \Phi)^2 + \rho \frac{\partial \Phi}{\partial t} = CONSTANT.$
This equation states that sum of the pressure, the kinetic and potential energy per unit volume is preserved over time.

In the Nemoh code, the diffraction-radiation problem is solved by following the boundary element method with Green's function. This last allows for including into the mathematical formulation of the boundary conditions at sea bottom, at the floating body, and at the free surface. The method consists of initially solving the radiation problem which concerns the forced sinusoidal oscillations of the floating body in water initially at rest. Afterwards, the diffraction problem is solved assuming the floating body is fixed. Following this approach, the hydrodynamic coefficients can be obtained.

In order to solve the fluid velocity field, the nonlinear boundary value problem needs to be evaluated each time. This mathematical problem is represented by the following system of equations (Delhommeau, 1987).

$$\begin{cases} \Delta\Phi = 0 \quad M \in \Omega \quad \textbf{(For all fluid volume)} \\ \frac{\partial\Phi}{\partial n} = \mathbf{V}\cdot\mathbf{n} \quad M \in S_B \quad \textbf{(On body surface)} \\ \frac{\partial\Phi}{\partial n} = 0 \quad M \in S_{seabed} \quad \textbf{(At seabed)} \\ \frac{\partial\eta}{\partial t} + \nabla\eta\cdot\nabla\Phi = 0 \quad M \in S_{FS} \quad \textbf{(Free surface kinematic boundary condition)} \\ \frac{\partial\Phi}{\partial t} + g\eta + \frac{1}{2}\left(\nabla\Phi\right)^2 = 0 \quad M \in S_{FS} \quad \textbf{(Free surf. dynamic boundary condition)} \\ \sqrt{R}\left(\frac{\partial\Phi}{\partial n} - ik\right)\left(\Phi - \Phi_0\right) \to 0 \quad R \to \infty \quad \textbf{(Wave radiation condition)} \end{cases}$$

As illustrated in Figure 2.8 Ω, S_B, S_{FS}, S_{seabed} and S_∞ are respectively, the fluid domain, the body's wetted surface, the free surface, the seabed (bottom boundary) and the lateral surface at infinity distance. **n** indicates the body surface normal vector and M is a generic fluid subdomain.

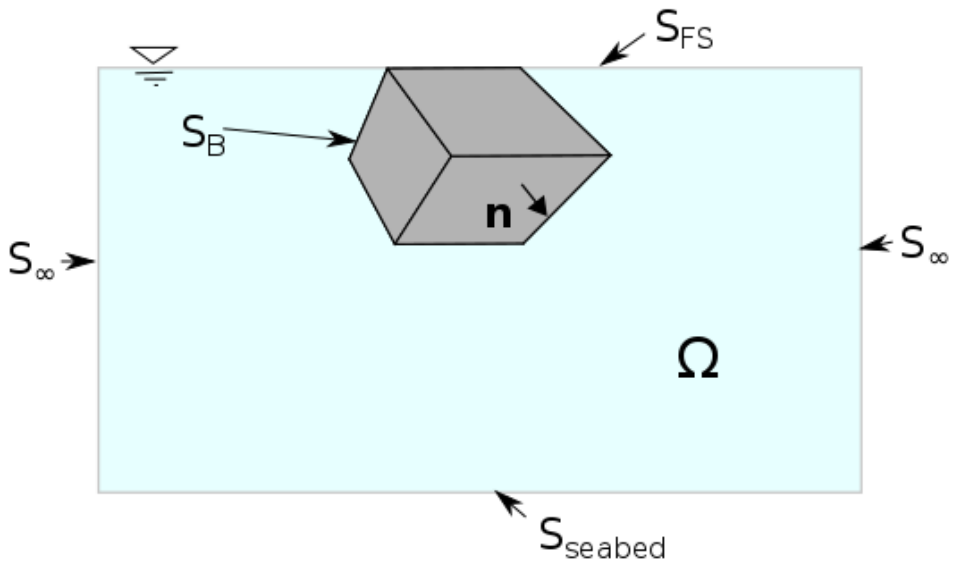

Figure 2.8: Boundary value problem scheme.

By manipulating the previously defined system of equations which defines a three-dimensional problem, thanks to the Green's third identity, this last can be simplified to a two dimensional one. The detailed explanation of the system of equations and their solution is not given in this thesis as this do not strictly relate to the scopes of this project.

In particular, the Nemoh code solves the boundary value problem to the first order. Similar codes capable of performing such task are the WAMIT, the Diodore, the Hydrostar, the Diffract and the Aquaplus.

In order to find the first order solution of the boundary value problem described, the following approximations have to be taken into account:

- Small motion from the mean position

- Free surface equations are linearised
- The boundary value problem is solved in the frequency-domain

Together with the hydrodynamic coefficients (added mass, radiation damping and excitation force), the Nemoh code provides the far field coefficients, representing the Kochin function, the free surface elevation and pressure field.

For a detailed description of the theory implemented in Nemoh, the computational procedures, mathematical and numerical formulation, reference is made to Delhommeau (1987), Delhommeau (1993).

In Chapter 5 validation evidence, by reporting comparisons with results obtained with other methodologies and with data available in the literature is reported, and the accuracy of the Nemoh code is proved.

In Chapter 3 numerical work concerning an Earth-reacting WEC is described, as anticipated, part of the numerical calculations were done with the aid of the Nemoh code. The Nemoh code was used for calculating the hydrodynamic coefficients and excitation forces for the floater component of the WEC. For this purpose, this last was modelled in Nemoh as a free (not moored) floating body. In Nemoh, taut moored floating bodies cannot be directly modelled. The code developed in Chapter 3 allows for adding a taut mooring line component to the floating body model, which otherwise would only be represented by a generic free-floating body.

2.3.4 Empirical studies on taut moored devices

In order to assess the validity of a numerical model for a WECs, it is imperative to compare results with empirical evidence. In fact, experimental work aiming at gathering valuable experimental data, which is representative of the WEC under study, is most of the times essential. Accordingly, during this PhD project, experimental work on a specific Earth-reacting PA WEC was carried out, this work is described in Chapter 4.

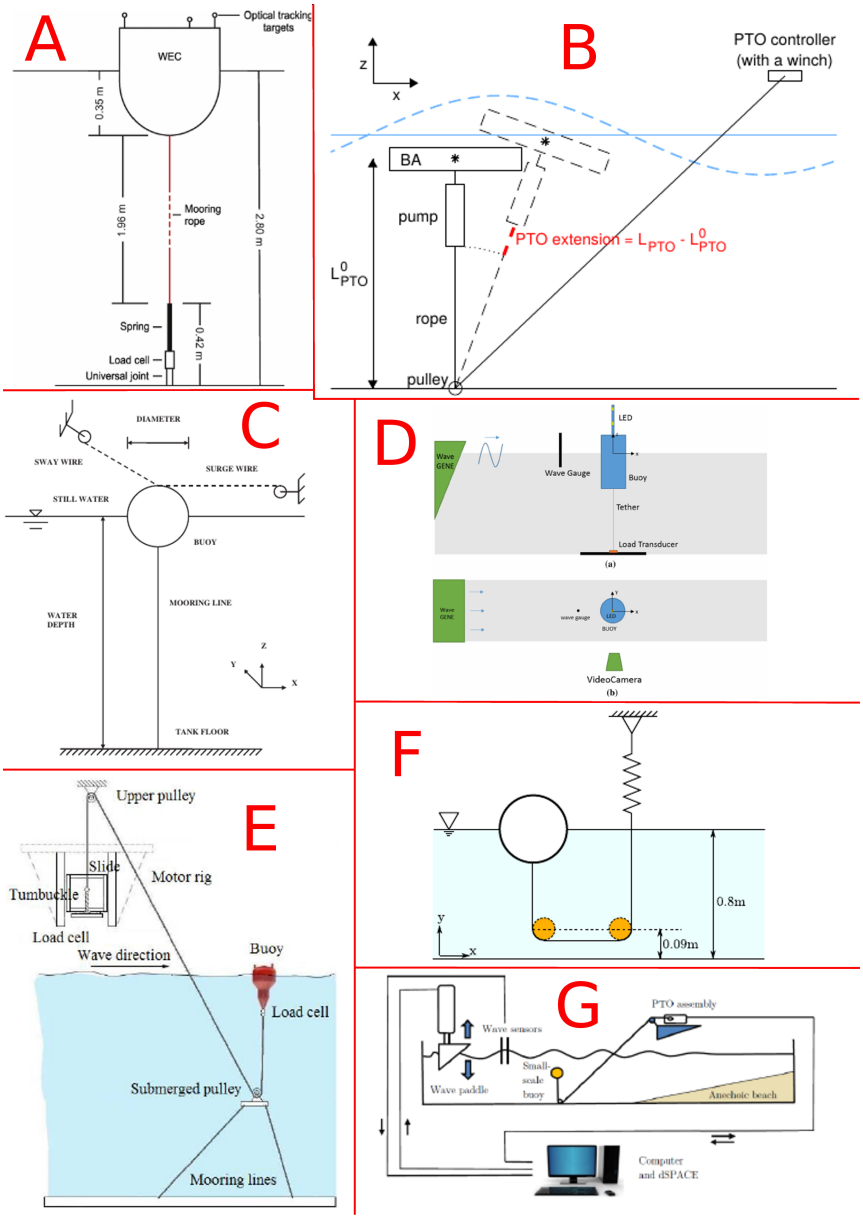

Figure 2.9: Schemes of experimental set-ups adopted during previous studies of: (A) Hann, Greaves, and Raby (2015); (B) Orszaghova et al. (2016); (C) Radhakrishnan, Datla, and Hires (2007); (D) Ma et al. (2016); (E) Wang et al. (2018); (F) Gunn, Rudman, and Cohen (2018); and (G) Ding et al. (2017).

Thus, in this section, a brief review of the previous work concerning taut moored configurations is presented.

Taut moored devices were studied experimentally by a few researchers. In Figure 2.9 are reported the schemes of experimental set-ups which were assembled during previous works. Each study reviewed had specific scopes. Despite this, all the subsequent cited studies concern model scale experimental testing on devices very similar to the one studied during this PhD project.

Recently, with particular focus on extreme loads and responses, Hann, Greaves, and Raby (2015) and Orszaghova et al. (2016) all analysed submerged PA WECs by running experiments on model scale devices (Fig. 2.7 Letters A and B). The first study related to snatch loading, findings indicated that the magnitude of extreme loading is not very dependent on the wave steepness, but body motion and displacement very influence it. The second study concerned the specific Ceto WEC, also in this case extreme loading were investigated. While Hann, Greaves, and Raby (2015) investigate extreme loading by increasing wave steepness and using breaking and non-breaking waves, defined with the NewWave theory, Orszaghova et al. (2016) used long irregular sea simulations and a numerical model for specifically understand maximum PTO extensions.

Other authors studied the instability of tethered floaters without PTO components. These studies concerned the analysis of the nonlinear body motion with free oscillations and waves tests. Experimental and theoretical work for finding the Mathieu's instability diagram was carried out (Radhakrishnan, Datla, and Hires, 2007; Ma et al., 2016). Their scaled models are reported in Figure 2.7 by Letters C and D. In contrast, Gunn, Rudman, and Cohen (2018) use a moored floating sphere with a spring component for understanding the validity of the Smoothed Particle Hydrodynamics (SPH) theory for modelling surface and structure interaction (Fig. 2.7 Letter F). They provided guidelines on which resolution to apply for correctly use SPH theory for studying such types of fluid-structure interaction problems.

For numerical models, validation Ding et al. (2017) and Wang et al. (2018) undertook

experimental work on scaled models of, respectively the Ceto and CorPower WECs. Their experimental set-ups are shown in Figure 2.7 by Letters G and E. Both studies compared numerical with experimental results. While in the first study CFD methods are applied for modelling the device, the second concern a numerical model based on the Cumins equation. For both studies, experimental work was carried out with scaled models consisting of a floater and a PTO assembly. The PTO system for the Ceto model was constituted by only a controlled servomotor which was emulating the desired combined spring-damping effect. For the CorPower WEC model, the PTO damping and spring effects were simulated mechanically. The negative spring force was exerted by an element made by some cylindrical pneumatic components.

2.3.5 WEC experimental model testing

Relevant topics of interest concerning testing WECs are briefly reviewed in this section.

Experimental work is undertaken for investigating particular aspects. These lasts are discussed by EMEC (2009) and Payne (2008) and are listed next.

- Proof of concept
- Hydrodynamics, dynamics and loads
- Power performances
- PTO principle and control
- Station keeping

Generally, for bigger experimental models and higher experiment complexity, more aspects can be investigated at the same time with fewer uncertainties. However, the cost involved with tank testing also accordingly increases. Physical models usually can be of any of the orders between 1:3 to 1:100 of the real-scale device.

In EMEC (2009) is discussed that for commercial development physical models should be first of small-scale (λ = 1:25-100) after of medium scale (λ = 1:10-25) and finally of large-scale (λ = 1:3-15). Where small-scale models can be used for investigating the validity of the concept, hydrodynamics, device motion, structural loads and estimation of device performance. Results of small-scale models can also be used for validation of numerical models. As for small-scale models medium scale models can be built to be tested in hydrodynamics laboratory. Once basics aspects have been optimized, medium scale models are required for project development. Usually with medium scale models, particular aspects regarding extreme Environmental conditions can be investigated. A model which is more representative of the real-scale device, including the mooring system and PTO realistic system, is built for this purpose. Ideally, medium scale models are tested in multi-directional irregular sea states including currents. Finally, large-scale models can be built, these are tested at sea or, exceptionally, at large wave basins. Large-scale models are fully operational devices which have all characteristics same as real-scale device. When testing these models, the developer can experience all realistic circumstances as it would be for a real-scale device.

In order to design a scaled model of a device, specific scaling rules have to be followed (Payne, 2008). In general, concerning mechanical interactions between fluids and solid structures, three types of forces are of particular importance. These concerns forces associated with inertial forces F_i, gravitational forces F_g and forces due to viscosity F_v. For each different phenomenon under study, the relative magnitude of these forces may vary; thus it is of fundamental interest to find a way to quantify what is the relative importance of these forces. Conventionally, this can be done by using two non-dimensional factors named the Froude number F_r and the Reynolds number R_e. These quantities are defined as follows.

$$F_r = \frac{U}{\sqrt{gl}} \propto \frac{F_i}{F_g} \propto \frac{inertia\ force}{gravitational\ force} \tag{2.9}$$

$$R_e = \frac{Ul}{\upsilon} \propto \frac{F_i}{F_v} \propto \frac{inertia\ force}{viscous\ force} \tag{2.10}$$

Where U is the fluid velocity, g is the gravitational acceleration, l is the characteristic length representing the fluid/body interaction phenomenon and υ is the kinematic viscosity.

For designing an excellent physical scaled model of a WEC, representing well the real-scale device, it is required to maintain the same balance between inertial, gravitational and viscous effects. In theory, this can be achieved by ensuring that the F_r and the R_e numbers relative to the scaled model experiment match the F_r and the R_e numbers relative to the real-scale case. Matching these numbers, in practice, is a difficult task. In fact, it happens that if one of the two non-dimensional number relative to the scaled model is about equal to the relative number for the full-scale device, for the other non-dimensional number usually is not the case. Thus, in almost every circumstance, especially for smaller scale experiments, a compromise has to be accepted. Depending on the phenomenon investigated, a solution to this problem consists of scaling a model by focusing on keeping only one of the two non-dimensional numbers constant.

As discussed by Payne (2008) the effects of viscosity concern usually the boundary layer (water-body interface) only. For the rest of the fluid, viscous forces usually are negligible. Viscous effects are not negligible only for WECs having sizeable wetted surface and sophisticated shape. Thus, for most of WECs, including the spherical WEC which will be studied in next chapters, the net influence of viscous forces is small. Meaning that main forces are of inertial or gravitational nature, and the effect of viscous forces is, to a certain extent, irrelevant. As a consequence, in most cases, the Froude scaling approach can be assumed to be valid. This approach concern assuming that the ratio of inertial forces F_i to gravitational forces F_g is kept the same for both, the scaled model and the real-scale device.

During the experimental study explained in Chapter 4, the Froude scaling approach

was implemented for identifying parameters of the physical models assembled at laboratories. Thus, in Table 2.1 are introduced Froude scaling laws of interest.

Quantity	**Scaling law**
Wave height and length	s
Wave period	$s^{0.5}$
Wave frequency	$s^{-0.5}$
Linear displacement	s
Angular displacement	1
Linear velocity	$s^{0.5}$
Angular velocity	$s^{-0.5}$
Linear acceleration	1
Angular acceleration	s^{-1}
Mass	s^3
Force	s^3
Torque	s^4
Power	$s^{3.5}$
Linear stiffness	s^2
Angular stiffness	s^4
Linear damping	$s^{2.5}$

Table 2.1: Foude scaling laws (Payne, 2008).

In Table 2.1 s is the geometric scale. These laws are derived by taking into account scaling factors relative to velocity and length. In details, in Expression 2.3.5 it can be noticed that U scales with $s^{0.5}$, as F_r and g are constant. Also, considering that the characteristic length s scales linearly, all other scaling laws can be derived from basic dimensional analysis.

2.4 Chapter's summery and conclusions

At first in Section 2.1, wave energy converters (WEC) categories, and mooring system requirements were discussed. It was found that for each type of WEC a particular mooring system may be more or less suitable. It was further discussed that WEC's mooring system requirements are diverse than requirements of conventional floating structures. However, various requirements are shared by the two kinds of floating

structures. Basic mooring line types were briefly introduced, and their suitability for the type of WEC technology and anchoring depth was discussed. In general terms, the conventional theory customarily applied for catenary calculations and for designing conventional mooring systems was briefly introduced. The different mooring analysis approaches were introduced and advantages of fully dynamic codes for moored WECs analysis were identified. Due to WECs characteristics, these lasts are better suited.

Next, a general literature review on the topic of mooring systems for wave power devices was provided (Section 2.2). The actual stage of progress was identified, and relevant works were collected so to define a broad picture of the state-of-the-art. In this section, all recent significant studies on mooring analysis and design for WECs were briefly mentioned. These were grouped by different topics of research, i.e., theoretical studies on Self and semi-Earth-reacting WEcs, experimental studies, specific projects, devices in arrays; extreme conditions analysis. At the end of this section also other inherent topics related to reliability and efficiency are briefly discussed. From this review it was found that for commercial development of WECs and their mooring systems, the following topics need to be further be addressed: mooring systems for arrays of devices; new materials; synthetic fibres for long-term use; fatigue life of components; interaction of moored devices deployed in arrays; and on experimental validation of theory and numerical methods.

A more specific literature review was presented in Section 2.3 where all topics of interest for later work were introduced. At first, commercial Earth-reacting WECs of recent projects were described. For this type of WECs, the previous theoretical work was then reviewed. The specific potential flow theory was explained, and the Nemoh code which is based on this theory was described. Successively experimental studies on taut moored devices were briefly reviewed, and WEC experimental scaling methods were treated. It was found that no extended study was published on experimental work on the PA in normal operating conditions with linear PTO damping and a linear spring. Despite this, in Section 2.3.4 the most relevant literature was cited. This section also concerned a review on works relative to previous experiments which were, to a certain

extent, relevant to the experimental work later discussed in Chapter 4.

Chapter 3

Earth-reacting wave energy converter

In this chapter is addressed the objective concerning the development of a numerical tool for practical simulating Earth-reacting wave energy converters of generic geometry. As explained in the introduction of this thesis, a new methodology for designing and analysing moored WECs is proposed. The generic methodology is put in practice for the specific case of Earth-reacting taut moored WECs. For this reason, the mentioned numerical tool, needed for solving the equation of motion of the entire taut moored WEC system, is developed.

3.1 Introduction

In this chapter, a computational method, developed for analysing moored Earth-reacting WECs, is presented. This method was defined for the Earth-reacting WECs type only. This type of WECs was selected among the other options as this is one of the most important categories of WECs. As mentioned in Section 2.3.1, there are various commercial WECs of this type which are at a good stage of commercial development.

Despite this, as discussed in the previous chapter, numerical and experimental studies on this type of devices are limited. The method is applied to a generic point absorber (PA) WEC, via a numerical tool, by which any type of axisymmetric geometry may be analysed. With this is possible to analyse devices which are moored to the seabed utilising a single inelastic tether. In this chapter, numerical techniques and results concerning numerical predictions of system performance are described and reported. Results concern the PA devices having half-immersed or fully submerged spherical floaters. Computational steps of the numerical tool are briefly showed in Figure 3.1.

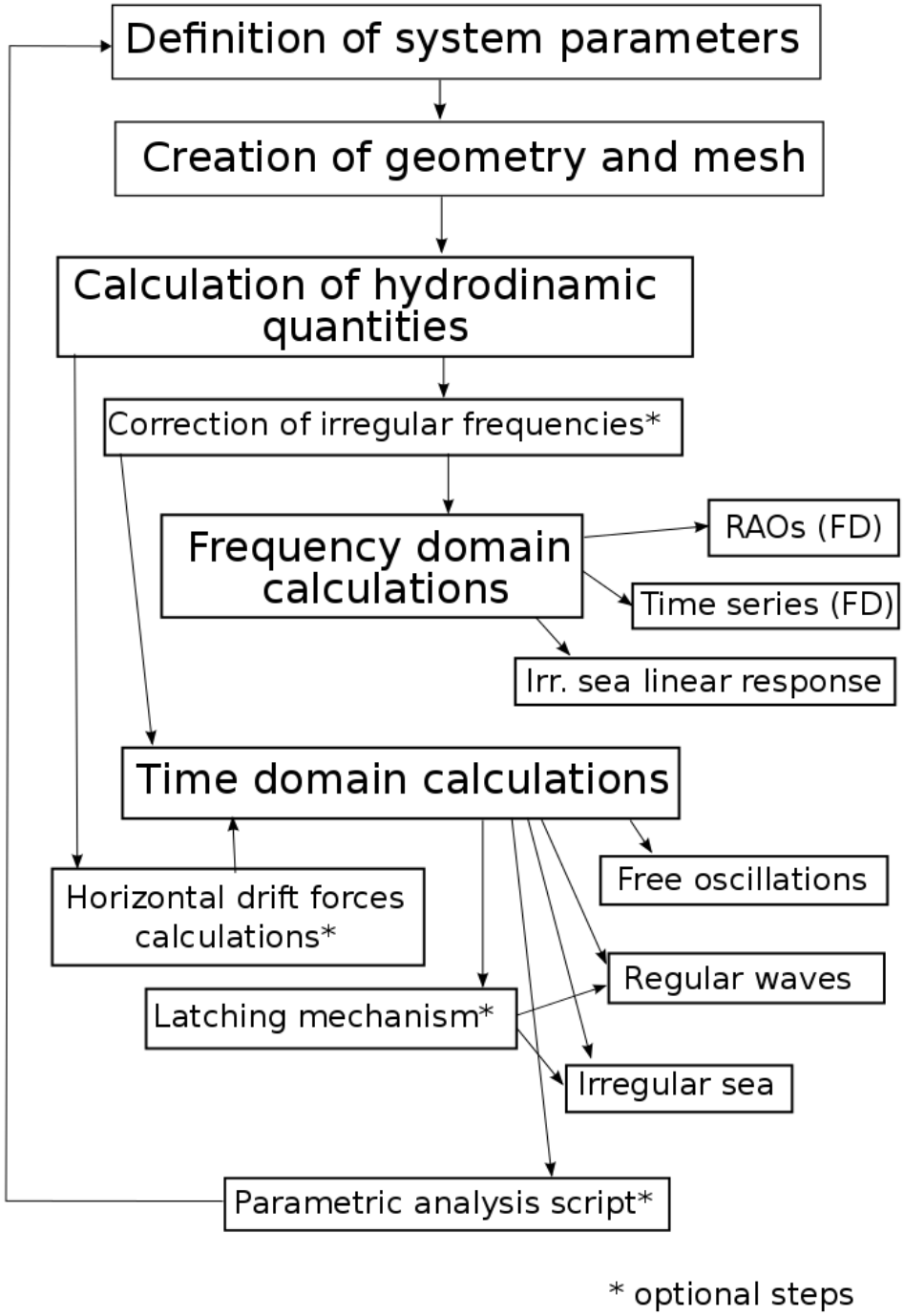

Figure 3.1: Flow chart of Earth-reacting computational tool developed.

3.1.1 Methodology

The computational tool developed, as illustrated in Figure 3.1, can be subdivided into various sections. Main computational steps are grouped as follows:

- Definition of system parameters
- Computation of floater geometry and mesh
- Calculation through boundary element method of hydrodynamic parameters and wave forces for the chosen floater geometry
- Frequency-domain calculations of system response and estimation of energy production (regular and irregular sea)
- Time-domain free oscillations (for heave and surge modes of motion)
- Time-domain calculations for system response and performances in regular and irregular seas
- Time-domain calculations including the modelling of a latching control system in the PTO mechanism and parametric analysis

Except for the calculations of hydrodynamic coefficients and forces which are done with the aid of the Nemoh code, the above steps are done with one or multiple Matlab scripts. The computational tool proposed can be subdivided into mainly two parts: the part of the code related to the frequency-domain calculations and the part of code solving the time-domain problem. Each of the two parts shares the computational procedures involved in the definition of the system geometry, the mesh of the floating body and the calculation of the hydrodynamic coefficients/forces. For both frequency-domain and time-domain problems, regular and irregular sea states can be set. For the time-domain also free oscillations tests can be simulated. An option for correcting irregular frequency is available, and there are three optional steps related to time-domain calculations, these are the evaluation of horizontal drift forces; the use of a latching control mechanism; and

the option for running the code in a loop for parametric analysis. While the *correction of irregular frequency* step is in general needed for improving numerical results, *horizontal drift forces calculations*, *latching mechanism* and *parametric analysis script calculations* are further optional steps that can be arbitrarily run. These are extra functions of the code.

In this chapter, the code developed is explained. Initially, some observations for determining the main system parameters are discussed. Will follow a description of an independent code, which is used for computing the hydrodynamic coefficients. After the frequency and time-domain formulations of the problem, the numerical implementation and numerical results are reported.

3.2 System parameters

In general, it can be said that a good WEC can be seen as a good wavemaker (Falnes, 2002). Dimension, weight, and shape of the floating body are the main factors that determine the wave energy extraction capability of a floating device. While for the case of a wavemaker the mass is not an important parameter, as this is activated by an external force, in the case of a wave energy device this should be optimized. Thus, in order to have optimal motion response, the floater's mass should be correctly chosen, so that the optimum oscillations are obtained. In fact, a small body which oscillates with large amplitude may be a better wave energy absorber than a larger one which instead oscillates with lower oscillation amplitude. Physical relations representing the problem in question are those of the Forced and Damped Harmonic Oscillator. In a first instance, taking apart hydrodynamic forces, Equation 3.1 dictates the relations between parameters of the classic mass-damper-spring system. This equation can be used for calculating the oscillation amplitude $|A(\omega)|$ of such system.

$$|A(\omega)| = \frac{F_0/m}{\sqrt{(\omega_0^2 - \omega^2)^2 + \omega^2\gamma^2}} \tag{3.1}$$

Where F_0 is the sinusoidal excitation force, m is the mass, ω_0 is the natural frequency of the system, defined as $\omega_0 = \sqrt{\frac{k}{m}}$, ω is the forcing frequency and the factor γ is equal to b/m. For $b = 0$ we have the maximum motion amplitude, but no power can be extracted. Optimum oscillations for power absorption happen when critical damping condition is set, i.e. $\gamma = 2\omega_0$. Differently, the Harmonic Oscillator is over-damped or under-damped if respectively $\gamma > 2\omega_0$ or $\gamma < 2\omega_0$ conditions are set. For a free-floating body the stiffness k is represented by the hydrostatic stiffness, this for axisymmetric shapes can be approximated as $\rho g A$, where A is the floater cross-sectional area defined by the perimeter obtained by the intersection of the calm free surface and the floater surface.

More specifically, for a defined type of monochromatic sea, by selecting correct system parameters, we can obtain optimum phase and optimum amplitude, so to finally get better power extraction performances.

Considering the case of a wave power generator represented by a moored floater connected to a linear spring in series with a linear damper, best values of floater mass, mooring line pretension, spring stiffness and PTO damping can be estimated. These parameters are denoted respectively as: m; F_{pre}; K_s; and C_{pto}. The pretension F_{pre} is needed for elongating the spring component by an initial offset. In this way, certain system compliance is obtained, and mooring peak loads are smoothed. Without pretension snatch loads, at fairlead, could occur. The pretension determines the mooring line be straight. For this reason, the mooring restoring forces are directly counteracted by the anchor. The spring component is needed for implementing the pretension and also for modulating the restoring force of the system. The C_{pto} damping represents the linear damping coefficient needed for modelling the absorbed power by the device thanks to the PTO mechanism.

In real life, depending on the installation site, we do expect different sea states probabilities function and distribution. For simplicity, the point absorber problem is initially limited to a single degree of freedom in regular waves. In this case, the average power

over a wave period can be defined by the following expression (Evans, 1980).

$$P = \overline{F_s(t)U(t)} - \overline{BU(t)^2} \tag{3.2}$$

where F_s is the incident force on the floating body assuming it to be fixed, U is the instantaneous velocity and B represents the added damping coefficients. Considering that,

$$F_s = Re\{F_s e^{i\omega t}\} \tag{3.3}$$

and

$$U(t) = Re\{U_0 e^{i\omega t}\} \tag{3.4}$$

the equation describing the power (Eq. 3.2), after substitutions and elementary integration, can be rearranged as the following relation:

$$\overline{P} = \frac{1}{8B}|\overline{F_s}|^2 - \frac{B}{2}|U_0 - \frac{1}{2B}\overline{F_s}|^2 \tag{3.5}$$

U_0 is the velocity amplitude of the sinusoidal floater's motion. From the above, we can observe that the maximum mean power can be obtained when $U_0 = \frac{1}{2B}F_s$ and its value is equal to the first term on the right-hand side of this equation. Precisely when the following condition happens.

$$\overline{P_{max}} = \frac{1}{8B}|\overline{F_s}|^2 \tag{3.6}$$

Falnes and Budal (1978) and Mei (1976) noted that this optimal condition might be achieved when the velocity U is in phase with the exciting force F_s.

Next we consider the following equation of motion for a heaving point absorber (Falnes,

2002; Vicente, Falcão, and Justino, 2013):

$$(m + A_z)\ddot{z} + (B_z + C_{pto})\dot{z} + (K_s + \rho g S)z = F_{ez} \tag{3.7}$$

where A_z and $B_z$are the added mass and radiation damping coefficients for heave, C_{pto} is the power-take-off coefficient, K_s is spring stiffness and F_{ez} is the vertical component of the wave exciting force. This equation and its derivation are further discussed in Section 3.4, where also it is extended to the surge motion.

After substituting $\ddot{z} = -\omega^2 z$, $\dot{z} = i\omega z$ in Equation 3.7 and ordering terms we obtain the following Equation 3.8.

$$Z = \frac{F_{ez}}{-\omega^2(m + A_z) - i\omega(B_z + C_{pto}) + \rho g S + K_s} \tag{3.8}$$

This, together with the optimal mean power definition, gives the conditions:

$$\omega = \frac{\rho g S + K_s}{m + A_z(\omega)} \tag{3.9}$$

and

$$C = B_z(\omega) \tag{3.10}$$

To note that ω in the above equation is assumed to be coinciding with the wave angular frequency ($\omega \equiv \omega_e$).

For simplicity, we considered a spherical geometry, and we computed the radiation damping coefficients for this shape. The mass is defined as follows.

$$m = \frac{1}{2}\rho\left(\frac{4}{3}r^3\pi\right) - \frac{F}{g} \tag{3.11}$$

considering the latter, plus Equations 3.9 and 3.10 we can define initial design values of stiffness K_s, mooring pretension F_s and PTO damping constant C_{pto}. In particular for best wave energy absorption, given a particular angular frequency of oscillation ω, the constant C_{pto}, representing the linear damping of the PTO mechanism should be equal of the radiation damping. In our case C_{pto} constant was set to be $2.5 \cdot 10^5$ Ns/m/s equal to the value of B_{33} radiation damping coefficient corresponding to $\omega = 0.85$ rad/s ($T_{per} = 7.4$ s.). As the Earth-reacting device in question absorbs most of the total absorbed power only from the heave motion, only the heave radiation damping coefficient was taken in consideration for defining the C_{pto} initial value. The reference value of ω represents generic recurrent waves on the southern European coast directly facing the Atlantic ocean. For defining the PTO damping value, the radiation damping coefficients were calculated with the use of the Nemoh code introduced in Section 2.3 of Chapter 2. The radiation damping value B_{33}, considered for defining the initial C_{pto} value, is representative of an unmoored heaving only device. For the reason of having a direct comparison, the value of PTO damping and other system parameters corresponded to parameters reported by Vicente, Falcão, and Justino (2013). These parameters are reported in Table 3.1.

Parameter	**Values**
radius	7.50 m
mooring length	60.0 m
mass	8.0362E+05 kg
depth (same as length of line)	60.0 m
damping	2.50E+05 N·s/m
stiffness	1.50E+05 N/m
pretension	1.00E+06 N

Table 3.1: System standard parameters (Vicente, Falcão, and Justino, 2013).

The pretension and stiffness parameters can be justified as reasonable values determined so to not modify much the natural frequency of the floater, at the same time to allow motion, and thus to avoid snatch loading during operation in moderate sea states.

The parameters reported in Table 3.1 were used for initial model verification. Where

not mentioned, these are the standard parameters taken as references which were used during calculations. The numerical tool presented in later sections can be used for optimising these parameters. The case studies discussed in later Chapter 6 are examples of how the mentioned numerical tool can be used to investigate best system parameters for a specific location.

The point absorber WEC modelled with the computational tool developed is described by the sketch represented in Figure 3.2.

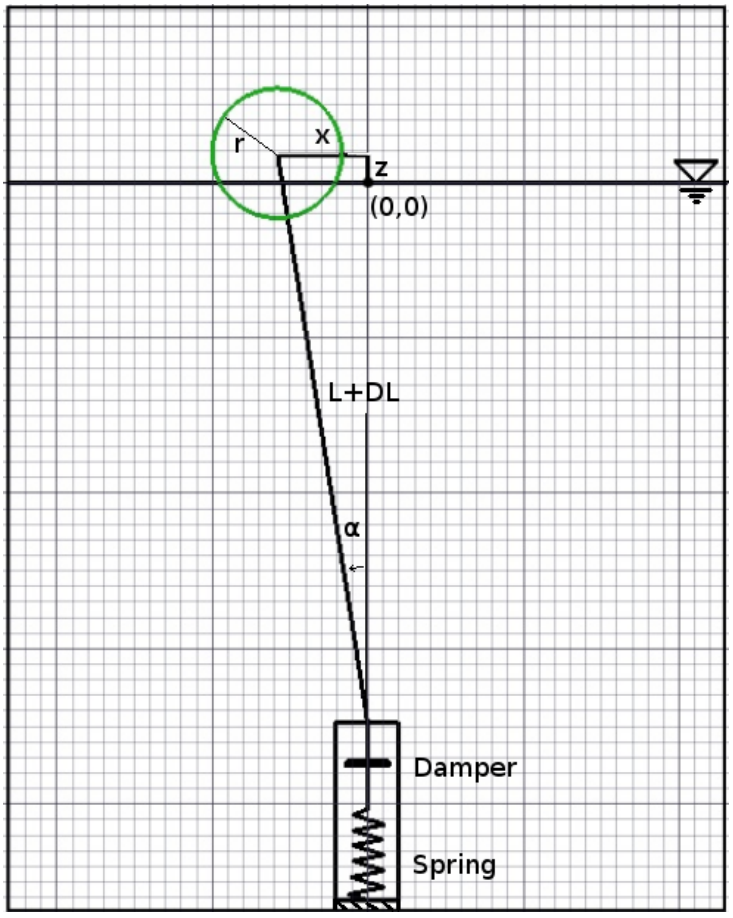

Figure 3.2: Sketch of the point absorber wave energy converter analysed.

3.3 Definition of geometries and computation of hydrodynamic quantities

For calculating the hydrodynamic quantities, which depend on the chosen geometry, the Nemoh code was used. This numerical code was introduced and described in Section 2.3 of Chapter 2.

A Matlab script was written for the automatic creation of spherical floaters geometries. These geometries are made by flat panels, in a format that can be used in Nemoh. The script is capable of creating geometries of half-immersed and fully submerged spherical floaters. For instance, the spherical geometries created are reported in Figures 3.3 and 3.4. As shown in these figures the arrows always point outwards, meaning that the normal of each panel is well oriented. Thanks to symmetry, for both floating bodies, only half of the geometry needed to be defined. These geometries were then entered in the Nemoh code. The half immersed and the fully immersed floaters were defined respectively by 200 and 338 flat panels. These number of panels resulted in being enough for obtaining correct hydrodynamic coefficients.

Results obtained with Nemoh, for verification, were compared to results obtained from analytical results given by Hulme (1982) and Wang (1986). These concern added mass and radiation damping coefficients and excitation force coefficients. Details of these comparisons are reported in Chapter 5 were also main other results are compared to experimental data.

A further geometry of a caisson was modelled for verification. This geometry and results are reported in Appendix A.2.

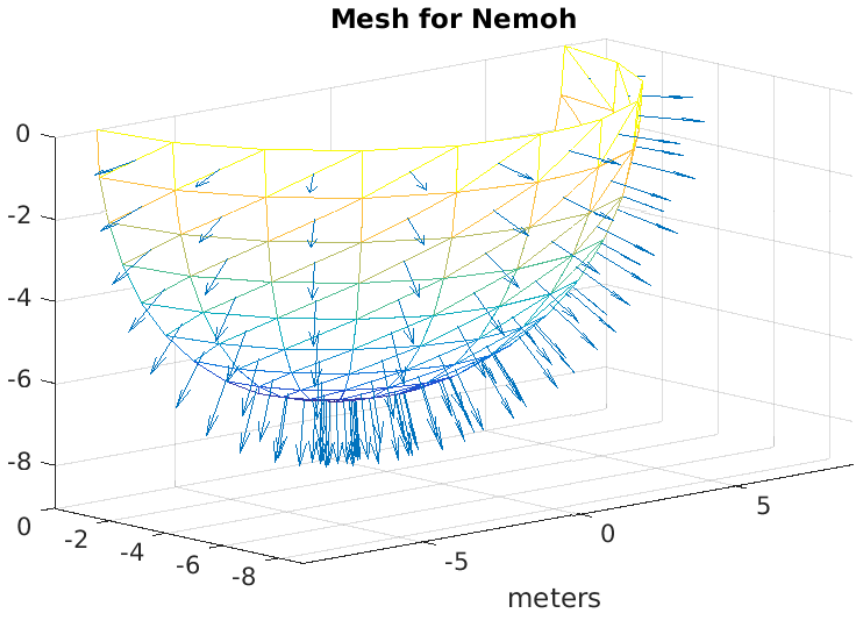

Figure 3.3: Mesh of hemisphere (200 panels)

.

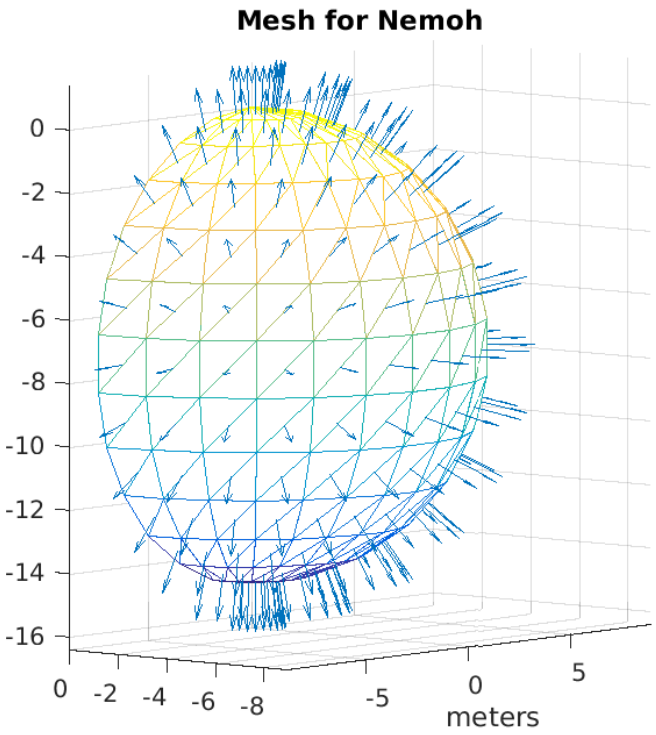

Figure 3.4: Mesh of submerged sphere (338 panels)

.

3.4 Frequency-domain analysis of spherical Earth-reacting point absorber

The point absorber (PA) WEC under study was represented in Figure 3.2. With more details the geometry of the device in question is reported again in Figure 3.5. By ℓ is denoted the axial displacement (ΔL) of the mooring line due to compression or extension of the spring component. By f is denoted the force exerted by the spring and damper components, this exclude the pretension load. Considering this geometry the mooring restoring force can be defined as: $\Phi = \sqrt{{\phi_x}^2 + {\phi_z}^2}$. Where ϕ_x and ϕ_z are the horizontal and vertical components. These equals to:

$$\phi_x = f_x + F_x = (|f| + F_p)sin(\alpha) \tag{3.12}$$

and

$$\phi_z = f_z + F_z = (|f| + F_p)cos(\alpha) \tag{3.13}$$

F_p, F_x and F_z are respectively the pretension load and its horizontal and vertical components. Whilst, f can be found from Equation 3.14.

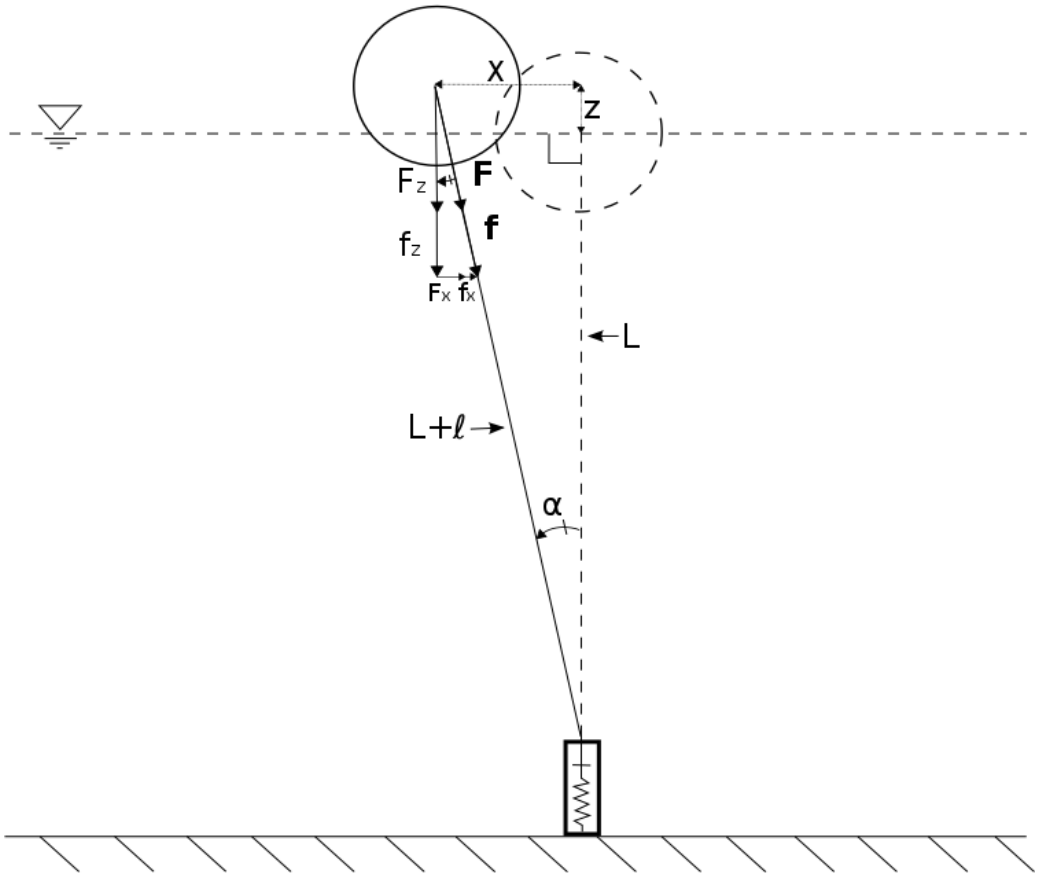

Figure 3.5: Scheme of the PA geometry.

$$f = K_s \ell + C_{pto} \frac{d\ell}{dt}. \tag{3.14}$$

To note that ℓ is found by applying Pythagorean theorem, giving $\sqrt{(L+\ell)^2} = \sqrt{(L+z)^2 + x^2}$. Thus ℓ is found to be:

$$\ell = \sqrt{x^2 + (z+L)^2} - L \tag{3.15}$$

Whilst, $\frac{d\ell}{dt}$ is found to be:

$$\frac{d\ell}{dt} = \frac{x\dot{x} + z\dot{z} + L\dot{z}}{\sqrt{x^2 + (z+L)^2}} \tag{3.16}$$

To further note that: $sin(\alpha) = \frac{x}{\ell+L}$ and $cos(\alpha) = \frac{z+L}{\ell+L}$.

For defining the frequency-domain equations, the mooring components are linearised. To do so it is assumed that only small surge displacements occur at all times, and α is a small angle. Thus, it can be assumed that $f_x \ll F_p$ and the horizontal mooring force component ϕ_x can be approximated as: $\phi_x \simeq F_p x/L$. For what concern the heave component, this is defined as $\phi_z \simeq F_p + K_s z + C_{pto}\dot{z}$, where $K_s z$ is the vertical restoring force due to spring stiffness and $C_{pto}\dot{z}$ is the PTO force.

Taking into account surge and heave (x,z) motions and including the linearised effects of the damper-spring system, the following decoupled equations[1] are defined (Vicente, Falcão, and Justino, 2013).

$$\begin{aligned} (m + A_x)\ddot{x} + B_x\dot{x} + \frac{F_p}{L}x &= F_{ex} \\ (m + A_z)\ddot{z} + (B_z + C_{pto})\dot{z} + (K_s + \rho g S)z &= F_{ez} \end{aligned} \tag{3.17}$$

where m is the mass, $A_{x,z}$ are the added mass coefficients, $B_{x,z}$ are the radiation damping coefficients, F_p is the mooring pretension, L the length of the mooring line, C_{pto} is the PTO damping constant, K_s is the spring stiffness constant, ρ is the water density, g is gravitational acceleration, S is the cross-sectional area of the spherical floater ($S = \pi r^2$) and $F_{e(x,z)}$ are the components of the wave excitation force.

By substituting $\ddot{x}_{1,3} = -\omega^2 x_{1,3}$, $\dot{x}_{1,3} = i\omega x_{1,3}$ and ordering terms, Equations 3.17 are converted in Equation 3.18, where mooring stiffness K_s and PTO damping C_{pto} are included in stiffness $\mathbf{K}$ and damping $\mathbf{C}$ matrices. This last equation gives the solution in terms of displacements when the frequency-domain approach is implemented.

[1] The first equation, for heave motion, was previously introduced (Eq. 3.7 Section 3.2).

$$\mathbf{x}_j(\omega) = [-\omega^2[\mathbf{A}_{i,j}(\omega) + \mathbf{m}_{i,j}] + i\omega[\mathbf{B}_{i,j}(\omega)] + [\mathbf{K}]]^{-1}\mathbf{Fe}_j(\omega) \tag{3.18}$$

3.5 Frequency-domain results

Results for the system represented in Figure 3.2, described by parameters reported in Table 3.1, were obtained by solving the equations of motion written in the frequency-domain (Eq. 3.18). Response amplitude operators (RAOs) and dimensionless power curve are reported respectively in Figures 3.6 and 3.7. Results are plotted to have on the horizontal axis the dimensionless wave number $k \cdot r$ which is defined by the wave number k and the floater radius r. This number was used so that the results of different scales used can be easily compared between each other.

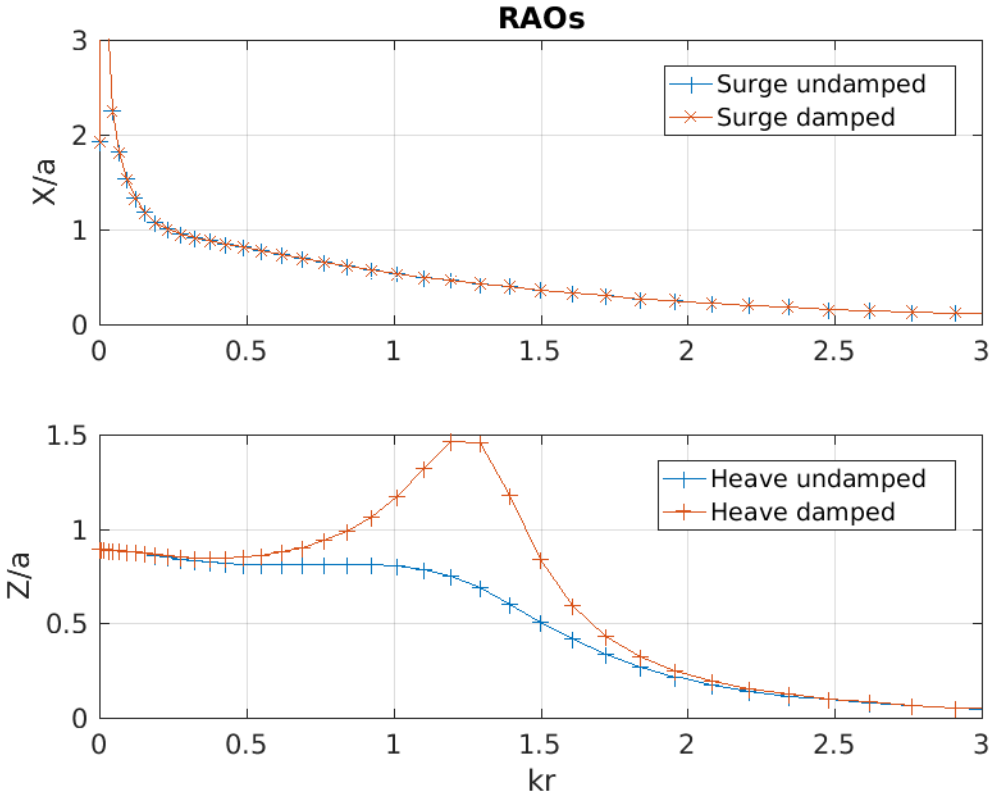

Figure 3.6: Heave and surge response amplitude operators from FD analysis.

Dimensionless power factor P_F is shown in Figure 3.7. This factor indicates the theoretical efficiency of the device, in literature is often also referred to as the *capture width ratio*. The defined power factor was calculated with the following formula.

$$P_F = \frac{\overline{P}}{\frac{\overline{P_{maxEnv}}}{2 \cdot r}} \tag{3.19}$$

where $\overline{P}$ is the mean power produced by the device (expressed in Watts):

$$\overline{P} = 1/2 \cdot C_{pto} \cdot \omega^2 \cdot |Z|^2; \tag{3.20}$$

and $\overline{P_{maxEnv}}$ is the mean power available, this is defined as for conventional linear water waves theory:

$$\overline{P_{maxEnv}} = \frac{1}{4 \cdot \omega} \cdot \rho \cdot g^2 \cdot a^2; \tag{3.21}$$

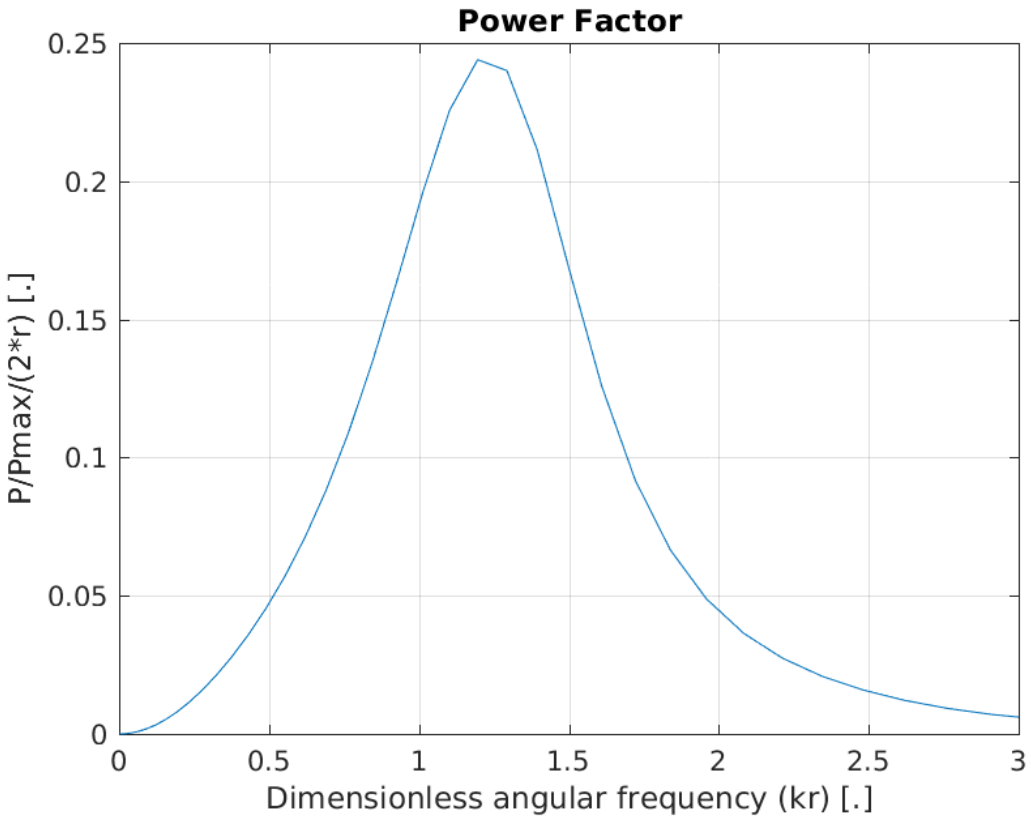

Figure 3.7: Dimensionless curve indicating power factor of point absorber with parameters as in Table 3.1.

3.6 Time-domain formulation

The time-domain formulation is based on the theory developed by Cummins (1962) who derived the general equation of motions for a floating body by introducing convolution integrals. The methodology implemented is normally used for sea-keeping applications. In particular, the added mass and radiation damping coefficients can be calculated independently. This operation is possible thanks to further findings of Ogilvie (1964) who derived the equations of motion for a ship separating the radiation and diffraction problems.

In practice, the hydrodynamic coefficients are calculated by the Nemoh BEM code introduced in Chapter 2 (Section 2.3), as was done for the frequency-domain approach.

The time-domain formulation proposed may be referred to as the weakly nonlinear time-domain method. For two dimensional case, the equations for surge and heave motions can be written as follows.

$$\begin{aligned}(m + A_{\infty x})\ddot{x}(t) + \int_0^t k_x(t-\tau)x(t)d\tau + \phi_x(t, K_s, C_{pto}, L, F_p) = F_{ex}(t) \\ (m + A_{\infty z})\ddot{z}(t) + \int_0^t k_z(t-\tau)z(t)d\tau + \rho g S z(t) + \phi_z(t, K_s, C_{pto}, L, F_p) = F_{ez}(t)\end{aligned} \tag{3.22}$$

Where m is the mass, A_∞ indicates added mass values for $\omega \to \infty$, and $\phi_{x,z}$ indicate horizontal and vertical components of the mooring restoring force. $x(t)$ and $z(t)$ represent the floater's surge and heave displacements. Two over-dots indicate accelerations (second-order derivative). The $k_{j=x,z}(t-\tau)$ is the casual kernel function present in convolution integrals which represents the memory effect of the radiation forces. This function is evaluated for a short period which represents system response in a previous interval (actual time step minus a defined short period of c.a. 20 seconds). The following formula defines the kernel function.

$$k(t) = \int_0^\infty B(\omega)cos(\omega t)d\omega \tag{3.23}$$

The mooring force components for the two dimensional PA case can be defined as introduced in Section 3.4, i.e. $phi_x = (f + F_p)sin(\alpha)$ and $\phi_z = (f + F_p)cos(\alpha)$. These are found by applying basic trigonometric laws to the geometry reported in Figure 3.5. These mooring force components depend on: floater's displacements and velocities, the spring stiffness coefficient K_s, the PTO damping C_{pto}, the mooring length L, and the mooring pretension F_p. Further explanations of how these components are calculated in the time-domain method proposed are reported in Section 3.7.2.

The advantage of the adopted theory compared to the frequency-domain approach is that transient effects, for example, existing due to the presence of the PTO mechanism or the mooring system, can be captured in the methodology.

In order to the formulation to be valid, it is assumed that displacements are small and that these are directionally proportional to the induced velocity of the water particles surrounding the body and *vice versa*. In practice, having assumed that only small displacements occur and that the fluid is potential the superimposition principle can be applied.

3.6.1 First order wave loads

First order wave excitation forces were calculated with the Nemoh code, and these were used to compute the time-dependent wave loads in both regular and irregular seas options.

The total wave excitation force, the Froude-Krylov and diffraction components are illustrated in Figure 3.8. This plot represents dimensional results obtained directly with the Nemoh code. As can be noted the Froude-Krylov part gives the main contribution to the total force. The Nemoh code uses the angular frequency ω as input and output,

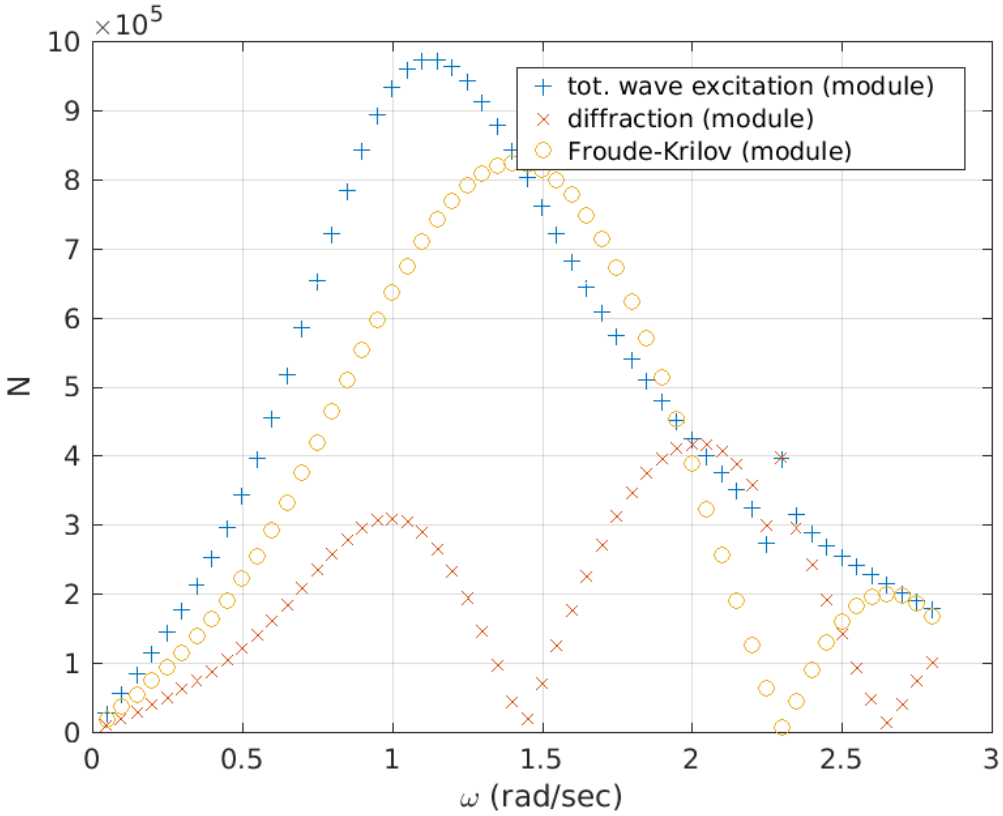

Figure 3.8: Illustration of wave exciting force and its diffraction and Froude-Krilov components for the considered spherical floater.

so instead of using the kr this time are plotted for ω (rad/s) on the horizontal axis.

In the numerical code, two methods were implemented. The first, named *direct wave loading option*, is based on the superimposition principle. While for regular waves, the sea is assumed to be sinusoidal, for the irregular sea case the force vector is created by adding together different sinusoidal functions of various amplitudes and frequencies. In contrast, the second option, named *impulse-response wave loading option*, concern the application of the impulse-response functions. These lasts are in all cases used for the computation of the radiation forces, in the case of the *impulse-response wave loading option* these are also used for calculating the waves excitation load terms. Thus, for this second option, the wave loads in regular and irregular seas depend excursively on the free surface signal $\eta(t)$. The latter can be determined, either same as for the *direct wave loading option* or by using a defined free surface elevation vector, which can be obtained from real sea measurements or by tank tests.

Direct wave loading option

For the regular waves case, the force was assumed to be varying in a sinusoidal way. The formula adopted for estimating loads, in this case, is reported in Section 3.7.

For the irregular sea option, the Bretschneider wave spectrum was at first implemented. The following formulas can define this (Journee and Massie, 2001).

$$S(\omega) = \frac{173 H_{1/3}^2}{(T_1 \omega)^5} e^{\frac{-692}{(\omega T_1)^4}} \tag{3.24}$$

The above was used for the particular case of $T_1 = 3.86\sqrt{H_{1/3}}$ where this formula it reduces to the One Parameter Pierson-Moskowitz wave spectrum (is shown in Figure 3.9). This spectrum was initially used as this was simpler to implement compared to other types of spectrum. In fact, this does not require any other particular parameter except T_1 and $H_{1/3}$. Besides, it was chosen this as it is representative of the Atlantic

Ocean conditions. A further sea spectrum was then implemented during case studies described in Chapter 6.

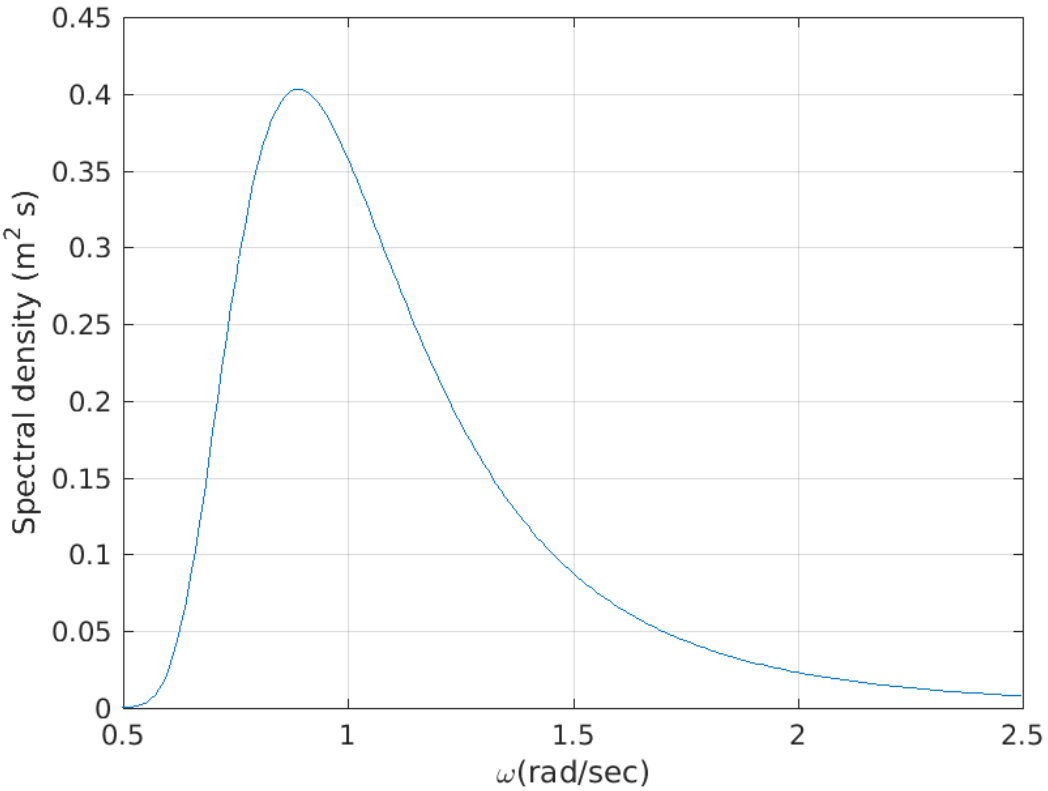

Figure 3.9: One Parameter Pierson-Moskowitz wave spectrum ($H_s = 2$ m).

Further details on how this option was implemented are reported in Section 3.7.

Impulse-response wave loading option

With the *impulse-response wave loading* option the wave loads, for both regular and irregular waves cases, are calculated through the use of the non-casual impulse-response function and the convolution integral, which were defined as following (Falnes, 2002).

$$F_w(t) = \int_{-\infty}^{\infty} f(t-\tau)\eta(\tau)d\tau \tag{3.25}$$

where the impulse-response function $f(t)$ is equal to

$$f(t) = \frac{1}{2\pi} \int_{-\infty}^{\infty} F_e(\omega) e^{i\omega t} d\omega \tag{3.26}$$

$\eta(\tau)$ is the free surface elevation signal, which represents time in the past and future. The $F_e(\omega)$ represent wave excitation force coefficients, which are calculated with the Nemoh code.

3.6.2 Second order wave drift loads

Estimation of drift forces in the time-domain was obtained through the development of a technique which concerned the definition of a reflection coefficient (C_{refl}). This factor can be used for calibrating the numerical code. It is determined from regular waves experimental tests data. In practice, for a series of regular wave tests (where the C_{pto} was set to the *high* value), the surge offset was measured, and the C_{refl} was defined as the value needed to tune the numerical result. The procedure was repeated for all regular waves laboratory simulations of angular frequencies reported in Table 3.2.

The technique developed within the code is similar to the method proposed by Hsu and Blenkarn (1970), which was also implemented by Remery and Hermans (1971). The process is based on the assumption that the free surface signal can be seen as a series of single waves. These have amplitudes equal to either the wave crest or to the absolute value of the wave trough. Their wave periods are found by doubling the time between two consecutive zero crossings. When peaks or troughs, in between a zero crossing were more than one, an average value was used. The drift force in the time-domain was then estimated, for both regular and irregular seas, by the following formula.

$$F_{drift}(t) = \frac{1}{2} \cdot \rho \cdot g \cdot [\cdot a(t) \cdot C_{refl}(t)]^2 \cdot 2r \tag{3.27}$$

This force was evaluated through a loop where the two terms $C_{refl}(t)$ and $a(t)$ depends on the instantaneous wave period and wave amplitude. The reflection coefficients C_{refl} are interpolated from a vector which is defined prior to the numerical simulation. For the half-immersed spherical floater PA (of *7.5 m radius*) values in Table 3.2 were used.

$\omega(rad/s)$	0.40	0.46	0.53	0.59	0.66	0.72	0.79	0.86	0.92	0.99	1.05	1.116	1.18	1.25	1.31
C_{refl}	0.10	0.11	0.15	0.25	0.30	0.35	0.40	0.45	0.45	0.50	0.50	0.55	0.60	0.70	1.00

Table 3.2: Reflection coefficients for the half-immersed floater.

Further details of the technique implemented are described in the next section (Sec. 3.7).

3.7 Numerical formulation

In this section, the numerical method developed for solving the time-domain formulation (concerning the theory explained in previous sections) is described.

The Equation of motion 3.22 is solved for the two degrees of freedom, namely, heave and surge motions. Where the former is positive towards the waves propagation direction. The system modelled is represented in Figure 3.2 as previously introduced. The mooring line is assumed to be connected at the centre of the sphere, where also the centre of mass is located. It is also assumed that there is not hydrodynamic coupling.

As previously stated, hydrodynamic coefficients, needed for solving the mentioned equation of motion, are obtained with the Nemoh code (at the beginning of the computation). These includes added mass coefficients ($A(\omega)_{11,33}$), radiation damping coefficients ($B(\omega)_{11,33}$) and wave excitation force coefficients ($F_e(\omega)_{x,z}$). The Nemoh code gives these coefficients in dimensional form. Thus, for simplicity, calculations and results of the numerical code always have dimensions. To also be noted that results obtained with the Nemoh code were found to be valid only when real-scale quantities were used.

Irregular frequencies obtained from Nemoh were eliminated. A Matlab script for this

purpose was created, which checks that all subsequent coefficients (when ω increases) were within a defined tolerance; otherwise, these are corrected. In particular cases, the polynomial fitting Matlab function was also used for this purpose.

3.7.1 Estimation of first and second order wave loads

First order wave excitation loads, for the regular waves case, when the *direct wave loading option* is selected, are estimated with the following formula.

$$F_{w_{x,z}}(n) = a \cdot |F_{e_{x,z}}(\omega)| \cdot sin(\omega t(n) + phase(F_{e_{x,z}}(\omega))) \tag{3.28}$$

The free surface elevation is defined as: $\eta(t) = a \cdot sin(\omega \cdot t)$.

For the irregular waves case (*direct wave loading option*) the free surface elevation, the horizontal and vertical components of the wave loads were instead determined by the following equations.

$$\eta(t) = \sum_{n=1}^{n} a_n cos(k_n x + \omega_n t + \epsilon_n) \tag{3.29}$$

$$F_{w_{x,z}}(t) = \sum_{n=1}^{n} |F_{e_{x,z}}(w_n)| a_n cos(k_n x + \omega_n t + phase(F_{e_{x,z}}(w_n)) + \epsilon_n) \tag{3.30}$$

Where a_n are wave amplitudes determined by $a_n = 2\sqrt{S(\omega)\delta(\omega)}$ and ϵ_n are random phase values created by defining uniform distributed random numbers between the interval $[0; 2\pi]$.

As introduced in the previous section, for the *impulse-response wave loading option*, wave loads are calculated by convolution integrals similar as for the radiation forces. Considering Equation 3.26, defining the casual impulse-response function, and noting the fact that this should be real so that $F_e(w) = F_e^*(-w)$, the following equation can

be derived which was found to be stable during the numerical integration occurring in main Runge-Kutta loop.[2]

$$f_{x,z}(t) = \frac{1}{\pi}\int_0^\infty [Re(F_{e_{x,z}}(\omega))cos(\omega t) - Im(F_{e_{x,z}}(\omega))sin(\omega t)]d\omega \tag{3.31}$$

Where the infinite limits of the above integral for computational efficiency are substituted by limited time values (both negative and positive values). For the analysed spherical floater (of *radius* = *7.5 m*) the decaying time of the above kernel function was to be c.a. +- 60 seconds.

Both, casual and non-casual, impulse response functions used to solve the convolution integrals, relative to respectively the wave excitation loads, and the radiation damping forces, are computed similarly. These, represented by Equation 3.23 (defined in the previous section) and Equation 3.31, are solved by using the trapezoidal rule. The obtained values are stored in vectors. These vectors are then cut to the corresponding time where the values are within a defined tolerance value ($\simeq nil$). The kernel of convolution integrals related to the radiation forces of the spherical floater considered was vanishing in c.a. 20 seconds, thus this value was adopted in most of the simulations. The obtained shortened vectors are flipped so that these can be easily incorporated, at each time step, in the convolution integrals, when the main equation of motion is integrated.

[2]the symbol * denotes the complex coniugate

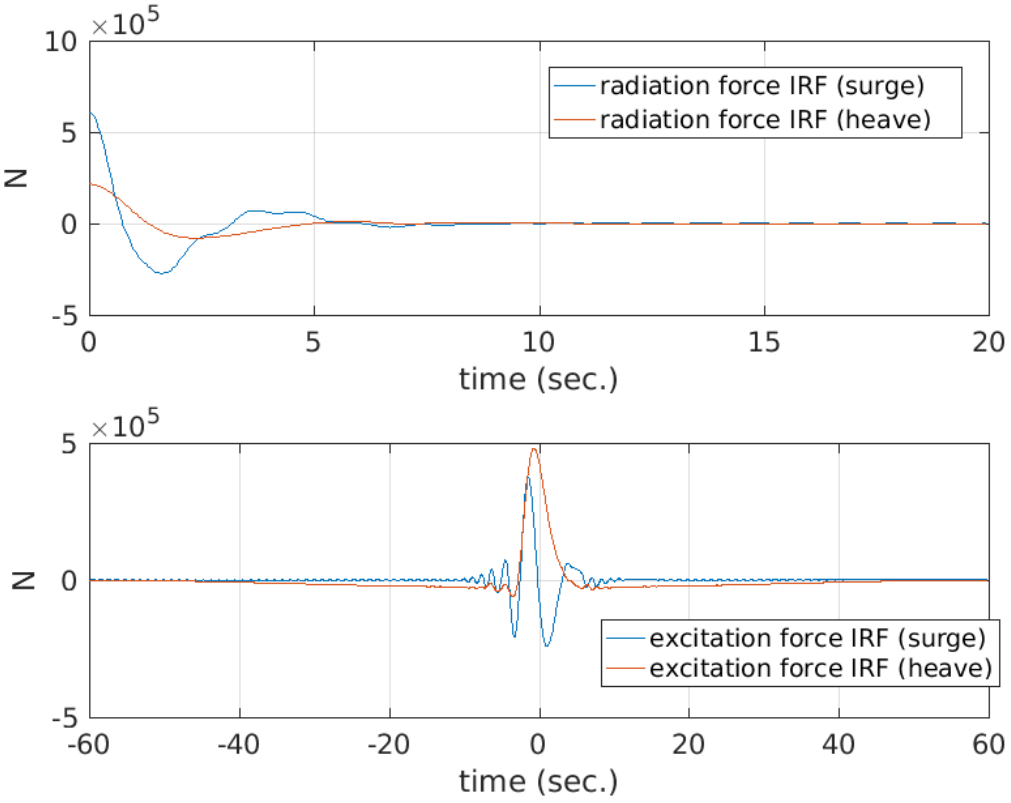

Figure 3.10: Illustration of impulse response functions (IRF) for spherical floater.

Wave drift forces can only be included in the simulation when excitation IRFs are used. For what concerns the wave drift forces in regular waves simulations, these were directly estimated with the formula already introduced in the previous section (Section 3.6.2), which is evaluated for each time step of all the simulation time. Diversely, for the irregular sea case, few other operations are carried out before evaluating the just mentioned formula. These operations are listed next.

1. Definition of the free surface elevation signal $\eta(t)$ through Equations 3.24 and 3.28 or by importing a defined $\eta(t)$ from real-time record.

2. Finding the points where peaks, through and zero crossings occur.

3. Defining a signal of the instantaneous wave period.

4. Interpolation of vectors found in the previous two steps.

5. Finding the closest correspondent of reflection coefficient to use, which depend on the instantaneous wave period.

6. Evaluation of Equation 3.27 (Section 3.6).

For both types of sea simulations, the found waves drift load vector is then added to the first order wave load horizontal component vector.

For an initial period of simulation time, the two wave load forcing terms (independently of the option considered), horizontal and vertical components, were multiplied by a cosine ramp function. Usually, the ramping period utilised was of c.a. 4 times the chosen wave period. An illustration of the ramping function is displayed in Figure 3.11.

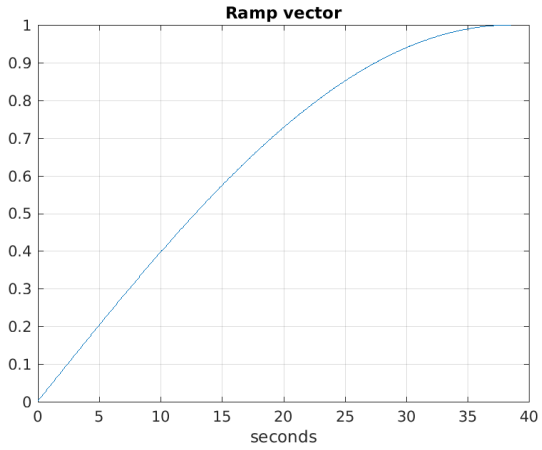

Figure 3.11: Illustration of cosine based ramping function (dim.less) implemented in the numerical tool for a chosen period of 40 seconds.

3.7.2 Mooring force components estimation

In previous Section 3.4 the vertical and horizontal mooring force components were defined with the symbol ϕ. Given the geometry of the device considered (Figure 3.5) Equations 3.12 to 3.16 were defined. These equations are considered again for defining mooring force components in the time-domain formulation.

For the time-domain formulation, the vertical direction of the mooring load is estimated with the following approximation.

$$\phi_z \simeq K_s \cdot z(t) + C_{pto} \cdot \dot{z}(t)^{expC} \tag{3.32}$$

This expression is similar as for the case of the frequency-domain formulation, only the $expC$ is added. The $expC$ is an exponent factor determining the type of damping desired. To model a linear PTO, this was always set equal to one. Eventually, for simulating a quadratic PTO force, $expC$ can be set equal to 2. To clarify, the C_{pto}, in this case, is again the power-take-off damping coefficient. As the mooring line is assumed to be inelastic, this is the only damping taken into consideration into the mooring components terms. $z(t)$ and $\dot{z}(t)$ are the heave displacement and heave velocity of the floater. K_s is the spring stiffness constant.

For finding a valid approximation for modelling the restoring horizontal mooring component ϕ_x the analogue mechanical system, shown in Figure 3.12 was considered. This system represents a mass that is attached to a rail by means of bearings, and this mass is free to oscillate along the horizontal direction. The horizontal restoring force is only due to horizontal offset.

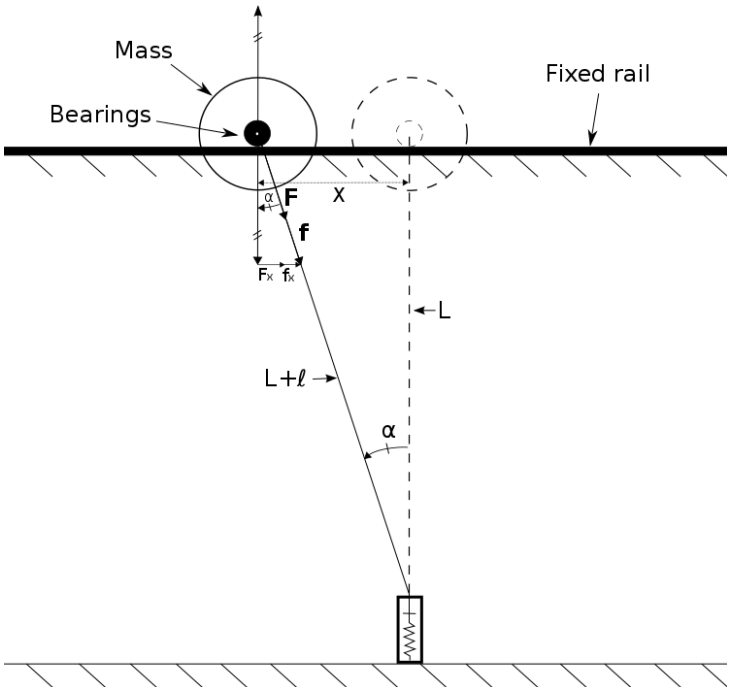

Figure 3.12: Mechanical system analogy considered for defining numerical approximation related to the horizontal mooring restoring force component.

Recalling Equations 3.15, 3.16, 3.14 and 3.12, the surge component is estimated by by assuming that the horizontal restoring force is independent of the floater's heave velocity and heave position. For surge motion the mentioned equations become:

$$\ell = \sqrt{x(t)^2 + L^2} - L \tag{3.33}$$

$$\frac{d\ell}{dt} = \frac{x(t)\dot{x}(t)}{\sqrt{x(t)^2 + L^2}} \tag{3.34}$$

$$f = K_s(\sqrt{x(t)^2 + L^2} - L) + C_{pto}\left(\frac{x(t)\dot{x}(t)}{\sqrt{x(t)^2 + L^2}}\right). \tag{3.35}$$

Thus, ϕ_x is approximated to be:

$$\phi_x \simeq (K_s(\sqrt{x(t)^2 + L^2} - L) + C_{pto}\left(\frac{x(t)\dot{x}(t)}{\sqrt{x(t)^2 + L^2}}\right) + F_p)sin(\alpha) \tag{3.36}$$

Where, K_s is the spring stiffness, $x(t)$ is floater's surge displacement, L is the mooring length, C_{pto} the the PTO damping coefficient, Fp is the mooring pretension and $sin(\alpha)$ is equal to: $sin(\alpha) = x(t)/\sqrt{x(t)^2 + L^2}$.

This time the effect of the PTO damping C_{pto} over the surge motion is considered, not neglected as in the case of the frequency-domain approach.

Horizontal and vertical components of the mooring tension were stored at each time step, throughout the entire integration of the main loop (described in the next section).

In particular, the mooring load was evaluated at two different points. The first point is needed to monitor the mooring line tension occurring at floater attachment point (fairlead), which in our case corresponds to the centre of the sphere (point no. 1). The second point was used for comparison of numerical results with empirical data[3]. The value of the mooring load at this point refers to the mooring tension after the effect of the damper and the spring modelling the PTO force (point no. 2).

3.7.3 Main integration loop

For solving the main equation of motion the classic Runge-Kutta 4^{th} order numerical integration scheme was implemented in the Matlab environment.

The Equation 3.22 representing second order differential equations was converted in two first-order systems of equations. To do so, the conversion $x_1 = x$ and $x_2 = \dot{x}$ was implemented in the equation for surge, and $z_1 = z$ and $z_2 = \dot{z}$ conversion was implemented in the equation for heave. These two first-order systems are Equations 3.37 and 3.38.

[3]This latter point was in the location of the load cell, to which the mooring line was connected and which was fixed to the carriage (as is further explained in Chapter 4).

$$\begin{cases} \dot{x_1} = x_2 \\ \dot{x_2} = \frac{-ConvInt_x(t,x_1)+F_{drift}(t)+F_{w_x}(t)-\phi_x(t,x_1,x_2,parameters)}{(m+A_{\infty x})} \end{cases} \tag{3.37}$$

$$\begin{cases} \dot{z_1} = z_2 \\ \dot{z_2} = \frac{-ConvInt_z(t,z_1)-Hydro_{ss}(t,z_1)+F_{w_z}(t)-\phi_z(t,z_1,z_2,parameters)}{(m+A_{\infty z})} \end{cases} \tag{3.38}$$

The $ConvInt(t)(x1, z1)$ indicate the convolution integrals mentioned in Section 3.6. These depend on previous floater displacements and are calculated by using the trapezoidal formula via a Matlab in-build function. To numerically solve these integrals is required to store the previous surge and heave displacement values in an array. At each time step, the necessary values from the array are read and, together with the kernel function (Equation 3.23), are used to compute the convolution integrals.

$F_w(t)_{x,z}$ are the first order wave loads components, these are calculated as was explained in Section 3.7.1. $F_{drift}(t)$ is the horizontal second order drift force and its calculation was also explained in Section 3.7.1.

For clarity, in Equations 3.37 and 3.38 all factors needed for evaluating ϕ_{x_1,z_1} are indicated with: $(t, z_1, z_2, parameters)$. These are the floater's displacement and velocity which depend on time and comprehend the fixed parameters that may be arbitrarily varied, e.g. at the beginning of the simulation. These parameters are the spring stiffness K_s, the mooring length L, the PTO damping coefficient C_{pto}, and the mooring pretension F_p.

The above systems (Eq. 3.37 and 3.38) were written in separate scripts. These were evaluated four times (for each of the Runge-Kutta scheme step) at each time step. The parameters, except for the damping value C_{pto} (varying when the latching control mechanism option is on), were always kept constant during each simulation. The terms related to the forces (radiation, excitation and mooring loads) were re-evaluated at each Runge-Kutta step. To note that the power-take-off (PTO) is modelled as part of the

restoring mooring force $\phi_{x,z}$.

3.8 Time-domain simulation results

The computational time in Matlab required to run a time-domain simulation 600 seconds long was usually less than 3 minutes (on a standard machine with a *i5* 2.27 GHz dual-core processor and with 6 Gigabytes of RAM). This figure includes initial time for initial calculations including the run the Nemoh BEM code.

In this section, some results for an illustrative purpose are reported. The detailed validation of the numerical code is then discussed in Chapter 5.

Results are obtained for system parameters previously introduced in Section 3.2, these are reported again in Table 3.3.

Parameter	**Symbol**	**Values**
radius	r	7.50 m
mooring length	L	60.0 m
mass	m	8.0362E+05 kg
depth (same as length of line)	L	60.0 m
damping	C_{pto}	2.50E+05 N·s/m
stiffness	K_s	1.50E+05 N/m
pretension	F_p	1.00E+06 N

Table 3.3: System standard parameters.

Where not explicitly mentioned system parameters used for running simulations are those reported in Table 3.3.

3.8.1 Free decaying oscillations

With the created numerical tool both surge and heave free decaying oscillations in the time-domain can be computed. Surge oscillations where obtained by setting the initial condition of $x(t0) = 1$ m, similarly heave free oscillations were obtained by setting

$z(t0) = 1$ m. Illustration of free oscillations simulations for the standard PA device are shown in Figures 3.13 and 3.14. For both figures reported, both damped and undamped oscillations are showed. At 1000 seconds the amplitude of the undamped ($C_{pto} = 0$) surge oscillations shows to be just c.a. 0.15 m more than the amplitude related to surge damped oscillations (Figure 3.13). While in the case of heave oscillations the floater almost stops in c.a. 50 seconds, for what concerns damped heave oscillations the motion stops just after c.a. 25 seconds. To note that for both cases, surge and heave free oscillations, when the C_{pto} damping is set to nil (undamped cases) the only damping acting on the floater is the hydrodynamic radiation damping, this only determining the gradual decay of floater motion. The radiation damping forces are always present. For undamped cases is intended that the C_{pto} coefficient is set to nil.

The computed natural frequencies of the device, for the standards parameters reported in Table 3.3, resulted in being equal to c.a. 0.02 Hz for surge and c.a. 0.2 Hz for heave motions.

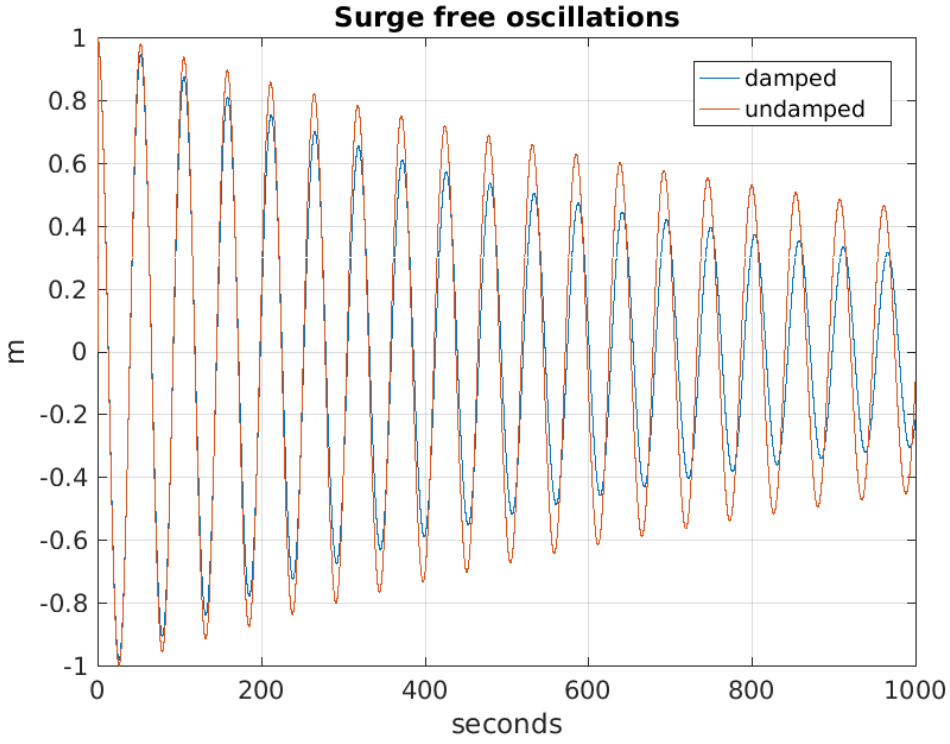

Figure 3.13: Illustration of surge free oscillations (x(t0)=1 m).

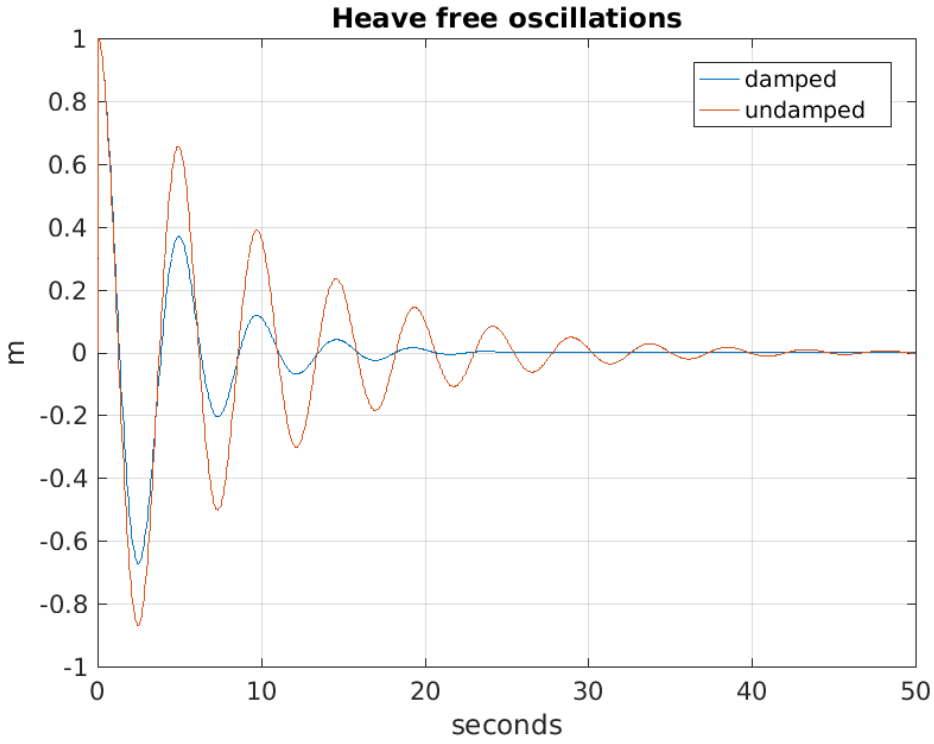

Figure 3.14: Illustration of heave free oscillations (z(t0)=1 m).

3.8.2 Regular waves

Examples of system response in regular waves (of 10 sec. period and 1 m amplitude) can be found in Figures 3.15 and 3.16. These figures respectively show the 500 seconds time series where drift forces are set to zero and time series of the case where horizontal drift forces are taken into account; both simulations were run with standard system parameters (as in Table 3.3). In these figures, the surge, the heave and the mooring load are shown. Both surge and heave are intended to be the displacements from the equilibrium position (calm conditions). The mooring load is the actual force experienced by the mooring component. This load includes the pretension.

By comparing Figure 3.15 with Figure 3.16, it can be noted that the surge motion clearly changes when drift forces are included. However, there is no sensible variation in the total mooring force. It was found that, for the regular waves simulated, the drift force amplifies the horizontal component of the mooring force (ϕ_x) only by a factor of c.a. $10e^4$ N.

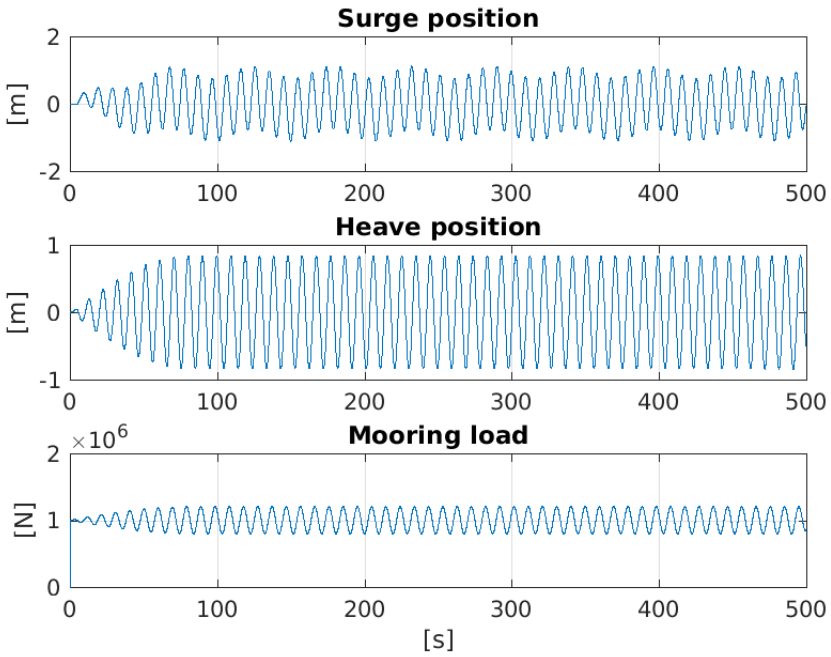

Figure 3.15: Illustration of time series indicating response in regular waves of 10 seconds period and 1 m amplitude.

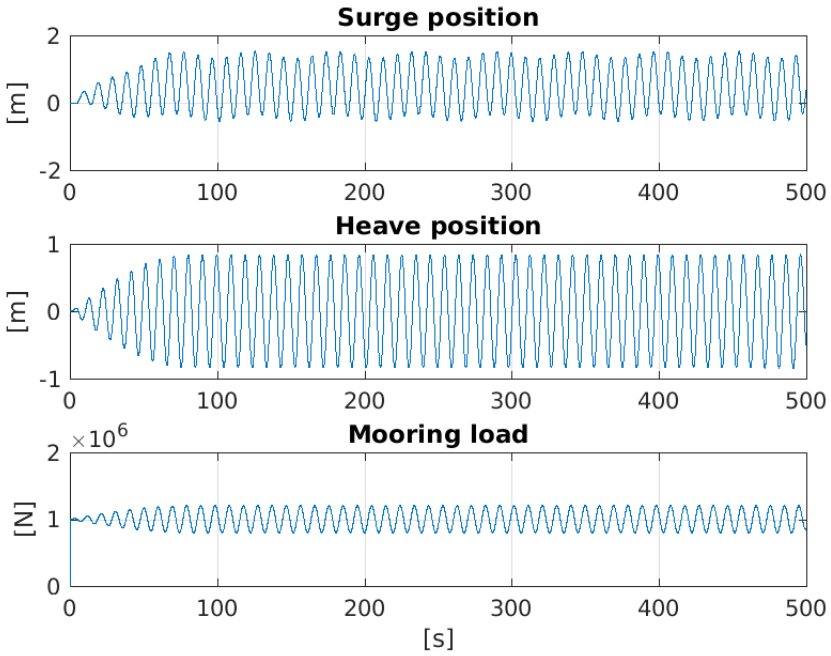

Figure 3.16: Illustration of time series indicating system response when horizontal drift forces were included (in regular waves of 10 seconds period and 1 m amplitude).

In Figures 3.17 to 3.20 are reported main results for time-domain simulations obtained with different C_{pto} damping values. All other system parameters were unchanged. The time-domain model was run within a loop so that regular sea states defined by 14 angular frequencies $0.1 < \omega < 2.7$ (rad/s) and 6 wave amplitudes $a = 0.5, 1, 1.5, 2, 2.5, 3$ m were simulated. These figures show that surge, for most ω, and heave RAOs are independent of the wave amplitude (a). As expected, the axial mooring displacement, reported in the third plot of all figures, is more for the undamped case (Figure 3.17). The fourth plot of figures shows the theoretical mean power that is produced by the device. To note that for simplicity no design rated power value is given to the device so the power increases when a or C_{pto} also are increased. The mooring load showed to be slightly higher in the case when no damping is applied (C_{pto}).

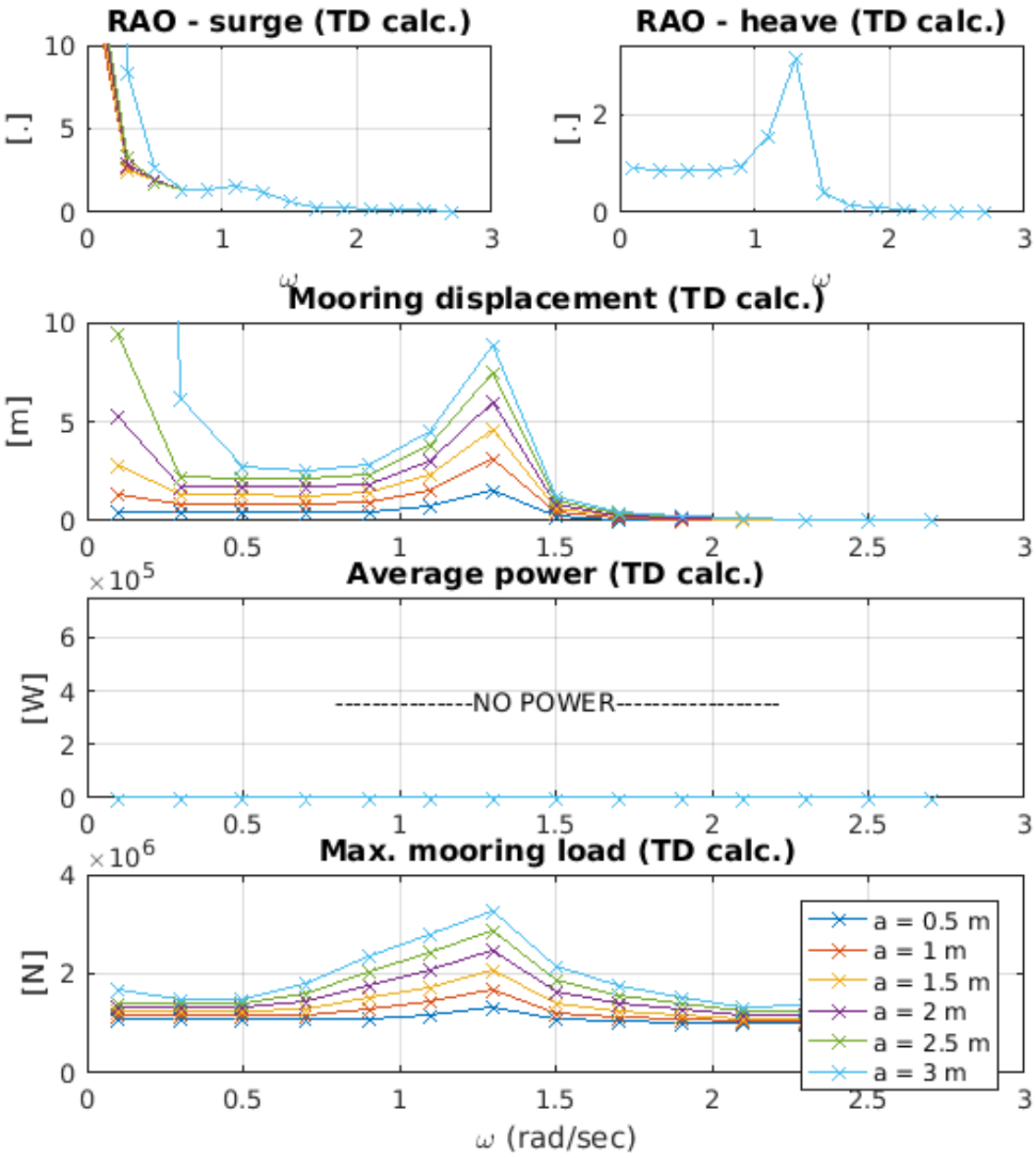

Figure 3.17: Simulation results for floating spherical PA with *Cpto=0* and standard system parameters (as in Table 3.1) for different wave amplitudes *(a)*.

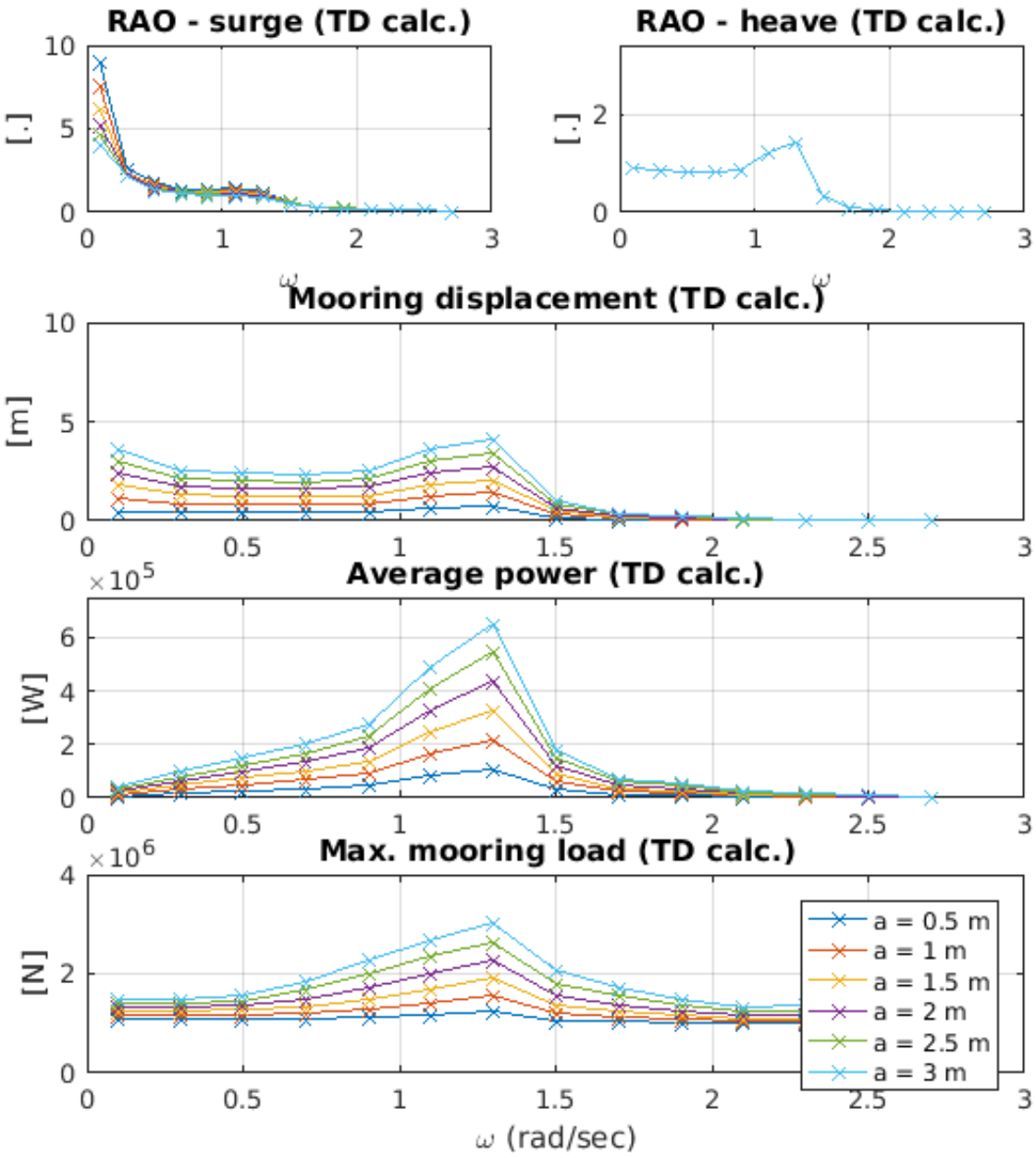

Figure 3.18: Simulation results for spherical PA with *Cpto=1.875E5 kg/s* and standard system parameters (as in Table 3.1) for different wave amplitudes *(a)*.

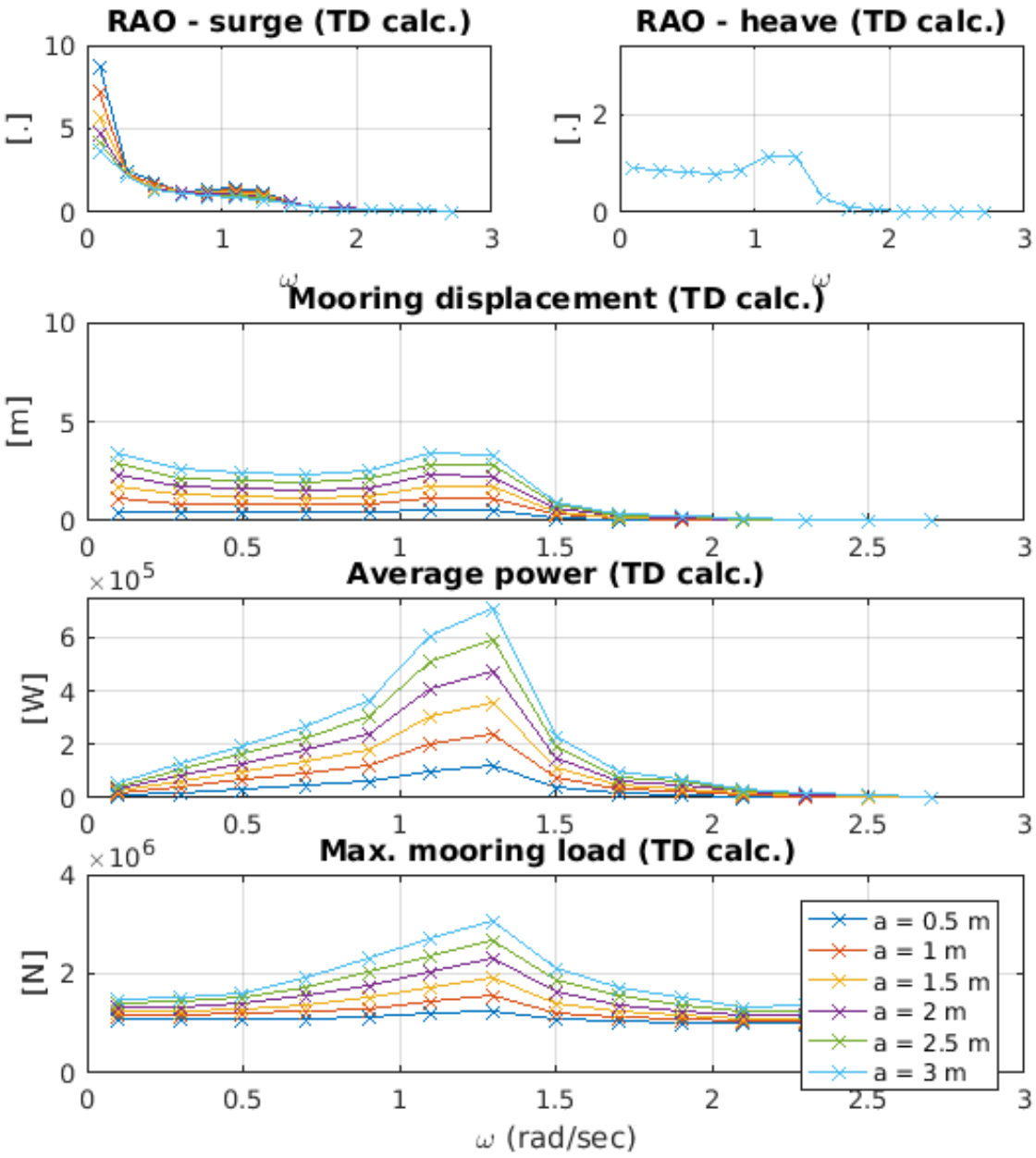

Figure 3.19: Simulation results for spherical PA with standard system parameters (as in Table 3.1, *Cpto=2.5E5 kg/s*) for different sets of regular waves of amplitude *a*.

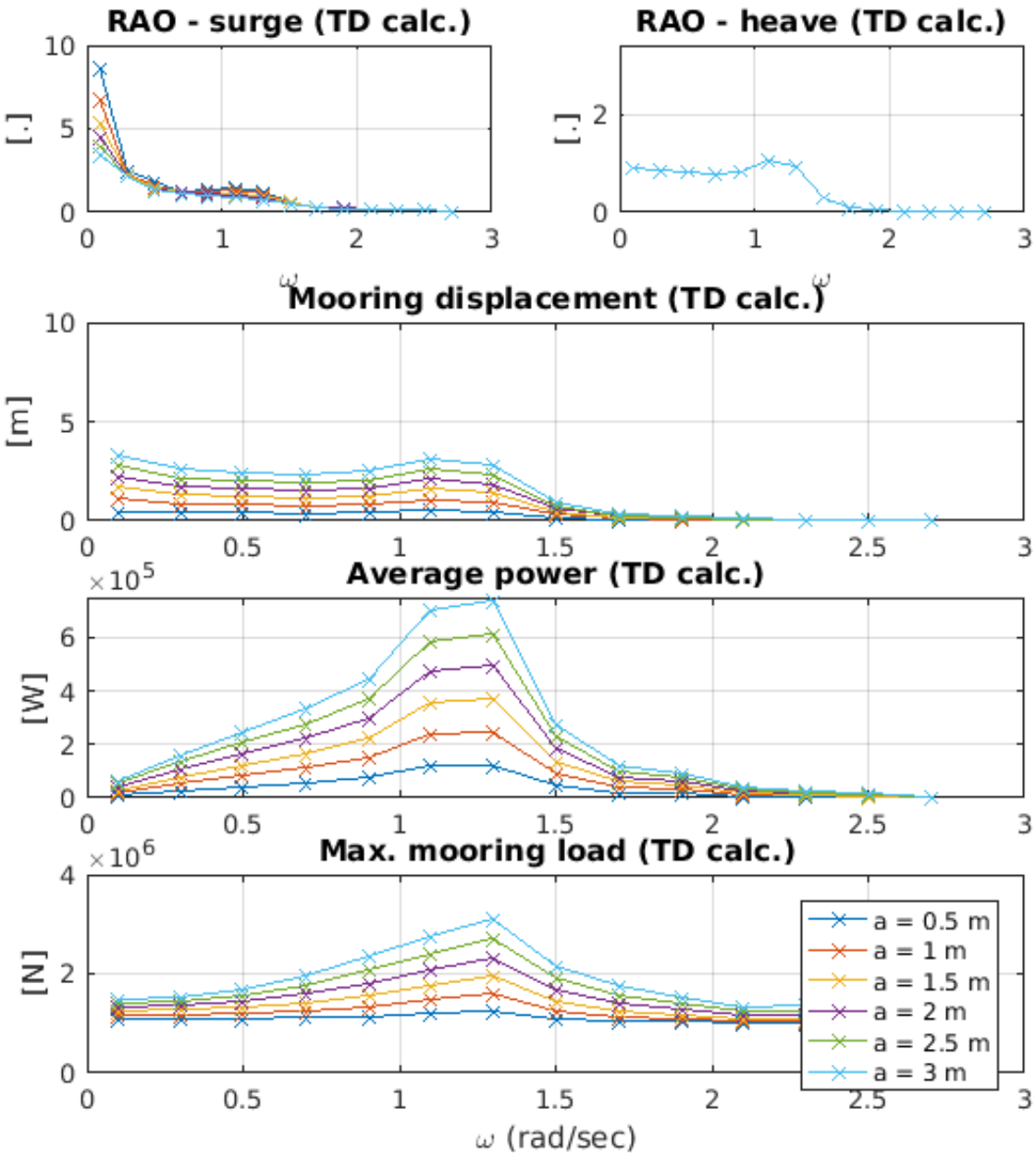

Figure 3.20: Simulation results for spherical PA with *Cpto=3.125E5 kg/s* and standard system parameters (as in Table 3.1) for different sets of regular waves of amplitude *a*.

3.8.3 Regular waves with latching control

A basic latching control method was implemented. This method is based on applying a very large damping constant C_{pto} for a defined interval starting at precise moments. It is a passive control technique, meaning that the energy is just extracted from the external environment (waves) at any time.[4]

The latching method applied is the one proposed by Budal and Falnes (1980), which consist in merely controlling the floater to oscillate with the velocity in phase with the wave force. In practice, the floater is locked for a period of one-fourth of the wave period T_p) by applying a very large damping constant C_{pto}. During this short time, starting when a minimum or maximum free surface elevation (every half wave cycle) occur, the mooring line is blocked. Afterwards, the floater is released causing a much greater floater's acceleration determining a substantial increase of the average power compared to the standard case where no latching control is implemented.

The method is applied for regular sea. Time series of motion and mooring loads relative to the spherical PA in regular waves of 10 seconds period T_p are shown in Figure 3.21. It can be noted that the surge displacements, when the latching method is implemented are similar as for the normal case (Figure 3.15). Heave motion, as expected is characterised by particular intervals in which this is reduced, meaning that for those intervals the floater's was only slightly moving. From the last plot of Figure 3.21 it can be noted that the mooring experiences sudden peaks and sudden low tension values. These both correspond with the beginning of latching periods. However snatch loads are not occurring, because the mooring load is never less than the pretension ($F_p = 10^6$ N).

As desired, in Figure 3.22 is shown the vertical velocity is in phase with the vertical component of the wave excitation force.

[4] In contrast other control methods exist (normally referred in the literature as reactive control methods), where due to particular mechanisms, the energy from the device, for short periods of time, is transferred to the external environment.

In Figure 3.23 results obtained with multiple wave amplitudes are shown. In this case, the latching method was implemented. System response varied from the standard no latching case (Figure 3.19). The surge RAO for all wave amplitudes is less. The heave RAO peak frequency is less, and its magnitude is c.a. double compared to the normal case. In particular, for frequencies $\omega < 1.0$ (rad/s), the extracted average power is reasonably higher than that of the normal case. This can be confirmed by comparing the fourth plot in Figure 3.23 (where latching is used) with the fourth plot in Figure 3.19 (standard case). However, for higher values of ω (> 1 rad/s) the latching method is not beneficial, this led to minimal power absorption. The mooring load for the range of frequencies where power incremented also is substantially increased.

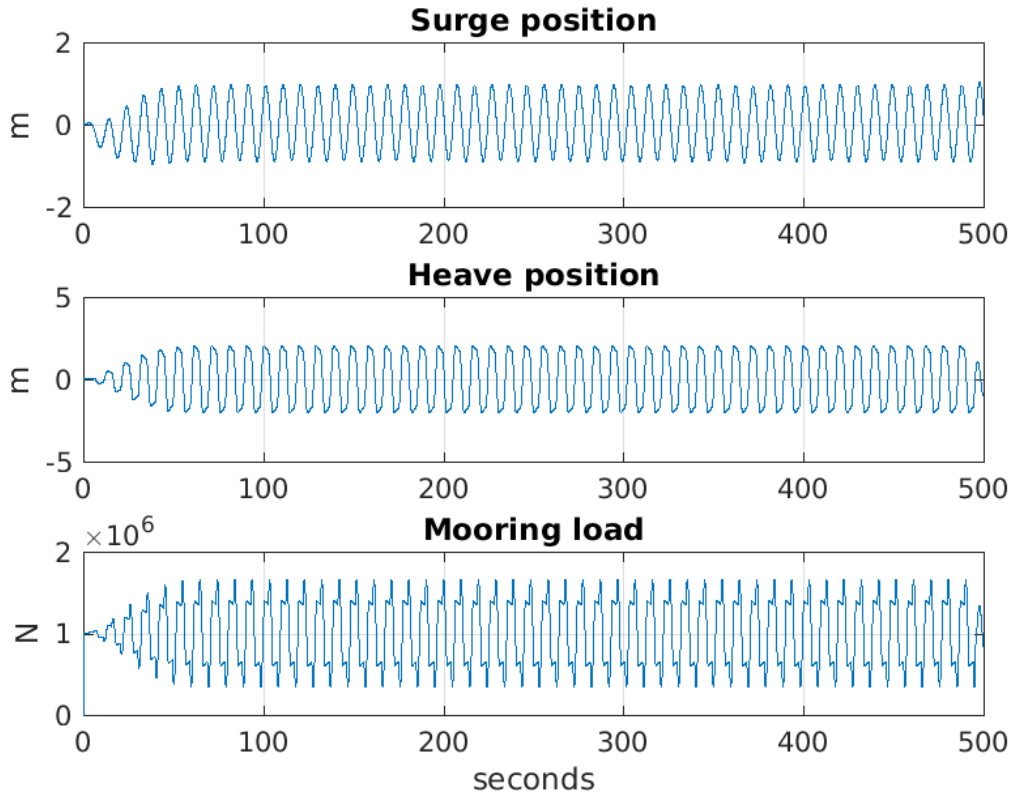

Figure 3.21: Illustration of results for regular waves of 10 seconds period with latching control.

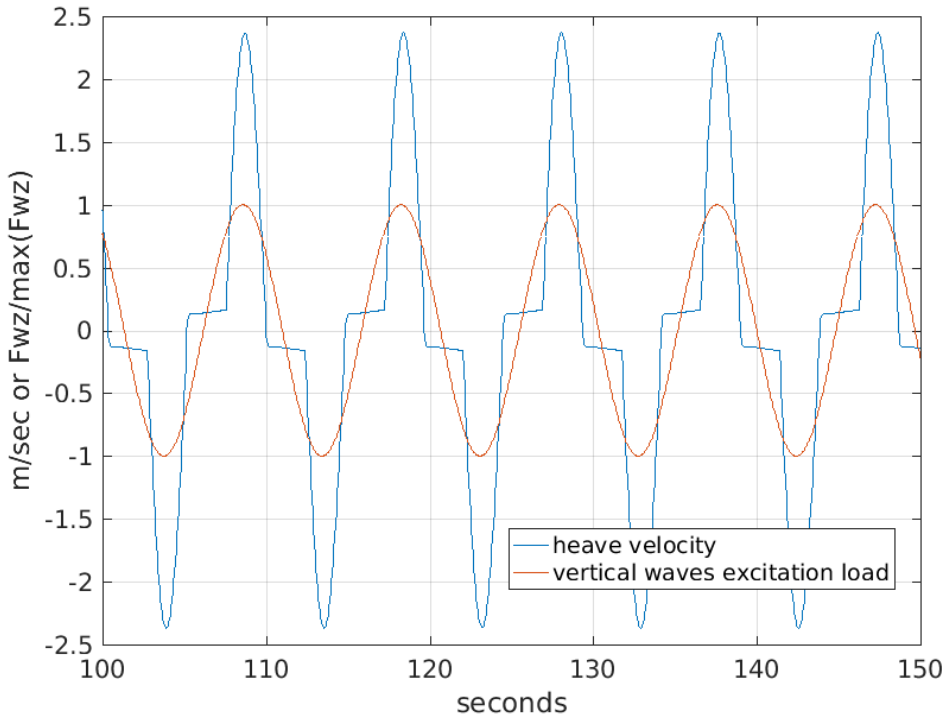

Figure 3.22: Illustration of heave velocity in phase with vertical component of wave excitation force when the latching control is applied.

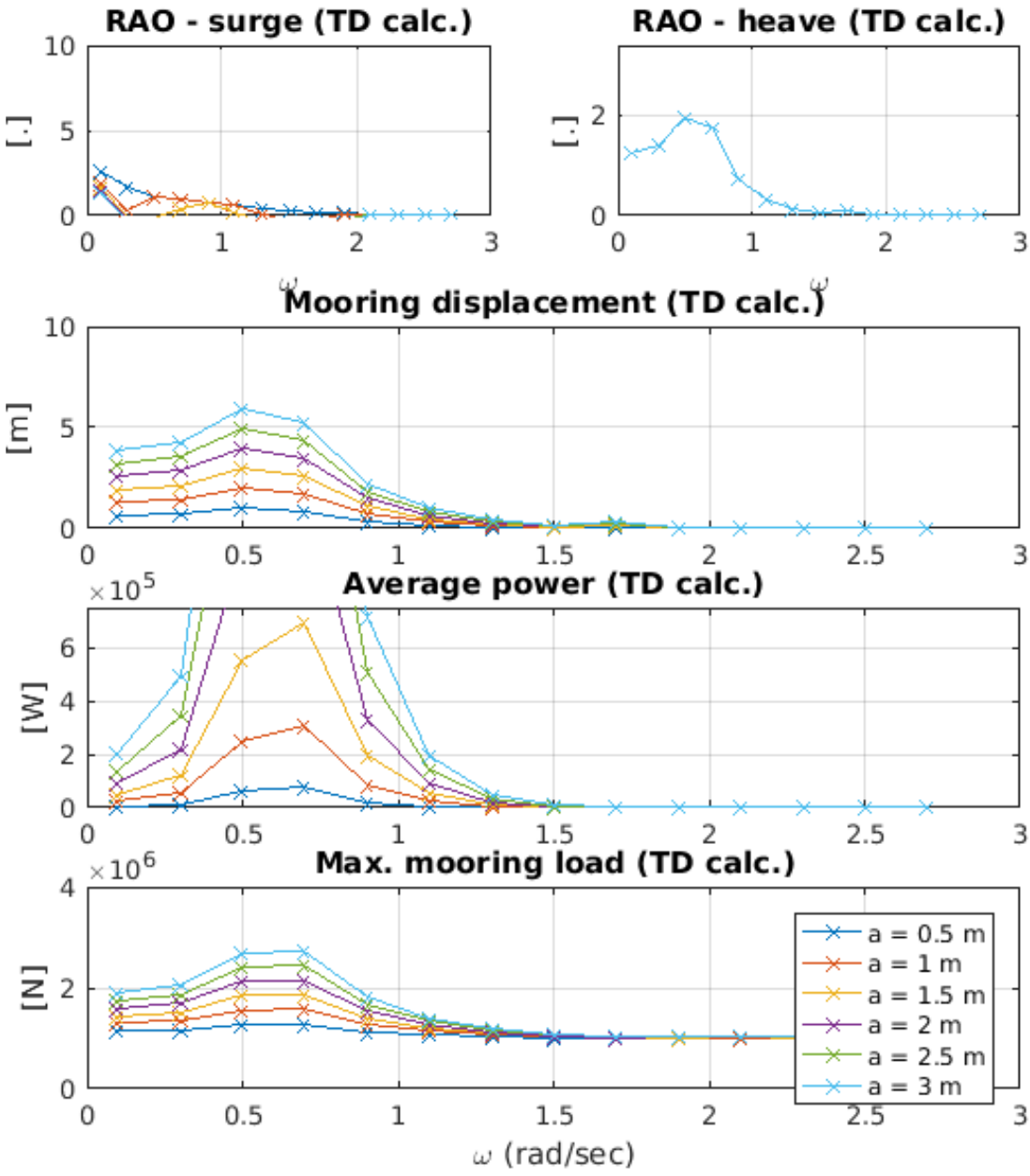

Figure 3.23: Simulation results for spherical PA with standard system parameters (as in Table 3.1, *Cpto=2.5E5 kg/s*) for different sets of regular waves of amplitude a, when the latching control method is used.

3.8.4 Irregular sea

As explained in Sections 3.6 and 3.7 for simulating the irregular sea the Pierson-Moskowitz sea spectrum is applied for defining irregular sea forces, these lasts may be included into the model by the *direct wave loading option* or the *impulse-response wave loading option*. Here next for illustration purposes are reported only results of the *direct wave loading option*. Results concerning the other option will be discussed in later Chapter 5.

In Figure 3.24, the results for an irregular sea simulation are illustrated. These concern an irregular sea state simulation defined by a significant wave high $H_s = 2$ m and wave energy period $T_e = 6$ s. System parameters used, as for previous results concerning free oscillations and regular waves, are those reported in Table 3.3. In this mentioned figure, surge, heave and mooring load time series are shown, these appear not to repeat them self, meaning that the irregular sea state is well defined. Surge and heave displacements at times are more than 1.5 m and less of -1.5 m. The mooring load is always contained between c.a. $1.5 \cdot 10^6$ and $-1.5 \cdot 10^6$ N.

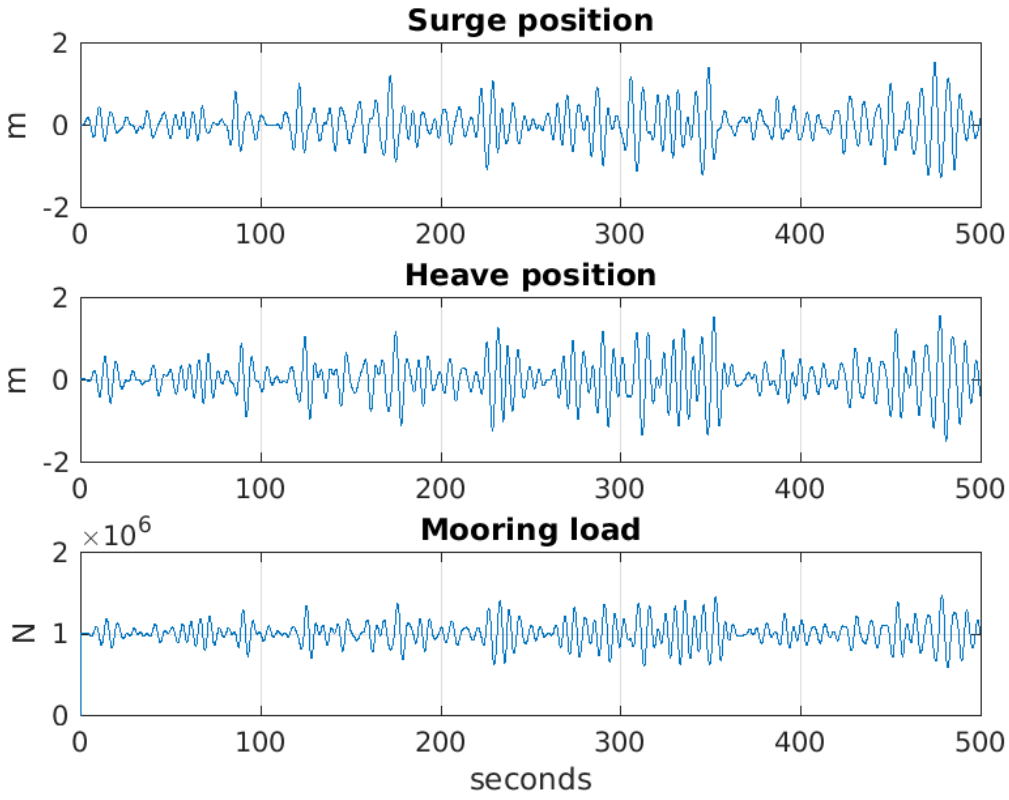

Figure 3.24: Time series of floater motions and mooring load during irregular sea created with the chosen spectrum ($H_s = 2$ m, $T_e = 6$ s and system standards parameters).

In Figure 3.25 is shown the free surface η time series along with normalised horizontal and vertical components of the total wave excitation forces. The normalisation was defined by dividing the forces by their maximum value. The free surface elevation correctly anticipates the vertical and horizontal normalised components of the wave excitation force.

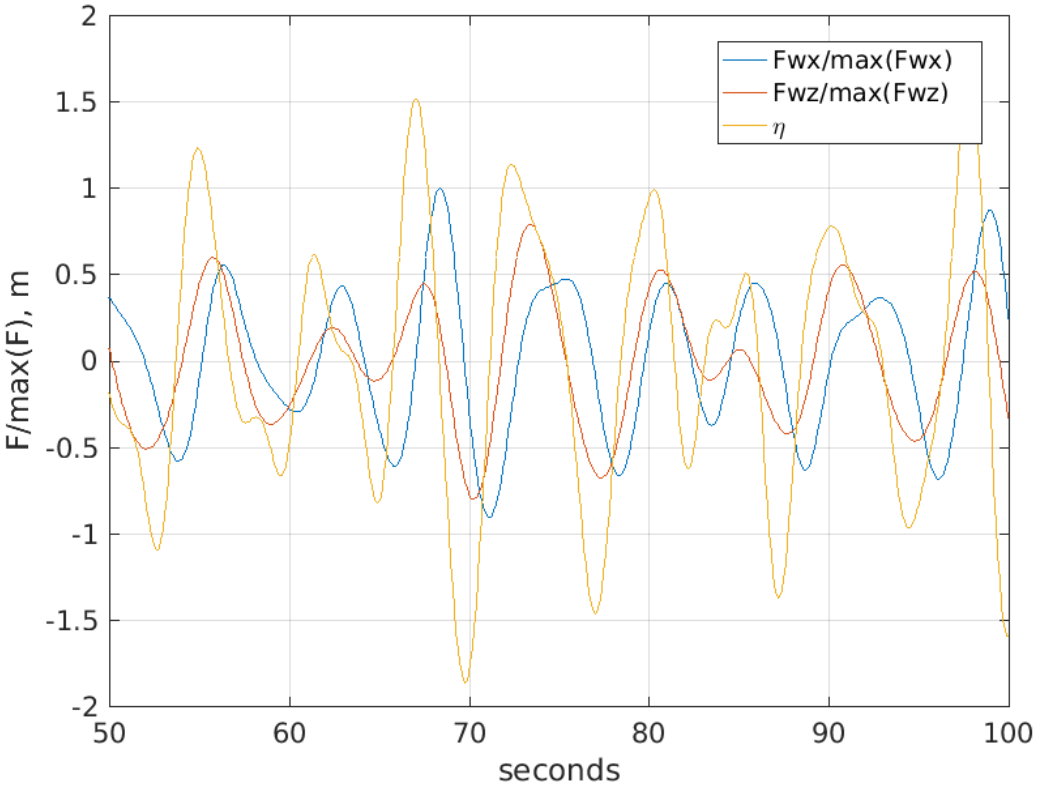

Figure 3.25: Normalized horizontal and vertical components of wave excitation force and free surface elevation during an irregular sea simulation.

3.9 Limitation of the proposed code

The proposed numerical code presents the following limitations:

- Two degrees of freedoms are considered. In reality, little motion occurs as well in the other 4 degrees of freedom namely sway, pitch, roll and sway.
- Horizontal and vertical mooring components are decoupled. Meaning that the horizontal force assumed to be independent than vertical motion and *vice versa*.
- Both frequency-domain and time-domain formulations are valid for relatively limited displacements from the equilibrium position (x=0, z=0). Both formulations

are based on modelling the device taking as reference the mean free surface. It is because hydrodynamic coefficients calculated with the Nemoh code are relative to the mean wetted floating body surface. In real life, during severe sea states large motions occur and thus the assumption concerning the mean free surface on which the method is based might lead to uncertain results.

- The mooring line is assumed to be inelastic. The only axial mooring displacement is due to the extension of the spring component. Depending on the material used, for a real installation mooring component elongation might be an important factor that needs to be as well considered.

- Viscous force are neglected. To note that for the typical size of wave power devices, operating in normal sea conditions, the viscous forces usually are c.a. one order of magnitude less than the first order wave loads. The proposed methodology is not intended to be used for modelling the device for studying extreme loads and motions concerning severe sea states conditions and when eventually viscous effects are more significant. Also for precisely estimate power absorption for relatively small devices, viscous forces might be relevant to be quantified.

- For simplicity, the mooring line is assumed to be attached to the centre. In practice, this is not possible. However due to the spherical shape considered and having assumed no viscous forces this simplification was possible to be implemented.

- The PTO system modelled is simulated as a linear damping mechanism for which a single C_{pto} damping coefficient can be set. Further work is required for including advanced options concerning the modelling of other types of PTOs, such hydraulic or phase controlled systems.

Chapter 4

Experimental study

In this chapter the following main objectives are addressed:

- To develop different experimental set-ups and methods to simulate the considered Earth-reacting device at hydrodynamics laboratories accurately.
- To obtain reliable and repeatable empirical results.

These objectives, as discussed in the introduction of this thesis, were set for obtaining empirical evidence which is needed to pursue the further objective concerning the validation process. This last is an essential step of the generic methodology for analysing and design moored WECs proposed in this thesis.

4.1 Overview

In the previous chapter, a notional full-scale device was described and modelled theoretically. This chapter concerns empirical work related to physical scaled models representing the same device. The experimental work was divided into three distinct sessions. One session concerns a 1:86 model-scale device and two sessions regard 1:33 model-scale

devices. All empirical work was conducted at the two hydrodynamics laboratories of the University of Strathclyde. In this chapter, the work related to experiments is described, explained and the main results are illustrated. The list of experimental models which were assembled and used is reported in Table 4.1.

Objectives of the experimental study were:

- To investigate in an empirical way: the motion response, the axial mooring line displacement, the mooring loads and the power absorption, for the considered device.
- To explore different experimental set-ups and methods to accurately simulate the considered device at hydrodynamics laboratories.
- To obtain reliable and repeatable empirical results.
- To quantify the uncertainties of the experimental results of the different conducted experiments.

Session no.	**Model ID**	**Description**	**Scale**	**Illustration no.**
1	1	Half-immersed floater	1:86	Fig. 4.1 and 4.2
2	2	Half-immersed floater	1:33	Fig. 4.7 and 4.8
3	3a	Half-immersed floater repetition	1:33	Fig. 4.13 and 4.14
3	3b	Submerged floater	1:33	Fig. 4.19 and 4.20
3	3c	Submerged floater without motor	1:33	Fig. 4.21

Table 4.1: Tested models.

At first, laboratories and instruments used are described. After, all five experimental physical models and their components are explained. Successively, calibration of equipment, uncertainty analysis, limitations of the experiments and data post-processing methods, are treated. At the end of the chapter, the primary results are reported.

The obtained empirical data was then used to validate the numerical code previously developed. The reader can refer to Chapter 5 for the validation of the numerical code with experimental results.

4.2 Tank facilities

In this section hydrodynamics laboratories used for testing the physical models are described.

Henry Dyer Laboratory

The 1:86 model was tested in the Henry Dyer laboratory. This facility is equipped with a single flap wavemaker controlled by an in-house developed software. This wavemaker is capable of producing regular and irregular sea states. Specifications for the facility are:

- Length = 21.6 m
- Width = 1.6 m
- Maximum water depth = 0.7
- Waves making: a single computer controlled flap.
- Fixed waves-absorbing beach.

The tank is equipped with a towing trolley travelling on aluminium rails over it. Given the scope of the experiment, this was not used.

The tank is made of fibreglass sections bolted together. On the area where Model 1 was tested there is a window from which it was possible to observe the model directly from a lateral perspective.

Kelvin Hydrodynamics Laboratory

Differently 1:33 scale models were tested in the Kelvin Hydrodynamics Laboratory. Specifications of this facility are reported by MARINET (2013). Main characteristics

of interest of this laboratory are listed next.

- Length = 76 m
- Width = 4.6 m
- Depth = 0.5-2.3 m
- Waves making: variable-water-depth computer controlled flaps wavemaker
- Beach: variable-water-depth sloping beach (with reflection coefficient typically less than 5%)

The maximum possible wave height depends on the set water depth. For 2 meters water depth, the value used during experiments, the maximum possible wave height was about 80 mm.

In the case of experimental work related to this project, the water depth was set to 2 m. This value is a typical setting for this facility. On a regular basis, the wavemaker is calibrated for the set depth. University staff does the calibration. The calibration process is repeated or checked weekly.

The 1:33 Models (2, 3a, 3b and 3c) were partly bounded on the carriage. This last is a wide wagon standing on rails and carries operators and equipment. The carriage is used for towing tank tests or as in our case just as a structure were to install all equipment for stationary experiments with waves.

In Section 4.5 calibration of wavemakers is discussed.

Repeatability of making waves in both tank facilities was analysed in Section 4.7 where the value of standard uncertainty (Type A) related to the wave probe indicates how well waves can be repeated.

4.3 Intruments

Various sensors were used for monitoring motions of system components, free surface elevation and loads. The list of these is reported in Table 4.2.

Instrument	Model ID	Model scale	Measure	Range	Unit
Motion capt. system	1	1:86	Floater displacements	0-28	mm
	2	1:33		0-500	
	3a	1:33		0-500	
Motion capt. syst. (underwater)	3b, 3c	1:33	Floater displacements	0-530	mm
Standard wave probe	1	1:86	Free surface elevation	0-30	mm
	2	1:33		0-320	
	3a	1:33		0-150	
	3b, 3c	1:33		0-150	
Sonic wave probe	3a	1:33	Free surf. elev. 5.7 m upstr.	0-150	mm
	3b, 3c	1:33		0-150	
Load cell	1	1:86	Mooring tension	1-2	N
	2	1:33		15-36	
	3a	1:33		15-34	
	3b, 3c	1:33		15-34	
Laser sensor	1	1:86	Mooring line displ.	0-30	mm
	2	1:33		0-320	
	3a	1:33		0-340	
	3b, 3c	1:33		0-340	
Motor tachometer	2	1:33	Mooring line displ.	0-260	mm
	3a	1:33		0-340	
	3b, 3c	1:33		0-340	

Table 4.2: All instruments used during experiments.

These instruments are described next.

4.3.1 Qualysis system

For logging floater's motion in six degrees of freedom a motion tracking system developed by Qualysis AB was used (Qualysis, 2016). Four Qualysis infra-red sensitive cameras were positioned around the tank and directed towards the floater. As it can be seen for Model 1 in Figure 4.3, the cameras were placed within a certain distance between them to ensure best capture accuracy. Precisely, the more are different the angles defined by the position of each camera and by the centre of the floater, the less

is the expected residual (error in determining the position of the floater computed by the system). For the requirement of the Qualysis system, four reflective markers were attached to the floater. In particular, these were spherical markers attached to a carbon fibre stick and installed on the top dry part of the floater or directly on the floater.

For what concerns the submerged floater, the underwater Qualysis system was used for motion monitoring. This system is similar to the standard system but works thanks to underwater cameras.

Further details and illustrative sketches on how both Qualsys systems were set up are reported in Subsection 4.5.2.

4.3.2 Laser sensor

The elongation of the spring (mooring line axial displacement) was measured and recorded by using a laser sensor connected to a CED power unit. This sensor had an operative range from 0.2 to 10 m. The device was accurately configured for obtaining better precision on the range and units required for each experiment session. The sensor was set to produce an analog signal that was adjusted and recorded with the Spike2 software. For measuring the spring displacement, small reflective panels were constructed, with a piece of light balsa wood for the 1:86 scale Model, with a hard plastic material for the 1:33 scale Models, these in both cases were firmly attached to the mooring line. For illustration this component is shown in figures reported in Section 4.4 (laser reflector).

4.3.3 Load cells

The mooring line tension at the point where the spring was attached was acquired by using load cells. For the 1:86 scale model a 10 kg rated load cell was used. While for the 1:33 scale models a 25 kg rated cell was chosen. The load cells were connected to a CED power unit and logged, similar to the laser sensor, with the Spike2 software.

4.3.4 Free surface elevation sensor

The free surface elevation was all times recorded by a wave probe; this was installed in line with the buoy and was connected to the CED power unit. The latter was needed for capturing the signal and for logging data by using Spike2, as for the case of the load cell and laser sensor.

Data from all sensors connected to the CED power unit was acquired with a 137.17 Hz sample frequency.

4.4 Models

For Sessions 1 and 2 two single test rigs configurations were used (Model 1 and Model 2) while during Session 3 three different experimental set-ups were investigated (Models 3a, 3b, 3c). For clarity in Table 4.3 the details of configurations tested, are listed. Each of the experimental set-ups will be described in next subsections.

Model ID	**1**	**2**	**3a**	**3b**	**3c**	
Scale	1:86	1:33	1:33	1:33	1:33	
Floater radius	0.09	0.23	0.23	0.23	0.23	m
Floater mass	1.23	19.78	21.70	47.00	47.00	kg
Water depth	0.70	2.00	2.00	2.00	2.00	m
Mooring line length	0.59	1.62	1.69	1.12 1.01 0.89	1.12 1.01 0.89	m
Immersion depth	0.00	0.00	0.00	-0.35 -0.46 -0.58	-0.35 -0.46 -0.58	m
Spring stiffness	20.30	177.00	177.00	75.00 355.00	75.00 355.00	N/m
Cpto damping	0.00 3.64	0.00 40.00	0.00 30.00 40.00 50.00	0.00 13.00 15.00 17.00 19.00	no motor	kg/s
Pretension	1.57	35.00	27.00	38.50	38.50	N

Table 4.3: Overview of models' parameters investigated during the experimental study.

In Table 4.3 where multiple parameters are shown means that various configurations were tested for that particular model. For example when tested Models 3b and 3c the mooring length value was varied. This last refers to the distance between the lowest point of the floater to the pulley attached to the bottom of the tank.

In Table 4.3, the *immersion depth* refer to the altitude of the floater's center relative to the horizontal plane.

Model ID	1	2 and 3a	3b and 3c	Real scale PA	Real sc. sub. PA	
Scale	1:86	1:33	1:33	1:1	1:1	
U	8.50E-02	9.76E-02	2.97E-02	5.74E-01	1.72E-01	m/s
l	1.74E-01	4.55E-01	4.55E-01	1.50E+01	1.50E+01	m
γ	1.05E-03	1.05E-03	1.05E-03	1.05E-03	1.05E-03	Pa·s
Re	1.41E+01	4.22E+01	1.28E+01	8.19E+03	2.46E+03	
Fr	6.50E-02	4.62E-02	1.41E-02	4.74E-02	1.42E-02	
Cd	1.00E+00	6.00E-01	2.00E+00	3.00E-01	5.00E-01	
r	8.72E-02	2.27E-01	2.27E-01	7.50E+00	7.50E+00	m
A_c	2.39E-02	1.62E-01	3.25E-01	1.77E+02	3.53E+02	m^2
Fd	8.63E-02	4.64E-01	2.86E-01	8.75E+03	2.62E+03	N

Table 4.4: Assessment of scaling.

A series of quantities were calculated to estimate how well laboratory models represented real-scale devices. In Table 4.4 are reported the Reynolds number Re and the Froude number Fr. Definitions of these numbers were introduced in Section 2.3 of Chapter 2. To calculate these numbers the relative velocity of the floater U corresponds to the mean relative velocity (with respect to still free surface) during peak heave resonance frequency. While for the scaled models the U value is the one relative to experiments, the U is relative to real-scale devices is obtained from frequency-domain calculations. The characteristic length of structure-fluid phenomena is assumed to be equal of one floater's diameter indicated by l. With γ is denoted the kinematic viscosity of water. It can be noted that: while the Reynolds numbers between scaled models and real-scale devices vary by about two orders of magnitude, the Froude numbers are very similar. In Table 4.4 is also reported the module of the estimated drag force Fd for each model in considerations (scaled and real scale devices). To estimate drag forces (at peak resonance condition), the Drag Equation was used ($Fd = 1/2\rho C_d A_c U^2$). In this equation the C_d is the drag coefficient depending on Reynolds number, A_c is the characteristic frontal area (assumed to be half of the wetted surface).

4.4.1 Spherical PA model tests at 1:86 scale - Session 1

Experiment set-up of Model 1

The 1:86 scale model of the point absorber WEC was constructed and was tested at the Henry Dyer tank laboratory.

From Figure 4.1 to Figure 4.3 it is shown the experiment set-up constructed for this set of tests. The floater was attached to a taut mooring line. As illustrated in Figure 4.4, a spring was connected to a load cell (rated 10 kg) and to the mooring line, this last was passing through a worm installed on a shaft of a servomotor. The mooring line then passed through an underwater pulley at the bottom of the tank. This consisted of a thin dyneema rope (0.2 mm) and, just for a short segment (corresponding to the motor's worm above the water), also of a 2 mm diameter polyester rope. A laser sensor pointing towards a reflector attached on the mooring line was installed for measuring mooring line displacements along the axial direction. The servomotor showed in Figure 4.4 was a servomotor with an incorporated tachometer. This component was connected to a microprocessor device called myRIO (produced by National Instruments) and controlled by a model created in Labview (National Instruments). The servomotor was controlled by the Labview model to generate the damping force simulating the PTO mechanism.

Parameters of Model 1 are reported in Table 4.5. These parameters were chosen by scaling down the standard parameters of the PA introduced in Chapter 3. Froude scaling laws were used. Real scale parameters, reported in Table 4.5, do not exactly match parameters introduced for the PA in Chapter 3 because of model making practical limitations.

In Figure 4.3 a picture showing the wave tank is reported. Both, the Qualysis cameras and the floater's position are shown.

Components of Model 1 installed above water are displayed in Figure 4.4. In this picture, all the parts needed for simulating the PTO and measuring the mooring line

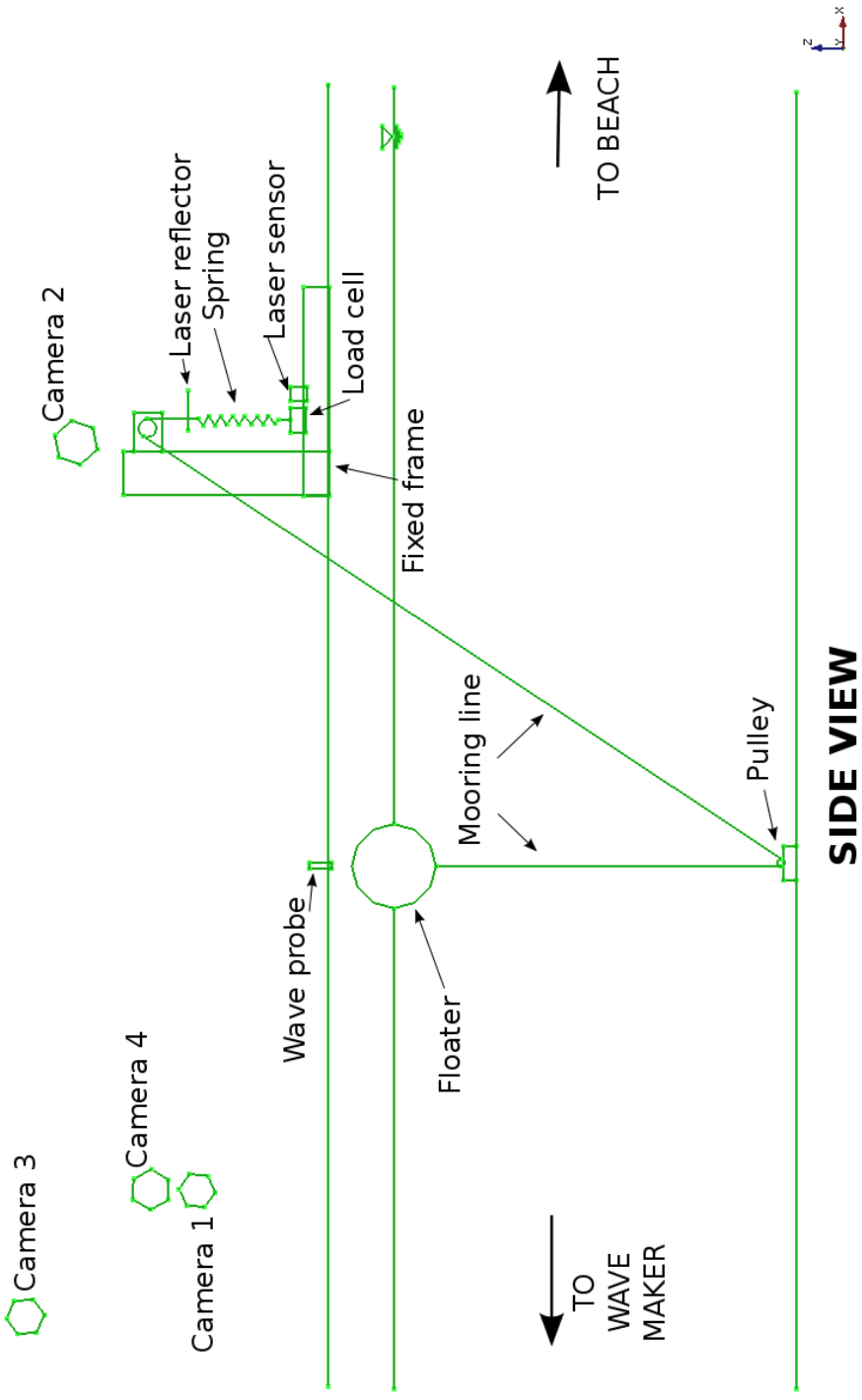

Figure 4.1: Experiment set-up illustrative sketch (side view).

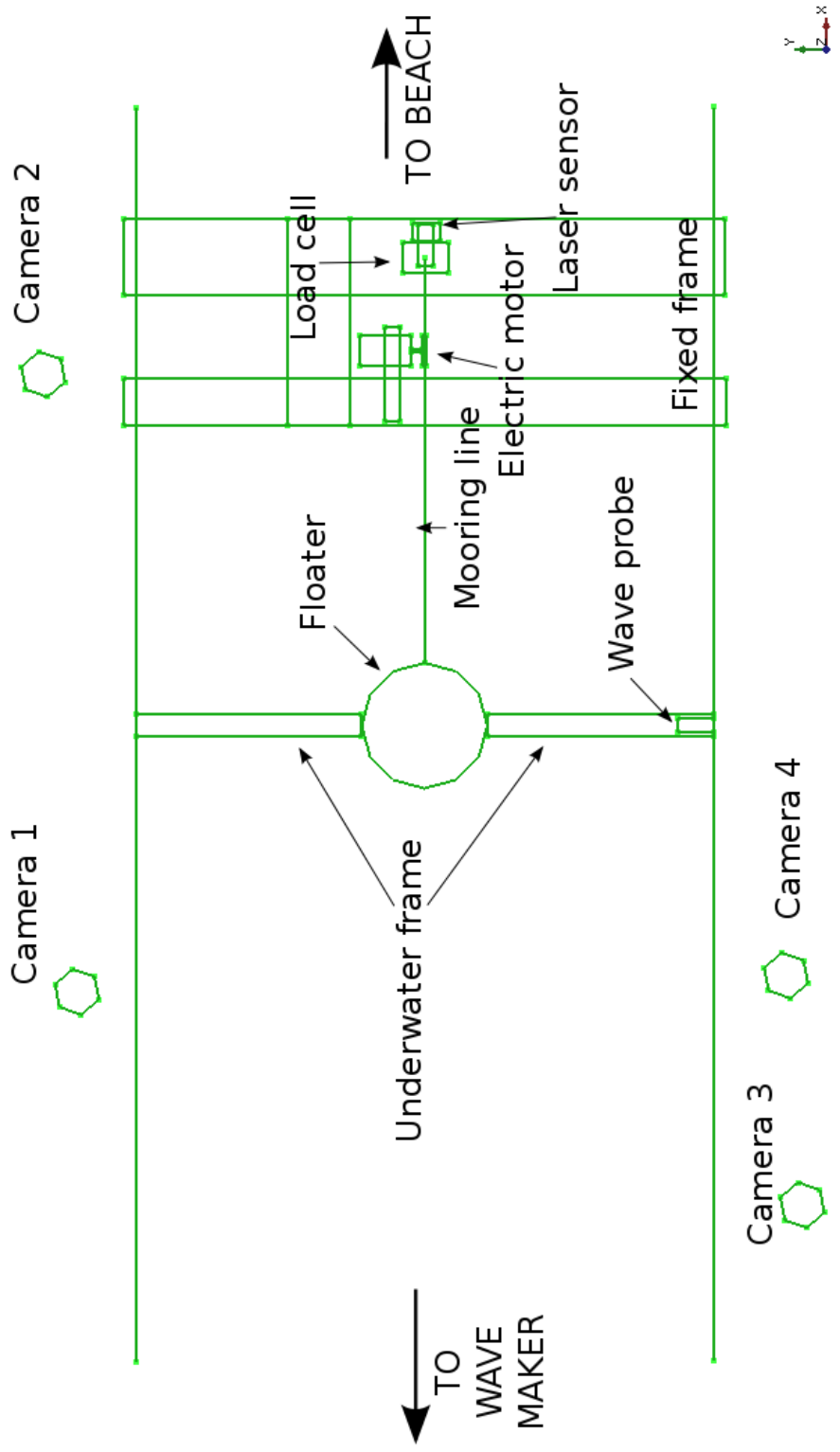

Figure 4.2: Experiment set-up illustrative sketch (top view).

	Model scale	**Real scale**	
	1:86	1:1	
Model ID	1		
Floater radius	0.09	7.50E+00	m
Floater mass	1.23	7.82E+05	kg
Water depth	0.70	6.00E+01	m
Mooring line length	0.59	5.10E+01	m
Immersion depth	0.00	0.00E+00	m
Spring stiffness	20.30	1.50E+05	N/m
Cpto damping	0.00/3.64	2.50E+05	kg/s
Pretension	1.57	9.99E+05	N

Table 4.5: System parameters for PA model tested in Henry Dyer towing tank (Model 1).

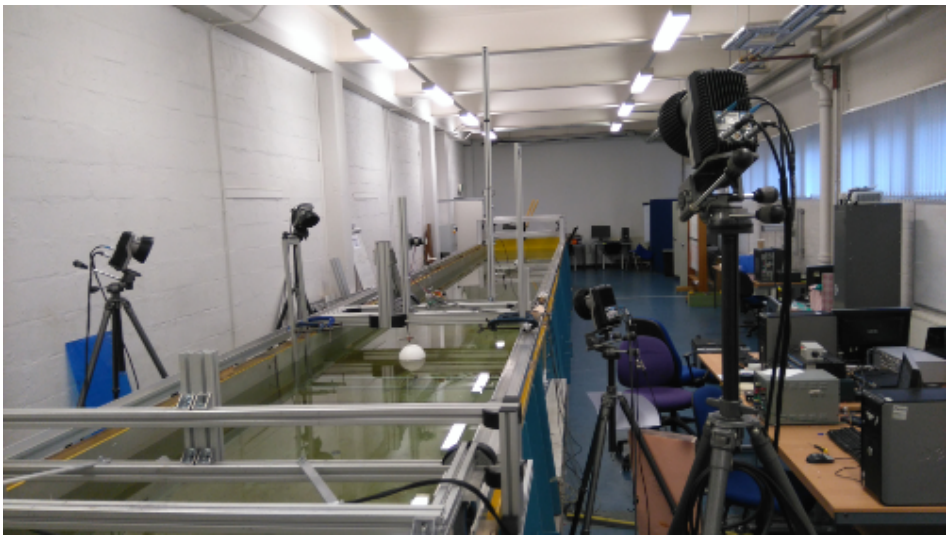

Figure 4.3: Experimental tests set-up: cameras of the motion capturing system (Session 1).

axial displacement are shown. As for other pictures, all significant details are labelled.

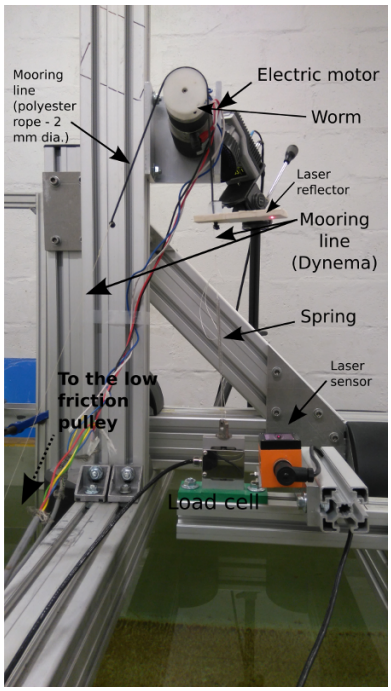

Figure 4.4: Experimental tests set-up (Session 1): digital damper (servomotor); spring; and sensors.

The floater, the submerged part of the mooring line and the pulley are shown in Figure 4.5. This picture was shot from the side window which is located on the wall of the wave tank. Here it is also displayed the underwater frame used for this experiment.

The spherical buoy of Model 1 was printed in polylactic acid (PLA) with an Ultimaker 3D printer with a 0.2 mm nominal resolution. Precisely, two hemispheres (as shown in Figure 4.6) were manufactured, glued together and covered (through painting) by a thin layer of transparent silicon, for making the floater impermeable.

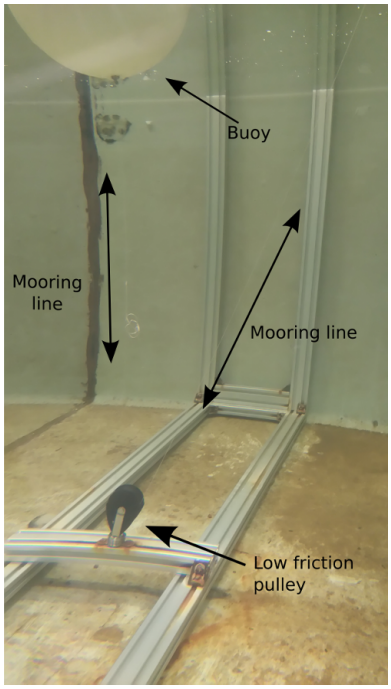

Figure 4.5: Experimental tests (Session 1) set-up (underwater view): mooring line; and the pulley.

Figure 4.6: 3D printed section of spherical buoy.

4.4.2 Spherical PA model tests: 1:33 scale - Session 2

A second model of a PA WEC was constructed at a larger scale (1:33) and tested during Session 2. This model was tested at the Kelvin Hydrodynamic Laboratory of the University of Strathclyde as also for, later, Session 3.

Experiment set-up and description of Model 2

The model constructed for this set of tests was similar to the one described in the previous section for the 1:86 scale experiments. This model consisted of a frame where a pulley was connected at its base, this was positioned at the bottom of the water tank (as shown in 4.9) and other model components were assembled above the tank over the carriage. The spherical floater was connected with a steel wire, this last after passing through the pulley and a servomotor, ended attached to a spring. In Figures 4.7 and 4.8 it is shown the experiment-set up for this session of tests.

In Table 4.6 are reported Model 2 parameters and corresponding real scale values.

As illustrated in Figure 4.7, differently than Model 1, for Model 2 the spring was positioned horizontally.

The floater on Model 2 was positioned downstream of the carriage, as showed in Figure 4.8.

The spherical floater, shown in Figure 4.9, in this case, was manufactured in foam, shaped by a 5m CNC router and painted for better finishing. Precisely, two hemispheres were created and then bolted together. To match the desired floater mass, at the centre of the sphere various cylindrical weights were installed.

In Figure 4.9 the pulley mounted on a fixed frame at the bottom of the tank and spherical grey reflectors, mounted on the floater needed for capturing motion with the Qualysis system, are shown. In this figure, it is also displayed the underwater frame,

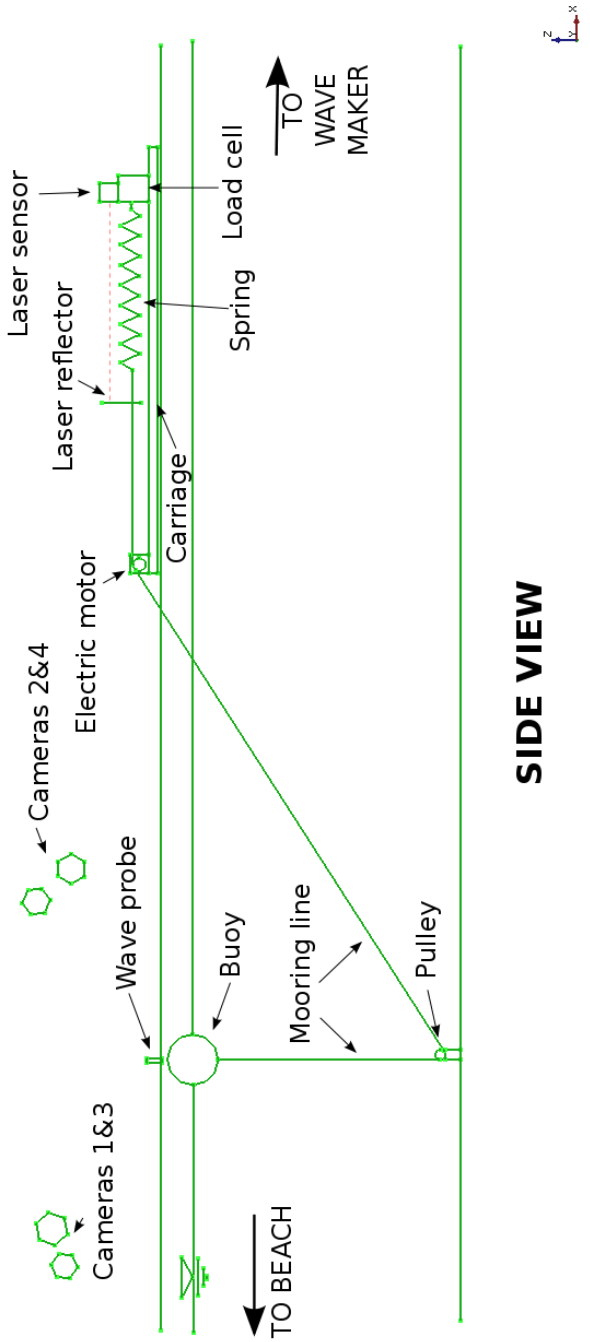

Figure 4.7: Experiment set-up illustrative sketch (side view).

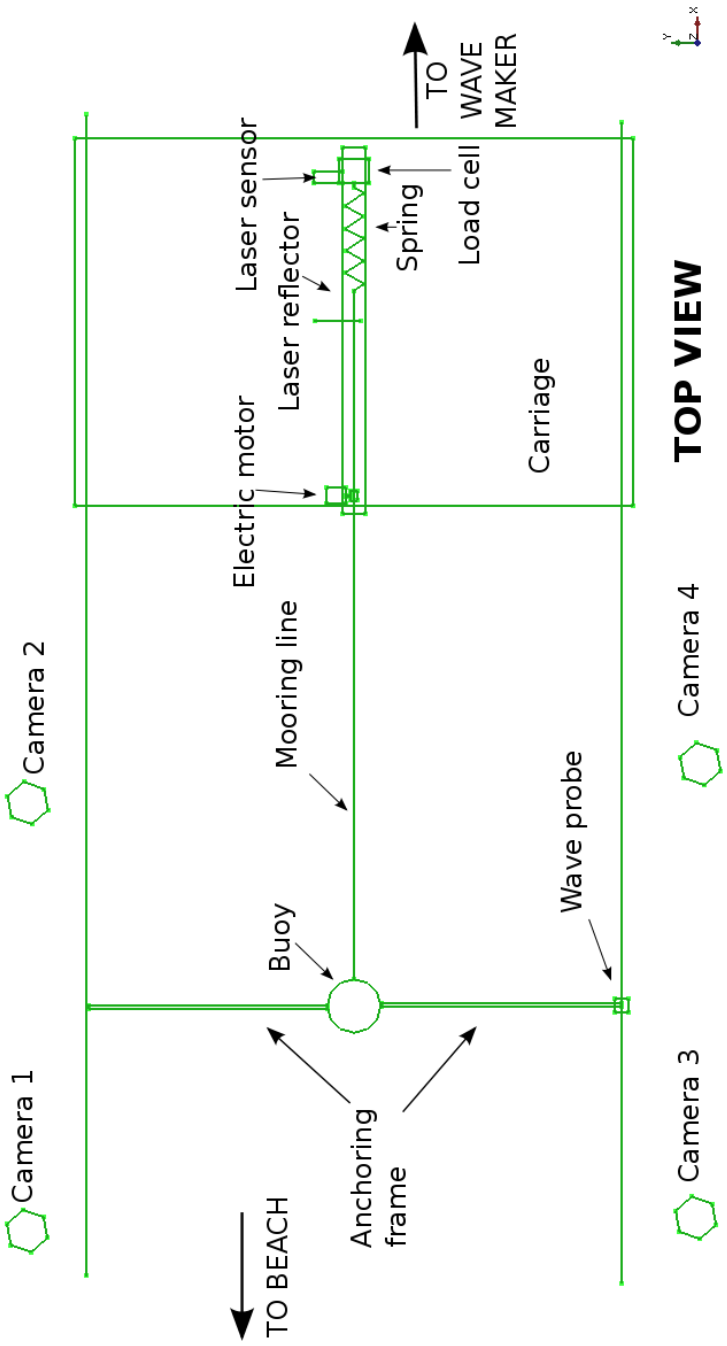

Figure 4.8: Experiment set-up illustrative sketch (top view).

	Model scale	**Real scale**	
	1:33	1:1	
Model ID	2		
Floater radius	0.23	7.49E+00	m
Floater mass	19.78	7.11E+05	kg
Water depth	2.00	6.60E+01	m
Mooring line length	1.62	5.36E+01	m
Immersion depth	0.00	0.00E+00	m
Spring stiffness	177.00	1.93E+05	N/m
Cpto damping	0.00/40.00	2.50E+05	kg/s
Pretension	35.00	1.26E+06	N

Table 4.6: Model 2 system parameters.

where the pulley was tied. This frame was not used in later experiments during Session 3. A better solution was then implemented.

Figure 4.10 shows the position of the floater relative to the carriage where the rest of the equipment was installed. The distance between the carriage and the floater for this experiment was c.a. 14 m. This distance was then radically reduced in Session 3.

The electric servomotor for this model was only connected to the power unit, which was possible to tune depending on the requested damping. The damping force applied this time was controlled by adjusting the analog amplifier only. The electric motor used is shown in Figure 4.11. For this experiment, the MyRio device used in Session 1 and 3 was not used. The reason of this is that at time of experiments of this session the servo motor and the MyRio device were not available.

As for Model 1 mooring line displacements and mooring tension were monitored respectively, by a laser sensor and a load cell. These sensors were assembled on a fixed

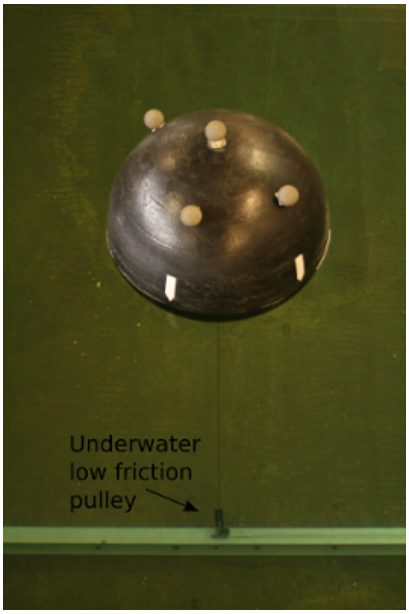

Figure 4.9: Experimental tests set-up: Qualysis reflector balls on floater and a pulley.

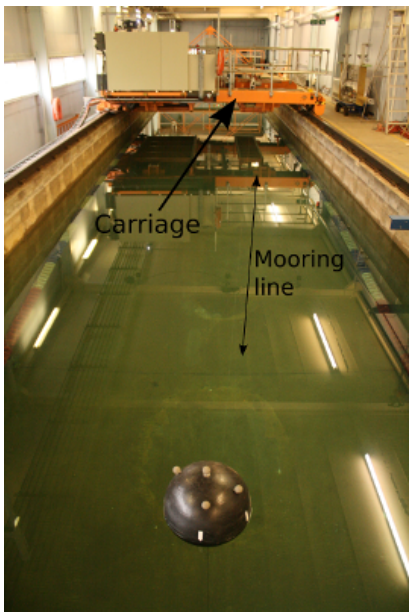

Figure 4.10: Experimental tests set-up: tank carriage and floater.

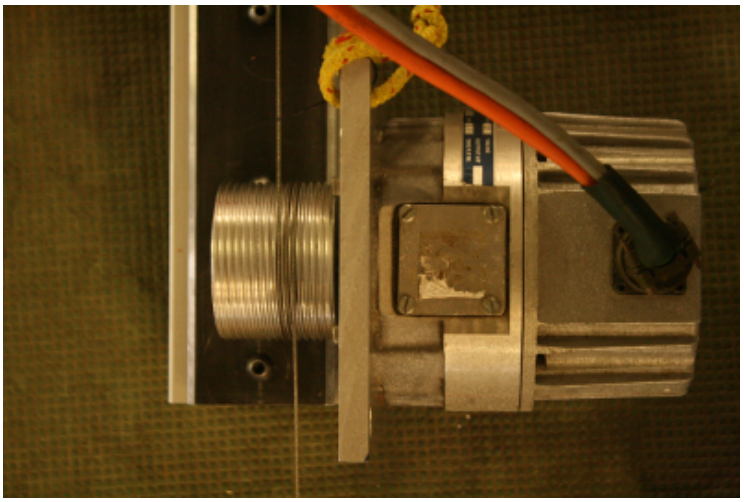

Figure 4.11: Experimental tests set-up: electric motor and motor worm used for simulating PTO damping force.

frame which is shown in Figure 4.12.

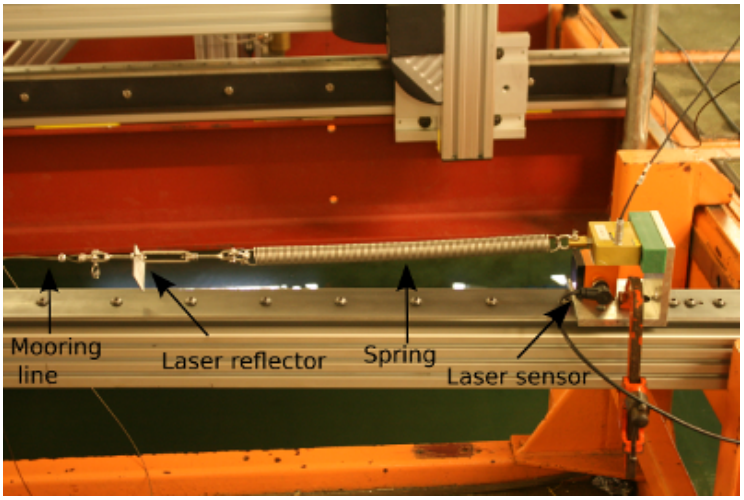

Figure 4.12: Experimental tests set-up: spring and laser sensor.

4.4.3 Spherical PA model tests: 1:33 scale - Session 3

The last session of tests was undertaken at the Kelvin Hydrodynamics Laboratory. In this case, the half-immersed sphere PA tested in Session 2 was re-utilised for a similar set of tests but with an improved experiment set-up. During this session, a submerged

spherical PA model, sharing the same new configuration, was also tested.

Various improvements were done in Session 3. At first, the electrical motor used was calibrated with a different method and with better accuracy. At the same time, the set-up was upgraded to minimise uncertainties. This step was achieved by changing system components and modifying the system set-up. Compared to Session 2, using the small servomotor as in Session 1 was found to be a good solution for containing friction and motor's inertia related uncertainties.

Half-immersed spherical PA Model 3a

The first spherical floater tested in Session 3 was almost the same one used in Session 2. This element was only improved by slightly correcting the internal mass distribution. Model's parameters are reported in Table 4.7.

While the floater was almost the same as for Model 2, Model 3a had a new experimental set-up. This last differs from Model 2 mainly by the installation frame, the mooring line, the pulley, the servomotor and the controller of the servomotor.

Experiment set-up of Model 3a

Illustrative sketches of Model 3a are reported in Figures no. 4.13 and no. 4.14. It can be seen clearly in Figure 4.15, except for the floater position relative to the carriage and the orientation of the damper/spring mechanism (PTO simulator), the experimental set-up is similar to the one of Session 2.

In Figure 4.13 is shown the the set-up for Model 3a. In this case, the floater was positioned c.a. 3 m upstream from the carriage.

The Qualysis cameras, as illustrated in Figure 4.14, were positioned two one side of the tank and two on the opposite side, similar as it was done for Model 1 and 2.

	Model scale	**Real scale**	
	1:33	1:1	
Model ID	3a		
Floater radius	0.23	7.49E+00	m
Floater mass	21.70	7.80E+05	kg
Water depth	2.00	6.60E+01	m
Mooring line length	1.69	5.59E+01	m
Immersion depth	0.00	0.00E+00	m
Spring stiffness	177.00	1.93E+05	N/m
Cpto damping	0.00	0.00E+00	kg/s
	30.00	1.88E+05	
	40.00	2.50E+05	
	50.00	3.13E+05	
Pretension	27.00	9.70E+05	N

Table 4.7: Model 3a system parameters.

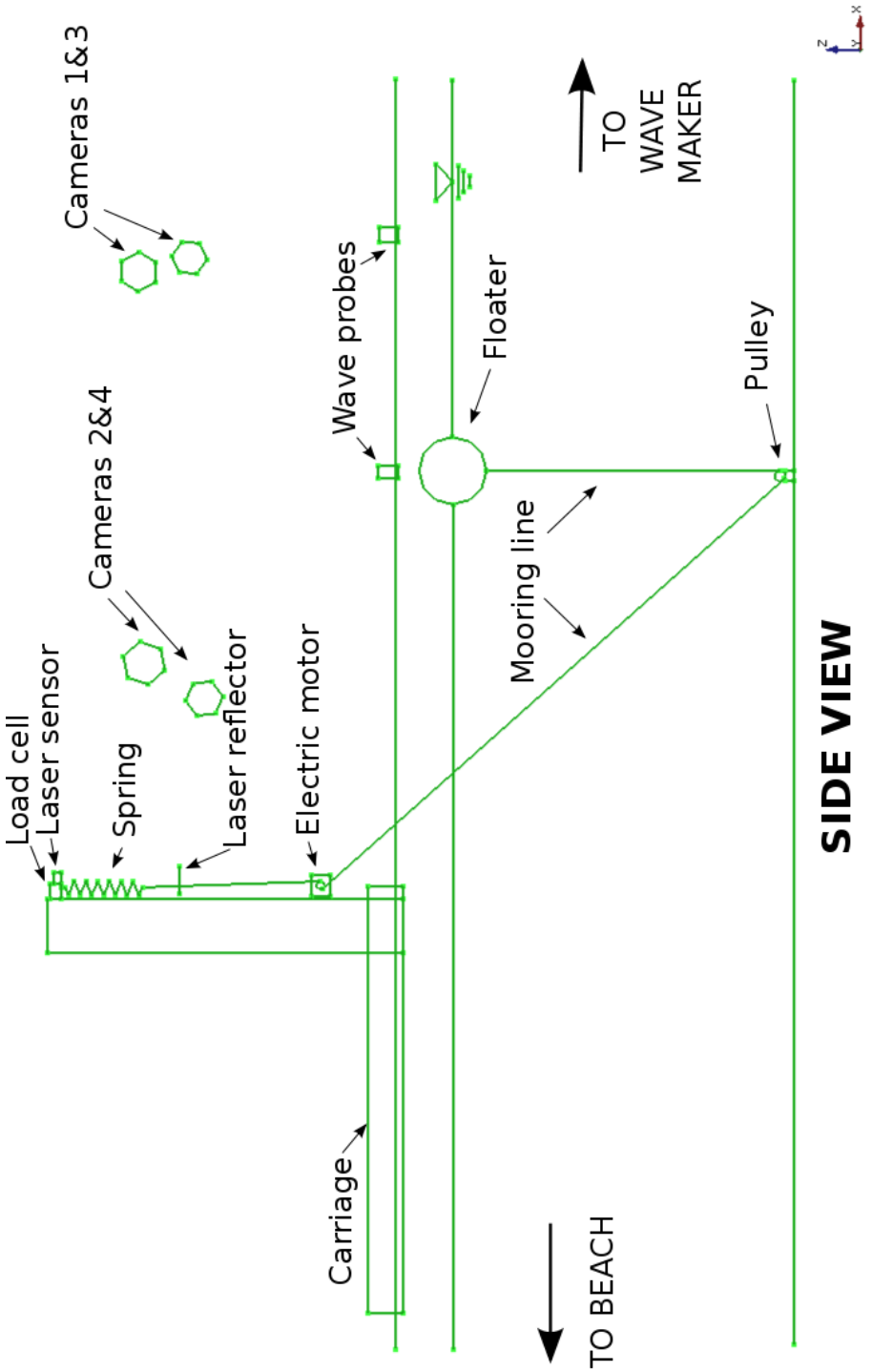

Figure 4.13: Experiment set-up illustrative sketch (side view).

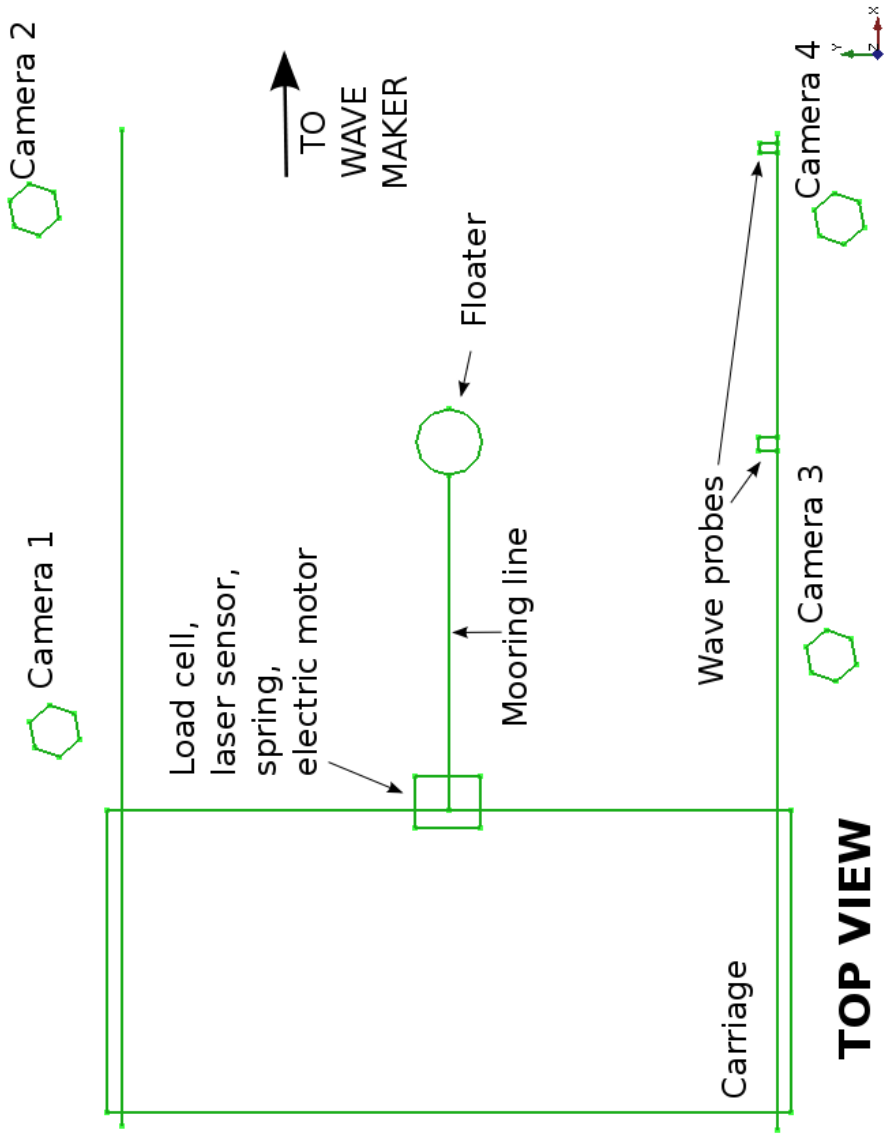

Figure 4.14: Experiment set-up illustrative sketch (top view).

The rig needed for simulating the PTO mechanism formed by the servomotor, spring and sensors, during this Session 2, was orientated horizontally. In contrast, in Session 3 this was orientated vertically. This assembly is illustrated in Figure 4.15.

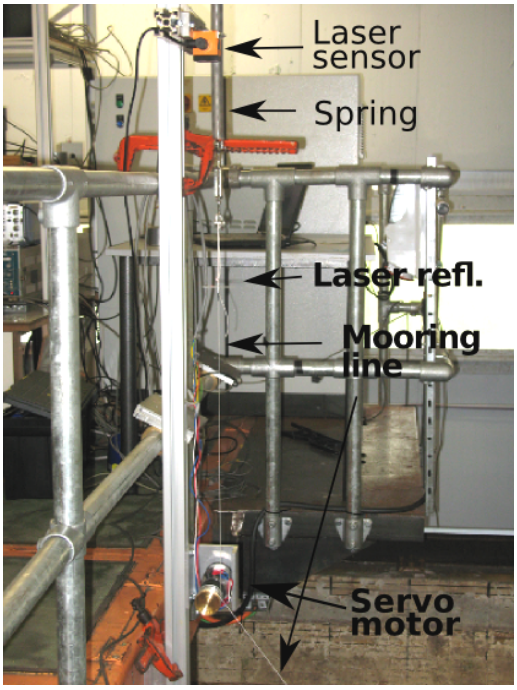

Figure 4.15: Experimental tests rig on carriage of Session 3: electric servomotor; spring; and laser sensor.

As it can be seen in Figure 4.16 for Model 3a four additional reflective markers were installed on the upper part of the floater. These were added to improve motion capturing precision by the Qualysis system.

Figure 4.16: Half submerged PA model tested in regular waves. The white small balls are the reflectors needed for motion capture by the Qualisys system.

Submerged spherical PA Models

The submerged floater, illustrated in Figure 4.17, was tested with a similar experimental set-up as the one used for the half-immersed floater. Except to the floater's mass, mooring length and damping, the other parameters were kept as close as possible to the half-floating model.

The submerged floater was tested in two different configurations. The first is referred as Model 3b which had the same above-water test rig configuration as for Model 3a. The second experiment set-up for the submerged model is referred as Model 3c and this varied from Model 3b only for the absence of the electric servomotor.

The same spring as Model 3a was used for most of the tests. However, since pretension was in practice higher than Model 3a, the spring's stiffness indicative value, which was measured for Model 3a, for Models 3b and 3c was found to be considerably less. Details are reported in Tables no. 4.7, no. 4.8 and 4.9. Also, another spring of higher stiffness was tested for the submerged models.

The Qualysis system for tracking the motion of the submerged model this time was utilised by connecting to it four underwater cameras. These other cameras were positioned all upstream of the floater, as illustrated in Figure 4.18.

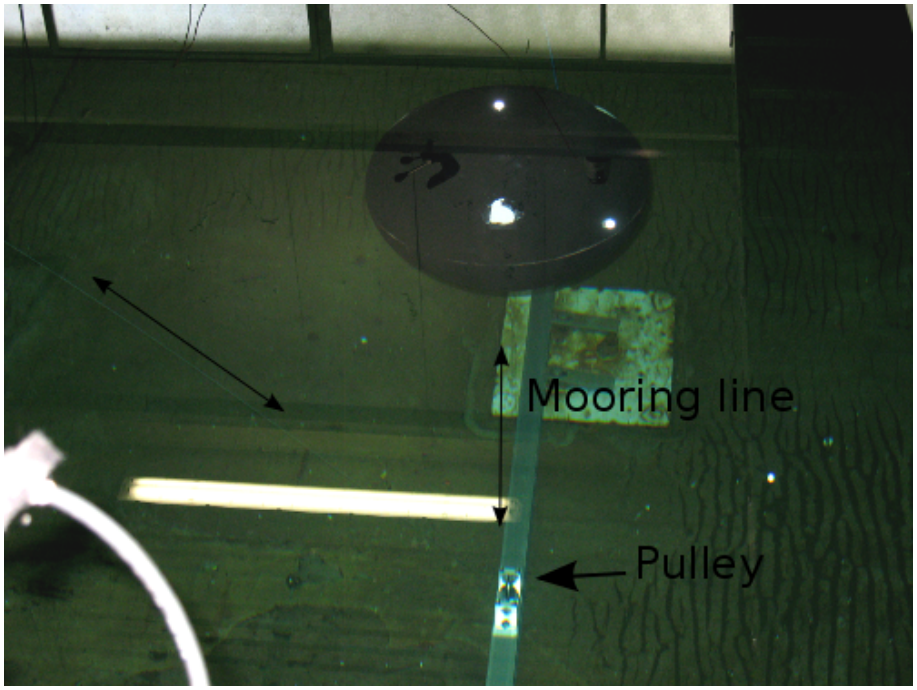

Figure 4.17: Submerged floater of Session 3. Here the low friction, in-house manufactured, pulley mechanism was used.

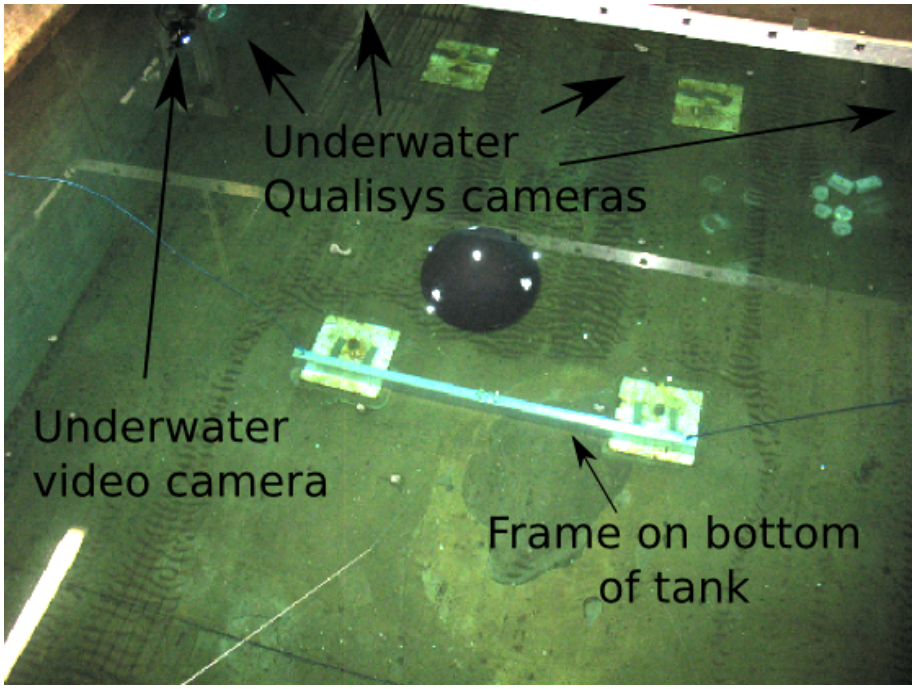

Figure 4.18: Underwater experimental tests set-up of Session 3: frame at bottom of the tank; underwater camera; and location of underwater Qualisys cameras used for motion capturing.

Experiment set-up of Model 3b

The set-up for Model 3b is shown in Figures no. 4.19 and no. 4.20. The rig attached to the carriage, consisting of the servomotor, spring and sensors, was exactly assembled as for Model 3a. In contrast, in this case, the floater was a different one. Model's parameters are reported in Table 4.8.

	Model scale	**Real scale**	
	1:33	1:1	
Model ID	3b		
Floater radius	0.23	7.49E+00	m
Floater mass	47.00	1.69E+06	kg
Water depth	2.00	6.60E+01	m
Mooring line length	1.12	3.70E+01	m
	1.01	3.32E+01	
	0.89	2.94E+01	
Immersion depth	-0.35	-1.14E+01	m
	-0.46	-1.52E+01	
	-0.58	-1.90E+01	
Spring stiffness	75.00	8.17E+04	N/m
	355.00	3.87E+05	
Cpto damping	0.00	0.00E+00	kg/s
	13.00	8.13E+04	
	15.00	9.38E+04	
	17.00	1.06E+05	
	19.00	1.19E+05	
Pretension	38.50	1.38E+06	N

Table 4.8: Model 3b system parameters.

As shown in Figure 4.19, the experimental set-up of Model 3b is different than Model 3a for what concerns the immersion depth of the floater and the position of the motion capturing cameras.

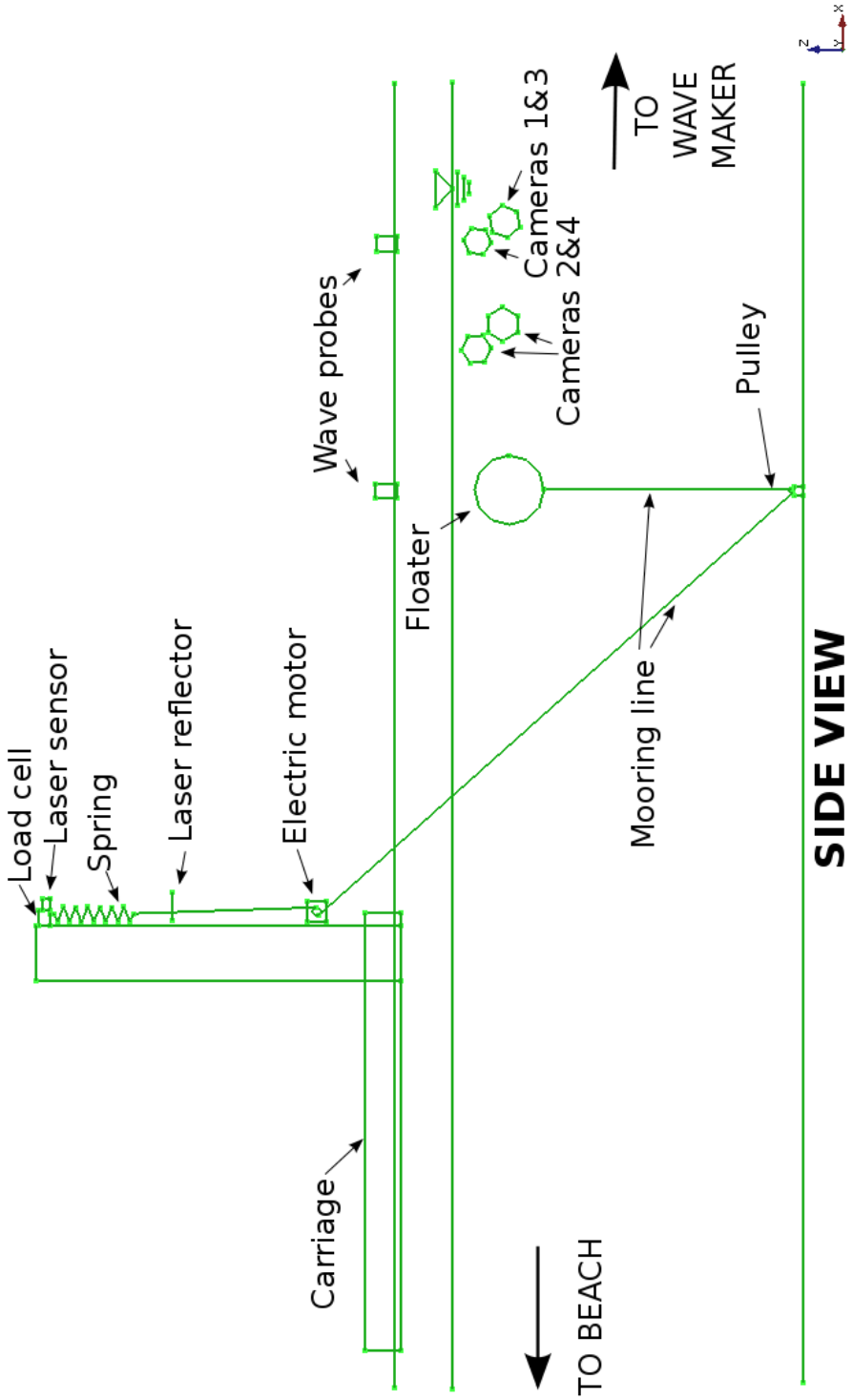

Figure 4.19: Experiment set-up illustrative sketch (side view).

As illustrated in Figure 4.20 the underwater Qualysis cameras were positioned only upstream of the spherical underwater buoy.

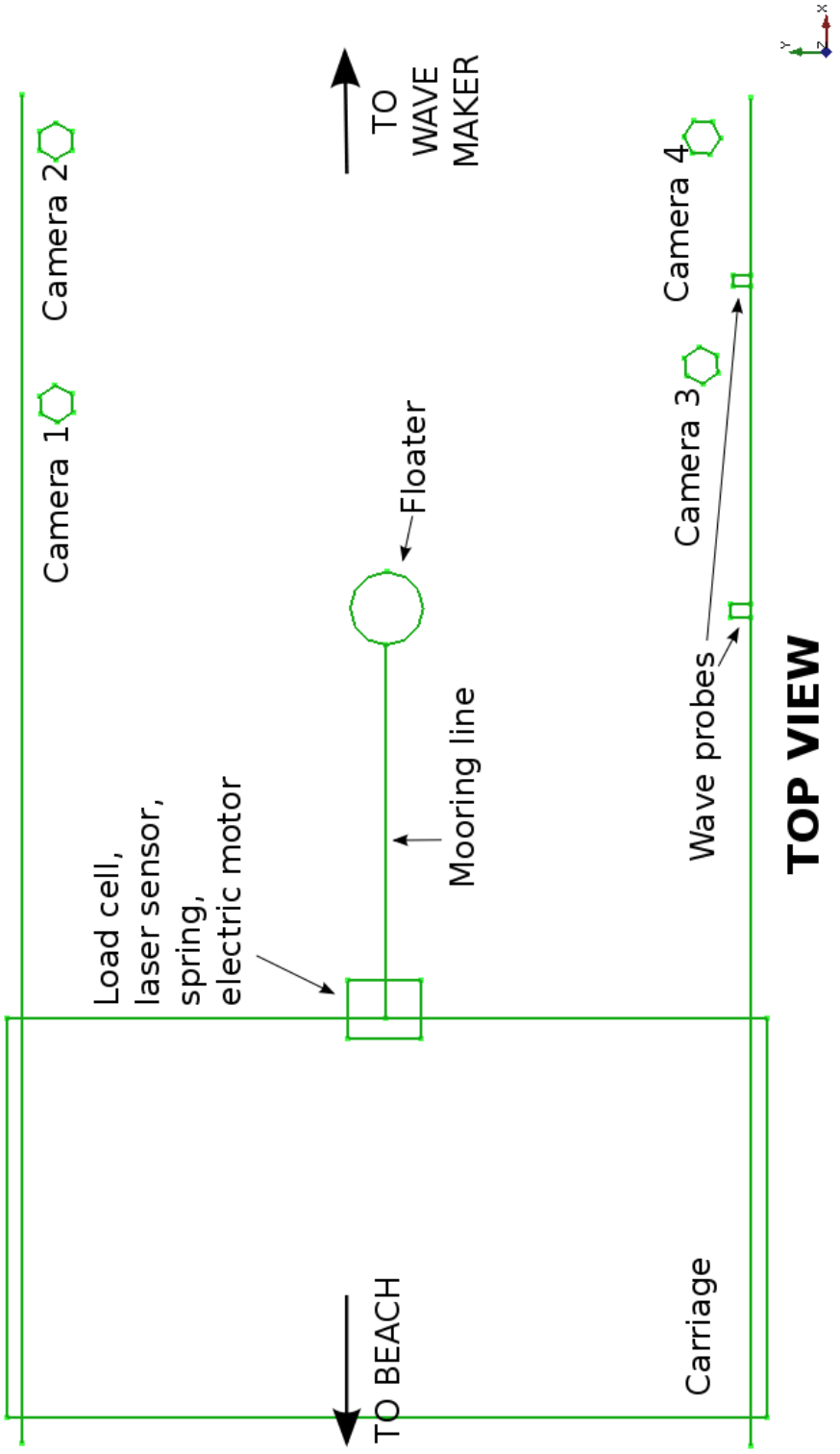

Figure 4.20: Experiment set-up illustrative sketch (top view).

Experiment set-up of Model 3c (no motor)

Model 3c was similar to Model 3b; the only difference is that in this case the motor was not installed. The side view sketch for this model is illustrated in Figure 4.21. For this model, the top view illustrative sketch is similar to the sketch of the first rig (only servomotor not present) (Figure 4.20). Model's parameters are reported in Table 4.9.

	Model scale	**Real scale**	
	1:33	1:1	
Model ID	3c		
Floater radius	0.23	7.49E+00	m
Floater mass	47.00	1.69E+06	kg
Water depth	2.00	6.60E+01	m
Mooring line length	1.12	3.68E+01	m
	1.01	3.32E+01	
	0.89	2.94E+01	
Immersion depth	-0.35	-1.16E+01	m
	-0.46	-1.52E+01	
	-0.58	-1.90E+01	
Spring stiffness	75.00	8.17E+04	N/m
	355.00	3.87E+05	
Cpto damping	no motor	no motor	kg/s
Pretension	38.50	1.38E+06	N

Table 4.9: Model 3c system parameters.

As for Model 3c, the servomotor was not installed, the spring axis was oriented directly towards the pulley as illustrated in Figures 4.21 and 4.22).

Because the spring was orientated differently, also the load and laser sensors had to be rotated, as shown in Figure 4.22.

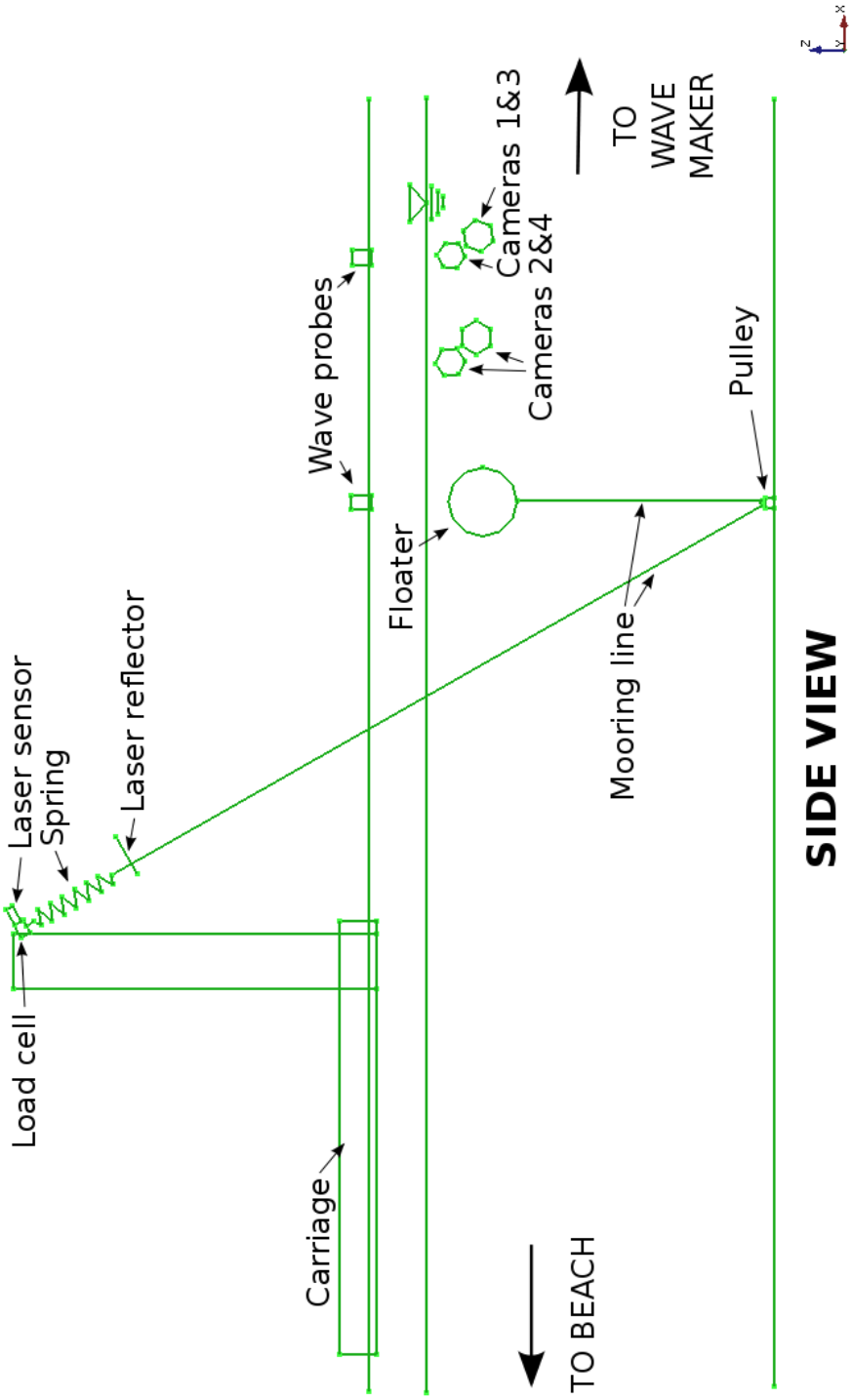

Figure 4.21: Experiment set-up illustrative sketch (side view).

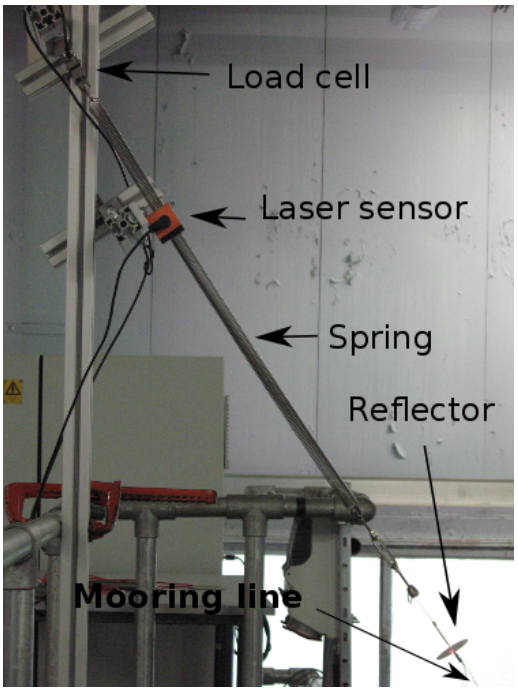

Figure 4.22: Configuration of experimental tests rig of Session 3 without servomotor.

4.4.4 System components description

Main system components details for each model tested are reported in Table 4.3.

	Model ID :	**1**	**2**	**3a**	**3b**	**3c**	
	Scale:	**1:86**	**1:33**	**1:33**	**1:33**	**1:33**	
Component	**Parameter**	**Value/descr.**	**Value/descr.**	**Value/descr.**	**Value/descr.**	**Value/descr.**	**Unit**
Spring	Stiffness	2.03E+01	1.65E+02	Multiple val.	Multiple val.	Multiple val.	N/m
Mooring line	Length of line	6.98E-01	1.82E+00	1.82E+00	Multiple val.	Multiple val.	m
	Diameter	2.00E-01	2.00E+00	2.00E+00	2.00E+00	2.00E+00	mm
	Material	dyneema	Stainless steel	dyneema	dyneema	dyneema	
	MBL	2.85E+02	2.75E+03	4.00E+02	4.00E+02	4.00E+02	N
Electric motor	Stall Torque	2.00E+01	1.33E+02	2.00E+01	2.00E+01		Ncm
	Power	6.00E+01	4.20E+02	6.00E+01	6.00E+01	No motor	W
	Voltage	3.60E+01	6.38E+01	3.60E+01	3.60E+01		V
Motor worm	Diameter	2.40E+01	3.50E+01	2.00E+01	2.00E+01	No motor	mm
Pulley	Radius	1.50E+01	1.50E+01	1.60E+01	1.60E+01	1.60E+01	mm
Floater	Radius	8.72E-02	2.27E-01	2.27E-01	2.27E-01	2.27E-01	m
	Mass	1.23E+00	2.17E+01	2.17E+01	4.70E+01	4.70E+01	kg

Table 4.10: Details of components of models tested during the experimental study.

Spring

For all Models tested, a spring was required for exerting the PTO restoring force and keeping the desired pretension. These were wire extension springs made of steel. The spring component was selected between different options available. For the first three models investigated (no.1, 2, 3a) the spring chosen was the one having the stiffness parameter closer to the desired one. For Models 3b and 3c the spring was the same as the one used for Model 3a, but in practice, as the pretension changed, the stiffness value was also sensibly different. Also, another stiffer spring was tested for these two last models. More details are reported in the *Calibration of equipment Section* 4.5.

Electric motors

The electric motor was needed for simulating a realistic damping force as the power-take-off damping force. During the experimental study, two different electric motors were used. Specifications of these are reported in Table 4.10. While for Model 2 the motor was controlled with an analog signal, produced by its power unit, for Models no.1, no.3a, no.3b the motor used (with an integrated tachometer) was a servomotor

connected to the power unit and controlled by to the myRIO device with a digital signal. This was connected as illustrated in Scheme 4.23.

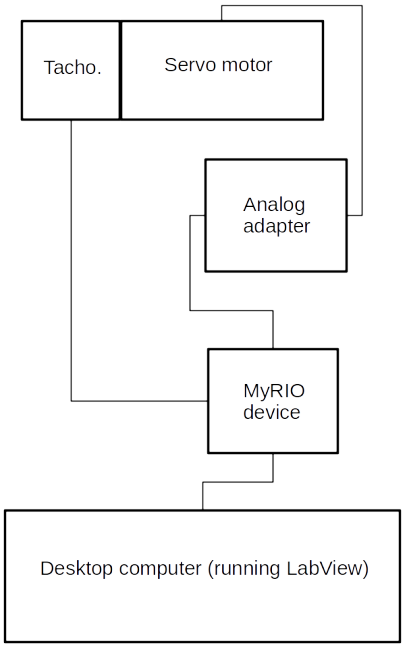

Figure 4.23: Scheme showing connections between desktop computer, MyRIO device and servomotor/tachometer.

The scheme represented in Figure 4.23 shows the control loop implemented during Sessions 1 and 3. Depending on motor rotational speed the torque was automatically adjusted by the MyRio micro-controller which processed information provided by the tachometer. The analog adapter, in this case, was needed only as a power supply unit. The desktop computer was needed for running a LabView model which controlled a MyRio device and permitted to change PTO damping settings during the experiments. Other three desktop computers were used for running the wavemaker, the Qualysis system and the Spike2 software respectively.

Mooring line

The mooring line components used for mooring the floaters were made of stainless steel wire (marine grade) or dyneema fibre (ultra-high-molecular-weight polyethylene).

While the steel wire was used in Session 2, two different dyneema ropes were used during Sessions 1 and 3. Steel wires are normally used for this kind of experiments. In contrast, the use of dyneema ropes is not that common. Thus, the elongation of dyneema ropes used was assessed in order to check if this was contained in reasonable values. Explanation of selection for this particular component is reported in Section 4.5.

Material	**Property** (min. values)	dyneema (UHMWPE)	Standard marine grade steel (316)	
	Density	9.60E+02	8.00E+03	kg/m^3
	Tensile strength	1.40E+03	5.80E+02	MPa
	Yield strength	1.40E+03	2.80E+02	MPa
	Youngs modulus	5.50E+04	2.00E+05	MPa

Table 4.11: Properties of mooring materials used (source IDEMAT (2003)).

Pulley

For all models, a pulley was required to guide the mooring line from the bottom of the tank to the servomotor and the spring outside of the water. Thus for this purpose, different pulleys were used and assessed. During Session 1 and 2, a standard nautical pulley was used, this is shown in Figures no. 4.5 and no. 4.9. Differently, during Session 3 an in-house manufactured pulley was build and used during all tests in water. This component can be seen in Figure 4.17. Further explanation on the various pulleys considered and on the selection process can be found in Section 4.5.

4.5 Calibration and selection of equipment

In this section, all procedures concerning the calibration, the selection and the setup of equipment are explained.

4.5.1 Calibration of wavemakers

For what concerns the Henry Dyer Laboratory, the wavemaker had to be calibrated. For tuning the wavemaker input parameters, a series of regular waves tests had to be run. The input parameters concerned voltage and frequency. Regular waves tests (no model in water) were run many times as required for each frequency reported in Table 4.12. After each test, the free surface elevation record was analysed with the Spike2 software. Once the wave height H was matching the wanted value, regularly for a minimum period, the voltage value used was kept and successively used as a calibrating factor. Thus at the time of the actual experiment, the calibration factors were then inserted in the control software for obtaining regular waves for a specific height. Calibration factors were determined for obtaining regular waves with 12.5 mm amplitude, as reported in Table 4.12.

Freq.(Hz)	**Control Voltage**
0.3	± 0.3
0.6	± 0.67
0.8	± 0.58
1	± 0.5
1.2	± 0.5
1.3	± 0.52
1.4	± 0.55
1.45	± 0.59
1.5	± 0.64
1.55	± 0.63
1.6	± 0.56
1.65	± 0.49
1.7	± 0.67
1.75	± 0.58
1.8	± 0.57
1.85	± 0.57
1.9	± 0.71
2	± 0.54

Table 4.12: Settings used to calibrate Henry Dyer wavemaker lab for obtaining regular waves with 12.5 mm amplitude.

For illustration in Figure 4.24 the registered wave amplitudes are compared with the wavemaker input value of 12.5 mm, for different ω. Each ω represents a regular waves test. The amplitudes in the worst case varied, from the target amplitude, by c.a. 0.25 mm. This last value is low. For allowing this value to be so little, the wave probe results (as also other later experimental results) were picked from a known period from the start of each regular waves test of specific ω. In fact, during the calibration process the time frames, in which wave amplitudes were matching for the most the target amplitude, were registered. These time frames were recorded for all ω of interest and then used as a reference.

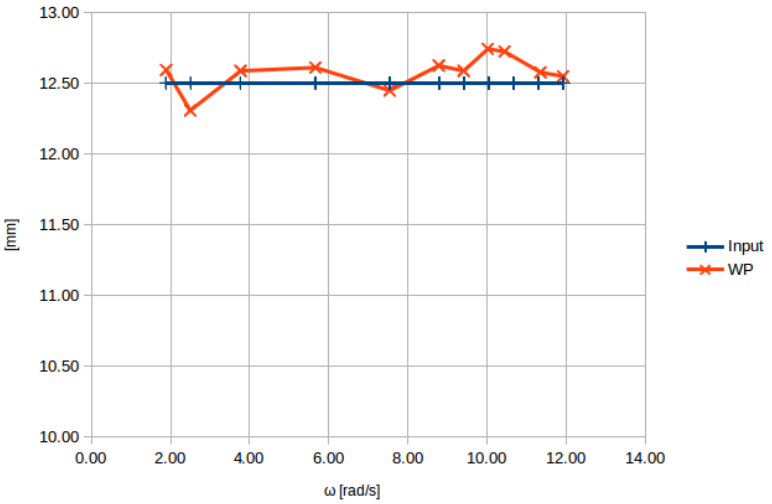

Figure 4.24: Illustrative Henry Dyer wavemaker curve.

For what concerns the Kelvin Hydrodynamic Laboratory the wavemaker was already calibrated. Its calibration is assessed on a regular basis by University staff and repeated if necessary.

For illustration in Figure 4.25 are reported the wavemaker curves for regular waves tests of different amplitudes and different ω. As can be noted here, in the worst case, amplitudes vary up to c.a. 10 mm from the target amplitude.

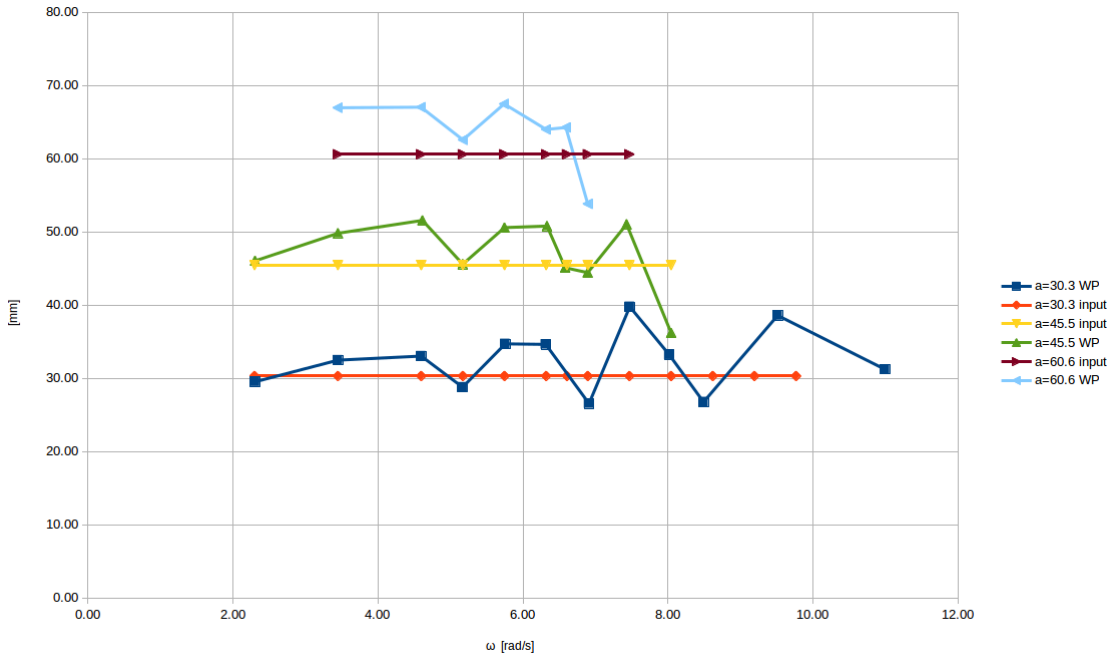

Figure 4.25: Illustrative Kelvin Hydrodynamics Laboratory wavemaker curves.

The repeatability of making waves in both facilities is discussed in Subsection 4.7.1. In this Subsection, uncertainty analysis results are discussed. Repeatability of making waves is intrinsically assessed in the wave probe related standard uncertainties Type A values. As will later be explained in details this uncertainty value is calculated by considering multiple readings thus is representative of statistical errors.

4.5.2 Sensors calibration

Qualysis system setup

The calibration of the Qualysis motion capturing system was similar for all three sessions. This system was calibrated following the protocol provided by its manufacturer. The Qualysis software guides the user through the calibrating procedure which consists of using a default floating frame and a default hand tool where on both are installed a number of reflectors. While the floating frame needs to be stationary, the hand tool

needs to be dynamically moved in a particular manner inside in the capturing volume. For further details refer to the Qualysis (2016) manual. The calibration procedure was usually repeated a few times until the residual errors, which determine the uncertainty of the measurement, are less than the defined threshold and when the motion signal was stable. For this purpose, few preliminary tests with regular waves were run. The capturing signal was also improved by choosing an optimal position of floater's reflectors.

For what concern the underwater Models 3b and 3c different Qualysis cameras were used but similar calibration procedure was followed. This procedure needed to be repeated more times before obtaining acceptable results. In fact, acquiring motion capturing signal by using the underwater cameras was much more difficult. This issue was due to signal reflections of the floater's markers below the water free surface. Orientation and position of the cameras were essential factors to be optimised. In fact, the underwater cameras had to be positioned only on one side of the floater so that these were not pointed toward each other and, in this way, interference between cameras was avoided. However, by having all cameras on one side, another issue occurred. This issue concerned that the floater at times was slowly rotating around the Z-axis and, in these circumstances, the signal was lost. To partially overcome this problem the reflectors on the sphere were increased and strategically positioned.

Illustrative sketches showing an indicative position of cameras for the half-immersed and for the underwater models of Session 3 relative to floaters are reported, respectively, in Figures no. 4.27 and no. 4.26.

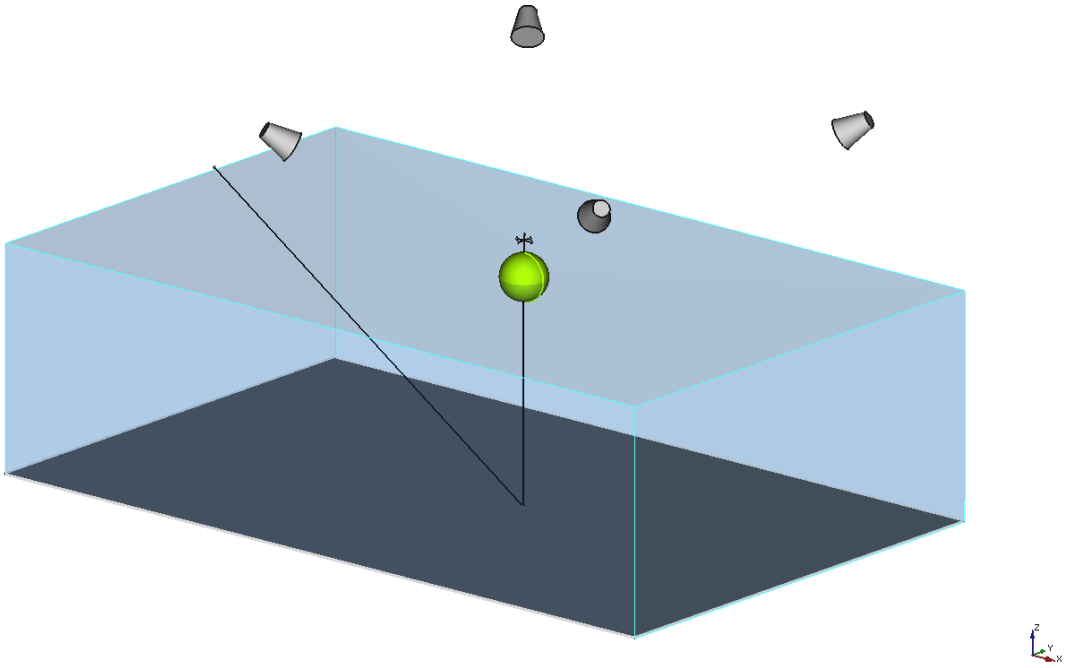

Figure 4.26: Indicative position of motion capturing cameras for the half submerged model tests.

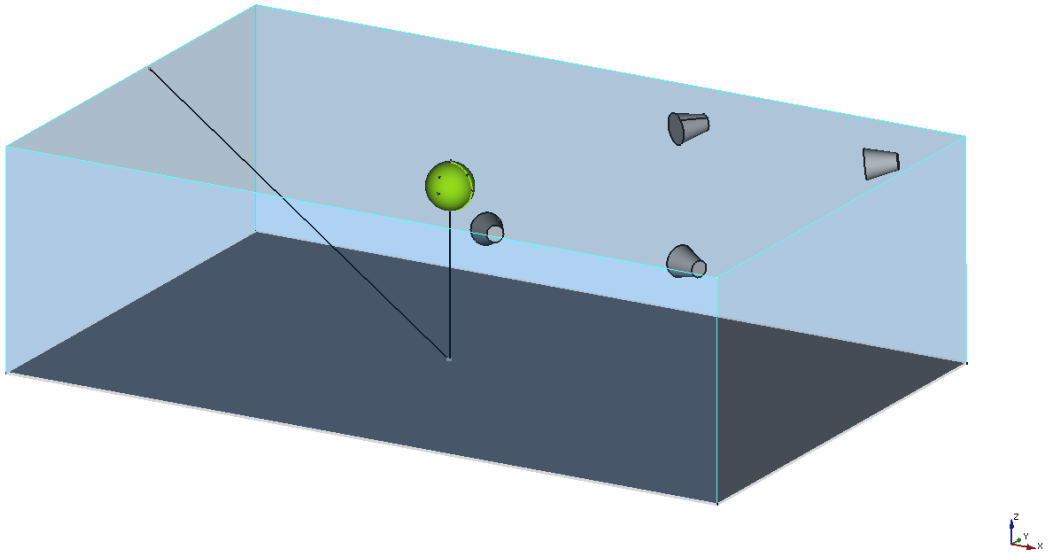

Figure 4.27: Indicative position of the motion capturing cameras for the fully submerged model tests.

Laser sensor

For what concern the laser sensor, following manufacturer guidelines this was set to analogue mode and optimized for the range of distance of interest. After doing so, the measurement was checked by using a simple rig made of a sliding laser reflector and a standard ruler. For Model 1 the Spike2 software screen-shot is reported in Figure 4.28 showing calibration data of the laser sensor. In this figure, the signal is already corrected with the calibration factor found. The 15 steps showed in the graph correspond to 15 distances of 1 millimetre.

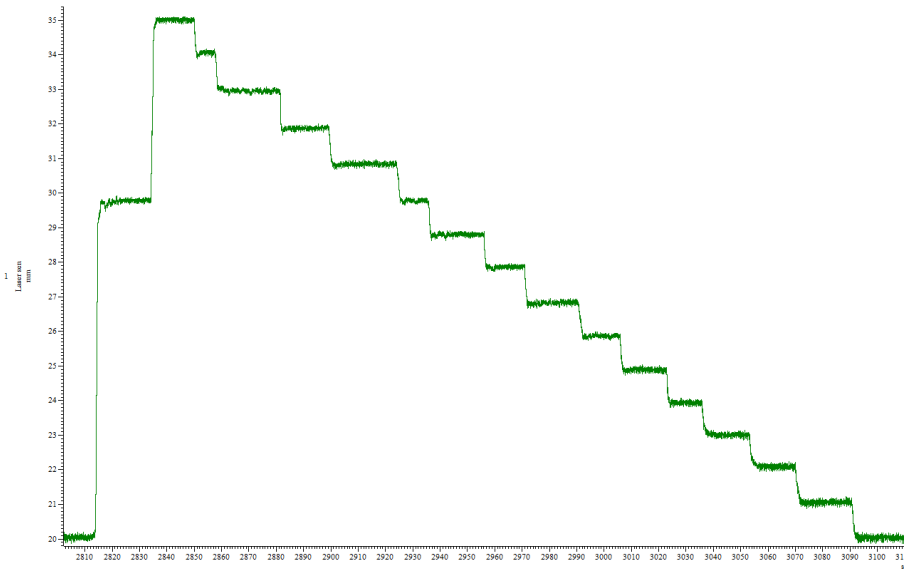

Figure 4.28: Spike2 screen-shot during calibration of laser sensor for Model 1.

Wave probes

The wave probes were calibrated by using a ruler on a sliding frame positioned over the tank. The method consisted of using at least ten different distances in between the range of interest. The voltage signal of the wave probe through the Spike2 software was recorded. Following a linear fit a factor for multiplying the signal, so that this last was matching the linear fit, was calculated and used to calibrate the raw signal. In practice, the process was same as for the laser calibration for which the Spike2 screen-shot is

reported (Figure 4.28).

Load cells

For all models, the load cells were accurately calibrated with different weights. The voltage signal, similarly as for the wave probes, was recorded; and with a linear fit, calibration factors were found.

For Model 1 weights up to 1.5 kg with a minor increment of 0.01 kg were used. Due to different model scale, for models used in Sessions 2 and 3 other weights values up to 5 kg were used. These weights were needed to simulate static loads. For illustration in Figure 4.29 it is shown the calibration curve relative to Session 3. The calibration of the load cells in all experiments was repeated at least two times, so to make sure that the process was repeatable.

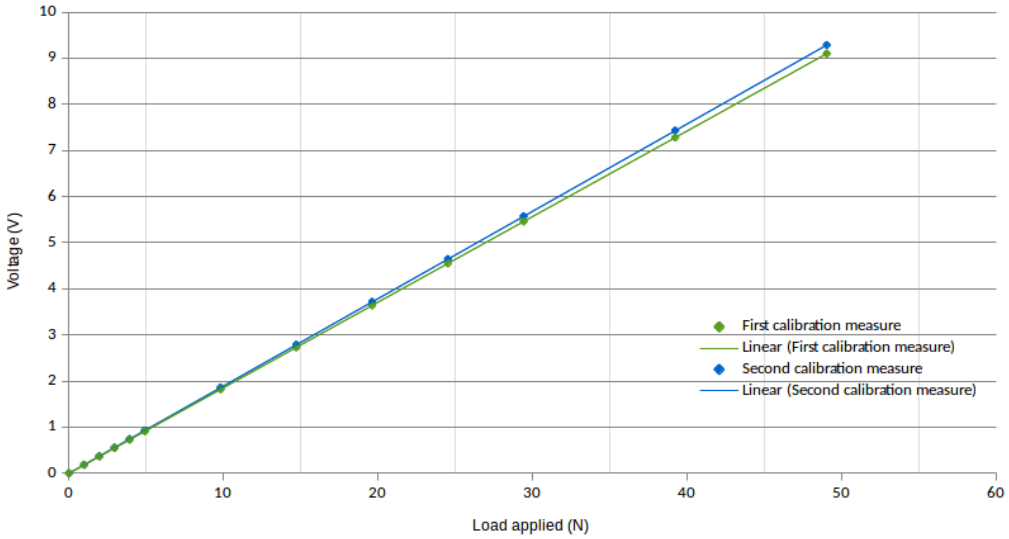

Figure 4.29: Calibration of load cell.

4.5.3 Mooring lines and pulleys

Depending on the type of mooring line and pulley used, in different ways, damping other than PTO damping was affecting the experiment. For this reason, best components aiming at reducing any source of extra damping were selected over the available options. This additional system damping was due to friction and viscous losses.

Compared to steel wire the dyneema ropes available were thinner and smoother. Thus, viscous and hydrodynamic damping due to its movement into the water was reduced. In addition, thanks to bending properties the dyneema rope, wherein contact to the motor worm and pulley, showed to be a better option for reducing the extra damping in the form of friction losses.

For what concerns Session 1 the mooring line was selected between two options: a steel wire and a dyneema rope. The latter rope was used in Session 1, this had a diameter of 0.2 mm. Due to its material properties, this value of diameter was assumed to be sufficient. For a 5.5 m long rope a preliminary test for assessing the elongation was conducted and results are shown in Figure 4.30. This test simply concerned tying one end of the line to a fixed point and the other end to a weight. Different weights were used so to measure axial extension due to stretching for different load values, as reported in Figure 4.30. The extension as illustrated in this figure is linearly proportional to the load applied. These results refer to a 5.5 meter rope. During the experiment the total length of the rope used was c.a. 1.5 m. Thus, considering the exact length of the mooring line and the tension range, by proportion the maximum extension of the line was estimated to be limited to c.a. ± 3 mm. Thus limited stretching occurred.

Differently, during Session 2 only the steel wire was available and, thus, this was used. This type of mooring line is conventional and given its thickness the elongation was not a concern. Thus, at the time of the experiment, this was not assessed. Despite this, due to roughness and thickness, viscous damping in water and friction due to contact with the pulley were successively assessed to be relevant. Viscous effects were roughly

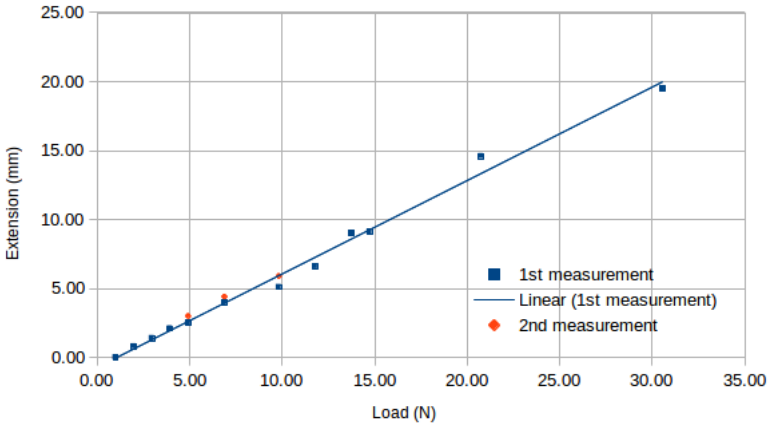

Figure 4.30: Preliminary test on elongation of the dyneema rope used during Session 1 (0.2 mm diameter).

evaluated by using the Morison's equation, and friction losses due to contact of the mooring line with the pulley were measured through dry oscillations tests. These lasts tests are described in Subsection 4.5.3.

As for Session 1 in Session 3, a dyneema rope was used for the mooring line component. This had a diameter of 0.5 mm. Results of the elongation test of this rope are reported in Figure 4.31. In this case, as loads are much greater than Session 1 and the rope is just 0.5 mm in diameter, the measured extensions are relatively higher than those measured for the 0.2 mm rope. As illustrated in Figure 4.31 the axial extension of the rope, also, in this case, is very linear. These tests results (Figure 4.31) represent the assessment for a 6 m long dyneema rope of 0.5 mm diameter used in Session 3. For the range of operation, the maximum extension of the line in Session 3 was estimated to be c.a. ± 6 mm. Again also, in this case, the stretching was limited.

To note that the measurement of the elongation of the mooring lines shown in Figures 4.30 and 4.31 comprehend stretching due to deformation, due to elasticity and due to knots' compression.

To select the best mooring line, between stainless steel and dyneema options available, to be used in Session 3, the forces acting on mooring lines were also estimated. For

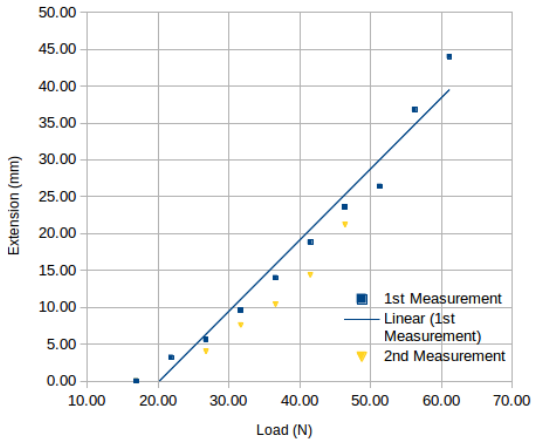

Figure 4.31: Preliminary test on elongation of the dyneema rope used during Session 3 (0.5 mm diameter).

roughly determine the magnitude of these forces acting on the mooring lines used during the experiments, a conservative estimation method regarding the use of the modified Morison's Equation (Eq. 4.1 (Sumer and Fredsœ, 2006)) was implemented. The factors utilised in the modified Morison's Equation 4.1 were chosen as maximum quantities occurring during experiments. In order to determine the total force acting over all the mooring component, the line was assumed to be a vertical axis cylinder divided into 10 sections.

$$F = \sum_{i=1}^{10} \left(\frac{1}{2} \rho C_D D (U_i - U_{w-i}) |U_i - U_{w-i}| + \rho C_M A (\dot{U}_i - \dot{U}_{w-i}) + \rho A \dot{U}_{w-i} \right) h_i \quad (4.1)$$

Equation 4.1 was evaluated for the case of maximum predicted buoy surge response X for each experiment (3 mooring lines). Where $U_i = \omega X$ is the floater's velocity amplitude at surge resonance frequency linearly decreasing with depth. The mooring line was discretized in 10 elements indicated by h_i. Where the horizontal water particles acceleration and velocity, U_{wi} and $\dot{U}_{wi}$, are calculated with the linear waves theory for each element h_i. The total force acting on the mooring line includes the Froude Krylov, drag and inertia forces. Together with the module of the total horizontal force, all

factors used for evaluating Equation 4.1 are reported in Table 4.13.

Quantity description	**Symbol**				**Unit**
Session no.		1	2	3	
Mooring line material		dyneema	stainless steel	dyneema	
Hydrodynamic mass coef.	C_m	1.00	1.00	1.00	
Drag coefficient	C_d	1.50	1.50	1.50	
Water density	ρ	1000.00	1000.00	1000.00	kg/m^3
Mooring line diameter	d	0.20	1.50	0.50	mm
Mooring line length	h	0.59	1.62	1.69	m
Max. $\dot{X}$	U	0.04	0.39	0.39	m/s
Max. $\ddot{X}$	$\dot{U}$	0.20	2.22	2.22	m/s^2
Max. surge	X	9.17	67.48	67.48	mm
Max. surge ang. freq.	ω_X	4.65	5.74	5.74	rad/s
Wave number	k	2.20	3.36	3.36	$1/m$
Wave amplitude	a	0.01	0.03	0.03	m/s^2
Total horizontal force	F	0.02	3.40	1.12	N

Table 4.13: Details of calculation of horizontal force acting on mooring lines.

In Table 4.13 it can be observed that by using the dyneema rope during Session 3 the module of the total horizontal force acting on mooring line is three times less than stainless steel cable used in Session 2. Thus the dyneema mooring line was chosen.

To note that the total horizontal force acting on the mooring line was calculated just for comparing the various options considered. This force is far greater than the real horizontal force exerted upon the buoy by the line. As the mooring line swivels along the pulley most of the total horizontal force calculated, which is acting on the mooring line, is counteracted by the pulley.

In Session 3 one dyneema rope and two steel cables, to be used as for the mooring line, and a series of pulleys, were also assessed a priori with oscillation tests. Friction losses concerning extra damping were quantified. The combination of a dyneema 0.5 mm thick rope, with an in-house build pulley having ceramic bearings, was found to be a better option compared to available components and parts used in Session 1 and 2. More details of preliminary oscillations tests concerning pulley selection will be discussed in Subsection 4.5.3.

Five standard nautical and manufactured in-house pulleys, during Session 1 and 2, were assessed. These were of different radius and quality. For Session 1 and 2 a conventional good quality nautical pulley with a diameter of 35 mm was used. Other pulleys were smaller and when manually rotated presented evident friction. These pulleys were then assessed in a better way during Session 3, as described in Subsection 4.5.3.

Assessment of friction losses during Session 3

During Session 3 the available pulleys were assessed in a more rigour manner, and the best combination of mooring line type and pulley was identified. Oscillations tests with a rig made of a spring, a mooring line and a weight, were run so to quantify friction losses (without motor). Six pulleys were assessed by monitoring oscillations time of the weights, as these last were released from a fixed initial position $z_0 = 0.1$ m. A damped mass-spring model (also used for calibrating the servomotor), explained in Subsection 4.5.5, was utilised to calculate an indicative damping coefficient reflecting friction losses for each pulley.

The set-up assembled for this preliminary tests is illustrated in Figure 4.32.

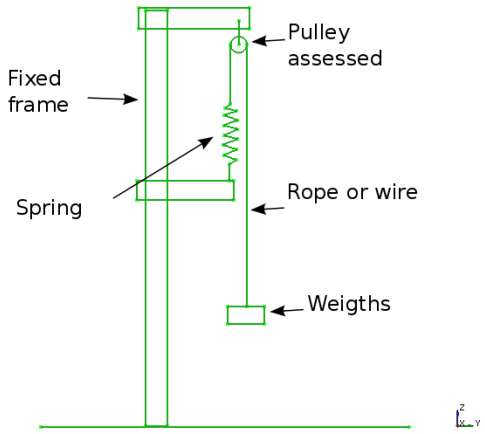

Figure 4.32: Test rig for selection of pulleys.

In Table 4.14 the results of oscillations tests are reported. As it can be observed in

this table, over the seven combinations, the custom-made pulley with ceramic bearings combined with the dyneema rope was the option by which oscillations were the least damped (18.9 seconds long). These new components were then selected and used in Session 3. For these tests, the weight value was chosen as the value needed for having the same pre-tension of the experiments in the water. Damping coefficients reported in Table 4.14 give an indication of the friction losses. For the selected in-house manufactured pulley with ceramic bearings, tested with the dyneema rope, the damping due to friction during the test was estimated to be c.a. 0.9 kg/s. This value is considerably less than the others.

Pulley descr.	**Wire/rope**	**Wire/rope diameter (mm)**	**Oscillation time (s)**	**Damping coefficent (kg/s)**
Custom allumium pulley	steel	2	9.28	2.50
Custom ceramic pulley	steel	2	9.29	2.49
Custom ceramic pulley	dyneema	0.5	18.90	0.90
Pulley A (Laser)	steel	2	4.03	5.00
Pulley B (Harken)	steel	2	3.87	5.50
Pulley C (Barton with no bearings)	dyneema	0.5	n.a. (overdamped)	30.00
Pulley D (Small Harken)	dyneema	0.5	3.21	6.00

Table 4.14: Results of friction losses assessment for different combinations of components

4.5.4 Spring component

The spring component was selected between available options. Some springs were cut so to obtain their spring stiffness closer to the wanted values. All springs were characterized by measuring their stiffness curve. For the illustrative purpose in Figure 4.33 are shown results of preliminary characterisation measurement tests on springs considered for Model 1. These tests, concerned merely of tying one side of a spring to a fixed frame, and to the other side a weight. By changing the weight value all springs displacements were recorded as showed in Figure 4.33. The same procedure was done for springs used during Sessions 2 and 3.

For Session 1 the spring defined as *medium stiffness* in Figure 4.33 was chosen. This spring is rated c.a. 0.015 N/mm and was finally adopted for all tests concerning Model 1.

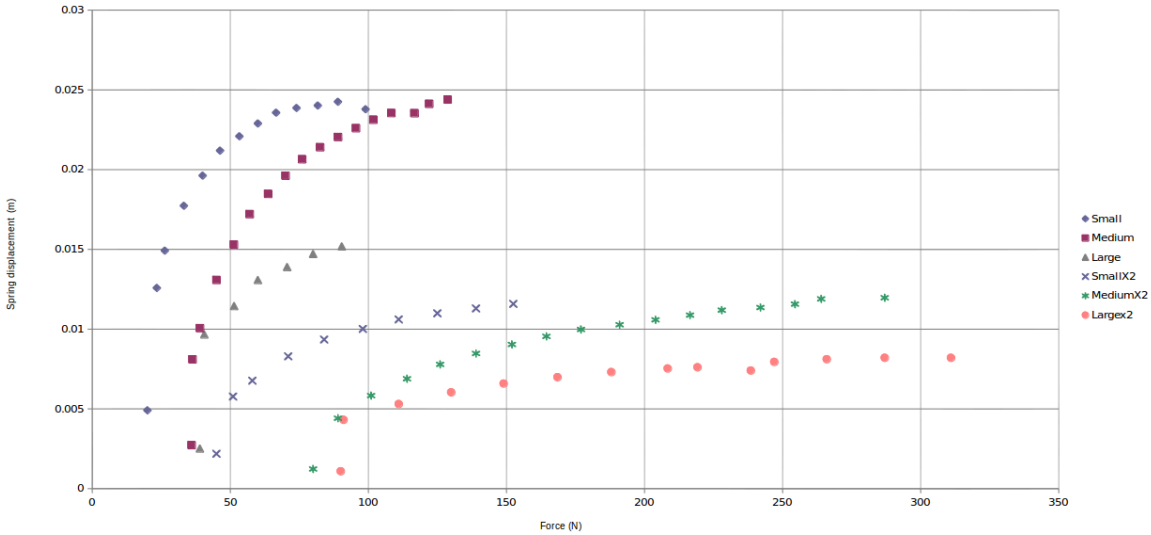

Figure 4.33: Characterization of different options for the selection of spring to be used for Model 1.

Similarly, for Sessions 2 and 3 other springs were assessed. The stiffness value of 9 springs was measured. The results for 5 of these springs are shown in Figure 4.34. The spring defined by *no.5* in Figure 4.34 was the one used in most of the tests relative to Sessions 2 and 3. This spring was selected from the available options as its stiffness range was more close to the desired stiffness value at the set pretension, i.e. 165 N/m. Also, another spring rated c.a. 355 N/m was used when tested Models 3b and 3c.

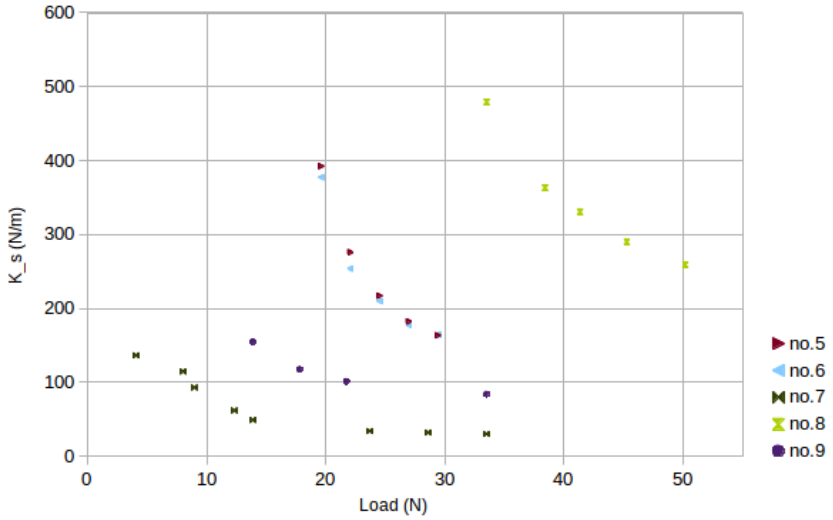

Figure 4.34: Measurement of springs' stiffness during Sessions 2 and 3.

4.5.5 Motor calibration

First method

Before starting testing the model in water, during Sessions 1 and 2 the electric motor, used as a damper, was calibrated by performing a series of tests. These tests were systematically conducted, for tuning the analog adapter (voltage gain and offset values) and for characterising the digital unit by which the electric motor used as a damper was controlled. During these tests, a series of weights were attached to a rope, which was driving the servomotor. For both, clockwise and counterclockwise directions the weights were dropped and time of 1 m fall was recorded. From the falling time information, the speed was calculated. For illustration, Figure 4.35 shows calibration tests results obtained for Model 1. This figure shows the results of the calibration for Model 1. The horizontal axis represents the force applied which is proportional to the weights used. The Y-axis represents the damping coefficients, these are calculated by dividing the force by the falling speed.

In Figure 4.35 the value of damping coefficient simulated by the servomotor in both directions of rotation is illustrated. For normal operation of the PA, a variation of

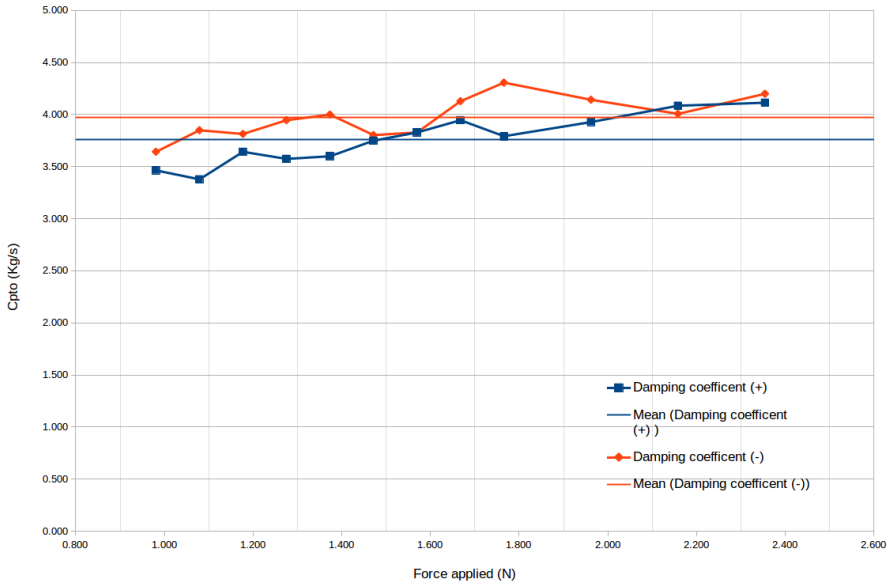

Figure 4.35: Calibration of motor (1st method).

ca. 0.4 (kg/s) of the target damping constant C_{pto} can be observed. Considering that the expected value of C_{pto} had to be equal to 3.64 (kg/s) the calibrated motor was simulating at times a damping coefficient distorted by a factor of c.a. $\pm$ 11%. Detailed uncertainty analysis is reported in Section 4.7. As a consequence, a better calibration method was then implemented in Session 3.

Second method

For calibrating the servomotor used as a PTO damping mechanism, together with free falling weights tests used during Sessions 1 and 2, in Session 3 also preliminary tests concerning free oscillations of weights were performed. The servomotor used was the one used in Session 1, and it was configured in the same way. Refer to Section 4.4.4 and Figure 4.23 for details.

The new method concerned of targeting the right damping force by tuning the analog amplifier and MyRio device during free oscillations tests. At first, the analog damper was roughly tuned following the *first method*. Successively the settings of the LabView

model, which controlled the MyRio device, were identified through oscillations tests. A test rig was used for this purpose, this is shown in Figure 4.36. This was mainly formed by a fixed frame where a spring component was tied to; a rope connected to the spring; and the electric motor which was driven by the line. In order to obtain oscillations in the required range of frequencies out of water, different springs were used to modify the natural frequency of the system. In practice, the mass was released from an initial offset and time series displacements of the oscillatory motion were monitored with the laser sensor, CED unit and Spike software. Successively, the classic second order differential equation, describing the motion of the damped harmonic oscillator, was solved a number of times at the end of each dry oscillation test for determining the damping coefficient value to assign to the oscillations under study. The parameters of the damped harmonic model were varied so to obtain a numerical solution matching the test result. In order to perform this task, a specific Matlab script was written and executed a number of times after each oscillations test. The oscillations tests were repeated for a range of damping values.

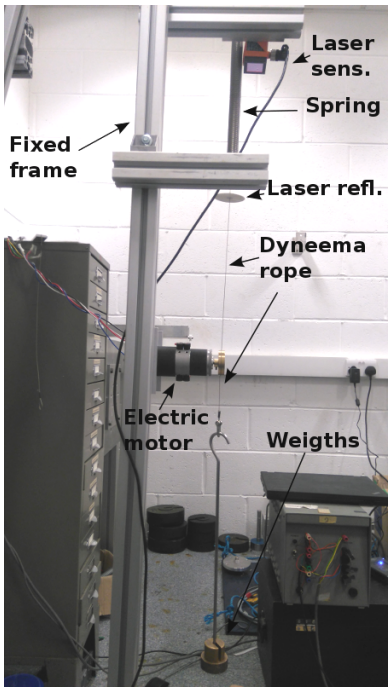

Figure 4.36: Rig constructed for calibrating the servomotor with the *second method*.

[kg/s]											
freq. (Hz):	**0.92**	**0.95**	**0.99**	**1.02**	**1.05**	**1.08**	**1.11**	**1.15**	**1.18**	**1.21**	**1.24**
ω (rad/s):	**5.80**	**6.00**	**6.20**	**6.40**	**6.60**	**6.80**	**7.00**	**7.20**	**7.40**	**7.60**	**7.80**
Digital gain (n.d.)											
1.00	40.00	38.60	37.20	35.80	34.40	33.00	31.60	30.20	28.80	27.40	26.00
1.10	41.00	39.46	38.06	36.66	35.26	34.10	32.72	31.34	29.96	28.58	27.20
1.20	42.00	40.32	38.92	37.52	36.12	35.20	33.84	32.48	31.12	29.76	28.40
1.30	43.00	41.18	39.78	38.38	36.98	36.30	34.96	33.62	32.28	30.94	29.60
1.40	44.00	42.04	40.64	39.24	37.84	37.40	36.08	34.76	33.44	32.12	30.80
1.50	45.00	42.90	41.50	40.10	38.70	38.50	37.20	35.90	34.60	33.30	32.00
1.60	46.00	43.76	42.36	40.96	39.56	39.60	38.32	37.04	35.76	34.48	33.20
1.70	47.00	44.62	43.22	41.82	40.42	40.70	39.44	38.18	36.92	35.66	34.40
1.80	48.00	45.48	44.08	42.68	41.28	41.80	40.56	39.32	38.08	36.84	35.60
1.90	49.00	46.34	44.94	43.54	42.14	42.90	41.68	40.46	39.24	38.02	36.80
2.00	50.00	47.20	45.80	44.40	43.00	44.00	42.80	41.60	40.40	39.20	38.00
2.10	51.50	48.82	47.40	45.98	44.56	45.30	44.06	42.82	41.58	40.34	39.10
2.20	53.00	50.44	49.00	47.56	46.12	46.60	45.32	44.04	42.76	41.48	40.20
2.30	54.50	52.06	50.60	49.14	47.68	47.90	46.58	45.26	43.94	42.62	41.30
2.40	56.00	53.68	52.20	50.72	49.24	49.20	47.84	46.48	45.12	43.76	42.40
2.50	57.50	55.30	53.80	52.30	50.80	50.50	49.10	47.70	46.30	44.90	43.50
2.60	59.00	56.92	55.40	53.88	52.36	51.80	50.36	48.92	47.48	46.04	44.60
2.70	60.50	58.54	57.00	55.46	53.92	53.10	51.62	50.14	48.66	47.18	45.70
2.80	62.00	60.16	58.60	57.04	55.48	54.40	52.88	51.36	49.84	48.32	46.80
2.90	63.50	61.78	60.20	58.62	57.04	55.70	54.14	52.58	51.02	49.46	47.90
3.00	65.00	63.40	61.80	60.20	58.60	57.00	55.40	53.80	52.20	50.60	49.00

Table 4.15: Extract of look-up matrix used to regulate the servomotor during experiments

More in details, for a specific factor named as *digital gain* defining the damping amplification due to the control of the myRio device, the equation of motion of the unidirectional spring-mass-damper system was solved multiple times. Each time the numerical results concerning the mass displacement were compared with the test results. For a range of *digital gain* values the damping coefficient C was searched. Essentially, to accomplish this, the script was evaluated, each time by correcting the C value, until both, numerical and measured displacement time series were matching.

Once all tests were performed for all *digital gain* values a look-up matrix was defined. With this matrix it was then possible to pick the correct *digital gain* value, when a particular waves frequency and a particular damping value C were chosen. An extract of this look-up matrix is reported in Table 4.15. Where the elements of this matrix are the damping coefficients C (kg/s). This matrix was then used during the experiment for setting the MyRio device depending on the desired damping value and regular waves angular frequency.

For illustration in Figure 4.2 is reported a screen-shot of the interface of the Spike2

software showing the time series of the mass displacement time series concerning an oscillations test.

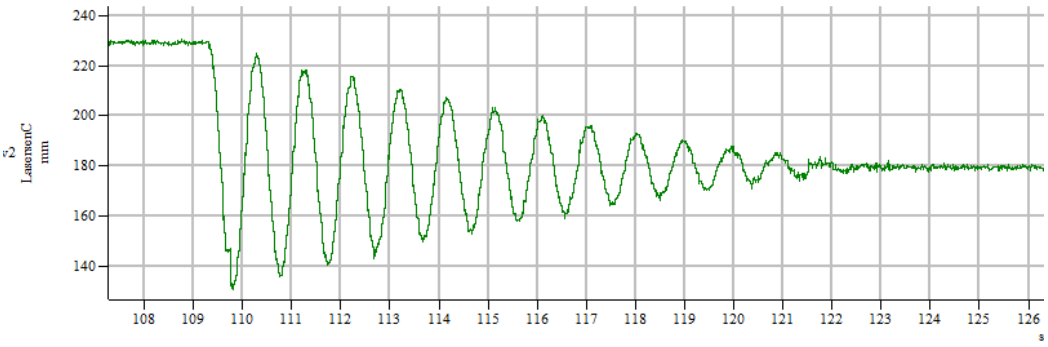

Figure 4.37: Example of test for calibration of motor following the second method (Spike screen-shot).

The damped harmonic oscillator model implemented is described by Equation 4.2.

$$m\ddot{z}(t) + C\dot{z}(t) + Kz(t) = 0 \tag{4.2}$$

where m is the mass, C is the damping coefficient and K is the spring stiffness constant.

Equation 4.2 was solved for finding the displacements of the mass in the time-domain. This was possible by using the *ode23* Matlab built-in algorithm.

4.6 Experimental data post-processing

The data, acquired during the experimental work carried out at both hydrodynamics laboratories, was analysed in two ways. The first way concerned extracting the data directly from the software Spike2. The other way related to using various Matlab scripts and functions which were written for post-processing purposes.

The first way was followed for only analysing regular waves tests results. This consisted of merely examining each Spike2 channel manually. The sinusoidal fitting function was used for obtaining the values of amplitude and frequency for each quantity recorded.

These values were calculated, always, for an interval for which the floater's heave motion was in resonance with waves. The interval represented a time period after transient effects, due to initial waves, have died out. The values were then copied into a spreadsheet.

The other way of post-processing data related to using a Matlab script. For regular waves tests, a code capable of making the sinusoidal fitting operation automatically was written and used for this operation. In order to check that the script was robust, the sinusoidal fittings obtained in Matlab were compared with the output obtained manually by using the Spike2 software. As desired, the sinusoidal fittings were the same. The advantage of using the Matlab script was that the results were analysed within a loop for all tests. The interval for which the fitting was computed, in this case, was defined by the number of oscillations. Also, in this case, the interval was taken when floater was in resonance with incoming waves and the effect of initial waves finished. In all circumstances, this period begins after a fixed time from the moment when the first wave was touching the floater. In order to discard tests with evident uncertainties, all data was preliminarily plotted in an automatic way. The tests that for any reason had uncertain validity, e.g. those where unexpected large yaw or pitch or roll occurred, were discarded manually.

For both mentioned ways, a sinusoidal fitting operation, described by Equation 4.3, was implemented for obtaining amplitude, offset and frequency values of the specific interval.

$$f(x) = \mathbf{a}_0 sin(\mathbf{a}_1 x + \mathbf{a}_2) + \mathbf{a}_3 \tag{4.3}$$

In Equation 4.3 $\mathbf{a}_1, \mathbf{a}_2$ and $\mathbf{a}_3$ represent coefficients that need to be found. These are searched by an algorithm starting from an initial guess. For both Spike2 software and Matlab script, when the solving algorithm did not converge, the coefficients relative to the wave probe signal fit were used as an initial guess. This resolution normally allowed

to find valid solutions. The operation was possible because the wave probe signal was the most regular sinusoidal oscillations between all channels acquired during all tests run.

For what concern time series of free oscillations regular and irregular sea tests, other Matlab scripts were written and used for analysing results. These scripts mainly served for: correcting the offsets, and for converting results to real scale or dimensionless form.

The Froude scaling laws, introduced in Chapter 2 Section 2.3, were used for scaling experimental results when these lasts had to be compared with real-scale numerical results.

4.7 Uncertainty and repeatibility analysis

Following the guideline provided by ITTC (2017b) the uncertainties of the different models tested were calculated. Tables no. 4.16, no. 4.17, no. 4.18 and no. 4.19 report results of the uncertainty analysis relative to all models tested. In this section the various types of uncertainty factors used are defined and calculations for obtaining these are explained.

In practice 5 types of uncertainty values were calculated, namely: the standard uncertainty Type A u_{s-A}, the standard uncertainty Type B u_{s-B}, the standard uncertainty u_s, the combined uncertainty u_c and the expanded uncertainty u_e. The operations for calculating these values are described next.

Standard uncertainty

The standard uncertainty u_s is defined as:

$$u_s = \sqrt{(u_{s-A})^2 + (u_{s-B})^2} \tag{4.4}$$

where the u_{s-A} and u_{s-B} are respectively the Type A and Type B uncertainties values.

Type A uncertainty reflects repeatability of tests. This dependents on statistical errors and it is calculated by the equation:

$$u_{s-A} = \frac{s}{\sqrt{n}} \tag{4.5}$$

where n is the number of repeated tests and s is the standard deviation defined as:

$$s = \sqrt{\frac{\sum_{k=1}^{n}(q_k - \overline{q})}{n-1}} \tag{4.6}$$

here q_k is the empirical reading associated to a particular test and $\overline{q}$ is the mean value obtained from all repeated tests in consideration.

The u_{s-A} values were calculated from repetitions of a particular test. For Model 1 and Model 2 regular waves test was repeated three times. For the first model the repeated tests were run with $a = 12.5$ mm and $\omega = 5.8$ rad/s. Instead, repeated tests of Model 2 were run by setting $a = 30.0$ mm and $\omega = 4.3$ rad/s. Differently, for Model 3a five tests were repeated three times plus one test was repeated five times. Finally, for Models 3b and 3c another test was repeated in total three times.

Type B uncertainty as discussed by ITTC (2017b) is not based on statistical methods and can be estimated by prior experience, calibration of equipment, manufacturers' specifications and other relevant information.

Concerning the wave probes, load cells and laser sensor the fundamental linear regression analysis, as reported by ITTC (2017a), was used to calculate u_{s-B} uncertainties. This method concerned using calibration data for each instrument. In practice, as for these sensors, the calibration data was very linear, a straight line was fitting well the calibration data; thus it was possible to use the following simple equations for calculating u_{s-B}.

At first the residuals were calculated (Equation 4.7).

$$Resid_i = y_i - a - bx_i \tag{4.7}$$

The residuals $Resid_i$ are the difference between the empirical data and the linear fit. The next step is the calculation of the sum of the square of residuals (Equation 4.8.

$$SS_R = \sum_{i=1}^{N} (Resid_i)^2 \tag{4.8}$$

Then the Type B standard uncertainty can be calculated with Equation 4.9.

$$u_{s-B} = \sqrt{\frac{SS_R}{n-2}} \tag{4.9}$$

For what concerns the u_{s-B} uncertainty of the floater motion (heave and surge) the value relative to maximum residual data obtained from the Qualysis software was used. The Qualysis software directly gave this.

Type B uncertainties were also calculated for the measurement of the PTO damping and spring stiffness.

Regarding PTO damping, another approach was implemented for evaluating its uncertainty $u_{s-B-PTO}$. This concerned of specific calculations of the motor's torque. Mostly, this was necessary so to justify the fact that during the experiment the motor's friction and inertia were neglected. Thus, the following torque relation was taken into account.

$$\tau_{motor} = \tau_{pto} + \tau_{inertia} + \tau_{friction} \tag{4.10}$$

Where terms on the right side of Equation 4.10 are respectively: desired motor torque, torque due to motor inertia and torque due to friction.

For the servomotor used in Sessions 1 and 3, the motor torque friction was estimated to be very low. The maximum torque friction value provided by Virgala, Frankovsky, and Kenderov (2013), who run experiments on a similar motor, was scaled up by a factor of 10 and applied to our motor. Considering the motor worm of a radius of 0.024 m the maximum existing load due to friction was estimated to be c.a. 0.0005 N. Thus, this value was taken as motor friction uncertainty $u_{s-B-friction}$.

The motor torque due to inertia is defined as:

$$\tau = J\frac{\ddot{z}}{r} = r|F_{inertia}| \tag{4.11}$$

where J is the motor's inertia constant provided by the manufacturer, and r is the motor worm radius.

Thus, after substituting $\ddot{z} = -\omega^2 z$ in Eq. 4.11, the module of the load due to motor inertia was evaluated by Equation 4.12.

$$|F_{inertia}| = -\frac{J\omega^2 z}{r^2} \tag{4.12}$$

Taking into consideration the average heave velocity of the floater at resonance, the uncertainty of damping constant due to both effects of inertia and friction was combined with Equation 4.13.

$$u_{s-B-C_{pto}} \simeq \sqrt{u_{s-B-inertia}^2 + u_{s-B-friction}^2} \tag{4.13}$$

Once springs selected were characterized, the linear regression analysis (Eq. 4.7 to 4.9) was used to evaluate the u_{s-B} uncertainty relative to the stiffness measurement.

Uncertainties in defining fixed models' parameters were also estimated. These concern floater's mass, floater's radius and mooring length. Depending on scales or rulers used,

reasonable values were picked for estimating u_{s-B} in this case.

The uncertainty in determine pretension was set equal to the uncertainty related to load cell.

Combined and expanded uncertainties

Successively, from the available information on uncertainties, the combined and expanded uncertainty values were estimated.

At first, the combined uncertainty concerning the measurement of power was estimated. The power was calculated from 3 inputs. In fact, this was an indirect measurement, and so another approach was required for calculating its uncertainty. Considering that power is defined as $P = C_{pto}\dot{\ell}^2$ where ℓ is the displacement of the mooring line and in the frequency-domain $\dot{\ell} = \pi f|\ell|$, power can be defined as: $P = C_{pto}\pi^2 f^2|\ell|^2$. The Data Reduction Equation for this last formula of power was found to be Equation 4.14

$$u_c^2(P) = \left(\frac{\partial P}{\partial C_{pto}}\right)^2 u_c^2(C_{pto}) + \left(\frac{\partial P}{\partial f^2}\right)^2 u_c^2(f^2) + 2\left(\frac{\partial P}{\partial |\ell|}\right)^2 u_c^2(|\ell|) \tag{4.14}$$

where the second term can be neglected because uncertainties of frequency f is almost nil. After substituting $\frac{\partial P}{\partial \pi^2} = \pi^2 f^2|\ell|^2$ and $\frac{\partial P}{\partial |\ell|} = 2C_{pto}\pi^2 f^2|\ell|$ into Equation 4.14 Equation 4.15 is obtained. This last was used to calculate uncertainty related to the power measurement.

$$u_c(P) = \sqrt{(\pi^2 f^2|\ell|^2)^2 + 8(C_{pto}\pi^2 f^2|\ell|)^2 u_c^2(|\ell|)} \tag{4.15}$$

With exception the power measurement uncertainty, for all other cases, the standard uncertainty u_s was set equal to the combined u_c uncertainty.

Following the calculation of the combined uncertainty u_c, the expanded uncertainty

u_e was calculated for all measurements. For this purpose, a 95% confidence level was assumed, and through the student's distribution table, a coverage factor $k = 4.30$ (for 3 repetitions) was identified. Given this coverage factor, the expanded uncertainty u_e was then calculated with Equation 4.16.

$$u_e = k u_c \tag{4.16}$$

4.7.1 Uncertainty analysis results

Results of the uncertainty analysis explained in the previous section are reported in Tables no. 4.16, no. 4.17, no. 4.18 and 4.19, respectively for the 5 models tested. For Model 3a more tests of particular regular waves parameters were repeated (Tab. 4.18). Where in the tables exists an empty space it means that for that particular case no value was possible to calculate. Instead, were 'NA' is indicated the value is not available, meaning that no repetitions were done for evaluating that particular value. All values reported in these tables are of plus-minus $\pm$ sign.

Depending on the model considered, the uncertainty values were calculated for repeated tests of regular waves of specific a and ω parameters. These parameters are stated in the second row of reported tables.

With Model 3a more tests were repeated. Two sets of repetitions concerned tests when the floater presented maximum heave resonance, one more set of repetitions regarded relatively low-frequency waves. Besides a further test was repeated five times for further investigating repeatability. For $\omega = 6.6$ rad/s maximum amplitudes were occurring (Table 4.18) and, thus, the uncertainties, in this case, were the highest compared to other waves frequencies.

Similarly for Models 3b and 3c maximum heave amplitude occurred for $\omega = 0.95$ rad/s. Uncertainties for these models are reported in Table 4.19.

Diversely, for Models 1 and 2, as the floater's heave motion results did not show a precise peak, tests with waves of other ω values were repeated for later calculate the uncertainties relative to these models. Despite this, the ω values considered for Models 1 and 2, reported in Tables 4.16 and 4.17, represent tests were heave amplitude was relatively high compared to other wave frequencies.

At predicted peak frequency heave motion was limited, meaning that the system damping, due to some reasons, was more than what was desired. For clarity, this extra damping was given by uncertainties concerning PTO damping calibration and extra damping due system friction.

In Table 4.16 there are shown results of the uncertainty analysis for Model 1 (1:86 scale). The uncertainties values reported concern regular waves tests of $a = 6.5$ mm and $\omega = 5.8$ rad/s repeated three times. As Session 1 concerned experiments at a smaller scale (with respect to Session 2 and 3) no direct comparison, between this and the other two sessions, of results is possible.

Model 1 - 1:86 scale		Units ±	u_{s-A} $a = 6.5, \omega = 5.8$	u_{s-B}	u_s	u_e $k = 4.3$
Direct measurements	Heave	Ampl.(mm)	0.130	0.600	0.614	2.640
		Freq.(rad/s)	0.028		0.028	0.122
	Surge	Ampl.(mm)	0.195	0.600	0.631	2.713
		Freq.(rad/s)	0.080		0.080	0.343
	Sonic probe	Ampl.(mm)	0.098	0.800	0.806	3.466
		Freq.(rad/s)	0.000		0.000	0.001
	Load	Ampl.(N)	0.002	0.015	0.015	0.065
		Freq.(rad/s)	0.001		0.001	0.005
	Displacement	Ampl.(mm)	0.082	0.850	0.854	3.672
		Freq.(rad/s)	0.003		0.003	0.012
Simulation of PTO	PTO damping	(kg/s)		0.919	0.919	NA
	Spring	(N/m)		3.860	3.860	NA
Fixed parameters	Mass of floater	(kg)		0.002	0.002	NA
	Radius of floater	(mm)		0.200	0.200	NA
	Length of line	(mm)		3.000	3.000	NA
	Pretension	(N)	0.002	0.015	0.015	0.065
Indirect measurement	Power	(W)				0.024

Table 4.16: Model 1 experiment uncertainties.

In Table 4.17 there are shown results of the uncertainty analysis for Model 2 (1:33

scale). The uncertainties values relate to one regular waves tests of $a = 17.5$ mm and $\omega = 4.3$ rad/s repeated 3 times.

Model 2 - 1:33 scale		Units	u_{s-A}	u_{s-B}	u_s	u_e
		$\pm$	$a = 17.5, \omega = 4.3$			$k = 4.3$
	Heave	Ampl.(mm)	0.456	0.800	0.921	3.960
		Freq.(rad/s)	0.057		0.057	0.247
	Surge	Ampl.(mm)	0.725	0.800	1.080	4.642
		Freq.(rad/s)	0.060		0.060	0.257
Direct measurements	Sonic probe	Ampl.(mm)	0.214	0.700	0.732	3.147
		Freq.(rad/s)	0.059		0.059	0.252
	Load	Ampl.(N)	0.049	0.015	0.051	0.219
		Freq.(rad/s)	0.054		0.054	0.233
	Displacement	Ampl.(mm)	0.525	0.850	0.999	4.296
		Freq.(rad/s)	0.053		0.053	0.228
Simulation of PTO	PTO damping	(kg/s)		9.318	9.318	NA
	Spring	(N/m)		14.602	14.602	NA
	Mass of floater	(kg)		0.005	0.005	NA
Fixed parameters	Radius of floater	(mm)		0.800	0.800	NA
	Length of line	(mm)		0.700	0.700	NA
	Pretension	(N)	0.049	0.015	0.051	NA
Indirect measurement	Power	(W)				0.667

Table 4.17: Model 2 experiment uncertainties.

In Table 4.18 the results of the uncertainty analysis for Model 3a (1:33 scale) are shown. The uncertainties values relate to 3 regular waves tests repeated three times. On the first row of columns 4, 5, 6 are reported the parameters (wave amplitude a in mm and angular frequency ω in rad/s) for the waves generated during repeated tests. Thus, in this table there are 3 columns for the u_{s-A}, u_s and u_e values.

As can it be observed by comparing Tables no. 4.17 and no. 4.18, uncertainties values related to direct measurements do not change much between Models 2 and 3a. Differently, for Model 3a the PTO damping standard uncertainty is c.a. six times reduced with respect to Model 2. Similarly, the expanded uncertainty in measuring power is greatly reduced in Model 3a (c.a. by a factor of 10).

In Table 4.19 are shown results for Models 3b and 3c. As it was for Models 1 and 2, also, in this case, one regular waves test was repeated three times ($a = 30$ mm and $\omega = 0.95$ rad/s). For these models, the surge and heave displacement related

Model 3a (1:33)		Units	u_{s-A}			u_{s-B}	u_s			u_e		
		±	$a = 30$	$a = 30$	$a = 60$					$k = 4.3$		
			$\omega = 2.3$	$\omega = 6.6$	$\omega = 6.6$							
	Heave	Ampl.(mm)	0.763	1.545	2.390	0.800	1.105	1.740	2.520	4.753	7.482	10.838
		Freq.(rad/s)	0.002	0.008	0.004		0.002	0.008	0.004	0.008	0.036	0.018
	Surge	Ampl.(mm)	0.660	0.123	0.310	0.800	1.037	0.809	0.858	4.460	3.481	3.690
		Freq.(rad/s)	0.005	0.017	0.003		0.005	0.017	0.003	0.021	0.073	0.013
Direct meas.	Wave probe	Ampl.(mm)	0.891	0.341	2.099	0.700	1.133	0.779	2.213	4.873	3.349	9.516
		Freq.(rad/s)	0.002	0.004	0.003		0.002	0.004	0.003	0.009	0.016	0.013
	Load	Ampl.(N)	0.056	0.119	0.138	0.015	0.058	0.120	0.138	0.250	0.517	0.595
		Freq.(rad/s)	0.001	0.007	0.004		0.001	0.007	0.004	0.006	0.031	0.016
	Displacement	Ampl.(mm)	0.822	1.730	2.176	0.850	1.183	1.927	2.336	5.085	8.288	10.044
		Freq.(rad/s)	0.002	0.006	0.003		0.002	0.006	0.003	0.007	0.028	0.011
Sim. of PTO	PTO damping	(kg/s)				1.473	1.473	1.473	1.473	NA	NA	NA
	Spring	(N/m)				13.212	13.212	13.212	13.212	NA	NA	NA
	Mass of floater	(kg)				0.005	0.005	0.005	0.005	NA	NA	NA
Fixed param.	Radius of floater	(mm)				0.800	0.800	0.800	0.800	NA	NA	NA
	Length of line	(mm)				6.000	6.000	6.000	6.000	NA	NA	NA
	Pretension	(N)	0.056	0.119	0.138	0.015	0.058	0.120	0.183	0.250	0.517	0.786
Indirect meas.	Power	(W)								0.030	0.328	1.221

Table 4.18: Uncertainties relative to Model 3a

uncertainties are higher than those related to Model 3a. This increase is due to the fact that the submerged floater displacements were much higher than Model 3a.

Besides, to further investigate repeatability of 1:33 model-scale experiments, one test of Model 3a was repeated five times. These tests concerned regular waves of $a = 30$ mm and $\omega = 4.6$ rad/s. Empirical results for these five tests and uncertainties factors are reported in Table 4.20. During these repetitions the electric motor was switched off (*digital gain* value set to zero) and all other parameters were the same as reported in first column of Table 4.7 of Section 4.4.3.

By comparing standard uncertainty u_s values obtained with 5 repetitions reported in Table 4.20 with u_s values relative to 3 repetitions as in Table 4.18, it can be noticed that increasing repetitions do not affects much results of standard uncertainties. Despite this, by having all times five repetitions, it would have permitted of to apply a coverage factor $k = 2.78$ instead of $k = 4.30$ (the student's distribution table reports these factors). Thus, accordingly to Equation 4.16 in that case, the expanded uncertainties values might greatly be reduced.

The standard uncertainty Type A value related to the wave probe intrinsically indicate repeatability concerning making waves in the two different facilities, related to each

Models 3b and 3c (1:33)		Units	u_{s-A}	u_{s-B}	u_s	u_e
		$\pm$	$a = 30, \omega = 0.95$			$k = 4.3$
	Heave	Ampl.(mm)	8.92058	1.500	9.046	38.897
		Freq.(rad/s)	0.00257		0.003	0.011
	Surge	Ampl.(mm)	6.47545	1.500	6.647	28.582
		Freq.(rad/s)	0.00104		0.001	0.004
Direct meas.	Wave probe	Ampl.(mm)	0.29473	0.700	0.760	3.266
		Freq.(rad/s)	0.00068		0.001	0.003
	Load	Ampl.(N)	0.61824	0.015	0.618	2.659
		Freq.(rad/s)	0.00226		0.002	0.010
	Displacement	Ampl.(mm)	8.37817	0.850	8.421	36.211
		Freq.(rad/s)	0.00246		0.002	0.011
Sim. of PTO	PTO damping	(kg/s)		1.386 (0)	1.386 (0)	NA
	Spring	(N/m)		13.212	13.212	NA
	Mass of floater	(kg)		0.010	0.010	NA
Fixed param.	Radius of floater	(mm)		0.800	0.800	NA
	Length of line	(mm)		5.000	5.000	NA
	Pretension	(N)	0.618	0.015	0.618	2.659
Indirect meas.	Power	(W)				0.026

Table 4.19: Uncertainties relative to Models 3b and 3c .

experiment. For both facilities, good repeatability was found. For three repetitions the wavemaker at the Henry Dyer laboratory produced waves with an uncertainty u_{s-A} of c.a. 0.1 mm (Table 4.16). For five repetitions the wavemaker at the Kelvin Hydrodynamics Laboratory produced waves with an uncertainty of u_{s-A} c.a. 0.44 mm. To note that these values include the measurement uncertainties (Table 4.20).

Test no.:		12	25	35	38	53	u_{s-A}
Heave	Ampl.(mm)	29.527	28.476	30.847	30.782	31.258	0.728
	Freq.(rad/s)	4.585	4.608	4.588	4.580	4.594	0.007
Surge	Ampl.(mm)	26.168	23.079	24.980	26.281	25.295	0.816
	Freq.(rad/s)	4.643	4.524	4.589	4.550	4.592	0.029
Wave probe	Ampl.(mm)	33.027	34.506	34.020	32.872	33.884	0.438
	Freq.(rad/s)	4.596	4.609	4.594	4.592	4.594	0.004
Load	Ampl.(N)	2.156	2.067	2.248	2.249	2.278	0.055
	Freq.(rad/s)	4.588	4.604	4.589	4.578	4.594	0.006
Displacement	Ampl.(mm)	29.732	28.305	30.742	30.927	31.253	0.758
	Freq.(rad/s)	4.587	4.603	4.589	4.578	4.594	0.006

Table 4.20: Regular waves tests ($a = 30$ mm and $\omega = 4.6$ rad/s) repeated 5 times.

As for the numerical code presented in Chapter 3 the inelastic mooring case was applied, during the experimental work (preliminary tests) the mooring lines elongation

of model's mooring components was assessed. This operation was done to understand uncertainties due to the inelastic mooring case assumption when experimental results are compared with numerical results. Given arguments and data presented, in Subsection 4.5.3, it was found that the inelastic case applied is generally justified. In fact, the elongation due to stretching is considerably less compared to axial mooring displacement due to the spring excursion. Besides, it was later found that considering results of peak frequency tests for Model 3a, the mooring load is only varying by c.a. 2.5 N. For this usual variation, taking into account further previous results reported in Subsections 4.5.3 related to the measurement of mooring elongation, is estimated an actual mooring elongation of 3.2 mm. This elongation for a mooring displacement of c.a. 60 mm meant 5.3% of inaccuracy. As a consequence it was found that in general the inelastic case can be applied, saying that by using the inelastic case assumption, the validation of numerical results with experimental data is plausible.

In general, results showed to be well repeatable also when tests were repeated after some time. The repetitions run for each model were at least 3, two repetitions were run after a few minutes, and the third repetition was done after hours or days. In particular, for Session 3, repeatability was more in-depth investigated. In all cases, some other tests were done between repeated tests, but this showed to not interfere with results.

With the second method applied for calibrating the servo motor, the desired damping was better tuned, and uncertainty in determining the damping was greatly reduced. In particular, by applying the second calibration method and having implemented model's improvements the PTO damping uncertainty u_s is reduced by a factor of c.a. 6.3 from Model 2 to Model 3a. This is clearly proved by the values of the PTO damping found in Tables no. 4.17 and no. 4.18. In particular, for the second method, all mechanical losses due to friction and uncertainties due to the inertia of the motor's rotor were intrinsic included in the measurement. As the PTO damping was better calibrated, in Session 3 the uncertainty in measuring power was also consistently reduced.

In general uncertainties values were the least for Session 3. The total errors in form of percentage are reported in Table 4.21 for Models no.3a, no.3b and no.3c. These total error values are obtained by dividing the expanded uncertainty u_e to the mean values of measurements from repeated tests and multiplying by hundreds. To note that for calculating u_e the coverage factor k given by the student's distribution table was equal to 4.3. These estimated errors may be reduced significantly if a lower coverage factor would have been applied.

	[± %]	Model 3a	Models 3b and 3c
Heave	ampl.	21.41	36.28
	phase	0.55	1.17
Surge	ampl.	20.68	18.33
	phase	1.11	0.47
Wave probe	ampl.	10.76	10.02
	phase	0.25	0.31
Load	ampl.	20.36	36.85
	phase	0.47	1.03
Displacement	ampl.	24.27	34.16
	phase	0.42	1.12
Power	ampl.	64.45	82.18

Table 4.21: Total errors in form of percentage related to models of Session 3 for repeated tests (peak frequency).

4.8 Results

In this section, the primary results for the five manufactured models tested in the two hydrodynamics laboratories are reported and discussed. Following the uncertainty analysis described in Section 4.7, depending on a specific model, only more relevant results are treated here. The focus was given for fulfilling the first objective of the experimental study stated in Section 4.1 (i.e. *to investigate in an empirical way: the motion response, the axial mooring line displacement, the mooring loads and the power absorption, for the considered device*).

Parameters investigated for each model are reported in Table 4.3 in Section 4.4.

4.8.1 1:86 scale results - Session 1

Experimental data of 68 tests were collected at the Henry Dyer Hydrodynamics Laboratory relative to Model 1 during Session 1. Over these tests: 50 tests were with regular waves; 12 concerned free oscillation tests; and 6 other tests related to irregular sea states. Regular waves in a ranges of $1.8 < \omega < 12.6$ (rad/s.) and $10.0 < a < 13.9$ (mm) were simulated. In Figure 4.38 points represent all regular waves tests run during Session 1. Brief descriptions of all valid tests are reported in Tables A.1 to A.2, these can be found in the Appendix of this thesis (Section A.1 of Appendix A).

Tests were run with a fixed value of PTO damping coefficient C_{pto} or for no active damping (electric motor off). Despite this, for all tests, the total system damping was more than what was desired. In fact as reported in Section 4.7, the PTO damping uncertainty for Model 1 was relatively high, i.e. $\simeq \pm$ 0.9 kg/s. As a plus, also friction losses were relatively high for this model; thus, the desired damping value (c.a. 3.64 kg/s), was always amplified to a certain extent.

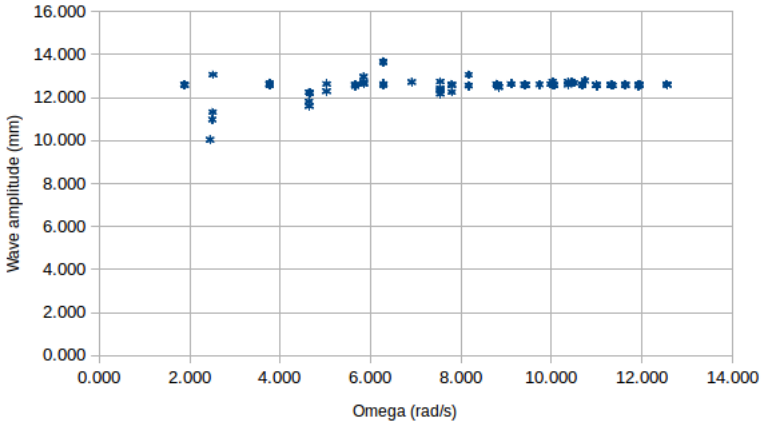

Figure 4.38: Regular waves tests - Session 1.

Free oscillations

At first free oscillations tests, for measuring the natural frequency of the device, were conducted. These tests concerned to release the buoyant from a position of few centimetres (both in the heave and surge directions) far from its equilibrium position and record the motion. Results of the free oscillations tests are summarized in the following table.

Test n.	**Test descr.**	**PTO**	**Aprox. Length (s)**	**Freq.(Hz)**
fo1	Z(0)=10 mm	no	<1	2.76
fo2	Z(0)=20 mm	no	<1	2.38
fo3	Z(0)=30 mm	no	1	2.63
fo4	X(0)=50 mm	no	100	0.17
fo5	X(0)=100 mm	no	140	0.18
fo6	Z(0)=10 mm	yes	<1	2.86
fo7	Z(0)=30 mm	yes	<1	2.13
fo8	X(0)=50 mm	yes	100	0.18
fo9	X(0)=100 mm	yes	140	0.18

Table 4.22: Summery of free oscillations tests results at 1:86 model-scale

The mean natural frequency found for heave free oscillations tests, reported in Table 4.22 (Tests no.fo1, no.fo2, no.fo3, no.fo and no.fo7), was equal to c.a. 2.55 Hz. For these tests the electric motor was switched firstly off (Test fo1-fo3) and after on (Test fo6-fo7). When the electric motor was switched off, the floater was damped exclusively by wave radiation damping and other sources of system damping such as motor's friction losses and friction due to the pulley. The PTO damping force at this scale did not modify much the heave natural frequency of the device.

Similarly, for surge free oscillations tests, Tests no.fo4, no.fo5, no.fo8 and no.fo9, as showed in Table 4.22, the PTO force applied did not modify the surge natural frequency, this last for all these tests was equal to c.a. 0.18 Hz. For these tests, the measurement of the free oscillations time was much simpler. In fact, in this case, the oscillations time was much longer compared to heave free oscillations.

In Figure 4.39 and 4.40 are shown for illustration surge and heave free oscillations tests time series. These figures represent data acquired for, respectively, Tests no.fo4 and no.fo3.

During Test fo4 as showed in Figure 4.39 the Qualisys signal for little time intervals was lost. For this reason a spline fit, indicated by the blue line in Figure 4.39, was also plotted.

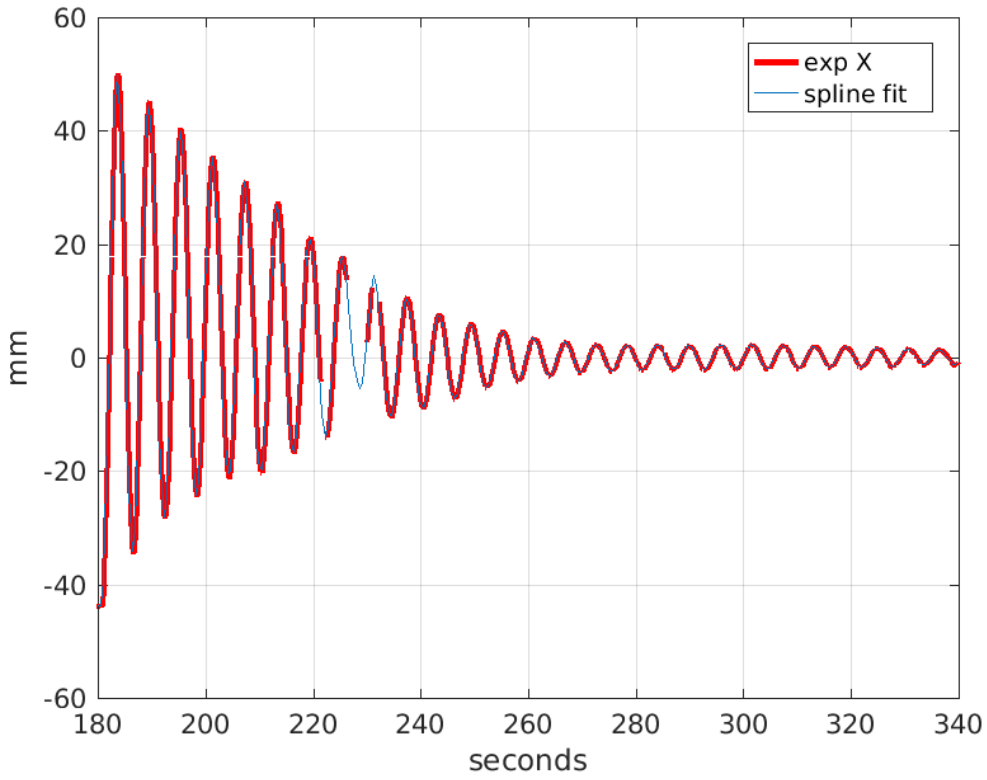

Figure 4.39: Illustration of surge free oscillations test ($X(t0) = 50$ mm nil digital damping value).

In Figure 4.40 is shown the time series for the free oscillation Test fo3. As can be noticed the free oscillations, in this case, are happening for a short time. In less than one second major oscillations ends.

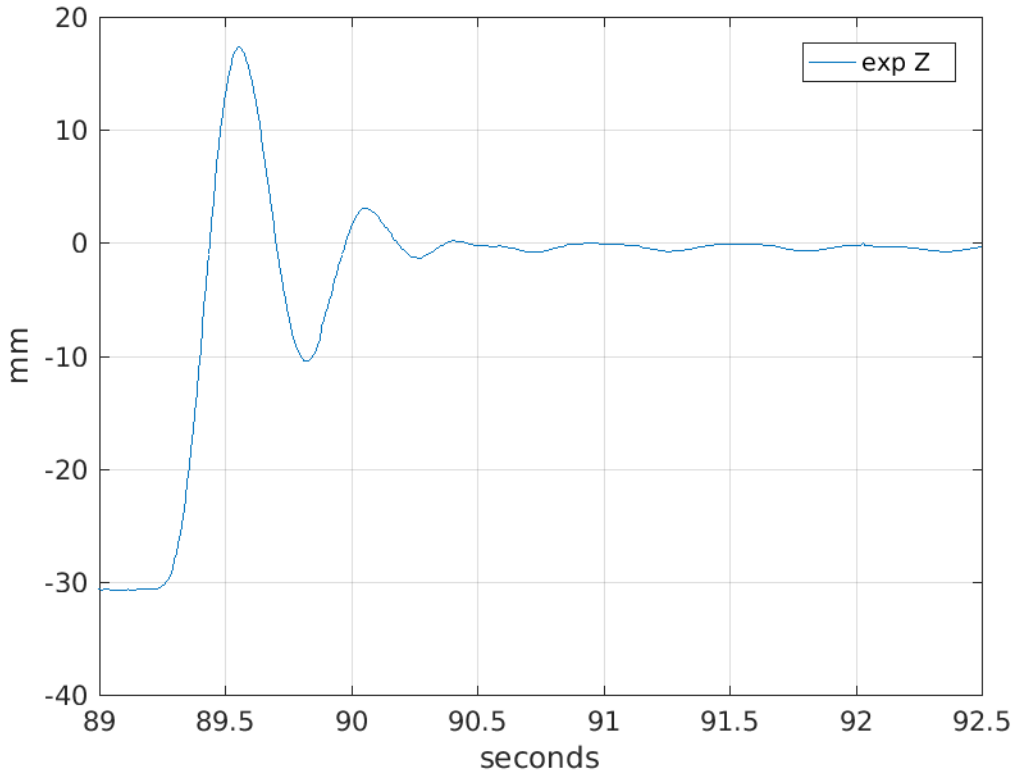

Figure 4.40: Illustration of heave free oscillations test ($Z(t0) = 30$ mm and with nil digital damping value).

Regular waves response

For this session of experiments, the regular waves tests results in the form of RAOs are reported in Figure 4.41.

As previously mentioned, in particular for what concerns the heave RAOs the experienced the damping force was much larger than the expected one. Thus, numerical results used for comparison were computed by correcting the input damping value in the numerical tool. In fact, for the FD calculation, the quantified extra damping due to friction losses was included, this was done by increasing the PTO damping value by a factor equal to 2/3 of the desired PTO value. This correction was done by modifying numerical input. Once numerical results were adjusted a discrete comparison between numerical and experimental results was found. This is shown in Figure 4.41.

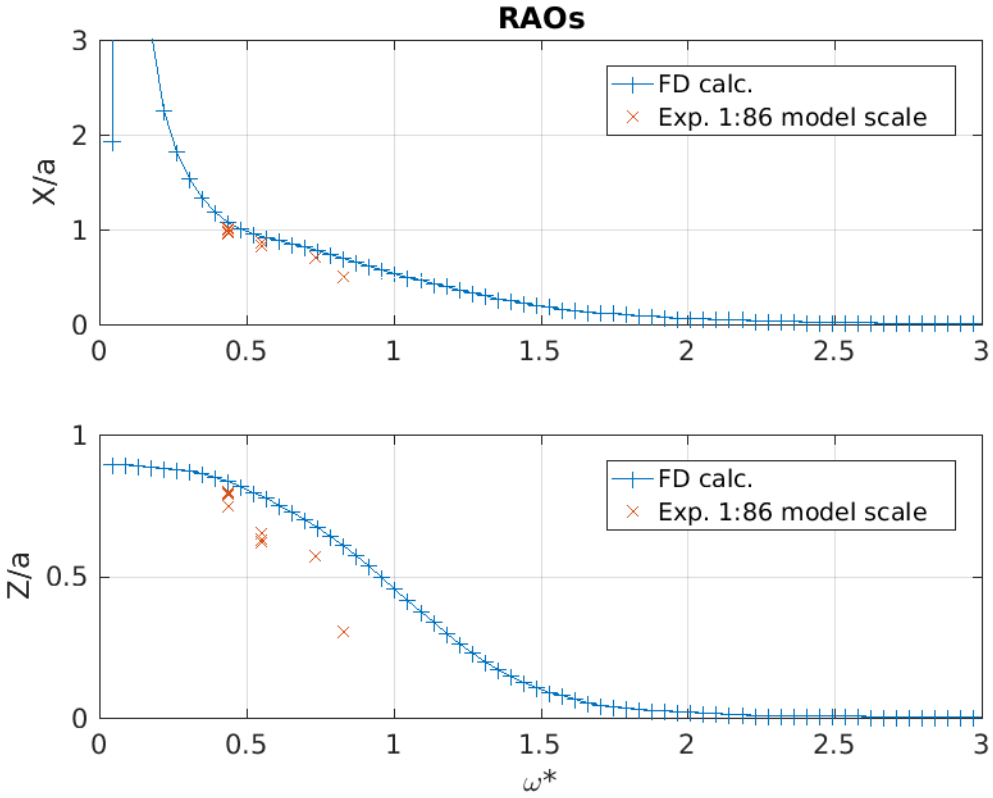

Figure 4.41: RAOs of the physical model of the PA compared with numerical results.

Regular and irregular sea time series

For illustration purposes, in Figures 4.42 and 4.43 are shown the buoy motion pattern and mooring line tension during Test no.50 and no.79, where respectively regular waves and irregular seas were implemented. As can be seen in the first figure, the regular waves response only concerning the surge is more irregular. In particular at the beginning of the time series, for surge motion, as shown in the first plot in Figure 4.42, a non-simple sinusoidal motion was happening. This kind of pattern which is constituted by the wave frequency response and by the lower surge natural frequency, it increases along with the increase of regular waves frequency. For both Tests 50 and 79, the surge motion is, in general, more than the heave showed in both second plots of these figures.

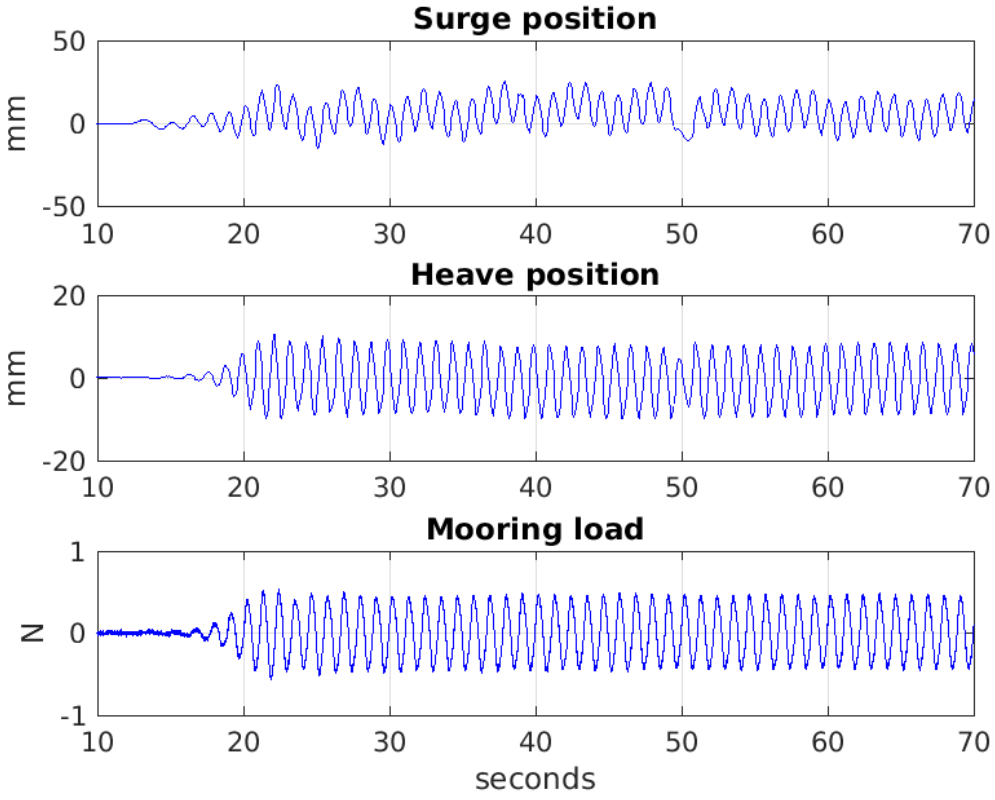

Figure 4.42: Illustration of time series indicating system response in regular waves of a=12.3 mm and $\omega = 7.54$ rad/s.

Due to irregularities of the model manufactured at this scale, the pitch, the roll and the

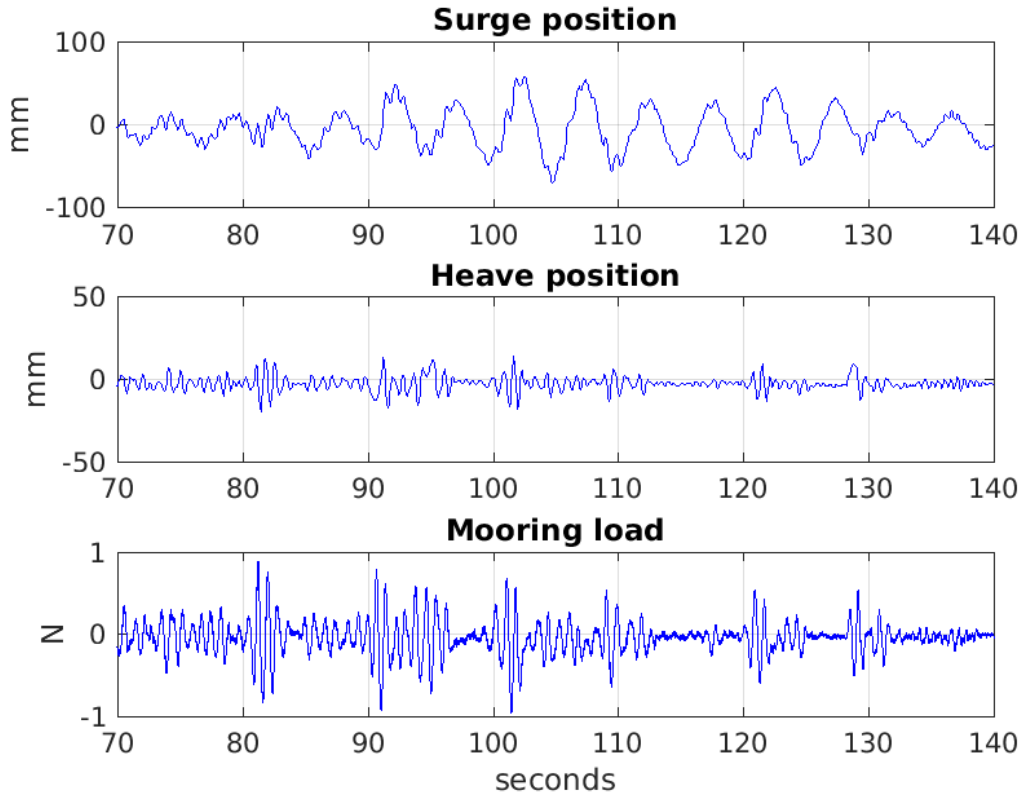

Figure 4.43: Illustration of time series indicating system response in irregular sea characterized by a generic energy spectrum created by setting: Hs=12.5 mm; Tp=0.8 s.; gamma=2.6; and gain=1.

sway motions, occurring during many tests, were often large, causing the data obtained from a test challenging to be analysed. Besides, as is further discussed in Section 4.7, because measurements uncertainties during this session were the highest, only these few tests results relative to Model 1 are reported in this thesis.

4.8.2 1:33 scale results - Session 2

In this subsection the results concerning the Session 2 of 1:33 model-scale tests (Model 2) are described.

Due to the larger manufactured model and dimensions of the water tank, the obtained data were, to a certain extent, more accurate than the data acquired at the 1:86 scale model of Session 1. Despite this, during this set of tests, the friction losses and uncertainties related to the PTO mechanism were still consistent. Thus even in this case results were partially compromised by these issues. As a consequence, the motion of the buoy even in this case, as for Model 1, was dampened more than what was predicted. For this reason, only significant results for Model 2 are reported here. These concern only regular waves tests where the wave amplitude a was incremented.

A tabular overview of all tests on Model 2 is reported in Appendix A.1.2.

Results concern surge and heave RAOs, the mooring displacement, the mooring load and the estimated efficiency factor, obtained during regular waves for different wave amplitudes. Following best practice, all results this time are reported in dimensionless form. For this purpose the following dimensionless quantities are defined:

- X/a and Z/a are the surge and heave RAOs.
- $F^* = F/(V_w \cdot g \cdot \rho)$ is the dimensionless axial mooring load, where the V_w is the volume of the immersed part of the spherical floater, g is the gravitational acceleration ($= 9.81 m/s^2$) and ρ is the density of fresh water ($= 1000 kg/m^3$).
- $\Delta L^* = (\Delta L/a)$ is the normalized axial mooring displacement, where ΔL is the

mooring line displacement.

- $P^* = P/(2rP_{max})$ is defined as the dimensionless efficiency factor relative to power absorption, where P is the estimated mean power from the device, r is the floater's radius and P_{max} is the wave energy flux (per unit width along the wave crest). This last is defined as $P_{max} = \frac{1}{2}\rho g a^2 c_g$, where a is the wave amplitude and $c_g =$ is the waves group velocity given from linear waves theory.

Regular waves

In Figure 4.38 points represent all regular waves tests run during Session 2.

Regular waves in a ranges of $1.0 < \omega < 9.0$ (rad/s)$(0.05 < kr < 2.00)$ and $10 < a < 80$ (mm) were simulated.

All tests were run with a fixed value of PTO damping C_{pto}.

Surge and heave RAOs are shown in Figure 4.45. On the horizontal axis the kr is the dimensionless wave number equal to $\frac{\omega^2}{g}r$, where r is the floater radius.

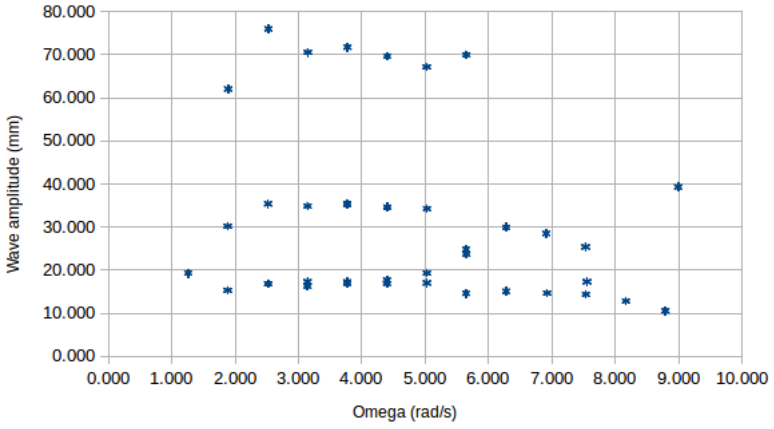

Figure 4.44: Regular waves tests - Session 2.

Main results for regular waves are illustrated in Figures no. 4.45, no. 4.46 and no. 4.47). Concerning surge heave and mooring line axial displacement, respectively showed in

Figure 4.45 and the first plot of Figure 4.46, these are found to be linearly proportional to the wave amplitude. This is indicated by the fact that for a same frequency, points obtained with a different wave amplitudes almost coincide between each-other.

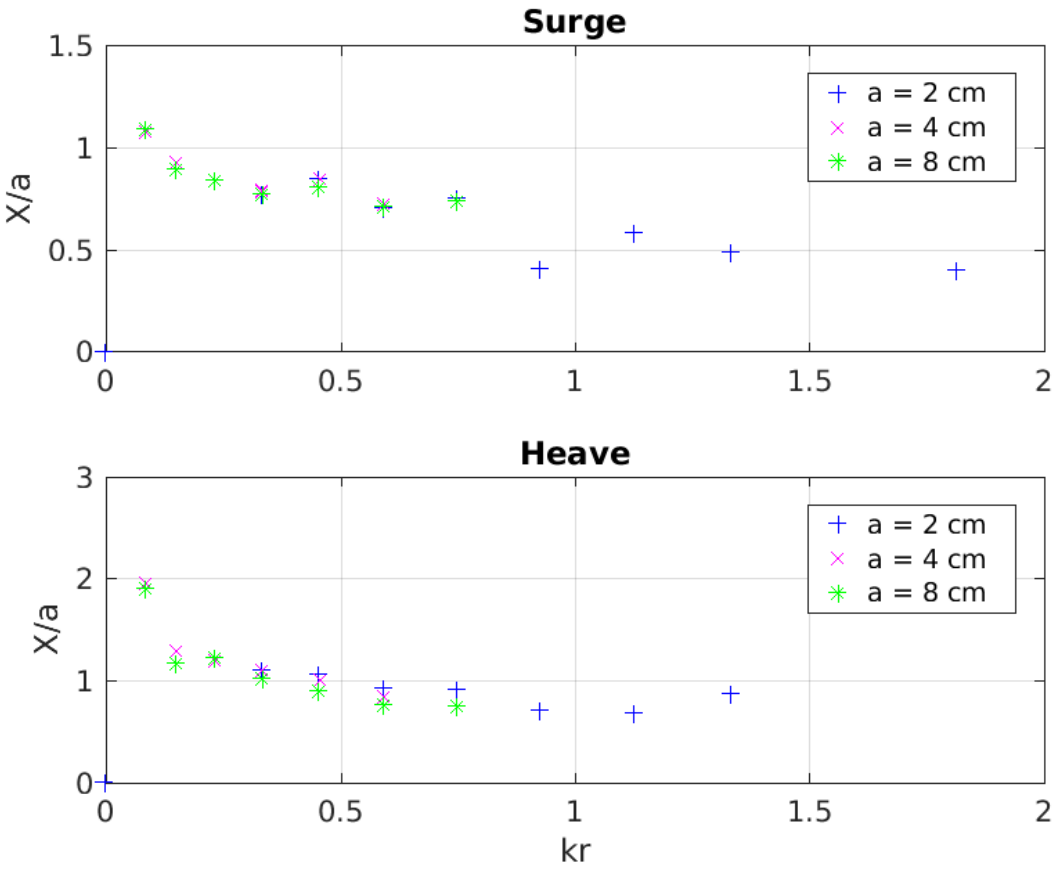

Figure 4.45: Response amplitude operators (RAOs) for regular waves of different amplitude (a).

The dimensionless mooring load and dimensionless power, respectively defined by $F^* = F_m/(Vg\rho)$ and $P^* = P/P_{max}/2r$, are shown in Figure 4.46 and in Figure 4.47. These values clearly increase along with the waves amplitude a. In particular this illustrated, in second plot of Figure 4.46, for the mooring load, and in Figure 4.47, for the power.

Because the Kelvin Hydrodynamics Laboratory was available for a limited time during Session 2, only a few tests were conducted and reported in this section. This also is the reason why not all regular wave frequencies tested for $a = 2$ cm could have been

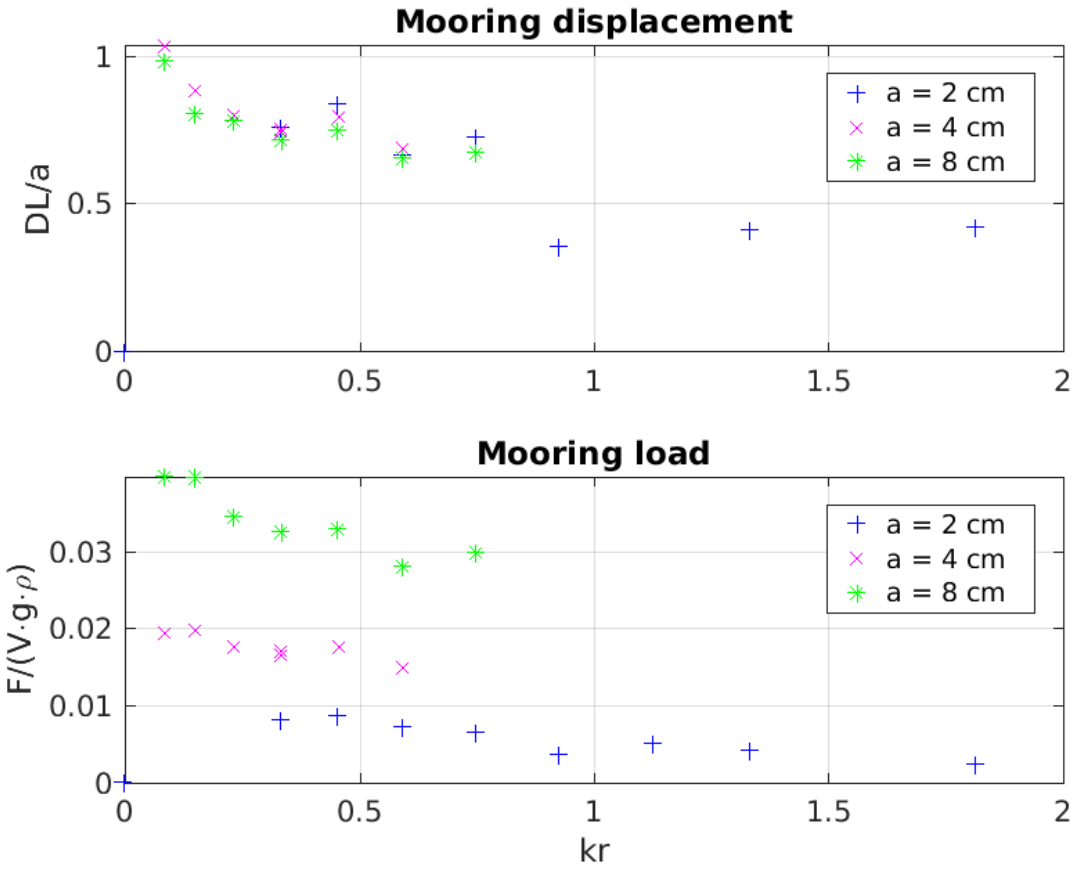

Figure 4.46: Mooring displacement and mooring load occurring during regular waves, for different wave amplitudes (a).

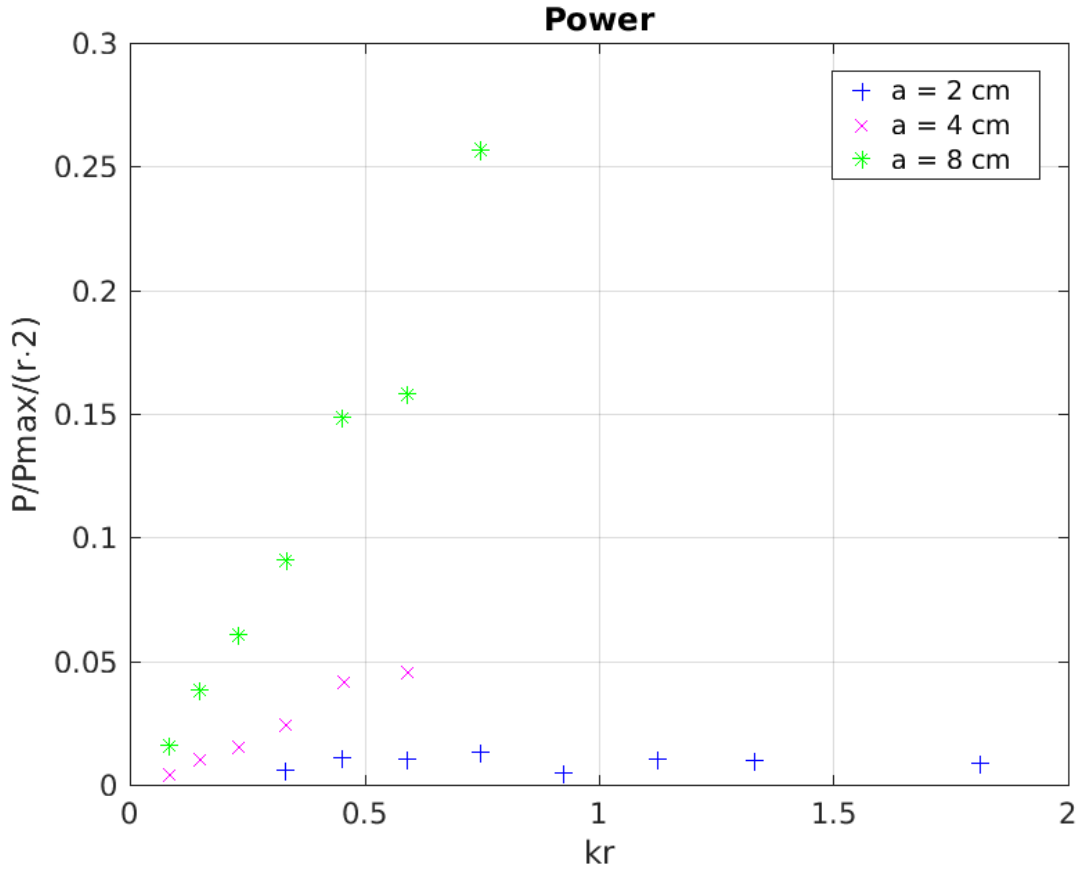

Figure 4.47: Estimated power factor relative to regular waves of different amplitude (a).

run for respectively $a = 4$ and $a = 8$ cm regular waves amplitudes. Despite this, the experiments concerning Model 3a and Model 2 were similar and, thus, there was no need of reporting more results in this section as further extended results are reported for Session 3. In fact, in Session 3 the facility was available for a longer time and also experimental uncertainties were consistently reduced. Despite this, it was found to be essential to report anyway best results of Model 2 so to have an additional set of results that can be compared with results of Model 3a so to give an extra indication on to which extent this type of experiments can be repeated.

4.8.3 1:33 scale results - Session 3

Major results concerning the half-immersed sphere and for the submerged sphere, are described and reported in the next subsections.

As for previous subsections regarding Models 1 and 2, models parameters investigated during Session 3 are reported in Table 4.3 in Section 4.4.

Results and details of all Session 3 tests are reported in tabular format in Appendix A.1.3.

Half-immersed spherical PA - Model 3a

Most of the issues relative to experiments of Session 1 and 2 for the half-immersed moored floater were solved in Session 3. The uncertainty analysis discussed in Section 4.7 proves this. Uncertainties relative to PTO damping for Model 3a were considerably reduced. Thus concerning the half-immersed moored floater results for Model 3a are the most reliable. These are reported in this section, and in Appendix A.1.3 where also data in tabular form can be found.

In this subsection, the experimental results of Session 3, concerning the half-immersed floater named Model 3a, are reported. As anticipated in Table 4.3, this model was tested for five different configurations of PTO damping.

Regular waves in ranges of $1.0 < \omega < 11.5$ (rad/s.)$(0.1 < kr < 1.8)$ and $15.0 < a < 70.0$ (mm) were generated during tests of Model 3a. In Figure 4.48 points represent all regular waves tests run during evaluation of this model.

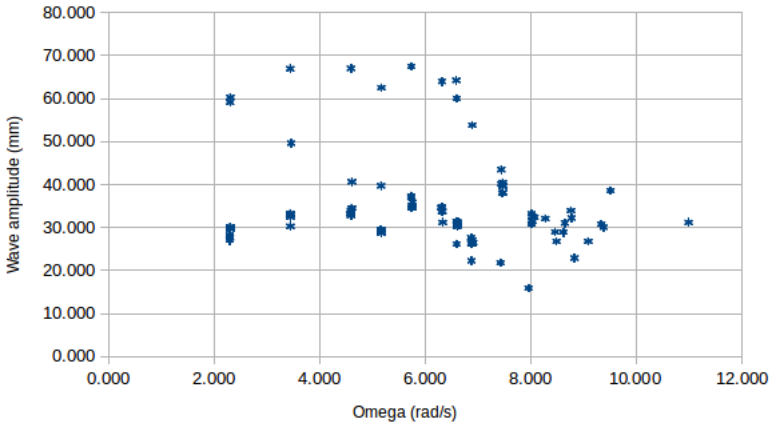

Figure 4.48: Regular waves tests - Model 3a.

In Figure 4.49 are shown results for tests with *normal damping*. The first two plots represent, respectively the surge and heave RAOs. The surge RAO almost linearly decreases when kr increases. In contrast, for $kr < 1.1$ the heave RAO is almost equal to 1, it present a slight peak during Test 58 when $kr = 1.15$ (peak frequency) and, then, it decrease for $kr > 1.2$. The dimensionless mooring load, was defined as $F^* = F/(V_w \cdot g \cdot \rho)$ (refer to Subsection 4.8.2 for details on dimensionless quantities), varied between 0.0075 and 0.01. The normalised axial mooring displacement defined as $\Delta L^* = (\Delta L/a)$, both in magnitude and for its pattern is very similar to the heave RAO. Diversely, the dimensionless efficiency factor, defined as $P^* = P/(2rP_{max})$, is greater for $0.6 < kr < 1.5$.

Results, as for Figure 4.49, relative to *normal damping* configuration where found also for the other PTO damping configurations. Despite this, as these results are very similar as Figure 4.49 these are not reported in this section. Results relative to the *low damping* and *high damping* configurations are reported in Figures A.1 and A.2 in Appendix A.1.3.

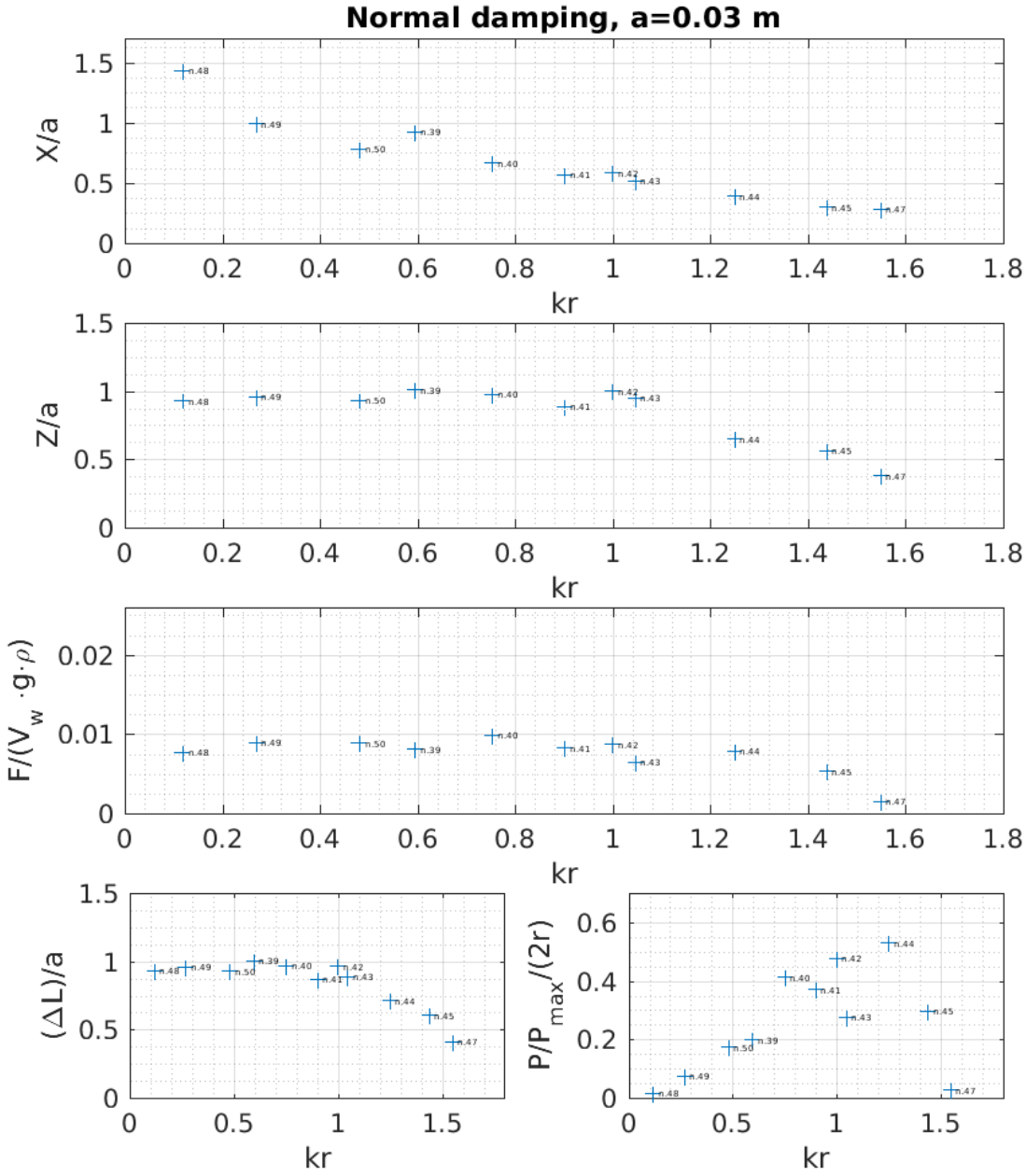

Figure 4.49: Experiments results related to the *normal damping* configuration of half-immersed PA in regular waves of amplitude a=0.03 m.

The *normal damping* PTO damping configuration was also tested in regular waves of $a = 0.045$ and $a = 0.06$. In Figure 4.50 are reported results for the model tested in regular waves of $a = 0.06$ m, i.e. wave amplitude value two times more as for tests related to Figure 4.49. For these waves, the floater presented a heave peak when $kr = 0.85$. Regular waves of $a = 0.06$ m and high frequencies $kr > 1$ were too steep, so these were not generated otherwise waves would have broke. Both RAOs and characteristic mooring displacement did not vary much compared to Figure 4.49. Also the efficiency factor is similar for both sets of tests (Figures 4.49 and 4.50), meaning that the efficiency of the device would not change much when wave amplitude varies. Despite this, the dimensionless mooring load F^* is almost doubled when $a = 0.06$ m. Similar results for $a = 0.45$ m regular waves tests are reported in Appendix A.1.3. Also considering this latter case, also when the normal damping configuration is implemented, the efficiency is unvaried.

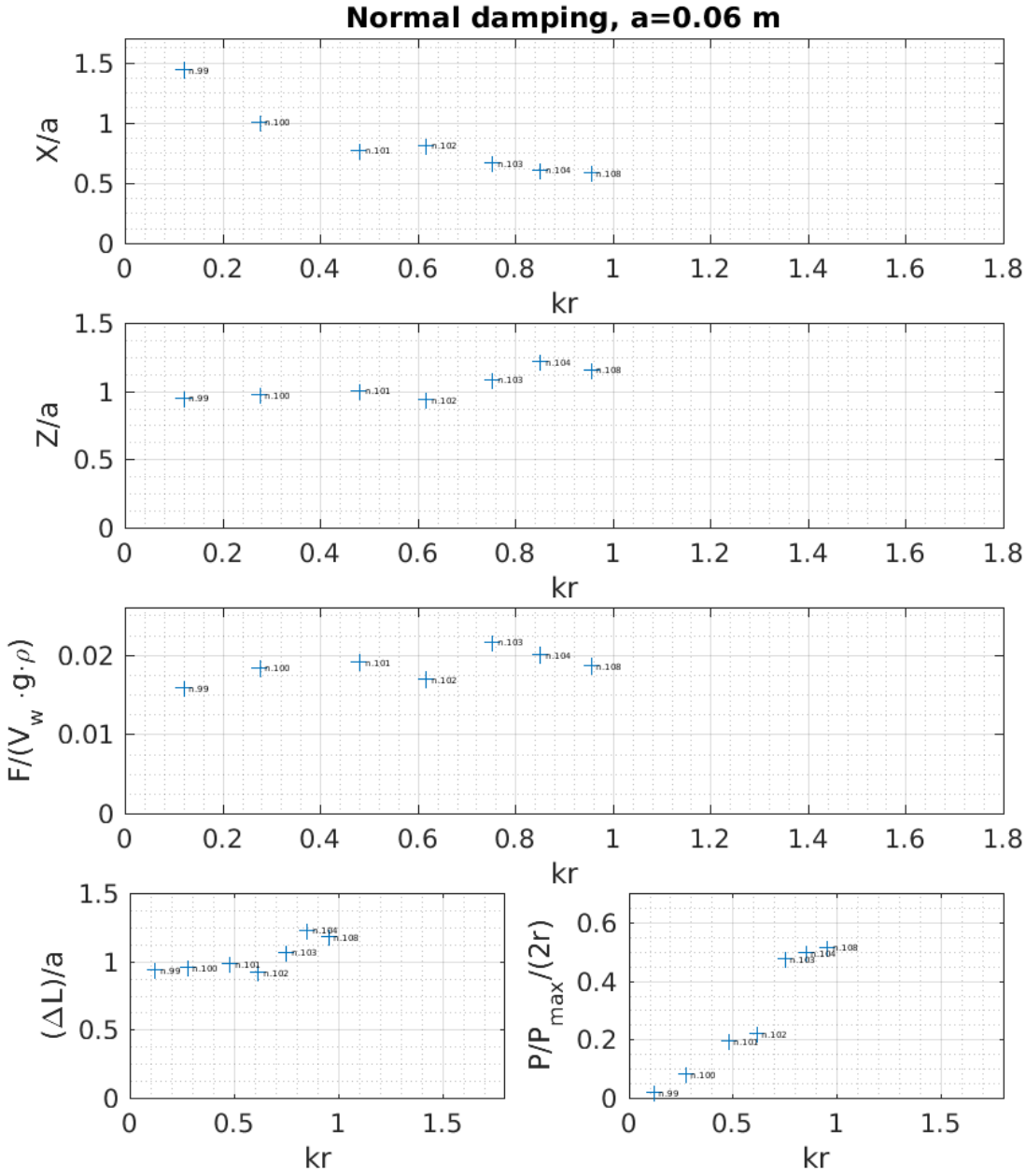

Figure 4.50: Experiments results related to the *normal damping* configuration of half-immersed PA in regular waves of amplitude a=0.06 m.

Submerged spherical PA - Session 3

In this section the results concerning the Models 3b and 3c are reported and explained.

Regular waves in ranges of $0.7 < \omega < 2.1$ (rad/s.) and $10 < a < 45$ (mm) were generated during tests. In Figure 4.51 points represent all regular waves tests run during evaluation of Model no.3b and no.3c (respectively in yellow and blue colors).

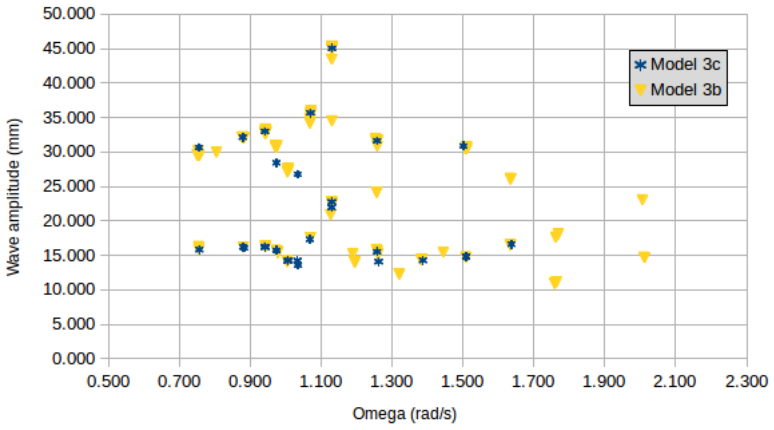

Figure 4.51: Regular waves tests - Model 3a.

A consistent number of configurations concerning different system parameters were evaluated. For each system configuration, the submerged floater was tested in regular waves of a range of relevant frequencies close to the frequency of heave peak frequency.

For Model 3b the PTO damping configurations this time were five, and these correspond to the following values.

$C_{pto}n_0 \cong 13$ kg/s (motor friction), n=0;

$C_{pto}n_1 \cong 18.5$ kg/s, n=1;

$C_{pto}n_2 \cong 24$ kg/s, n=2;

$C_{pto}n_3 \cong 28.1$ kg/s, n=3;

$C_{pto}n_4 \cong 31.5$ kg/s, n=4;

where n is the value assigned to the digital controller used (in the tables of the empirical results this is named digital gain value).

The vertical position of the spherical floater corresponded the length of the mooring line minus the immersion depth. The latter was also varied by three different values. These were set to the dimensionless values of $f/r = 1.5$, $f/r = 2$ and $f/r = 2.5$. Were f is the length between the free surface and the centre of the spherical floater and r is again is the floater's radius. At the experiment scale these depths corresponded to the following values:

Immersion depth no.1 ($f/r = 1.5$) = 0.345 m

Immersion depth no.2 ($f/r = 2$) = 0.46 m

Immersion depth no.3 ($f/r = 2.5$) = 0.575 m

The spring used for the majority of tests was the one also used during tests concerning the half-immersed sphere. Along with the submerged model also another spring was used. This spring had a spring stiffness of c.a. 400 N/m.

Next, are reported results only concerning the main findings. Each of the following figures represents tests related to a particular system configuration. From Figure 4.52 to Figure 4.54 the immersion depth was varied from Imm. depth 1 to Imm. depth 3.

Differently, for obtaining results in Figures 4.55 and 4.56 the damping value was changed.

In Figures 4.57 the results for the configuration where the servomotor was removed are shown. These results can be compared with results shown in Figure 4.53 concerning the same Imm. depth when the damping value was set to $C_{pto}n_4$.

For the 3 immersion depths and for most quantities investigated (Figures 4.52, no. 4.53 and no. 4.54), the peak frequency is almost the same. This frequency for F^*, ΔL^* and P^* is c.a. $kr = 0.06$. The heave RAO peak frequency is slightly less. i.e. $kr \simeq 0.058$.

Concerning amplitudes, a little reduction can be noted for what concern heave, mooring load and power by varying from Imm. depth 1 to Imm. depth 3. This is due to the fact that at lower depth less wave energy is available. All other quantities are almost unvaried. In fact, the amplitude of quantities at peak frequency did not change between Immersion depths 1 and 2.

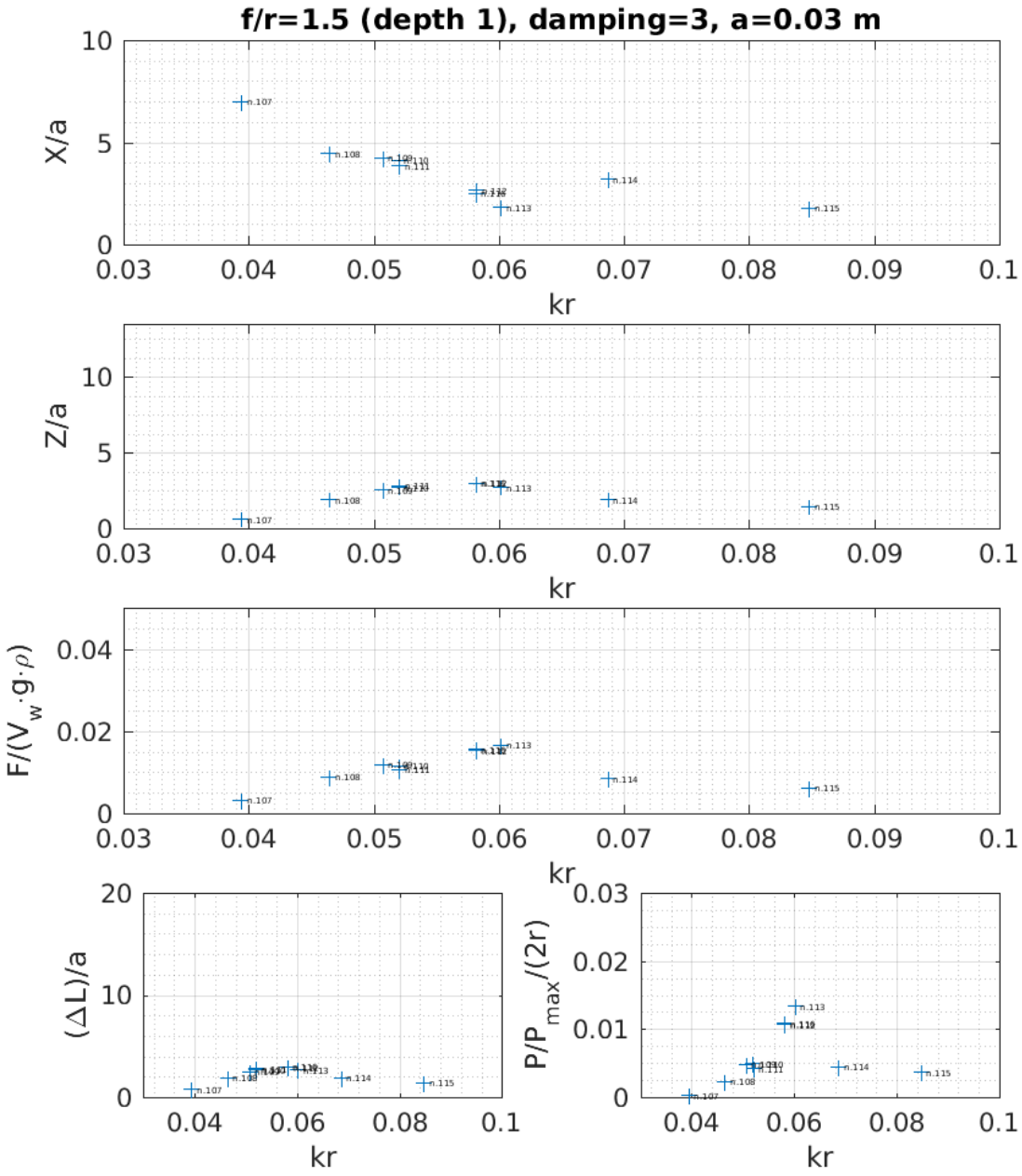

Figure 4.52: Experiments results related to the Damping n.3 at Depth n.1 of submerged spherical PA in regular waves of amplitude a=0.03 m.

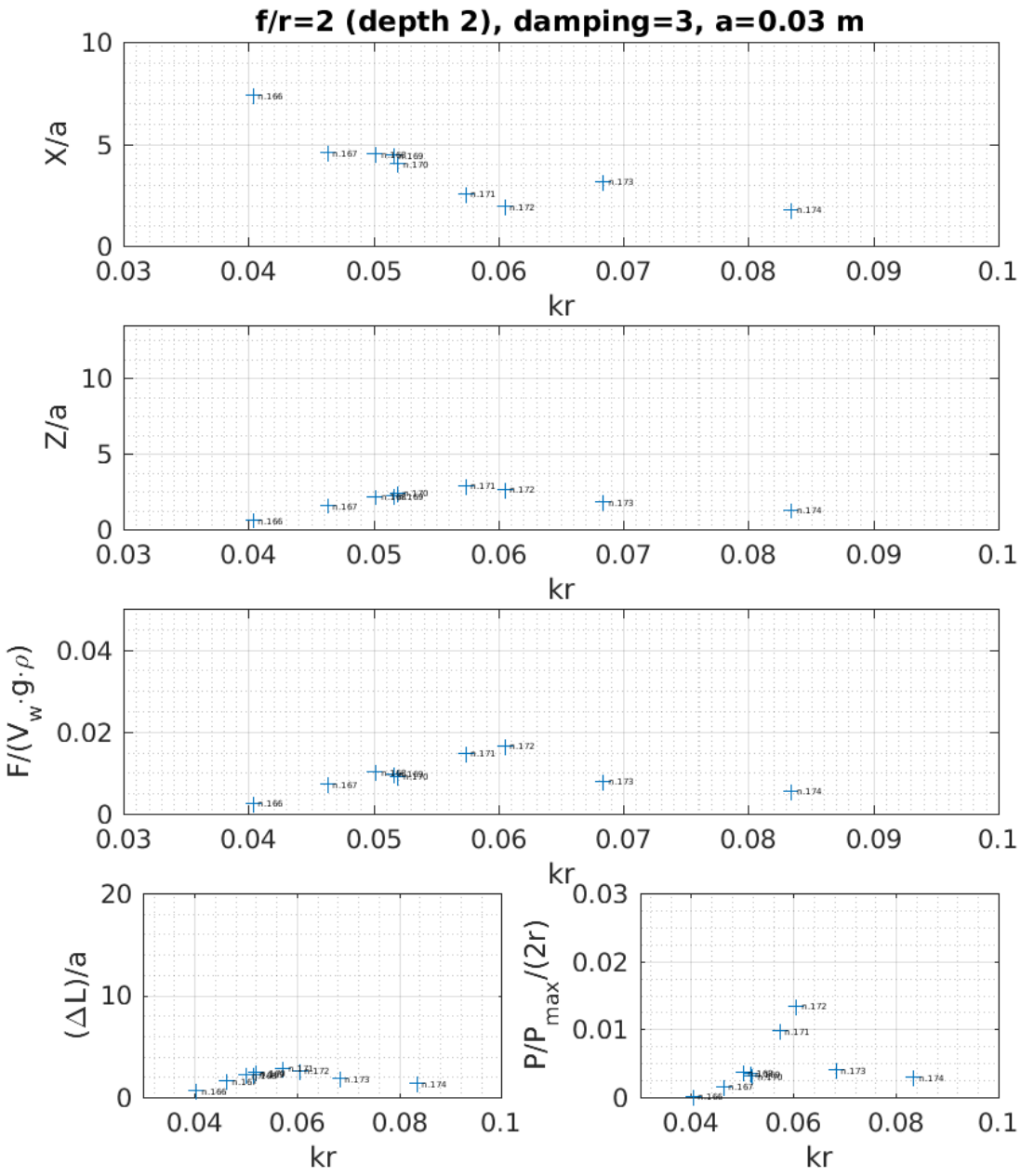

Figure 4.53: Experiments results related to the Damping n.3 at Depth n.2 of submerged spherical PA in regular waves of amplitude a=0.03 m.

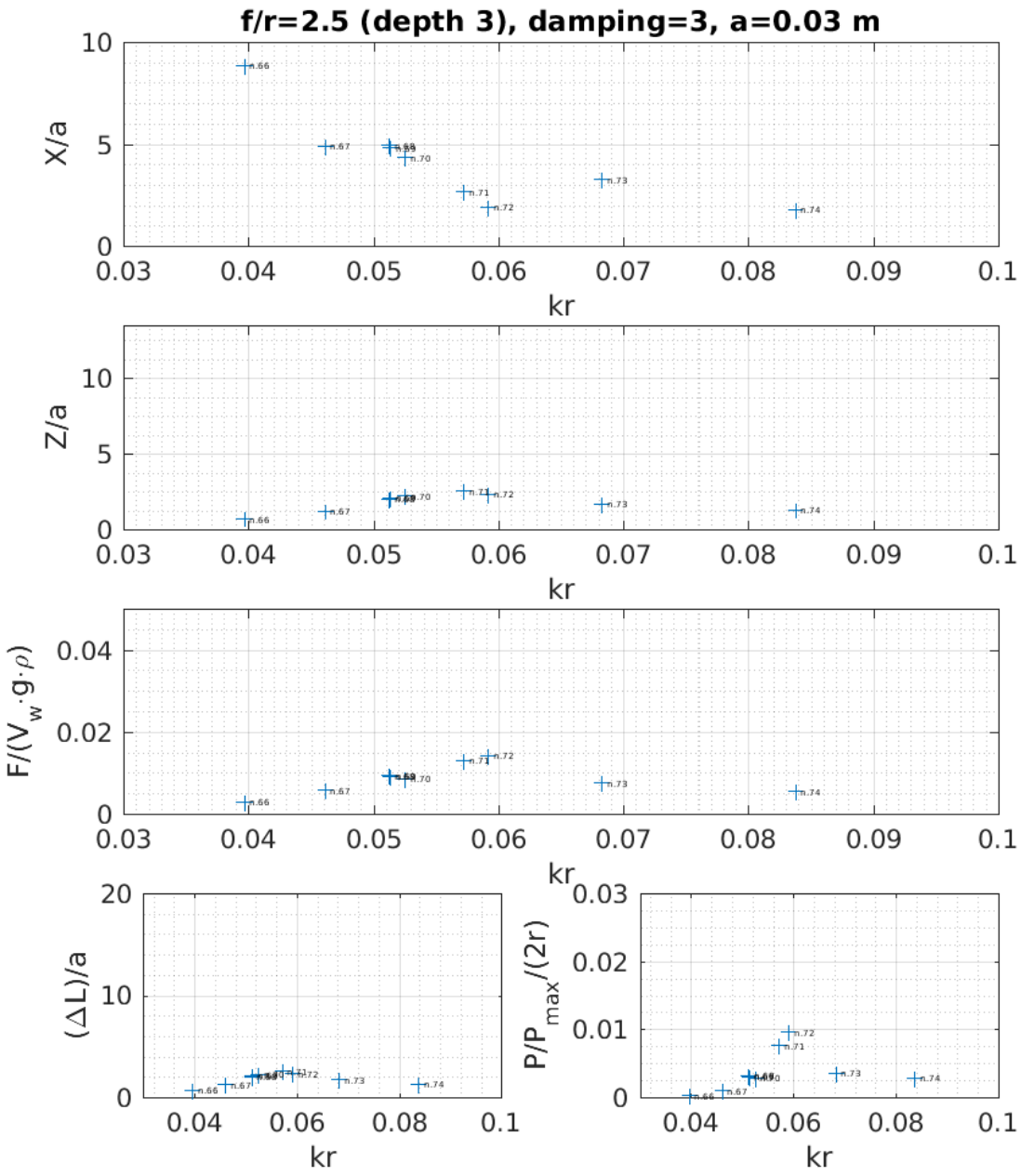

Figure 4.54: Experiments results related to the Damping n.3 at Depth n.3 of submerged spherical PA in regular waves of amplitude a=0.03 m.

At Immersion depth 2 the effect of damping is investigated. In Figures 4.55, no. 4.56 and

no. 4.57, respectively results for Damping 1, Damping 4 (Model 3b) and no servomotor (Model 3c) configurations are shown. In the first figure, it can be noticed that the heave RAO and ΔL^* peak frequencies are less than for configuration relative to Figure 4.53, where higher damping was simulated.

In Figure 4.55 the amplitude of F^* is higher compared with results relative to Figures 4.53 and Figure 4.56. This finding is due to the way the mooring load is recorded at the laboratory. In fact, as the load is measured after the effect of the PTO damping mechanism, the more damping is simulated, the less mooring load is measured at the load cell point. Despite this, for real devices, the mooring load amplitude should decrease when damping reduced as compliance would be increased.

As can be seen in Figure 4.56, when Damping 4 was implemented, compared to the other configurations, the heave RAO and efficiency factor are sensibly reduced.

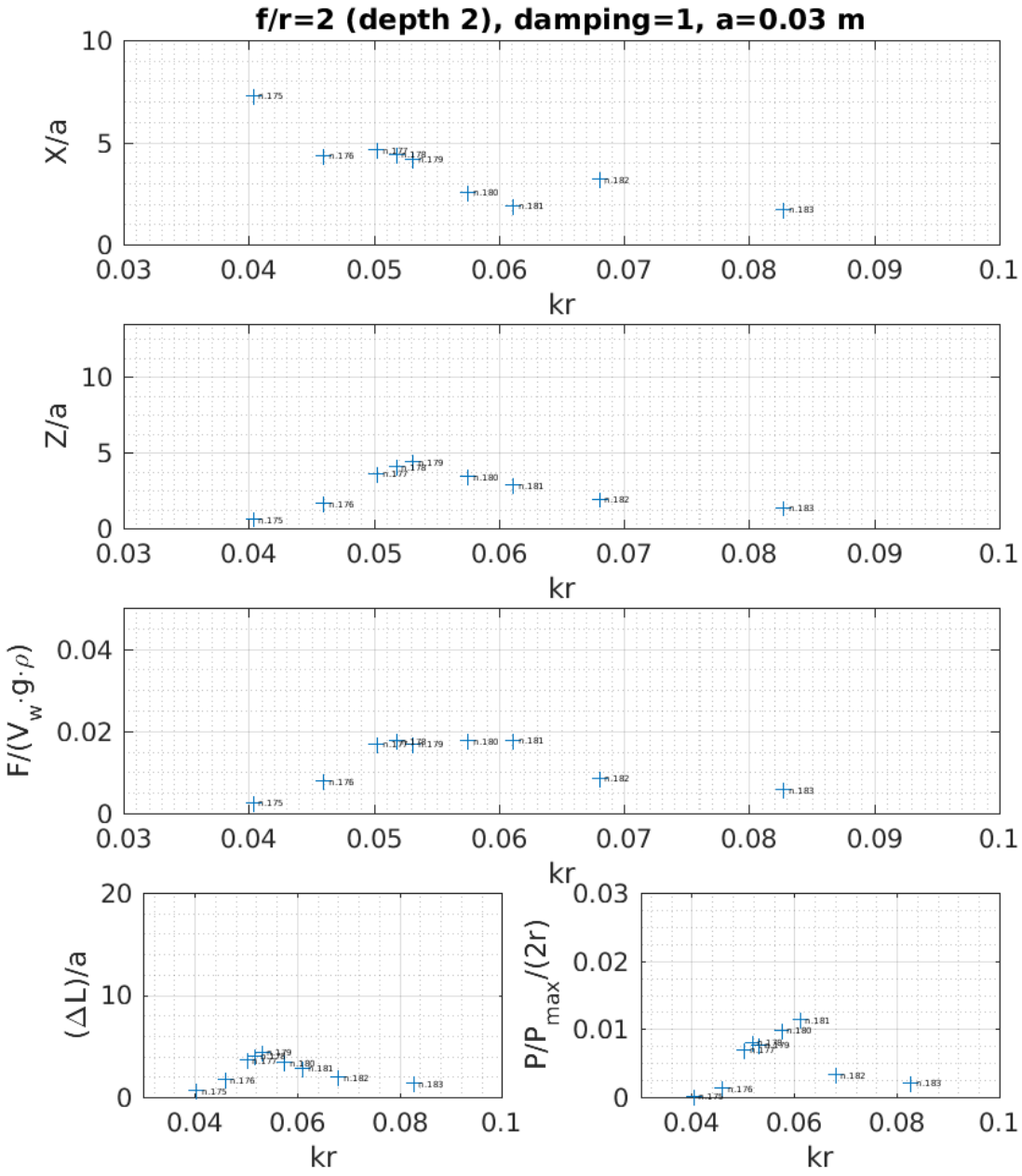

Figure 4.55: Experiments results related to the Damping n.1 at Depth n.2 of submerged spherical PA in regular waves of amplitude a=0.03 m.

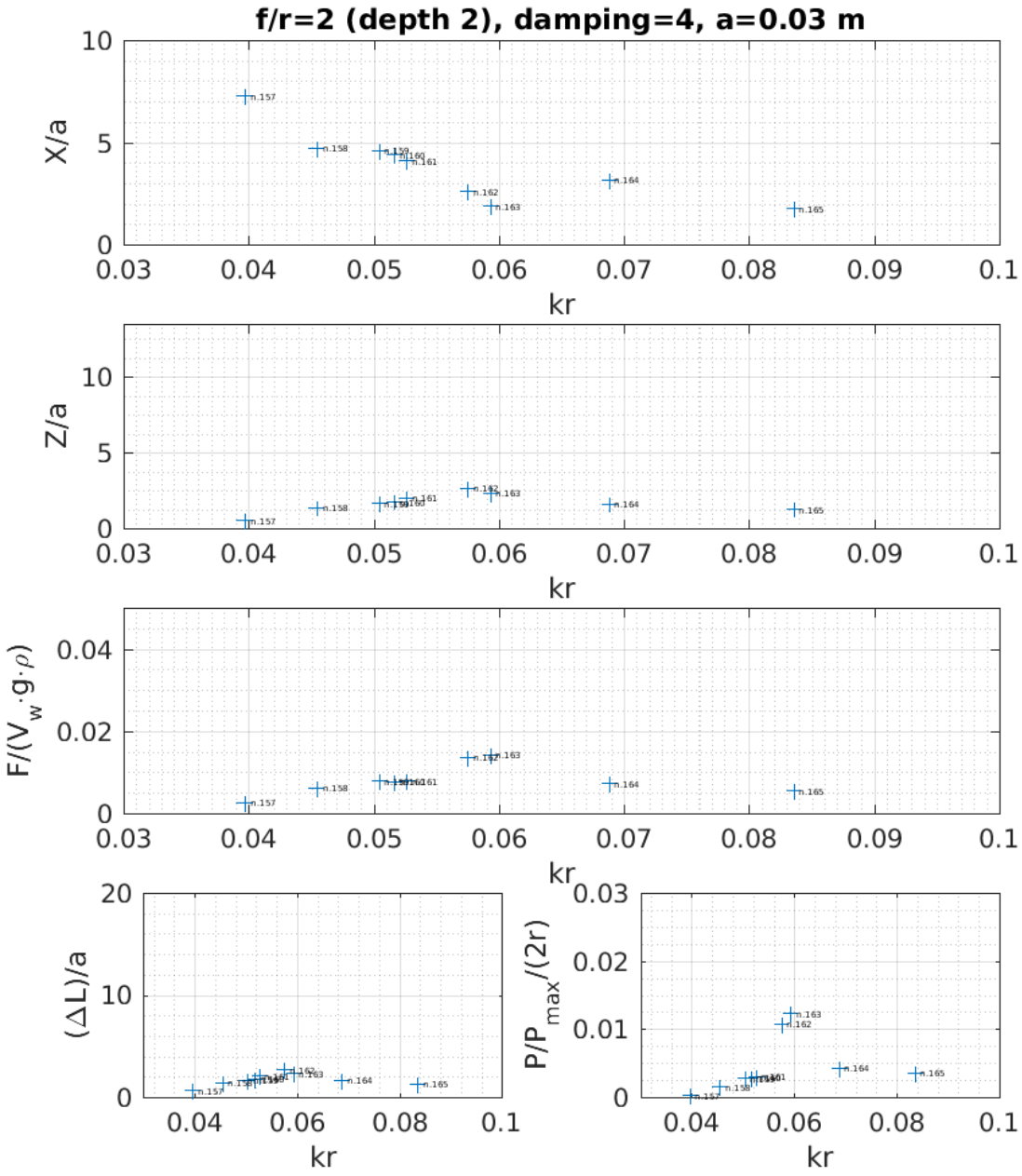

Figure 4.56: Experiments results related to the Damping n.4 at Depth n.2 of submerged spherical PA in regular waves of amplitude a=0.03 m.

Results of tests concerning the configuration without the servomotor (Model 3c) at

Immersion depth 2 are shown in Figure 4.57. Because the floater's motion was undamped, the heave amplitude for waves of $a = 0.03$ m resulted too large, causing the floater to go out of the water. Thus, for this model the wave amplitude a was reduced to $a = 0.015$m. For this configuration the peak frequency for all quantities is c.a. $kr = 0.055$, similar as for Damping 1 configuration (Figure 4.55). Despite this, the heave RAO and ΔL^* amplitudes at peak frequency are two times more for Model 3c (Figure 4.57), with respect to Damping 1 configuration of Model 3b. Considering that for tests relative to Figure 4.57 the wave amplitude was reduced by half, i.e. $a = 0.015$ m instead of $a = 0.03$ m, the F^* in the case of $a = 0.03$ m would had been almost doubled. This is supported by findings discussed when tests concerning Model 3a, represented in Figures 4.49 and 4.50, were compared.

To note that results relative to Figure 4.57 were obtained by using the configuration referred as Model 3c which to a certain extent was different than the configuration used for getting all other results reported in this section obtained with Model 3b.

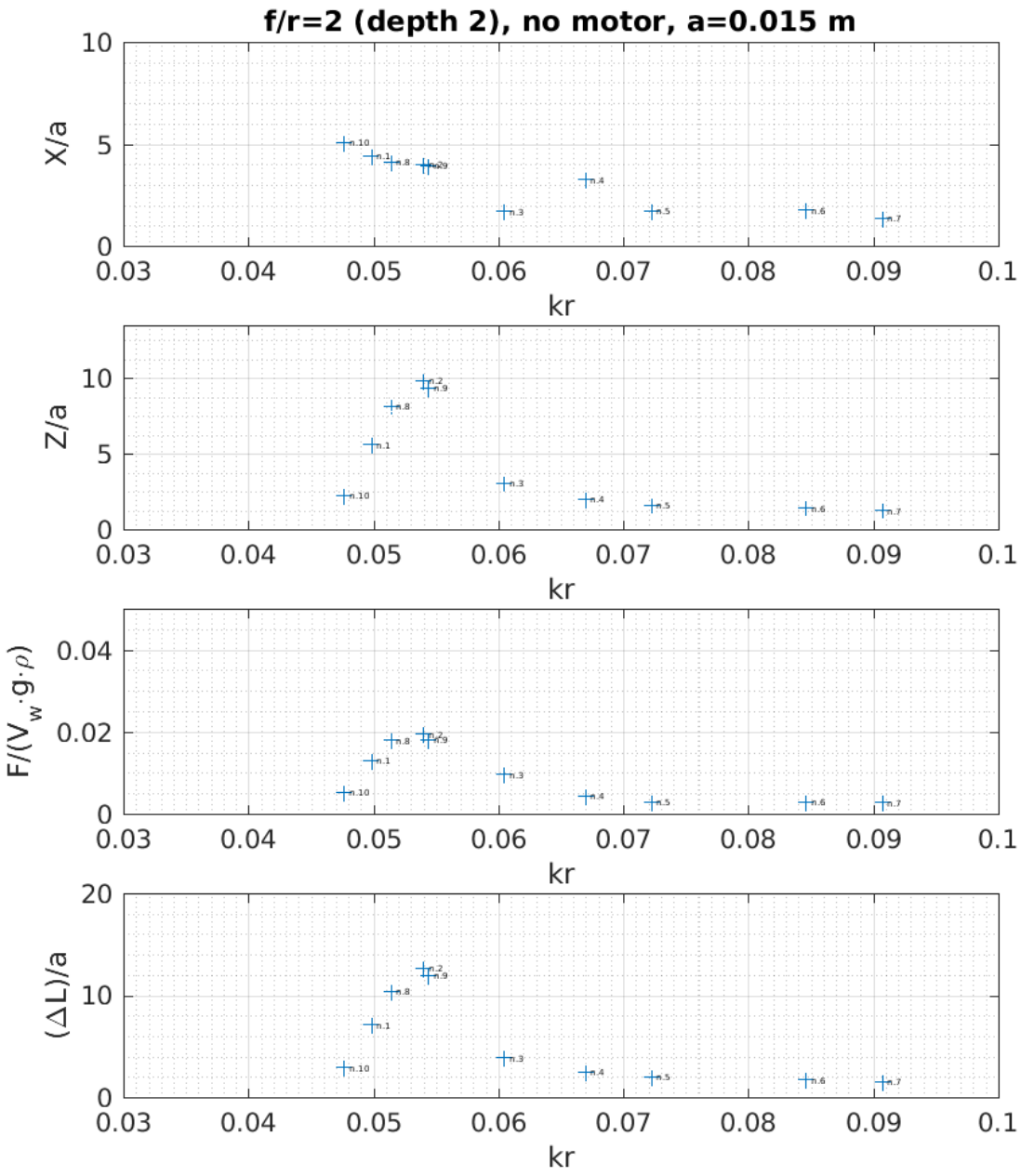

Figure 4.57: Experiments results related to submerged spherical PA in regular waves of amplitude a=0.015 m when the servomotor was removed (Model).

For the objectives of the experimental work, there was no need to report and discuss

further results concerning free oscillations and irregular sea tests for Session 3 in this section. These were illustrated already in Session 1 for Model 1. These results showed to be similar as for Session 1. However, some of the results concerning irregular sea and free oscillations of Session 3 are used for validation of the numerical code in Chapter 5. Thus further results of this session are presented in the mentioned chapter. Overall for this session of tests, the above-reported results showed to be qualitatively valid. In fact, all values correctly and sensibly varied when the wave amplitude, damping, or the Immersion depth were varied.

4.9 Limitations of experiments and general discussion

The most accurate experimental data was acquired during Session 3, where issues of Sessions 1 and 2 were resolved. In general, only a few tests run at 1:86 model-scale were accurate enough to be used for the validation of the numerical code. At 1:86 scale, due to an unexpected imperfection of the floater, and to the considerable damping uncertainty, various data of tests from Session 1 were uncertain. In particular, due to the small dimensions of the buoy, the extra mass added internally was not correctly aligned with the vertical direction, and not precisely located at the correct place. This issue determined that the floating sphere was slightly inclined, causing that, when the buoy was yawing, the sway offset reading was increasing towards either negatives or positives values. To overcome this drawback, only tests where little yaw and sway occurred were kept and used for validating the numerical code. Diversely, results of tests run at 1:33 scale during Sessions 2 and 3, given the dimensions of the models, were much more accurate.

There are a series of extra factors which were not entirely investigated. Reasons for this concern: avoiding over complications; impossibility of examining particular aspects; time limitations; effort to not affect experiments results with other sources of uncertainties.

The first main limitation concerns how to practically assemble the experiment set-ups and build the resulting manufactured model. For example, floaters' mass distribution was not exactly symmetrical, and the centre of mass was not exactly coinciding with the centre of the floater. As a consequence, models tested in labs were not only heaving and surging. A small motion was always occurring in also other four degrees of freedom, namely: sway, roll, pitch and yaw. This issue was a source of uncertainty. This limitation was due to the imperfection of the floater's mass distribution and because the mooring line was not attached at the centre of the buoy, as for theoretical PA device. Despite this, the uncertainty due to this issue was quantified, this was intrinsically included in the values of surge and heave motions' uncertainties reported in uncertainties tables of Section 4.7.

Due to manufacturing factors target models parameters were always not matching to the desired values. Despite this, thanks to measures after model fabrication, calibration procedures and uncertainty analysis, an understanding of these differences was to a certain extent acquired. Thus, the actual model measured parameters were then used for validation purposes. Meaning that numerical calculations were run by eventually correcting nominal system values by taking into account this apparent differences.

Other limiting factors concerned the viscous damping on the floater and viscous damping on the pulley. In fact, drag forces due to viscosity were neglected, the exact effect on these was not entirely assessed. Despite this, the following remarks need to be pointed out:

- The module of viscous forces acting on mooring line was roughly assessed (Section 4.5.3). As was found that from only surge motion no sensible power can be extracted from the device, it can be sustained that also no particular losses are induced by horizontal drag forces acting on the mooring line. No evidence was found that these type of forces acting on the mooring line would affect heave motion.
- For what concerns drag forces on the floater, these were roughly quantified in

Section 4.4 (Table 4.4). These forces are low, but in the case of experimental models, these may be significant. In fact, these were estimated to be about c.a. 1/5 of the mooring load for what concerns the undamped case ($C_{pto} = 0$). Despite this the estimation was made by using the highest possible relative velocity between an assumed stationary fluid and the oscillating body, in reality, this is not the case. Depending if the body is oscillating in phase with the fluid or out of phase, different results might occur.

Besides there are other limitations that have to be mentioned, during the study no particular attention was made for deeply investigate these: rigidity of mounting frames; rigidity of floater; effects of waves reflections on tanks walls and blockage effects.

Chapter 5

Verification and validation of the numerical code

The final aim of this chapter is to provide evidence to prove the validity of the numerical code introduced in Chapter 3. The overall validation process is a crucial fundamental step in the generic methodology proposed in the introduction of this thesis. For the specific device studied in previous chapters, the validation step is discussed here. In this validation process, it is also included a verification section as this share the same objective as the validation task itself.

This chapter is structured into two main sections. The first concerns the verification of the code without using empirical data. The second part regards the validation of the numerical results with the most reliable empirical obtained data.

5.1 Verification

The code is firstly verified by checking the hydrodynamic coefficients obtained with Nemoh and by comparing different options by which wave forces are calculated.

5.1.1 Calculation of hydrodynamic coefficents

As previously introduced in Chapter 3, with the aid of the Nemoh code, hydrodynamic coefficients are calculated. To check if these coefficients are correct, in this section results for both the hemisphere and the fully submerged sphere are compared with results obtained analytically by others.

Added mass and radiation damping coefficients of the hemisphere represented in Figure 3.3 of Section 3.3, were compared to analytical results reported by Hulme (1982) in Figures 5.1 and 5.2. Generally, except at particular irregular frequencies, the coefficients calculated with Nemoh are in good agreement with coefficients given by Hulme (1982). Hulme (1982) provides these coefficients for free-floating hemispheres oscillating in waves by performing an analytical study.

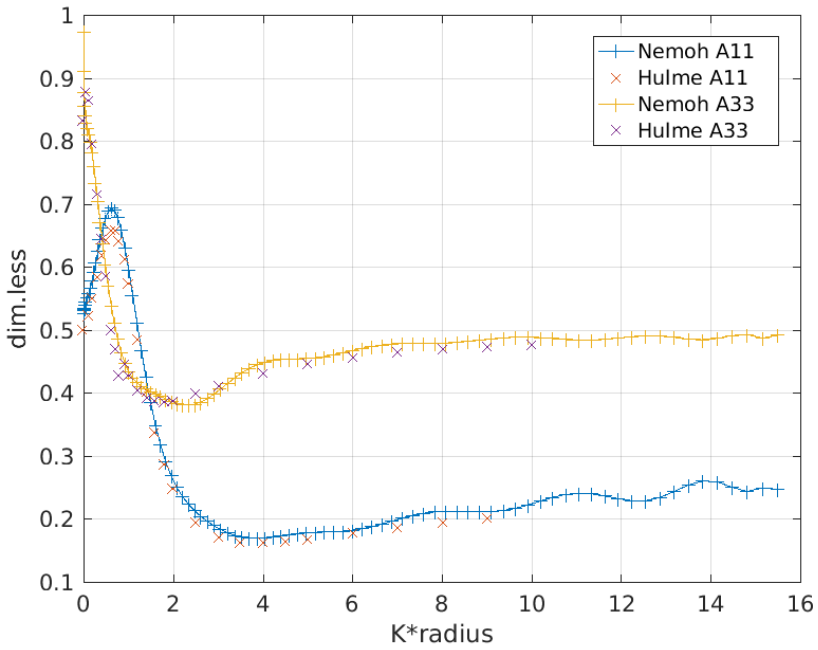

Figure 5.1: Added mass coefficients for the half immersed spherical (half-immersed) floater.

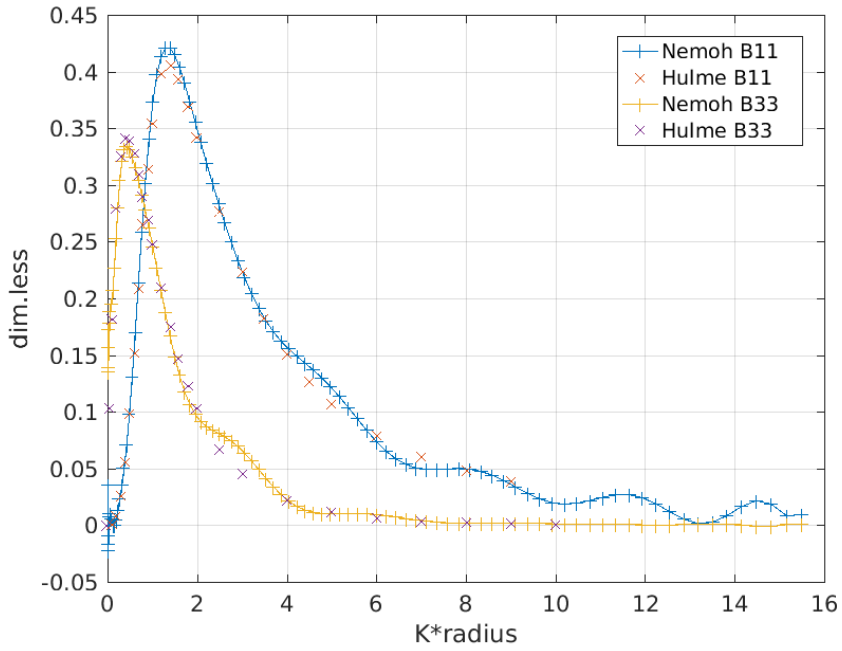

Figure 5.2: Radiation damping coefficients for half immersed spherical floater.

For the case of the fully submerged sphere, the results obtained with Nemoh were compared with values given by Wang (1986). For finding dimensionless values, corresponding to the case *(immersion depth) / (sphere radius) =1.5* as results presented by Wang (1986), a nominal immersion depth of 11.25 m was set, and the radius was set to be 7.5 m. Added mass coefficients, estimated with Nemoh, are just slightly larger than those obtained by Wang (1986) (as showed in Figure 5.3). Furthermore, radiation damping coefficients obtained with both the Nemoh code and with analytical methods, as shown in Figure 5.4, these are almost coinciding. Only the added mass coefficients computed by Nemoh are slightly larger. However, the maximum difference observed is c.a. 9%. Overall good matching is obtained.

Further results for another geometry are reported in Appendix A.2. This geometry concerns a caisson, results obtained with Nemoh are compared with results found in the literature. In this case, also wave forces and RAOs are compared. Even for this different geometry good agreements were observed, indicating that the Nemoh code is

robust. As a plus, it is showed that the way the Nemoh code was embedded in the Earth-reacting numerical tool is valid.

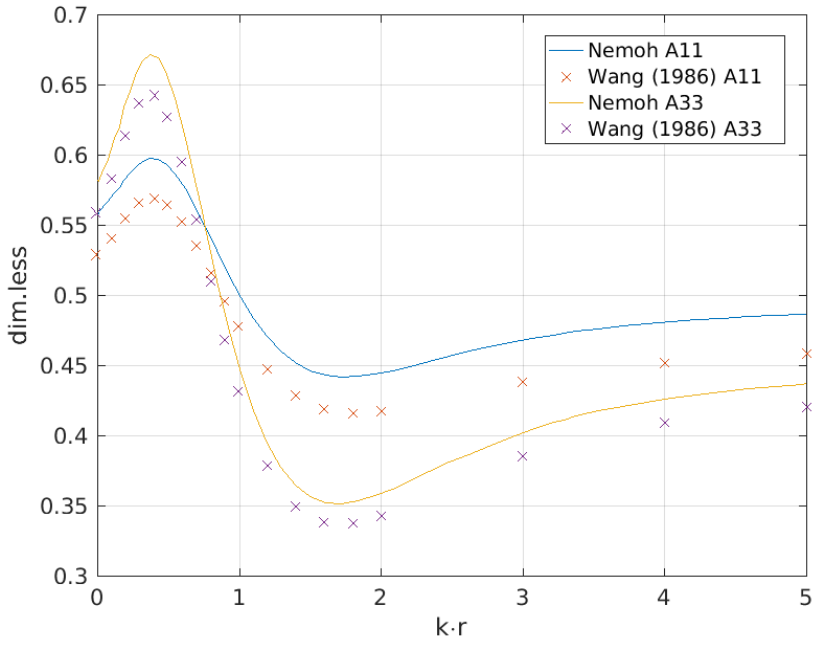

Figure 5.3: Added mass coefficients for sphere, submerged at depth/radius=1.5.

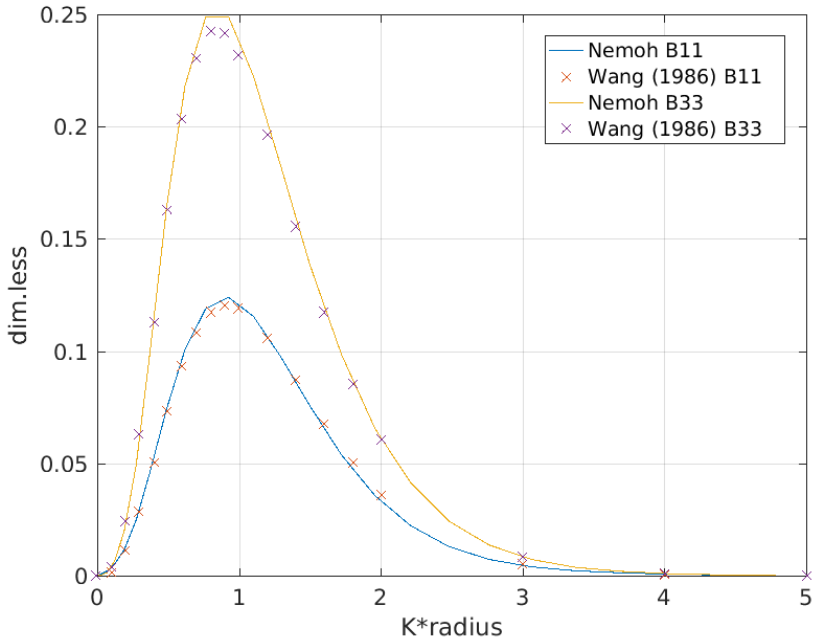

Figure 5.4: Radiation damping coefficients for sphere, submerged at depth/radius=1.5.

5.1.2 Verification of wave loading options

In Chapter 3 Section 3.6.1 it was explained how first order wave loads are modelled. For including these loads, two different options were established. The first was referred as *direct wave loading option* and the second as *impulse-response wave loading option*. To verify the second option, results of this option are compared with results given by the first option.

When convolution integrals are used (*impulse-response wave loading option* is on) in irregular sea numerical runs, the results of motion response are almost coinciding with results obtained with the *direct wave loading option*. Precisely, for the same free surface elevation signal $\eta(t)$, in Figure 5.5 is shown a direct comparison of two time series obtained with the two different mentioned options. For both, surge and heave displacements results obtained with the two options match. Thus, the validity of the *impulse-response wave loading option* was proved. To note that for this verification task, the wave drift forces are not included. To not include these it was necessary, as

for the *direct wave loading option* it is not possible to include wave drift forces. Thus also the numerical simulation run with the *impulse-response wave loading option* had to be set with no wave drift forces.

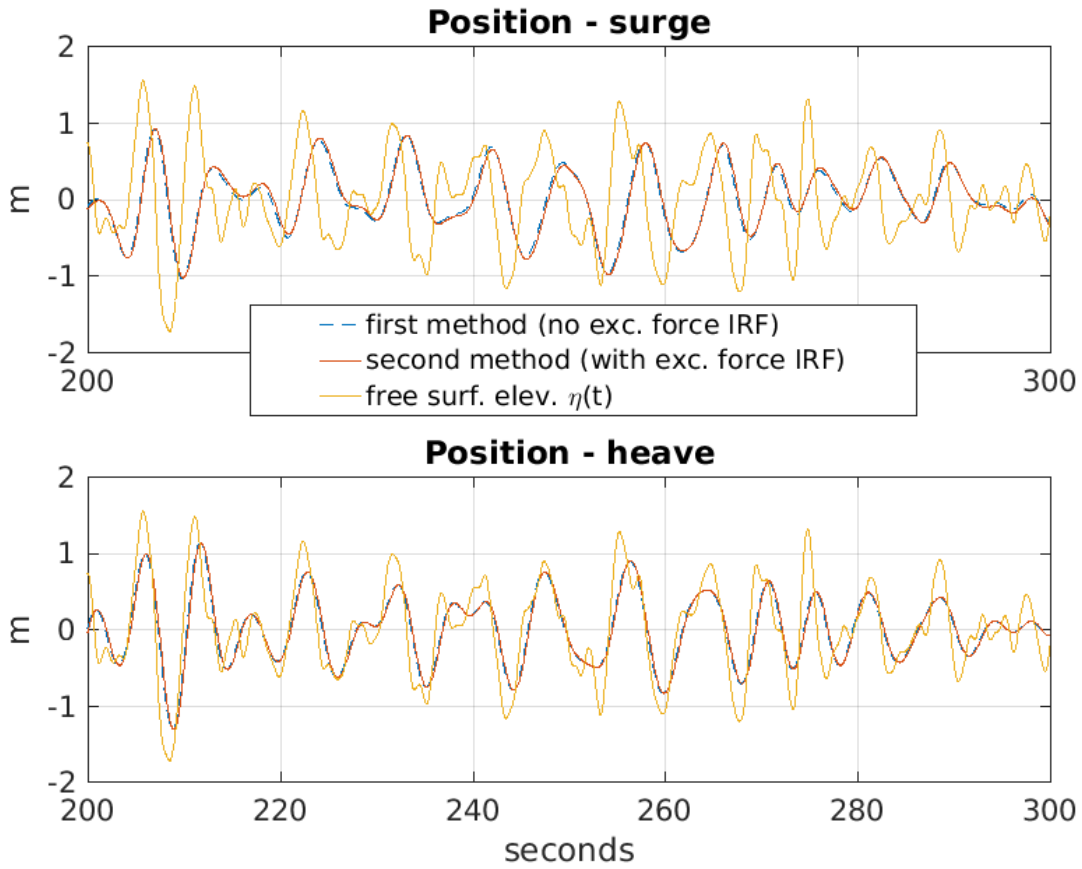

Figure 5.5: Comparison of prediction of system response in irregular sea with the two option for estimating time dependent wave loads.

5.2 Validation

The only verification step described in the previous section does not prove alone the validity of the numerical code developed. In fact, extended verification is not always possible. On the one hand, only few published results exist for the type of devices studied, on the side, not always there is a method to verify the code by its results, as

for the case of the wave loading options. A further step is required, this concerns the validation of numerical results with experimentally obtained measurements.

Through the comparison of numerical results with experimental measurements, the numerical tool proposed was validated. This was done in both, qualitative and quantitative ways. All numerical calculations used for validation were performed by setting real scaled laboratory models parameters as input in the code. Details of all models can be found in Chapter 4. For what concern regular waves tests, results are compared by plotting these against along frequency. Besides, these are converted into standard dimensionless form. In contrast, all other results concerning time series used for validation, for simplicity, are left with dimensions. The reason for this is that to make time series results dimensionless is a more complicated task. This task is less common; thus it was ignored. Real scale values are used when validating floater trajectories (one regular wave test), free decaying and irregular sea tests.

5.3 Regular waves tests

At first, the floater's trajectories and mooring load plotted against the surge position are compared. This comparison is shown in Figure 5.6. This figure gives an overview on how in general the heave, surge and mooring load is estimated by numerical calculations and by experiments. Plots of Figure 5.6 represent a real scaled regular sea test. Results reported are of numerical simulation and laboratory tests, these are representative of regular waves defined by *10 s* period and *1 m* amplitude (real scaled values). Obviously, in laboratories small waves were simulated, successively, through Froude scaling laws, results were scaled. Experimental results are relative, for Session 1, (1:86 scale experiments) of Test no.63 and for Session 3 (1:33 scale experiments), of Test no.49. The nominal system parameters were those reported in Table 3.1 on Chapter 3. Details of experimental models, instead, are reported in Chapter 4. In this figure in the first column are shown the floater's trajectories. While the vertical axis represents heave displacement, the horizontal axis represents the surge displacement.

It can be observed that the time domain (TD) calculations qualitatively correctly predict the drift towards the positive X-axis. This remark is justified as the drift is also observed in both experiments results. This drift is due to wave drift forces. To justify this finding a similar figure, where drift forces are not included in the TD calculations, is reported in Appendix A.2. In fact, for the latter figure in TD calculations drift is not observed. In the second column are shown the patterns of the mooring load plotted against the surge displacements. It is observed that for the TD calculations (first row) and 1:33 experiments (third row) the mooring load trajectories are more stable with respect to 1:86 test results. Overall it is further observed that the range of numerical predictions of both, floater trajectories and mooring load with respect to surge, in all cases cover the experimental results. This observation, at least, is valid for the regular waves considered. As a consequence for this case, the code appears to be valid, and this showed to not underestimating the quantities assessed.

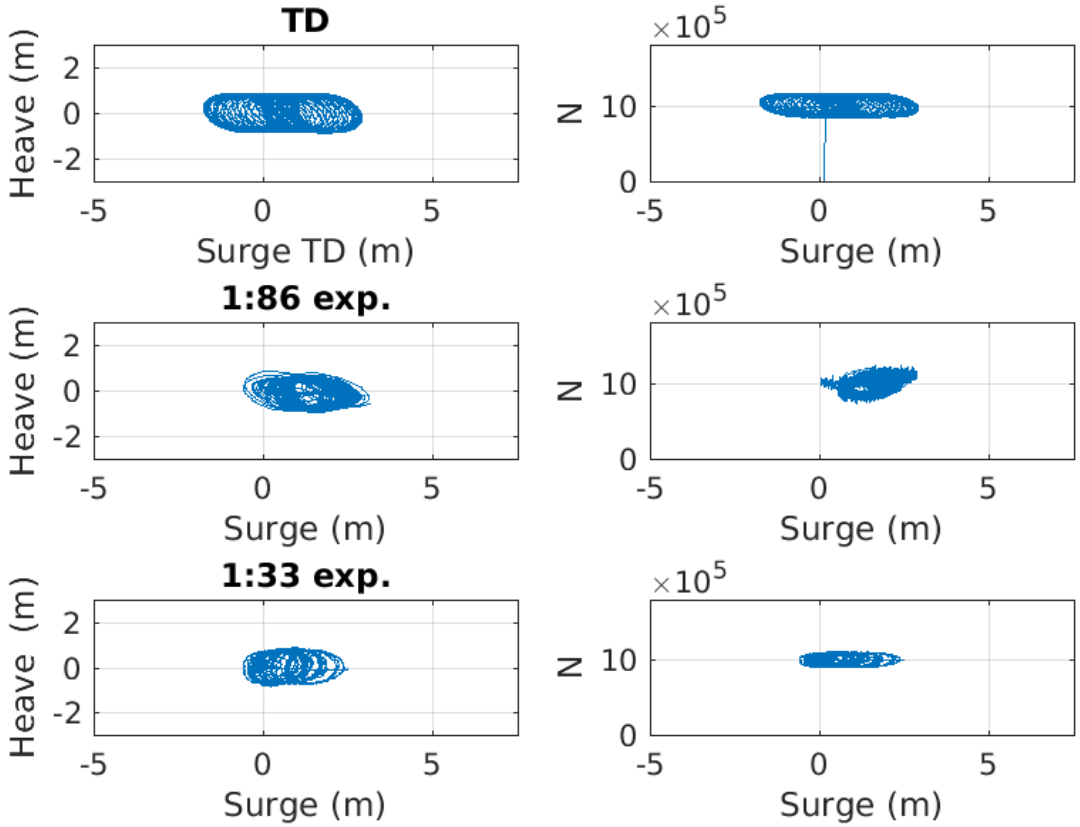

Figure 5.6: Comparison of time-domain calculations with experimental results at 1:33 and 1:86 model-scales. On left-hand side, the floater trajectories are shown. On right-hand side figures, the mooring loads (at load cell point) according to the surge position are shown. The above concerns . For obtaining the TD results a ramping period of *20 s* was set.

Results of each regular wave test were then compared to simulation results.

To summarise the validation of the regular sea tests graphically, each test result is represented by a point. All results, in this case, are presented in the dimensionless form and plotted against the dimensionless wave number kr defined by the wave number k and the floater radius r. The main reason for this is that results in this form may be quickly taken for comparison by others whom for example perform experiments with a spherical floater of different radius and use a different model scale.

For what concern the half-immersed floater models, a comparison of RAOs between those obtained by numerical calculations and those related to empirical tests is reported in Figure 5.7. In this figure as for Figure 5.8 four entities are compared. These are TD, frequency-domain (FD) numerical results and empirical results obtained by the three sessions of experiments, i.e. one session with 1:86 model-scale and two more sessions with 1:33 model-scale.

In general, time-domain and frequency-domain calculations predict well the 1:33 model-scale experimental measurements.

Due to higher uncertainties (details reported in Chapter 4) for what concern mooring displacements results of Session 1 are not compared. Besides, when comparing the mooring load and the power, only results of Session 3 are kept. These comparisons are shown in Figures 5.8 and 5.9.

Together with RAOs curves, the mooring line displacement, the mooring load, and the power factor are predicted with reasonable accuracy by the numerical code.

From Figure 5.7 to A.12 the experimental derived values are compared to the numerical predictions.

The numerical code resulted in being valid also for what concerns the submerged case studied. In fact, numerical results even in these case are relatively close to empirically estimated quantities.

In almost all cases offsets between empirical and numerical results are contained between ranges defined by experiments uncertainties in the form of percentage errors, this lasts reported in Chapter 4 Section 4.7.1. This observation means that, by taking into account experiments uncertainties, the numerical predictions are within empirically justified valid ranges.

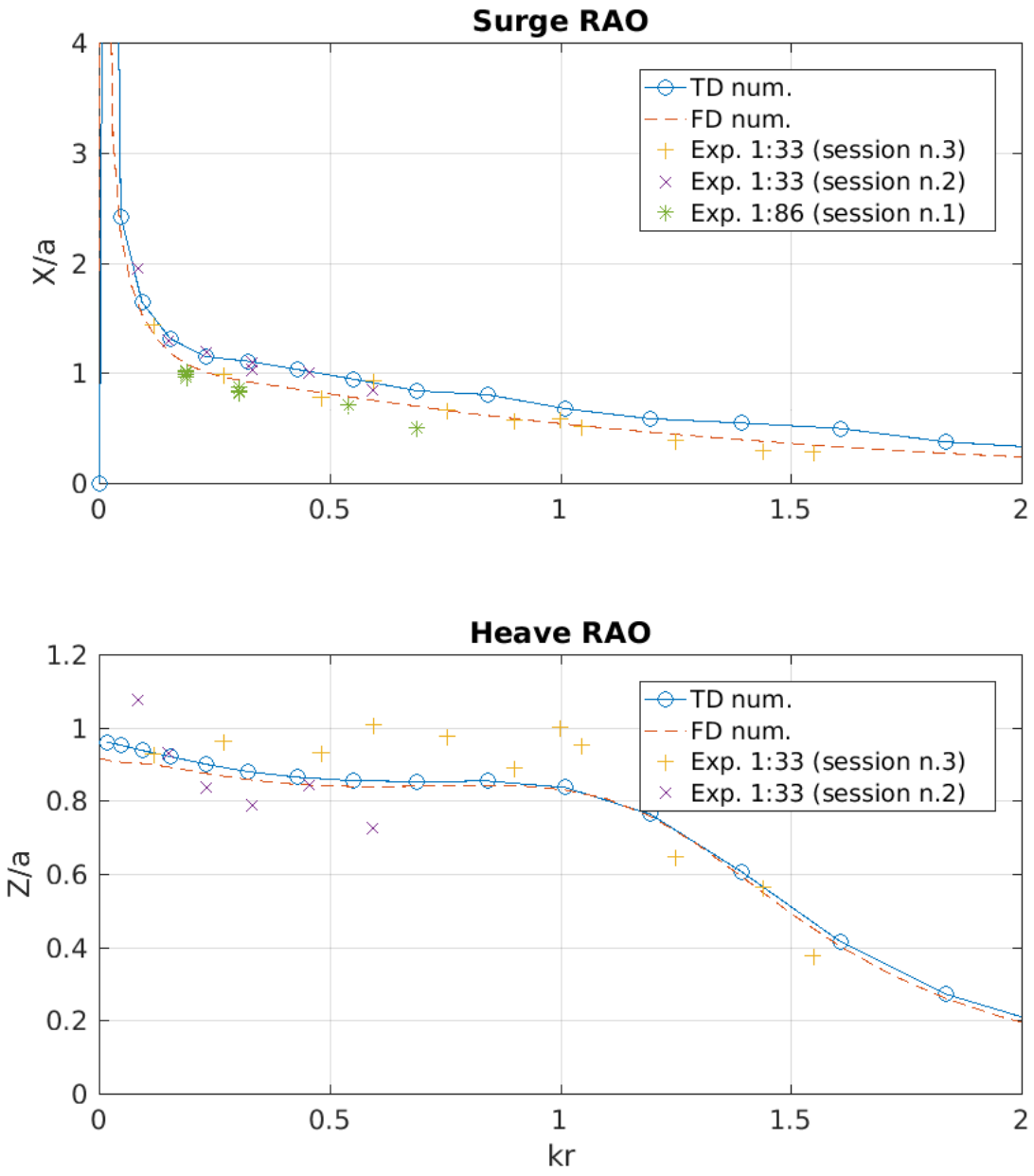

Figure 5.7: RAOs obtained with different methods: TD and FD calculations; experimental results. System parameters are always same as specified in Table 3.1.

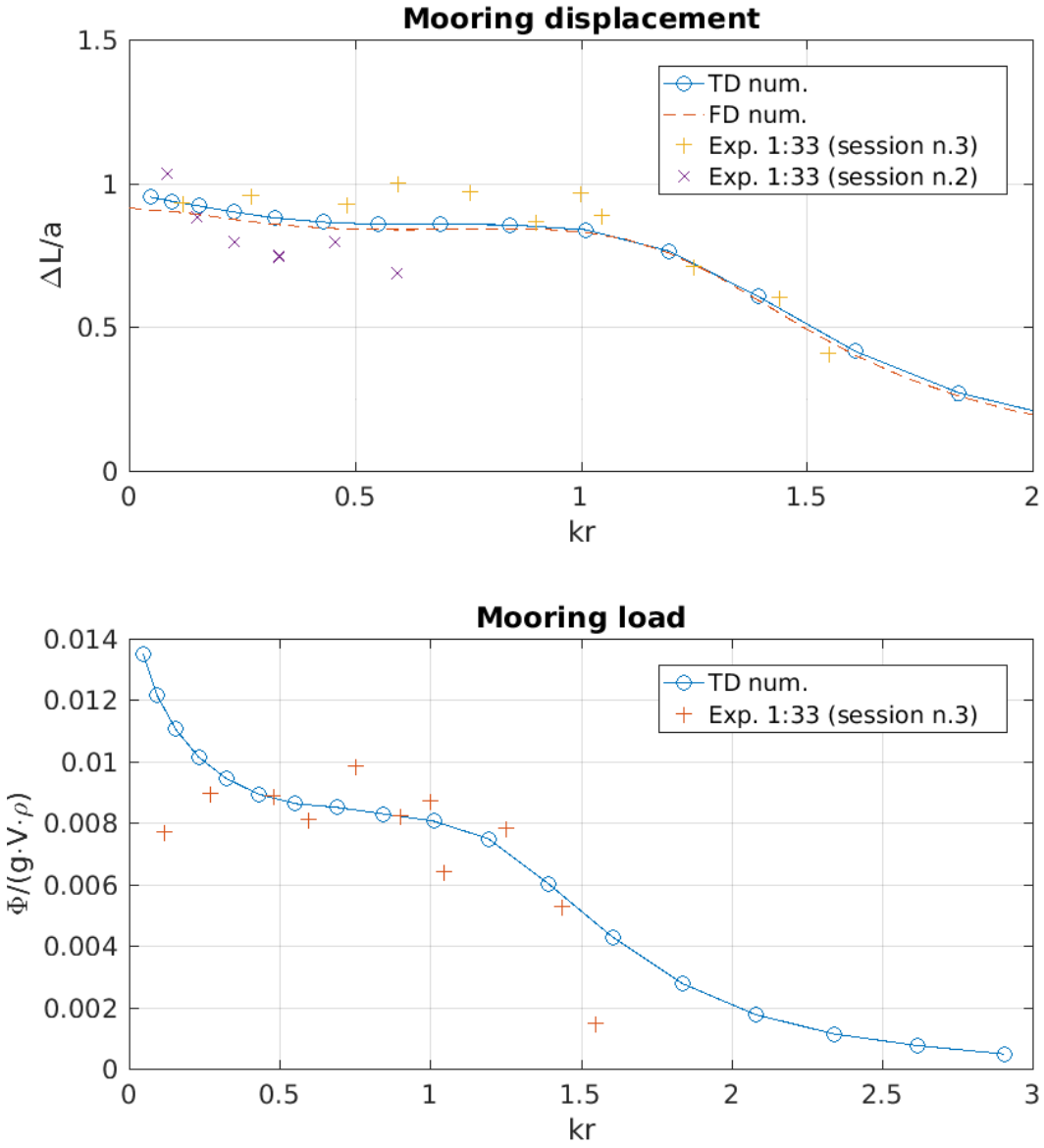

Figure 5.8: Comparison of mooring displacement and mooring force (at load cell), between numerical code and experiments.

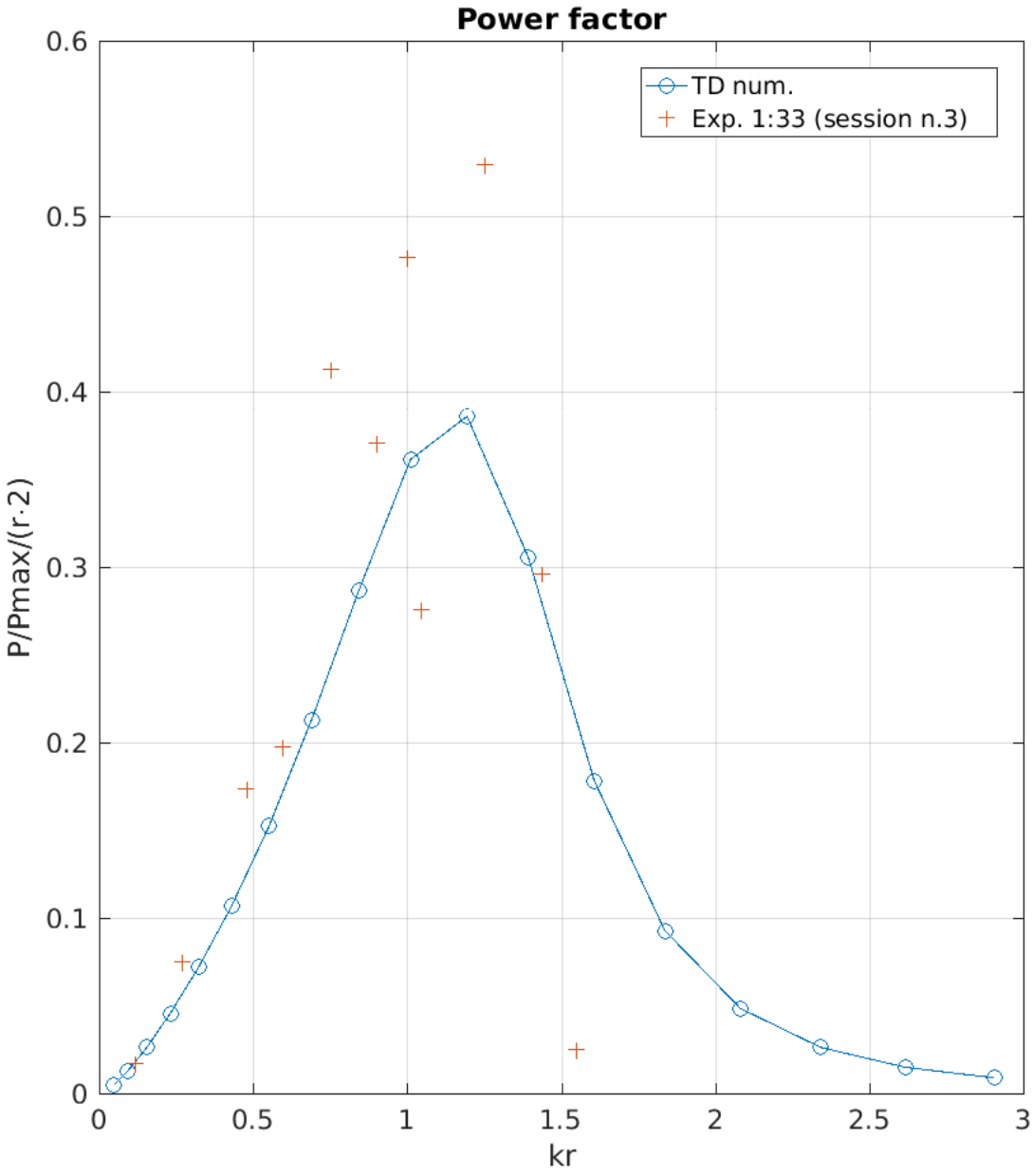

Figure 5.9: Estimated power factor from experimental data and from the numerical code.

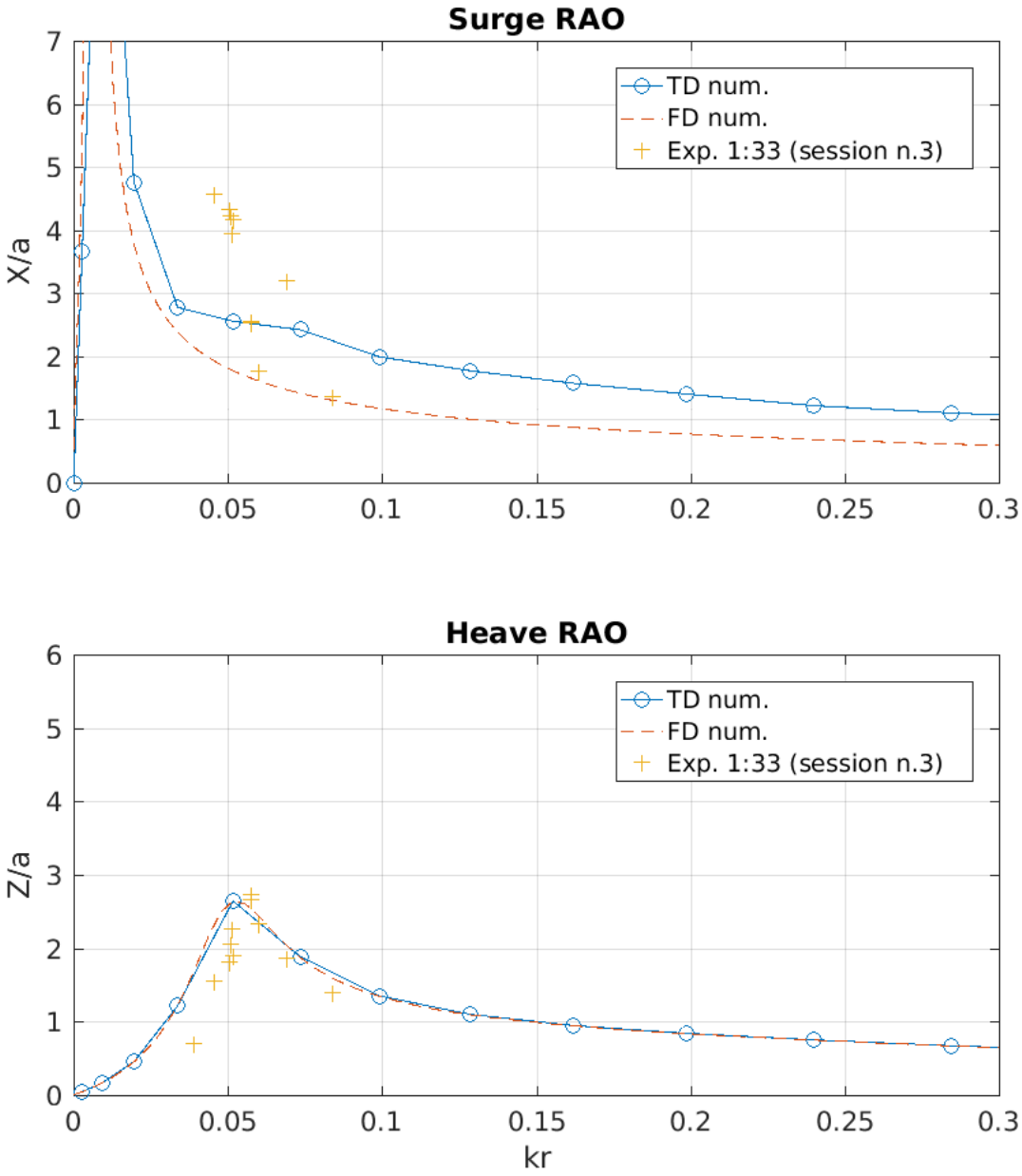

Figure 5.10: Comparison between RAOs obtained with TD and FD calculations with experimental derived quantities for the submerged model tests. The depth for these tests was set to *f/r=1.5* (Depth n.1) and the damping value corresponded to the value referred as *Damping n.4* (refer to Section 4.8.3).

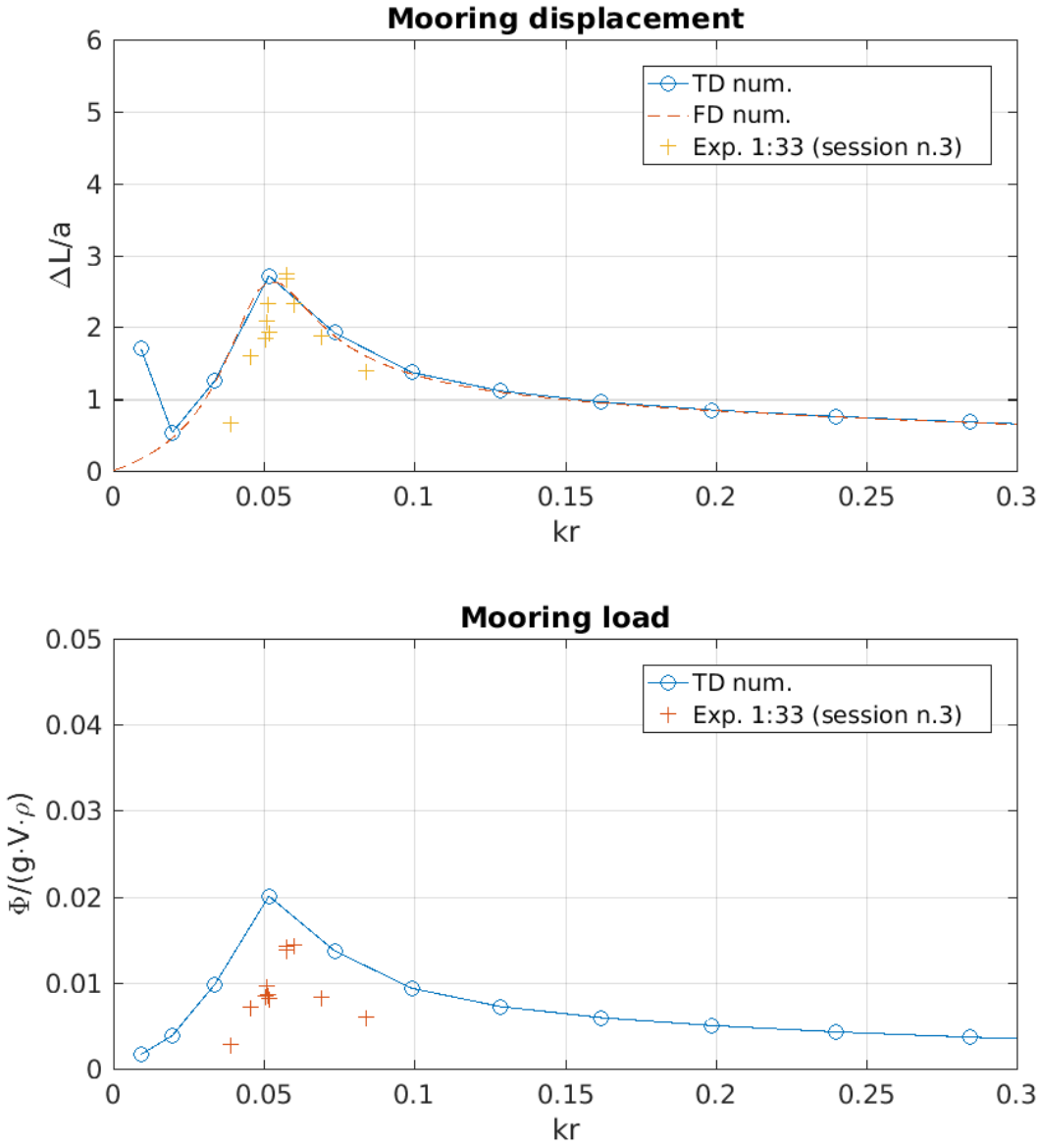

Figure 5.11: Comparison of mooring displacement and mooring force (at load cell). The depth for this set of tests was set to *f/r=1.5* (Depth n.1) and the damping value corresponded to the value referred as *Damping n.4* (refer to Section 4.8.3).

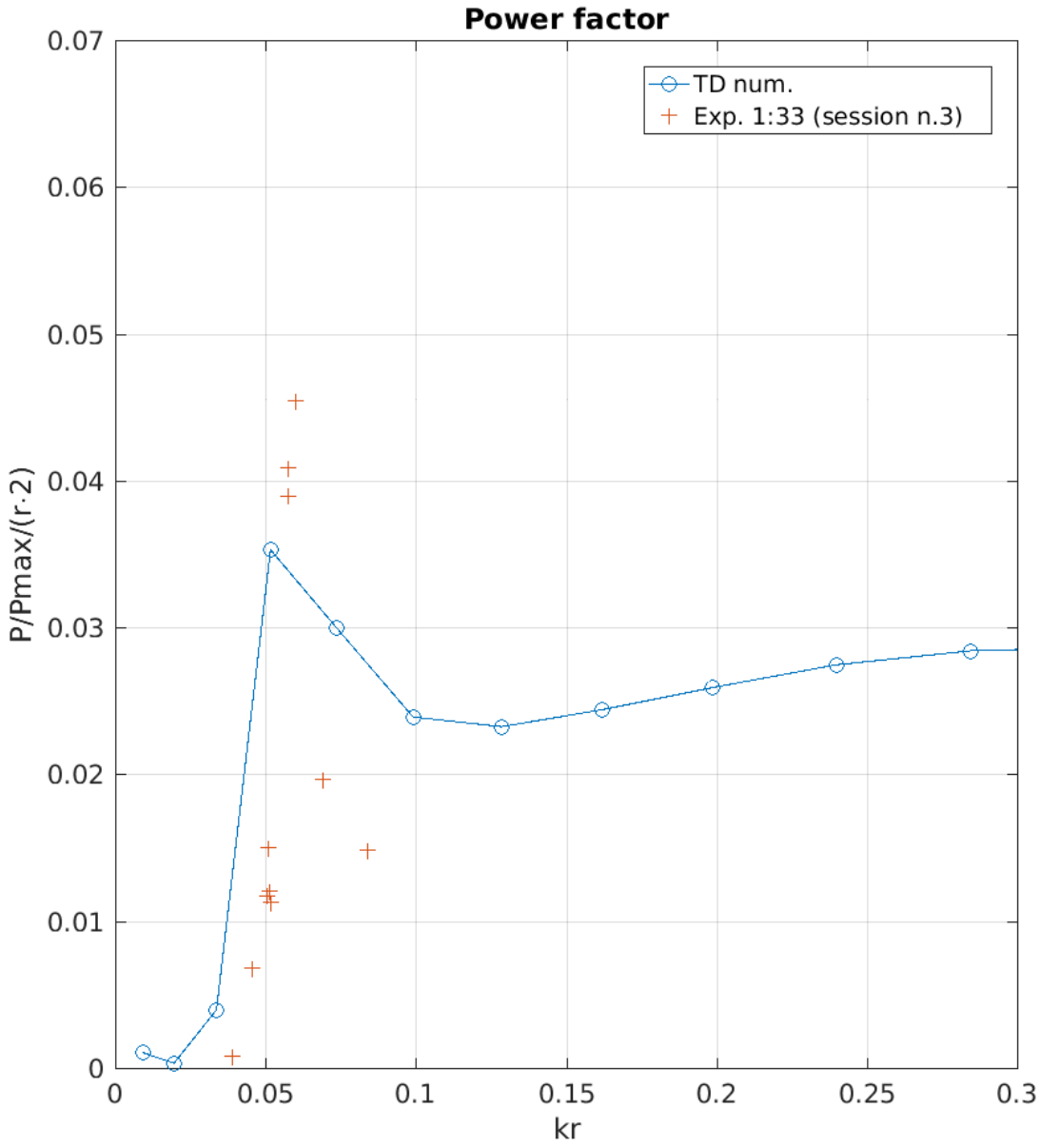

Figure 5.12: Estimated power factor values derived from experimental data and the one obtained by the numerical code. The depth for these tests was set to *f/r=1.5* (Depth n.1) and the damping value corresponded to the value referred as *Damping n.4* (refer to Section 4.8.3).

5.4 Free decaying tests

Free decaying oscillations tests run at both scales are compared with time-domain results. For this reason, all experimental readings are scaled to real-scale quantities. Froude scaling laws introduced in Chapter 2 (Subsec. 2.3.5) were implemented.

In Figures 5.13 and 5.14 are shown respectively surge and heave free decaying tests. For making this figures horizontal and vertical offsets were corrected.

The time series relative to both tests obtained during experiments do not differ much with the predicted surge response. To note that the 1:86 free decaying test result is more precise than the 1:33 test. This finding is due to practical reasons. While at the larger tank (Kelvin Hydrodynamic Laboratory) the floater was manually released, in the small tank (Henry Dyer facility) free oscillation tests were performed by cutting a rope which held the floater at the initial offset. Therefore for the 1:33 scale test the surge motion is a little more irregular, and for a small interval the motion was lost from the capturing system (as indicated by the horizontal segment at about t=170 s). Overall for the first three oscillations the numerical and 1:86 test amplitudes are almost matching. The frequency of oscillations is nearly the same for all the three entities.

In Figure 5.14 the predicted heave motion during free decay is compared to only the experimental data of Session 3. This fact was due that in Session 3 uncertainties concerning the implemented damping, in general, were the lowest. Free decay tests during Sessions 1 and 2 showed to be shorter than what had to be, thus are not reported here. The floater motion was more dampened for obvious reasons. Uncertainties related to system damping are discussed in Section 4.7. For the comparison with results of 1:33 scale reported in the mentioned figure, it is observed good matching between numerical and experimental time series. The free decay test illustrated here was run with a damping coefficient estimated to be C_{pto} equal to the half of the *nominal damping value*. In real scale C_{pto} was equal to $1.25 \cdot 10^5$ Ns/m. This value for C_{pto} was also applied in numerical calculations.

Both, numerical and experimental (concerning Models no.1, no.2 and no.3a) obtained natural frequencies, converted to real-scale quantities, are almost the same. Besides, these match well the values provided numerically by Vicente, Falcão, and Justino (2013), i.e. ca. 0.02 Hz for surge and c.a. 0.28 Hz for heave.

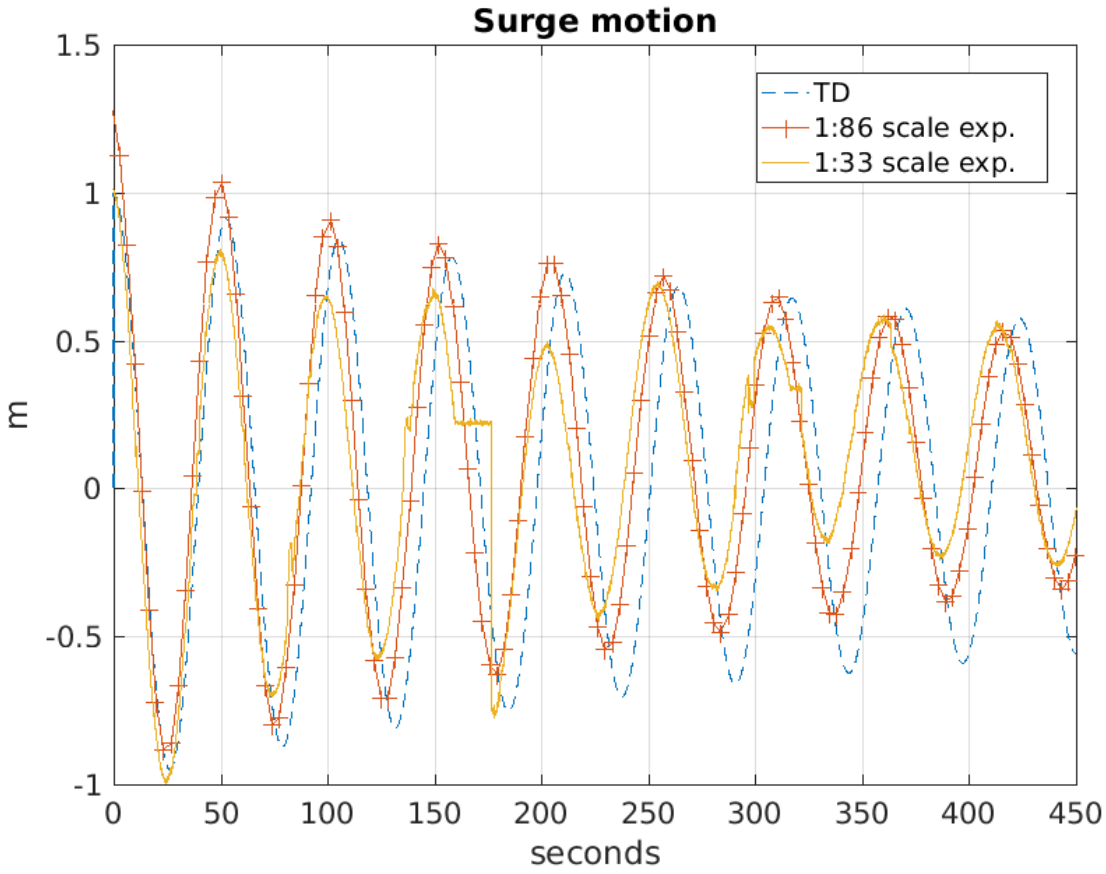

Figure 5.13: Comparison of surge free oscillations (real scaled values) from X(0) = 1 m.

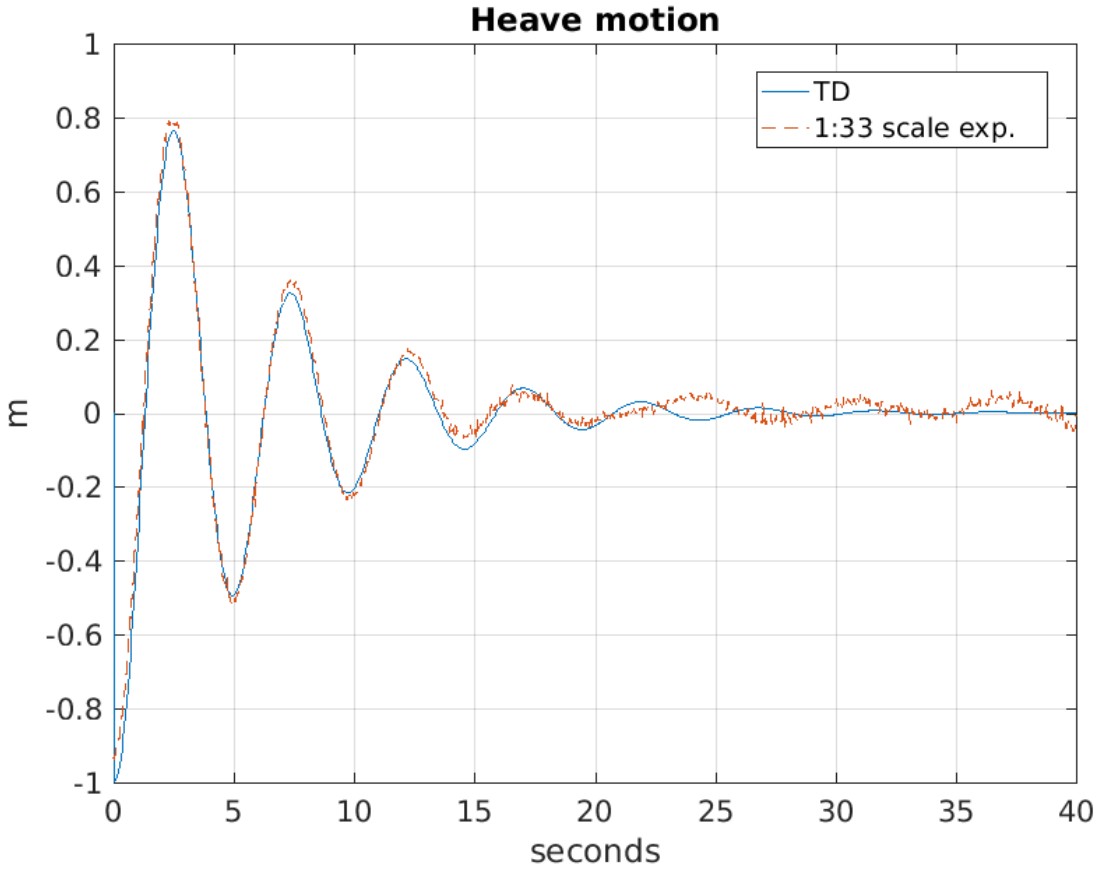

Figure 5.14: Comparison between numerical prediction and experimental measurement of heave motion during free oscillations (real scaled values) from Z(0) = -1 m.

5.5 Irregular sea

Successively, the numerical code was benchmarked by comparing its predictions to the experimentally derived quantities obtained during the irregular sea states laboratory tests of only Session 3. For this reason, specific free surface signals, extracted from experimental tests were used for running time-domain simulations. For this purpose, the *impulse-response wave loading option* was used. As for the case of free decaying tests, empirical measurements were scaled to real-scale quantities. Froude scaling laws were also used in this case.

For illustration results of Test n.109 are compared with numerical results. Initially wave drift forces in the numerical simulation were set to nil, from Figures 5.15 to 5.17 the time series of surge, heave, and mooring loads are compared to quantities obtained empirically.

When drift forces are set to nil (Figures 5.15 to 5.17), for what concerns the surge motion in irregular sea, it is observed that the predicted surge (TD) does not match well the actual measured motion. However, the predicted surge follows a similar pattern and match the same phase of the high frequency of oscillation. Differently, the heave motion is well predicted by the numerical tool also when the drift forces are not included. Good agreement between numerical prediction and experimental values, even for what concerns the mooring load occurred. For this latter quantity, the patterns match well. The model slightly underestimates only the oscillation amplitude at specific peaks.

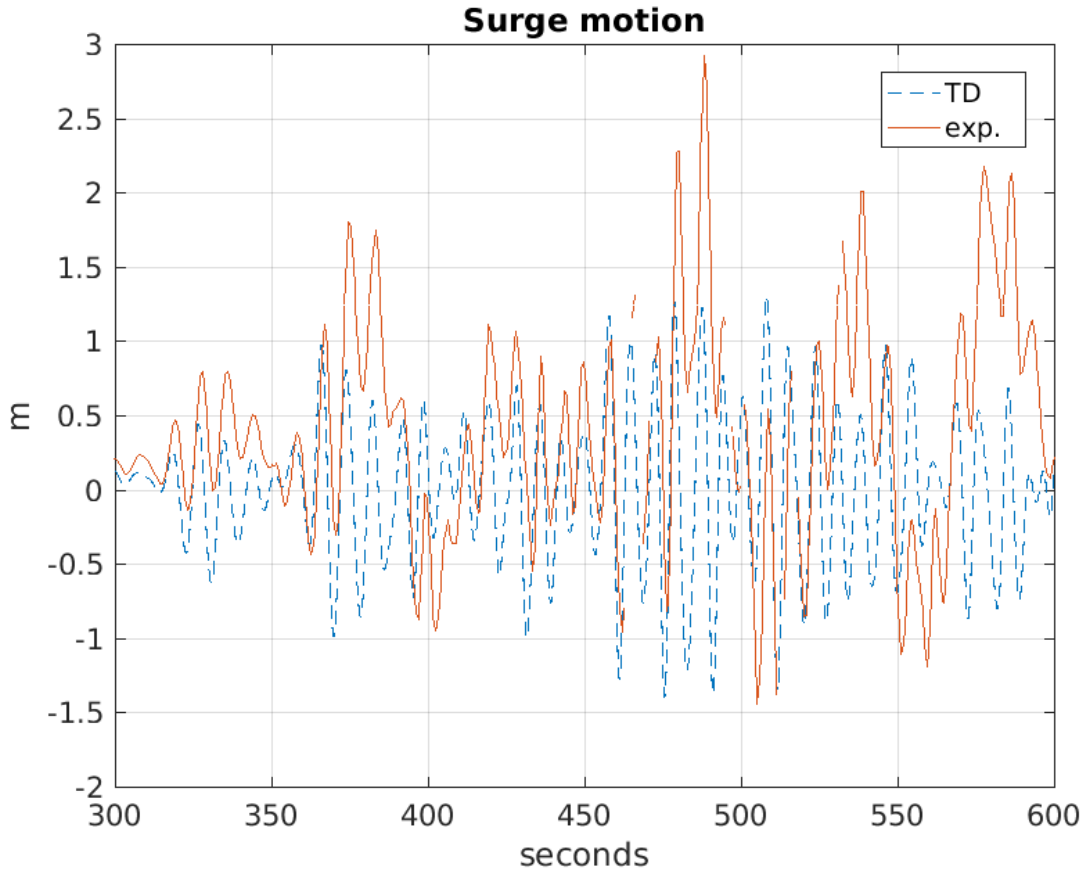

Figure 5.15: Comparison between time-domain predicted surge motion and measured surge motion in irregular sea. The same free surface elevation signal $\eta(t)$ was used in the time-domain simulation.

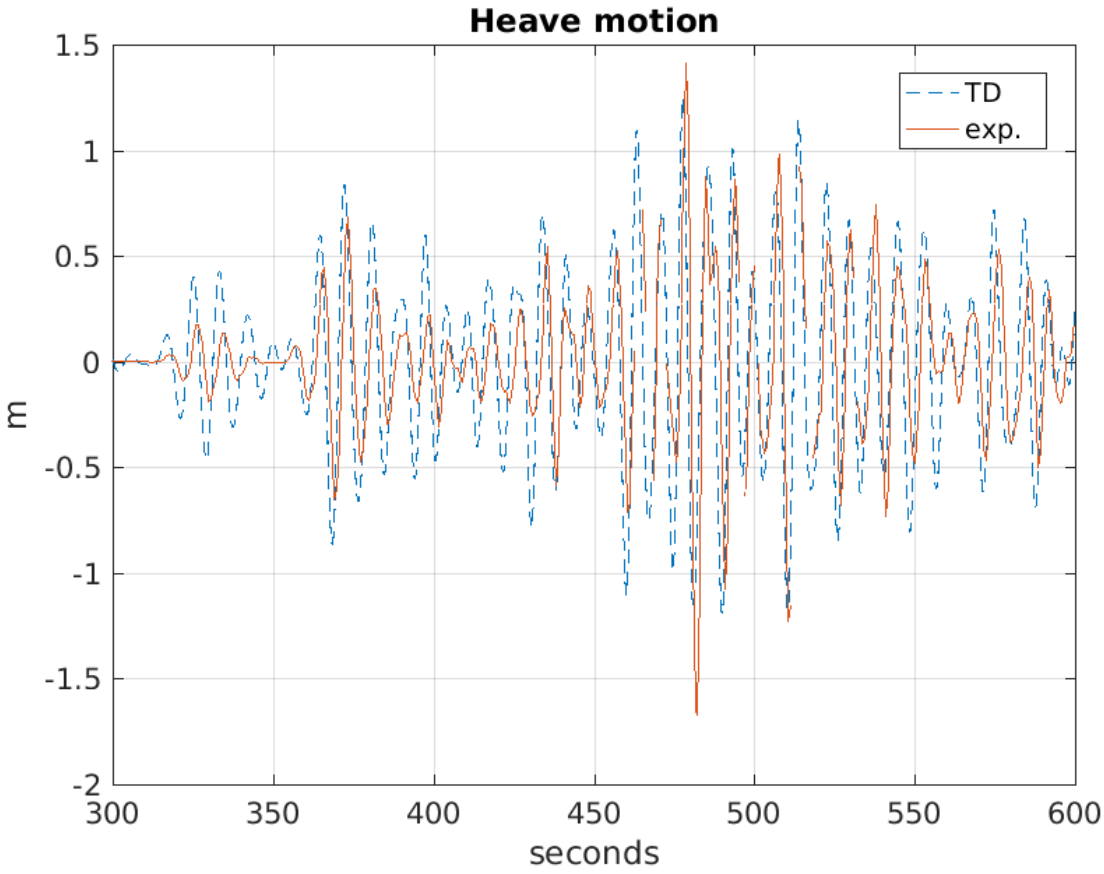

Figure 5.16: Comparison between time-domain predicted heave motion and measured heave motion in irregular sea. The same free surface elevation signal $\eta(t)$ was used in the time-domain simulation.

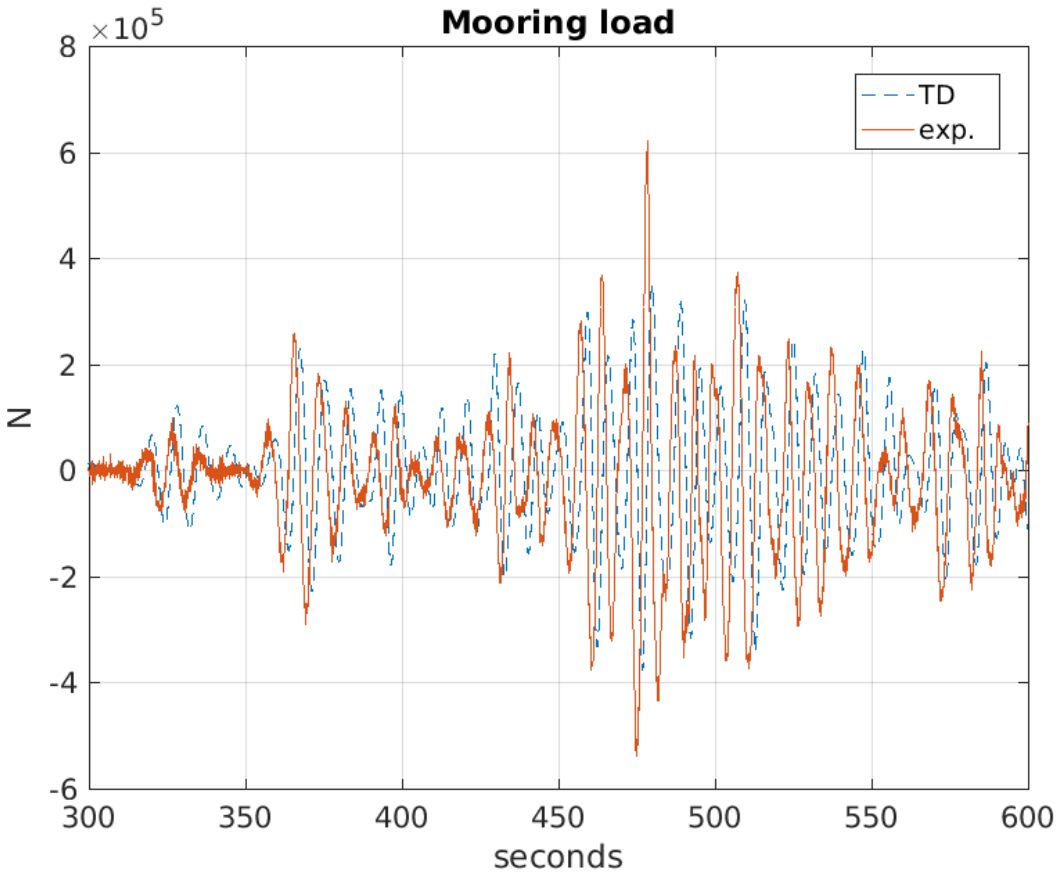

Figure 5.17: Comparison between time-domain predicted mooring load and the measured one of irregular sea. The same free surface elevation signal $\eta(t)$ was used in the time-domain simulation.

In Figures 5.18 and 5.19 are compared empirical values with numerical results obtained by including wave drift forces. These are the surge and the mooring load time series. The figure for heave is not reported as this is identical to Figure 5.16. The reason of this is that the heave phase result, obtained by the numerical code when wave drift forces are or are not included, is always the same. Due to the solving approach implemented described in Chapter 3, only surge phase results are varying. A part of this, the comparison of experimental values with time-domain results, when drift load is included, revealed that the numerical code well predicts both the surge motion and mooring load.

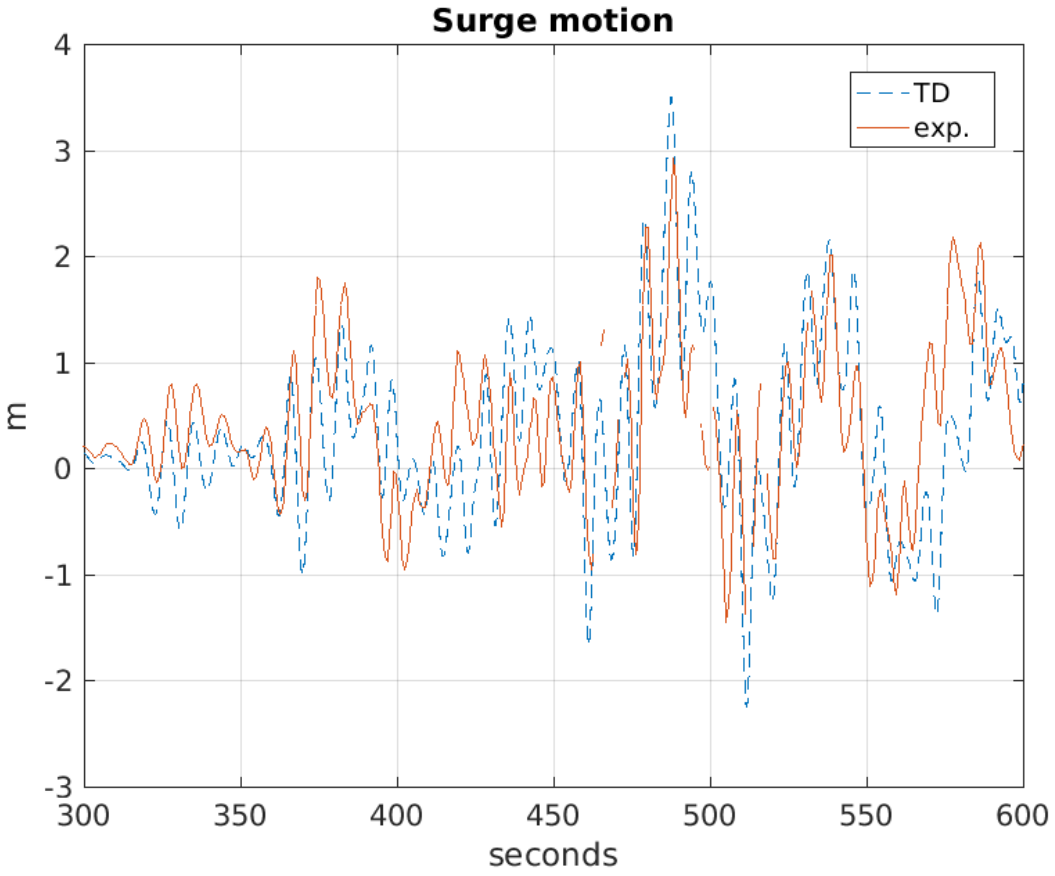

Figure 5.18: Comparison between time-domain predicted surge motion and measured surge motion in irregular sea. The same free surface elevation signal $\eta(t)$ was used in the time-domain simulation. The time-domain results showed here were obtained by including the estimated drift force.

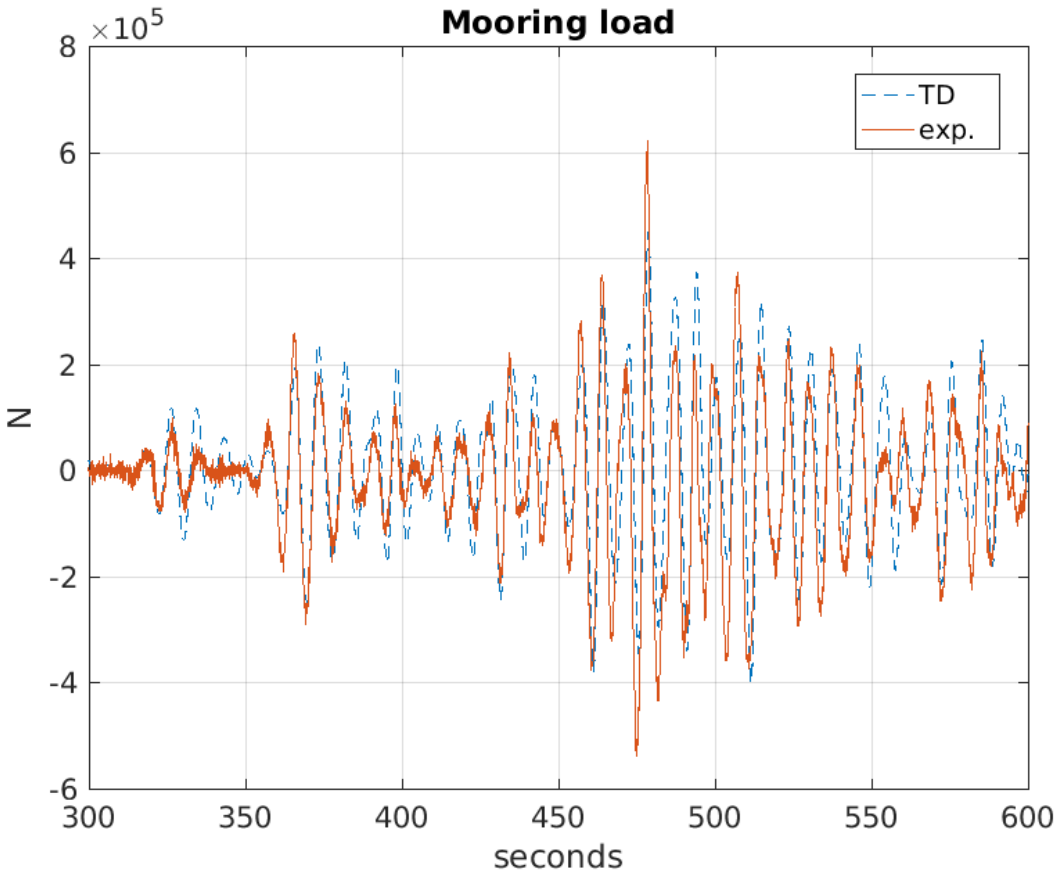

Figure 5.19: Comparison between time-domain predicted mooring load and the measured one. The same free surface elevation signal $\eta(t)$ was used in the time-domain simulation. For this illustration the drift load was included in the simulation.

In Figure 5.20 are shown results of the spectral analysis of the numerical and experimental surge displacements time series of irregular sea tests previously commented. For obtaining these results, the Fast Fourier Transform (FFT) algorithm was applied. A time interval corresponding to 900 real-scale seconds was in all cases extracted for the analysis. It is observed that two frequency peaks are evident for what concern the FFT numerical results obtained by including the drift forces. While the first peak corresponds to the surge natural frequency of the device (c.a.0.02 Hz), the second peak corresponds with the peak frequency of the free surface elevation, which for irregular sea test taken into account is 1.33 Hz. The mentioned numerical FFT matches well both,

frequencies and amplitudes relative to the FFT obtained from the signal corresponding to empirically measured surge time series. In contrast, the FFT of the numerical surge displacements, relative to the case when no drift forces are included, presents only a small peak at the surge natural frequency. This finding indicates that surge oscillations at the surge natural frequency are primarily due to the presence of drift forces.

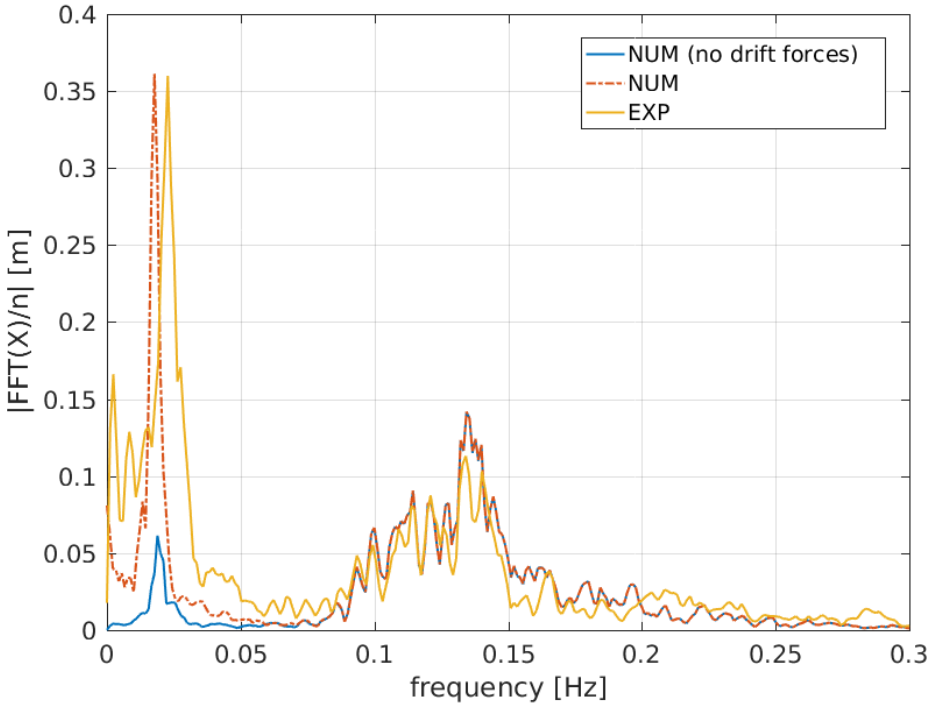

Figure 5.20: Fast Furier Transform results for the surge displacement obtained from numerical and experimental data.

The accuracy of the numerical predictions for irregular sea tests was quantified. A set of numerical simulations, run with free surface signals concerning data acquired during irregular sea tests at 1:33 scale (Session 3), were used. The root-mean-square (RMS) was calculated for each quantity of interest and both, numerical and experimental values. The RMS corresponding to a numerical quantity was subtracted to the corresponding empirical quantity (RMS difference). An indicative error value was then defined by taking into consideration the RMS value relative to the experimental time series.

Results of this analysis are reported in Table 5.21. In the last column, the indicative error in predicting quantities is reported. While when this error value is negative, it means the quantity is overestimated, when this is positive the quantity is underestimated. The following remarks can be observed:

- The surge motion is predicted with an indicative error less than ±14% for tests of the half-immersed device and less than ±21% for two tests of immersed devices.
- For all tests analysed, the indicative errors in the prediction of the heave motion, of the mooring displacement are respectively less than ±11% and ±14%.
- For all tests, the indicative error in the prediction of the mooring load is less than ±5%.
- The indicative error in predicting power for the test of the floater immersed at depth 3 is the highest, and this amounts to c.a. ±13 %. For the other tests, the error is less than ±7%.
-

	Test n.	System configuration	Tp (s)	Hs (m)	Length of time serie (s)	Quantity	Exp RMS	RMS difference	Units	Error %
Half immersed floater	112	Motor off	7.5	2.0	2,266.3	Surge	0.778	-0.105	m	-13.494
						Heave	0.394	0.028	m	7.226
						Mooring displacement	0.411	0.045	m	10.900
						Mooring load	969,608.755	-35,991.245	N	-3.712
						Instantaneus power	n.a.	n.a.	W	n.a.
	109	Nominal damping	7.5		2,248.1	Surge	1.236	-0.123	m	-9.958
						Heave	0.426	0.045	m	10.575
						Mooring displacement	0.443	0.061	m	13.827
						Mooring load	974,575.911	-33,024.089	N	-3.389
						Instantaneus power	45,670.964	-2,948.036	W	-6.455
	111	Nominal damping	12.5		2,144.7	Surge	0.706	-0.093	m	-13.177
						Heave	0.445	0.032	m	7.247
						Mooring displacement	0.478	0.064	m	13.491
						Mooring load	980,096.004	-24,903.996	N	-2.541
						Instantaneus power	24,898.288	746.288	W	2.997
Submerged floater	UW147	Depth n.1, damping n.2	12.5		2,144.7	Surge	0.469	0.092	m	19.546
						Heave	0.381	-0.036	m	-9.554
						Mooring displacement	0.380	-0.038	m	-10.065
						Mooring load	958,982.187	-44,417.813	N	-4.632
						Instantaneus power	10,382.431	-506.569	W	-4.879
	UW92	Depth n.3, damping n.2	12.5		2,144.7	Surge	0.415	0.085	m	20.487
						Heave	0.330	0.004	m	1.153
						Mooring displacement	0.295	-0.031	m	-10.622
						Mooring load	989,740.285	-12,459.715	N	-1.259
						Instantaneus power	6,894.139	885.139	W	12.839

Figure 5.21: Results of the quantitative analysis concerning the numerical code accuracy when irregular sea is simulated. All quantities are converted in real-scale values. RMS values are calculated with all samples for the entire length of time series. The negative values indicate that the numerical code is overestimating empirically measured quantities. Inversely, the positive values imply that the code underestimates related empirical measurements.

Chapter 6

Case studies

To show possible applications of the numerical tool developed, in this chapter two case studies are presented. The first case study concern an investigation of various system configurations obtained by varying damping coefficient and immersion depth. In this case, the theoretical spherical point absorber (PA) WEC previously introduced is again considered. Diversely, in case Study 2, a new PA WEC similar to the spherical model WEC is assessed. The new device is of a realistic design. System performances for optimal damping coefficients configurations and a realistic installation are estimated. While the objective of Case Study 1 is to investigate the effect of varying C_{pto} damping coefficient and floater immersion depth over the system performances, the aim of Case Study 2 is to optimise C_{pto} damping coefficients and to estimate annual energy extraction by the optimised realistic WEC defined.

Both these case studies are an example of applications of the generic methodology proposed in the introduction of this thesis. With this methodology, the entire WEC and its mooring component are analysed and optimised. In both case studies the, main steps of the method are put into practice. These concerned, defining some inputs, solving the equation of motion by taking into account the entire system dynamics and obtaining results for different system parameters. In both cases, best design was

investigated. While Case Study 1 mainly is limited to explore possible solutions, Case Study 2 focuses on optimal PTO damping for a realistic device.

6.1 Case Study 1

Following the validation of the numerical code, a first case study was developed. The aim of Case Study 1 is to show how the code proposed may be used to investigate the best system design parameters, analyse the mooring load and at the same time to the estimate the system efficiency over a year of operation. For this purpose, time-domain irregular sea states simulations were run for multiple system configurations. The influence of the mooring length (=depth minus the floater's immersion), and of the PTO damping, over the annual energy total production and mooring load cycles, was evaluated. Precisely, a simplified sea model of 21 sea states was created. Afterwards, by predicting the efficiency and simplified mooring load statistics, some system configurations determined by six different values of the mooring line lengths and five values of PTO damping were analysed. The same combinations of damping values and mooring lengths were also assessed for when a latching mechanism was included. In Table 6.1 gives an overview on the combinations assessed. These configurations were obtained by keeping the mooring pretension F_p constant. For achieving this, the mass also had to be varied depending on the floater's immersed volume.

24 sea states
X
6 immersion depths
X
5 C_{pto} coefficients
X
2 types of PTO (latching and no latching used)
=
1440 configurations

Table 6.1: Overview of configurations tested in Case Study 1.

6.1.1 Simplified sea model

To estimate system performances over a period of a year a simplified sea model was defined. This task concerned the creation of multiple sea states defined by an empirical sea spectrum formula. Each sea state created was simulated for a time series of length equal to 30 minutes. After obtaining the information on the performance of the device in each particular sea state, with a sea state occurrence probability table, annual statistics were calculated.

The Torsethaugen sea spectrum formula was used for defining a simplified sea model. Torsethaugen (2004) defined this particular sea spectrum, he analysed empirical data from the North Sea and considered both, swell a new wind-sea seas statistics. The spectrum is a two-peaked one and its implementation requires only the significant wave height H_s and the spectral peak period T_p. While the peak at lower frequencies represents the swell sea, the second peak represents wind-sea waves at higher frequencies (Fossen, 2011). When $T_p > 6.6H_s$ the higher peak is the one representing swell, and in the case of $T_p < 6.6H_s$ the higher peak represents the wind generated sea. In Case Study 1 and for Case Study 2 the Torsethaugen's spectrum was chosen, as this spectrum was simpler to be implemented. This spectrum was standardised under the Norsok Standard (1999). Using other spectra such as the JONSWAP spectrum would still permit of defining a sea model, but it was found more straightforward to implement the Torsethaugen spectrum as this last did not require particular parameters such as the γ parameter which is needed to define the JONSWAP spectrum. Another reason why the Torsethaugen spectrum was chosen instead of other conventional spectra such as the JONSWAP, the Pierson-Moskowitz or the ITTC ones, is that with this spectrum more various sea states are defined. In contrast, the other mentioned spectra are typically used for representing extreme sea states and are generally the particularly representative of wind-generated developing waves (excluding swell).

The probability of sea states occurrence table reported in Figure 6.1, was used for calculating the wave energy available at a specific site. The total annual energy available

at sea was estimated by assuming that the average power available during each sea state was equal to $P = \frac{1}{64\pi}\rho g^2 H_{m0}^2 T_e$ (W/m) (Herbich, 2000). The annual energy available for each sea state was multiplied by the corresponding probability value. Then, the available energy quantities from all sea states were added together to obtain the total annual energy available at the site.

H_m0 (m)	0.75	1.25	1.75	2.25	2.75	3.25	3.75	4.25	4.75	5.25	sum
T _10 (s)											
6	10.93	2.21	0.42	0	0	0	0	0	0	0	13.56
8	15.78	9.99	3.69	1.49	0.46	0.03	0	0	0	0	31.44
10	6.88	8.23	6.09	3.56	1.63	0.66	0.13	0.01	0	0	27.19
12	2.69	4.29	4.89	3.31	1.62	0.99	0.44	0.26	0.08	0.03	18.6
14	0.35	0.65	1.48	1.47	1.26	0.65	0.57	0.42	0.16	0.07	7.08
16	0.05	0.1	0.24	0.37	0.3	0.2	0.22	0.3	0.18	0.17	2.13
sum	36.68	25.47	16.81	10.2	5.27	2.53	1.36	0.99	0.42	0.27	100

Figure 6.1: Occurrence of sea states in form of probability values. These, relate to the Portuguese site of the mouth of Douro river, published by Henriques et al. (2013). Here the probability values are independent of incoming waves direction.

For saving computational time and memory in Case Study 1 only sea states which had probability values more than 0.5 were evaluated. These were 24 and are reported in Figure 6.2. The sum of the occurrence probabilities related to these is 95.43. Despite this, it has to be noted that in general the simulation of a 30 minutes long sea state is run in about just a few minutes, but given the number of configurations assessed (5x5) and the number of sea states, all computational time was c.a. 30 hours. In the case that all sea states were included the total computational time was estimated to be 50 hours (25 configurations). Besides, the number of sea states considered in this case study was limited to 24, so that in this way the size of data stored was also considerably less and thus data could have been easily handled on the standard machine.

H_m0 (m) / T _10 (s)	0.75	1.25	1.75	2.25	2.75	3.25	3.75	4.25	4.75	5.25
6	1	7								
8	2	8	14	20						
10	3	9	15	21	27	33				
12	4	10	16	22	28	34				
14		11	17	23	29	35	41			
16										

Figure 6.2: Index numbers of the sea states used. These were all those with a occurrence probability more than 0.5.

6.1.2 Earth-reacting WEC configurations

The PA with the spherical floater was simulated at the following six immersion values. Which are the distance from the free surface at calm condition to the centre of the spherical floater.

- Immersion value n.0 = 0 m (half-immersed floater case)
- Immersion value n.1 = -3.25 m ($= -r/2$)
- Immersion value n.2 = -7.5 m ($= -r$)
- Immersion value n.3 = -11.25 m
- Immersion value n.4 = -15 m ($= -2r$)
- Immersion value n.5 = -18.25 m

The mass was defined similarly as in previous chapters (Chapter 3), this for all immersion depths can be defined with Equation 6.1.

$$V_w \cdot \rho - F_p/g \tag{6.1}$$

In the above equation V_w is the volume displaced by the floater at the equilibrium condition. This last is equal to the half of the floater's volume for the case of Immersion n.0 and equal to the whole floater's volume for immersion depth values n.2 to n.5. In

contrast, for the case of Immersion n.1 this volume was defined with the following formula.

$$V_w = V_f - \pi/3(r + immersion)^2 \cdot (3 \cdot r - (r + immersion)) \tag{6.2}$$

Where the last term is the volume of the spherical cap outside the water. Equation 6.2 was also implemented in the numerical code for calculating the instantaneous hydrostatic restoring force. In particular, this equation, when only part of the floater was over the mean free surface, was evaluated within an *if* statement.

As introduced, together with the immersion value, also the PTO damping (C_{pto}) was varied. Five values, listed here below, were used. This except the third which is the original value C_{pto} are adjusted values.

- $C_{pto} = 0.5 \cdot C_{pto}(0)$(kg/s)
- $C_{pto} = 0.75 \cdot C_{pto}(0)$ (kg/s)
- Original value: $C_{pto}(0) = 2.5 \cdot 10^5$ (kg/s)
- $C_{pto} = 1.25 \cdot C_{pto}(0)$ (kg/s)
- $C_{pto} = 1.5 \cdot C_{pto}(0)$ (kg/s)

All other system parameters except the mooring length, mass and C_{pto} were left constant (same as in Table 3.1. Chapter 3). The mooring length was varied so to obtain the different immersion values previously mentioned.

To keep the pretension F_p constant, the mass was indirectly varied by applying Equation 6.1. This detail has to be kept in mind when results of results of different immersion depths have to be compared between each other, as the masses of floaters are consistently different. Due to different mass value also the natural frequency of the various configurations varied.

Same damping and floater's immersions values were also utilised for investigating the effect of the latching mechanism.

The simple latching method initially implemented in regular waves was modified and used in irregular sea simulations. At first, it was found that when the method was directly used in irregular sea simulations, this often showed not to be beneficial. Precisely, it was found that the simple latching mechanism, when used in irregular sea simulations, caused power performance improvements only to occur for sea states when $T_s > 10$ sec and the $H_{m0} > 1.25$ m were set. Thus, the latching method, to be effective, was further extended to irregular sea cases. A modification was made so to effectively increase performances when the latching method is implemented at Immersion depth n.0. This concerns by simply applying an *if* statement defining for which single waves to perform the latching strategy. Only where the wave amplitude was more than 1 m, the buoy was latched. Illustration of the technique is shown in Figure 6.3. In this figure can be seen that before and after single waves of amplitude over the reference value, the floater is latched, meaning that for short periods of time its velocity rapidly decreased to zero and its heave position was remaining almost constant.

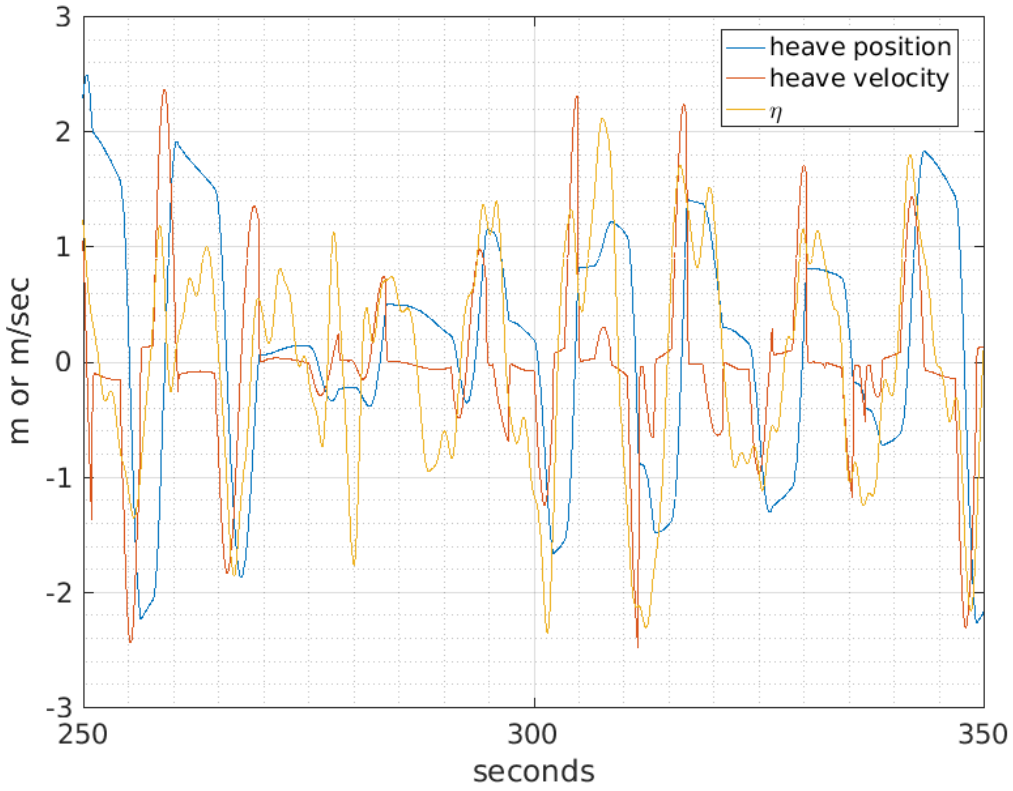

Figure 6.3: Illustration of results for irregular sea with latching control. Sea state no. 22 and configuration relative to Imm. n.0 and C_{pto} n.2 were used.

6.1.3 Simulation results and discussion

In this section, results of the case study are discussed. At first, the efficiency for the different configurations is reported. Afterwards, mooring load simplified statistics are analysed.

Tables shown in Figure 6.4 are displaying the values of the efficiency factors for all configurations of the two cases evaluated. The efficiency factors were found by dividing the annual energy produced by the annual energy present in the sea Environment (Figure 6.4). These indicate an estimation of the system performance depending on specific configuration, which varied by immersion depths and C_{pto} damping values. In this figure, it can be noted that at Immersion n.0, when the highest C_{pto} damping value is used the system is more efficient, with respect to all the other configurations assessed. At higher immersion depths, the efficiency decrease because less wave energy is available. It is also noted that the efficiency increase for all immersion depths, when the C_{pto} coefficient is increased. Due to this reason, it is expected that the optimal C_{pto} values given the specific sea model implemented are major than the investigated ones. The task of optimising these coefficients is performed in later Case Study 2. In general, it can be further noted that below Immersion n.2 the efficiency of the device is considerably less, i.e.$<$ 50% compared to Imm. n.0. Differently than other immersion depths, at Immersion n.1 is predicted that the device would convert more energy when the lowest damping value investigated is chosen. To note that results presented in this figures do not take into account the rated power limit and mechanical losses, which for real device exist. These factors will then be taken into consideration during Case Study 2 when is power absorption from a realistic device is estimated.

Normal cases:

(Eff. factor)	CptoX0.5	CptoX0.75	Cpto	CptoX1.25	CptoX1.5
Imm. n.0	0.090	0.122	0.148	0.171	0.191
Imm. n.1	0.150	0.126	0.126	0.130	0.134
Imm. n.2	0.067	0.089	0.112	0.135	0.157
Imm. n.3	0.033	0.049	0.064	0.077	0.090
Imm. n.4	0.023	0.033	0.043	0.053	0.060
Imm. n.5	0.016	0.023	0.030	0.037	0.042

Latching cases:

(Eff. factor)	CptoX0.5	CptoX0.75	Cpto	CptoX1.25	CptoX1.5
Imm. n.0	0.153	0.194	0.234	0.264	0.288
Imm. n.1	0.071	0.085	0.097	0.104	0.109
Imm. n.2	0.046	0.063	0.082	0.098	0.113
Imm. n.3	0.024	0.034	0.043	0.051	0.060
Imm. n.4	0.015	0.021	0.026	0.031	0.036
Imm. n.5	0.010	0.014	0.017	0.020	0.023

Figure 6.4: Annual energy production and efficiency factors for the various configurations investigated.

The modified latching method used showed to be effective only at Immersion depth n.0 (as shown in Figure 6.4). Comparing to the standard cases, where there was no latching, the efficiency at this immersion depth, for the five damping values, is between 41 to 57 % more.

For further comparing the various configurations analysed, regarding mooring load cycles, some threshold values were defined. These lasts were reference values used for defining five specific ranges. These ranges were then needed to analyse mooring load statistics. The threshold values are defined as:

- F_{m0} = mooring load mean value
- F_{rms} = RMS of the mooring load
- F_{m3} = mean of the 1/3 of the highest peaks of the mooring load in the irregular sea simulation time record.
- F_{m10} = mean of the 10% of the highest peaks of the mooring load in the irregular

sea simulation time record.

where the mooring load F_m is intended to be the absolute value of the actual load at the floater's fairlead minus the mooring pretension F_p.

With the mentioned threshold values the following ranges where defined:

- Range A as $F_m < F_{m0}$
- Range B as $F_{m0} < F_m < F_{rms}$
- Range C as $F_{rms} < F_m < F_{m3}$
- Range D as $F_{m3} < F_m < F_{m10}$
- Range E as $F_m > F_{m10}$

For illustration, in Figure 6.5 are shown the numbers of cycles categorised by ranges, for the configuration defined by Damping n.3 and Immersion n.0. For this configuration, the magnitude of the mooring load was, for the most of the cycles, contained in the range defined by the RMS and the mean of the third of the highest peaks of the mooring load (F_{m3}), for all sea states. As expected, the most of the cycles occur during most probable sea states. For all sea states, the number of cycles occurring in the first three ranges is predicted to occur with similar proportions for each of these ranges. It can also be noted, that higher numbers of cycles occur at higher load ranges, during moderate sea states which are less probable.

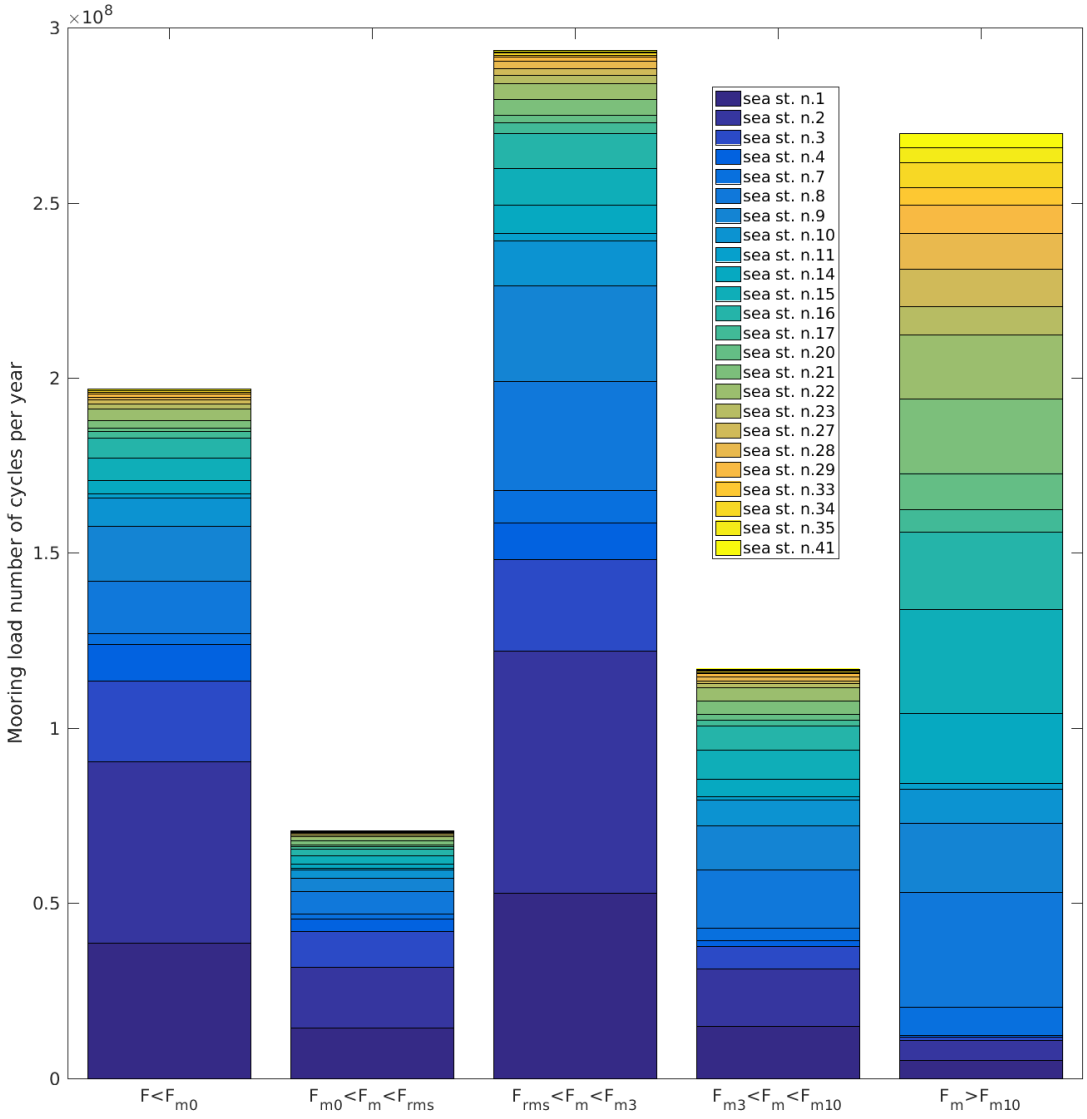

Figure 6.5: Annual mooring load number of cycles for Immersion depth n.1 and $C_{pto} = 1/2 \cdot C_{pto}$. Here colors represent the sea states evaluated.

Figures 6.6 and 6.7 shows how the numbers of annual mooring load cycles occurring within the five ranges, which are indicated by Type A to E and are defined by the previously mentioned thresholds values. For analysing and comparing all configurations

between each other, the threshold values relative to simulation results of sea state n.7 were used. These in particular concerned the configuration defined by setting the floater at Immersion depth n.0, the damping to C_{pto} n.3 and with the latching method implemented. The reason of this is that by choosing these threshold values it was possible to compare the *no latching method* and *with latching* sets of configurations between them. If threshold values relative to the set of configurations with no latching method had been used, this comparison would not be possible, as those threshold values were relatively higher. Thus, these lasts could not have be used for assessing the set of configurations with the latching method, for which mooring load peaks are of higher values.

In Figures 6.6 and 6.7 each set of five bars represents one of the configuration analysed. While in the first figure are reported results relative to the set of configurations were no latching method was implemented, the second figure reports results for the cases were the latching method was used. Each coloured bar represents the number of mooring load cycles within a particular range of mooring load. The various ranges previously defined are indicated by a different colour. While, in purple are indicated mooring load cycles in the lower range of magnitudes, with the yellow colour are indicated the mooring load cycles in the highest mooring load magnitudes. The other colours indicate the number of cycles in the other intermediate ranges.

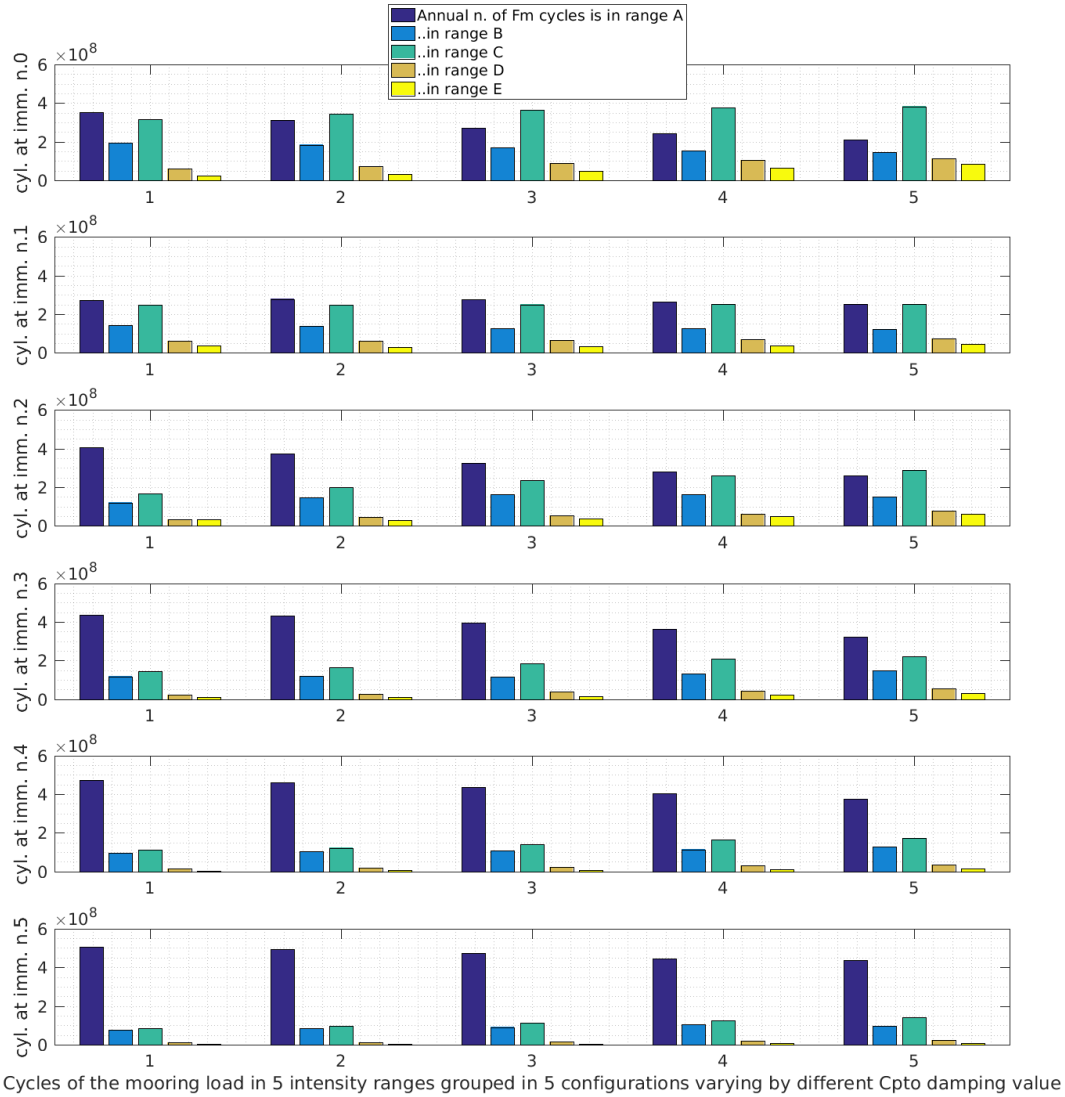

Figure 6.6: Annual number of cycles of the mooring load in 5 different ranges of magnitude for all configurations investigated when no latching was implemented. Here, colors indicate how many mooring load peaks are predicted within the different ranges of magnitude defined.

Considering both, the first table in Figure 6.4 and Figure 6.6, it can be noted that at Immersion depths n.3 to n.5 the system performance, in terms of efficiency, is to a great extent reduced, in contrast, intense mooring load cycles (those in ranges D and

E) are still relatively numerous. This observation may indicate that the only action of decreasing the mooring length (increasing immersion) is not enough for reducing intense mooring load cycles. In other words, the device is immersed below Immersion depth 2 would still experience a considerable number of mooring peak loads. For decreasing the mooring peak loads, it is seen to be more effective to reduce the damping C_{pto} value instead of increasing the immersion depth.

The device at Immersion n.1 set with Damping n.4 or n.5 has relatively good efficiency, meanwhile, at the same time, the number of intense mooring load cycles are also reduced by about half. At Immersion n.2 when the highest level of damping was used a good amount of energy may still be produced, but the device would experience intense mooring load cycles similarly as for Immersion n.0 Damping n.3.

When the latching method is implemented, the numerical tool predicts efficiency at Immersion n.0 is considerably more, and, at the same time, mooring loads are significantly higher. In fact, while for standard cases (no latching) is predicted that more mooring load cycles would occur in the range defined by the range D rather than in those occurring in the range E. For the latching cases more mooring load cycles would happen in the range E instead of range D. This can be noted by considering both, firsts plots of Figures 6.6 and 6.7. For most configurations when the latching method is used, the mooring load cycles occur mostly in range A, i.e. the mooring load peaks are minor than the RMS value. However, also the number of intense mooring load cycles increases significantly, in particular for Immersion n.0.

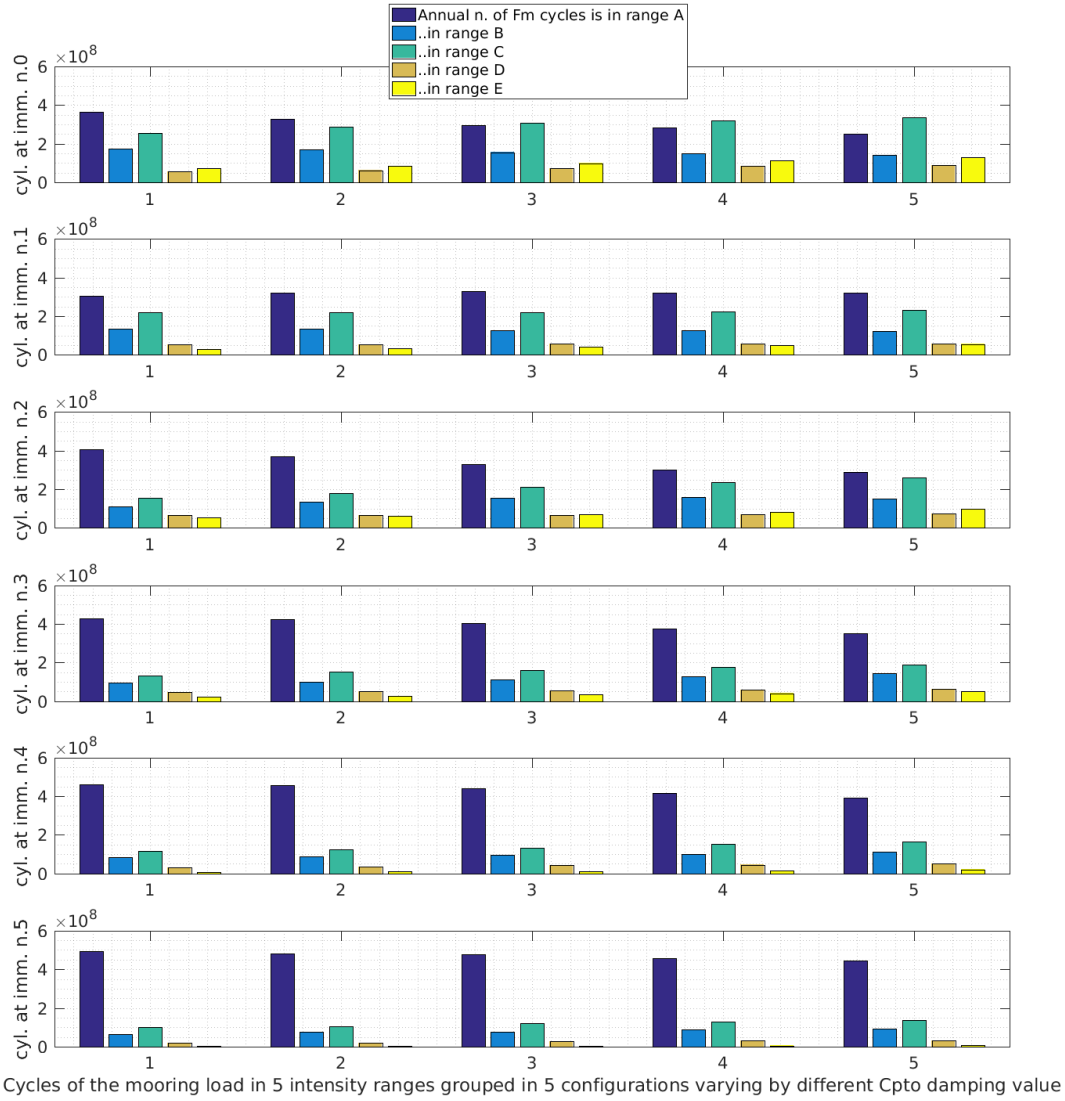

Figure 6.7: Annual number of cycles of the mooring load in 5 different ranges of magnitude for all configurations concerning the latching method. Here colors indicate how many mooring load peaks are predicted within the different ranges of magnitude defined.

As expected, for the sea states considered, the highest mooring loads occur during sea state n.41. For the normal cases highest peaks are approximately $9 \cdot 10^5$ N, meanwhile for the cases of the latching method, the mooring load may reach values up to about

$2.7 \cdot 10^6$ N. For having an idea on the number of intense mooring load cycles during this moderate sea state, a further mooring load cycles range was defined. The latter (range F) is defined by the limits of $(F_{m10} + F_{m10} \cdot 0.5)$ and $(F_{m10} + F_{m10} \cdot 1.5)$. Mooring load cycles having peaks in this range were in the order of $3 \cdot 10^4$ for normal cases, and about $1.1 \cdot 10^6$ for the latching method cases (Immersion n.1 Damping n.3).

Even considering the limitations of the applied theory, the found figures can be seen as a preliminary indicator of what would be the device's performance and of the mooring load cycles, which depends on the system configuration investigated. For example, in this case study it was found that the latching option is to a certain extent disadvantageous for what concerns high mooring load cycles. On the other hand, the efficiency, when the latching strategy is used at Immersion n.0, would be much higher. Thus, based on the figures found, a preliminary financial study, aiming at understanding the most advantageous configuration, would then give a final answer.

6.2 Case Study 2

While Case Study 1 concerned the investigation of the effect of variation of mooring length and damping on the performance of an ideal spherical PA device, Case Study 2 is about a study on a realistic device. Optimal PTO damping coefficients for the defined realistic device to be deployed on specific water depth and are found. The annual power generation of this device with a defined floater shape for a particular installation location is estimated.

Overview of the analysis performed during Case Study 2, for finding best C_{pto} damping configurations and estimate annual energy extracted, is reported in Figure 6.8. In this Figure is summarised the method implemented, this concerned numerical simulations and post-processing numerical calculations. During simulations, all data of interest, such as instantaneous power absorbed and mooring load time series were stored. The with a post-processing step of the stored data was analysed.

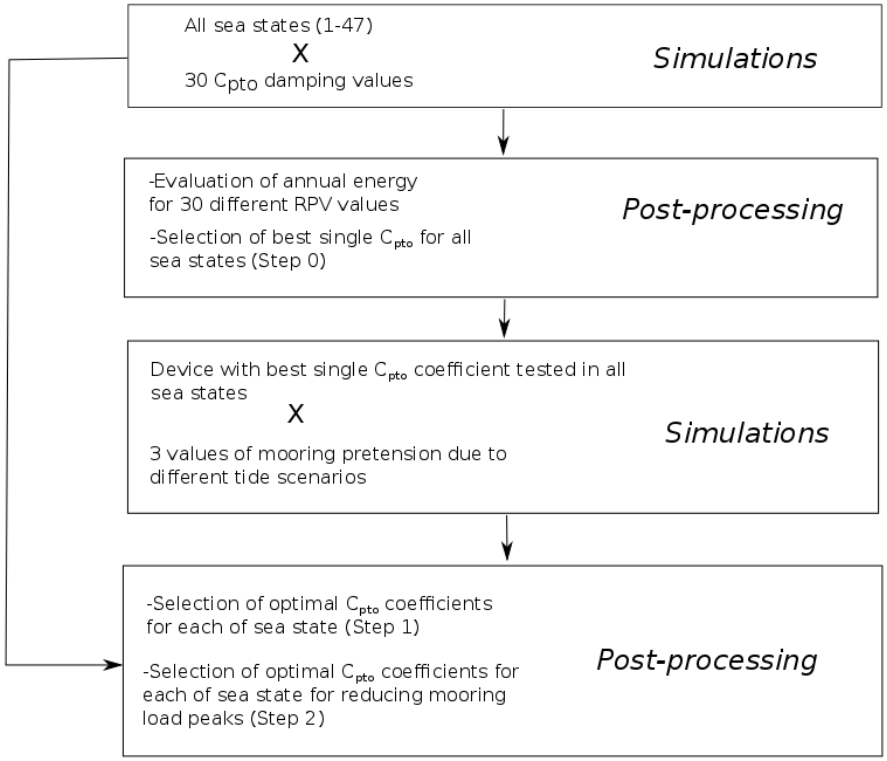

Figure 6.8: Overview of analysis performed during Case Study 2.

6.2.1 Device geometry and parameters

The spherical floater considered in previous chapters and Case Study 1 it is impractical to be built. Due to the spherical shape, the manufacturing process would be expensive and complicated. Another geometry is proposed, this is more realistic. The new geometry is shown in Figure 6.9, this has a segmented profile and is axisymmetric. A floater of this new geometry would be simpler and cheaper to be manufactured compared to the spherical floater previously considered. This new shape would also allow the buoy to stand on the ground stably on its own, thus avoiding technical complications during transport and temporary storage. In this way, project costs could be reduced.

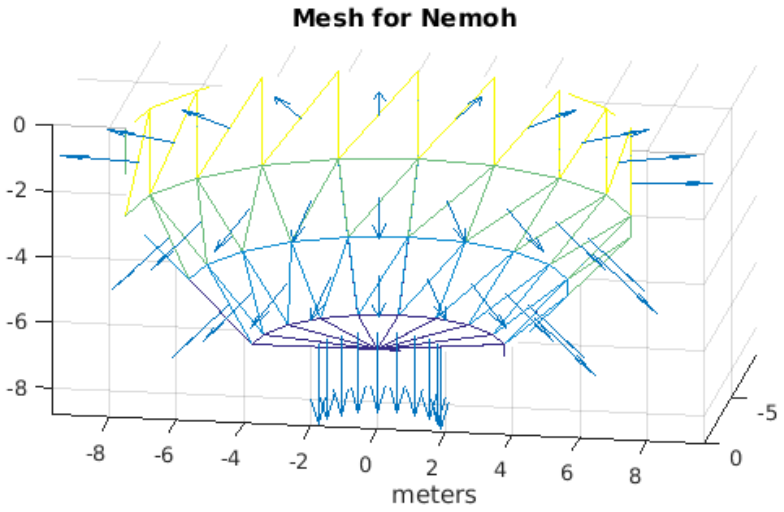

Figure 6.9: Mesh of floating component of the PA WEC analysed.

Dimensions of the new floater's geometry along with overall dimensions of the realistic device, analysed in this section, are reported in Figure 6.10. The diameter is kept the same as the one of the spherical floater previously studied, i.e. 15 m. The floater's height was chosen so that the volume of the new floater also corresponded to the one of the spherical floater; this is set to 12.812 m. The chamfers diagonal edges, as illustrated in Figure 6.10, are designed by setting a chamfer length equal to half of the floater radius, i.e. 3.75 m.

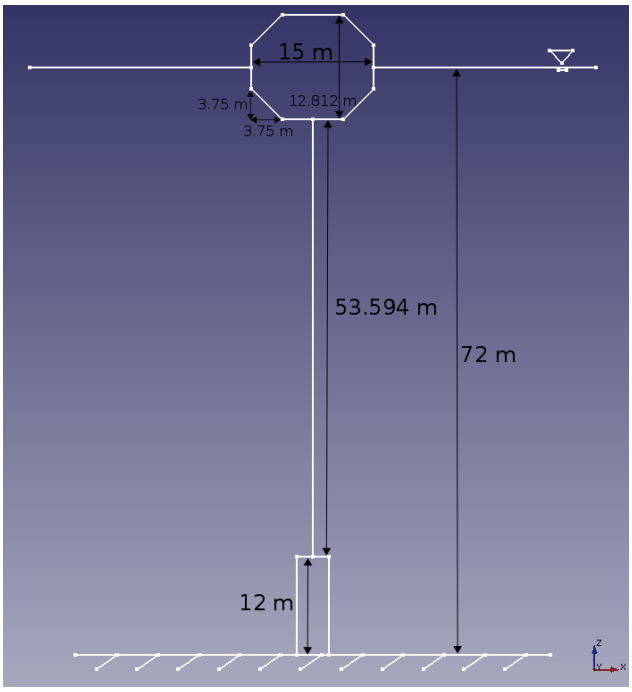

Figure 6.10: Dimensions of analysed PA WEC.

As discussed in Case Study 1, the device is more efficient when the floater is not immersed. Thus only this preferred option is considered in this case study. For a 72 m water depth site, the realistic device is designed to be moored with a tether 53.59 m long. A fixed power unit deployed on the seabed is designed to be 12 m height. Similarly, as was intended for the theoretical PA of previous chapters, the power unit comprehend the linear PTO (damper) and spring components. Overview of all parameters of the proposed device is reported in Table 6.2.

Parameter	Values
radius	7.50 m
chamfer length	3.75 m
height	12.812 m
fixed power unit height	12 m
mooring length	53.594 m
mass	8.0359E+05 kg
depth	72.0 m
stiffness	1.80E+05 N/m
pretension	1.00E+06 N

Table 6.2: System parameters of new PA device.

6.2.2 Device modelling

So to model the considered PA WEC realistically, in this case study, more factors have been considered. These concern the inclusion of PTO end-stops and the rated power limit. In addition, generator and viscous related losses and the tide range effect over the power absorption performance are also taken into consideration.

In Figure 6.11 is reported the scheme of the power unit. Upper, lower end-stops and a translator element are also included so to define a more realistic power unit. The end-stops of 0.15 m height are modelled as large dampers. A damping value of $0.5 \cdot 10^8$ kg/s was attributed to both end-stops. Thus, the cable is allowed to displace along the axial direction for the initial spring offset minus both end-stops height and minus the stator height. The numerical tool was configured so that at those instants when the translator reached the end-stops, no power was absorbed by the device.

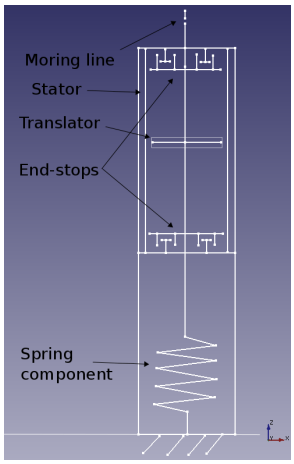

Figure 6.11: Illustrative scheme of the power unit.

So to take into account viscosity and generator related losses, a generic coefficient C_{losses} is used to estimate realistic instantaneous effective power absorbed by the device. Having considered results provided by Babarit et al. (2011) for a bottom-referenced heaving buoy; this coefficient is set equal to 0.5.

6.2.3 Analysis

As for Case Study 1, the sea states occurrence probabilities (Fig. 6.1 Sec. 6.1) for the specific site of the mouth of Douro river is applied for defining a simplified annual sea model (as for Case Study 1).

H_m0 (m)	0.75	1.25	1.75	2.25	2.75	3.25	3.75	4.25	4.75	5.25	sum
T_10 (s) [MWh/m]											
6	1.59 n.1	0.89 n.7	0.33 n.13	0.00	0.00	0.00	0.00	0.00	0.00	0.00	2.81
8	3.05 n.2	5.37 n.8	3.89 n.14	2.59 n.19	1.20 n.24	0.11 n.29	0.00	0.00	0.00	0.00	16.20
10	1.66 n.3	5.53 n.9	8.02 n.15	7.75 n.20	5.30 n.25	3.00 n.30	0.79 n.34	0.08 n.38	0.00	0.00	32.11
12	0.78 n.4	3.46 n.10	7.72 n.16	8.64 n.21	6.32 n.26	5.39 n.31	3.19 n.35	2.42 n.39	0.93 n.42	0.43 n.45	39.28
14	0.12 n.5	0.61 n.11	2.73 n.17	4.48 n.22	5.73 n.27	4.13 n.32	4.82 n.36	4.56 n.40	2.17 n.43	1.16 n.46	30.52
16	0.02 n.6	0.11 n.12	0.51 n.18	1.29 n.23	1.56 n.28	1.45 n.33	2.13 n.37	3.73 n.41	2.79 n.44	3.22 n.47	16.80
sum	7.22	15.96	23.19	24.75	20.11	14.08	10.93	10.79	5.90	4.81	1.38E+02

Figure 6.12: Annual energy available for each sea state at the site considered.

Thirty damping values for all sea states were simulated. A simulation period of 15 minutes, all times, was set. Results including instantaneous power, mooring load and

displacements time series for each different PTO damping value configuration assessed in each sea state were stored.

By applying different rated power values (RPV) results of the instantaneous power were post-processed so to obtain the effective mean power absorbed by the device in each simulation performed.

Post-processing calculations also included the optimisation operations.

Optimization

Initially, an optimal single C_{PTO} damping value for all sea was identified (Step 0). The next step concerned finding optimal C_{PTO} damping values for each sea state (Step 1).

At last, in last step (Step 2) damping coefficients were optimised for those sea states where the mooring load F_m presented peaks over two times the pretension value (2.00E6 N). Best damping coefficients were found so to obtain a compromise concerning the reduction of intense peaks and, at the same time, maximising power absorption.

Treatment of the end-stops

So to model the end-stops, a methodology similar to the one used for implementing the latching method introduced in Chapter 3 was adopted. The latching method consisted of applying large damping during particular periods. Similarly, in this case, the mooring line axial displacement was evaluated at each time step, and when the upper end-stop was reached, a large damping value was simulated. At times that the upper end-stop was reached higher peaks of the mooring load are expected due to the axial mooring displacement that was constrained by the large damping. Diversely, for what concerns the lower end-stop, when this is reached is expected that the mooring line got slack, in this case, there is no need to impose a large damping numerically. In practice, the damper element representing the lower end-stop is only needed for stopping the

translator inertia. So to calculate the power generation realistically, for those instants when the translator element reached one of the two end-stops, the instantaneous power absorbed was set to nil.

Effect of tide

Besides, it was further investigated an extra important factor; this concerned the effect of the tide over the mean absorbed power by the device.

For assessing the effect of the tide on the device operation, it was considered the semidiurnal tidal range of 2.5 m, which is about the average semidiurnal tidal range between spring and neap tides for the specific location considered (data for Porto, Tideforcast (2018)). Given this range, a mean high and low tide displacements of ± 0.8 m were assumed for evaluating the mean annual power absorbed by the device. In Figure 6.13 is shown one sinusoidal cycle for the semidiurnal tide in consideration and the corresponding mean values adopted.

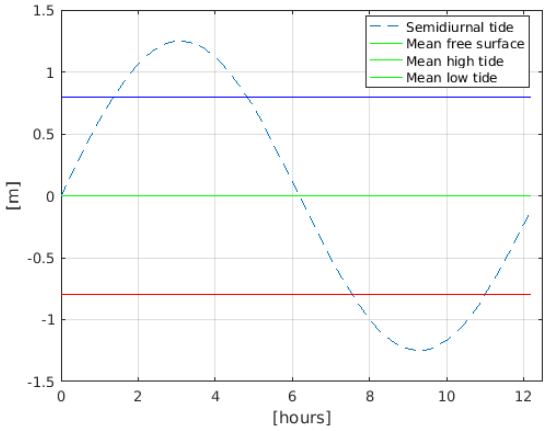

Figure 6.13: Tidal range and mean tide levels analysed.

The different mean free surface levels due to the tide variation were taken into consideration by implementing a different mooring pretension. The ratio between spring displacement and vertical displacement due to buoyancy is equal to 0.1. Thus for 0.8 m

of mean free surface variation, the floater is the only c.a. 0.08 m submerged or risen. As a consequence, the tide range is primary determining a change of the mooring tension and not a sensible variation of the immersion of the floater. This last parameter for simplicity is neglected. While for mean low tide a pretension value of $F_p = 0.855 \cdot 10^6$ N was set (-0.8 m of tide variation), for mean high tide a value of $F_p = 1.44 \cdot 10^6$ N was implemented (+0.8 m of tide variation).

	Offset [m]	Average power [KW]
Mean low tide	-0.8	13.8
Mean level	0.0	15.6
Mean high tide	0.8	13.6

Table 6.3: Average absorbed power of all sea states depending on different free surface elevations investigated.

In Table 6.3 are reported results concerning the annual average absorbed power from the device in all sea states. These figures are obtained having considered different free surface elevations due to tide variations. When the translator reaches the end-stops no power is produced. Depending if is low or high tide, respectively the lower or upper end-stops are hit more times. As a consequence power is absorbed differently than for the mean free surface level. In Table reftab:AnnualEnergyResultsCaseStudy2 results of the average absorbed power for three free surface elevations scenarios investigated are compared. The average absorbed power is calculated by considering all sea states and their probabilities of occurrences. The average annual power for both, mean low and mean high tide is about 12.2% lower than average annual power absorbed if the device was always operating at the mean free surface level.

6.2.4 Results

To optimise the device in consideration 30 C_{pto} damping values were investigated, these ranged from $2 \cdot 10^5$ to $6 \cdot 10^6$ Ns/m. Configurations characterised by each different value were simulated in each of the 47 not nil sea states considered. In Figure 6.14 are shown results for the annual energy produced by the device for all C_{pto} damping configurations

analysed. The Y-axis represents the rated power value (RPV) also usually referred to as the nominal power. As for about an RPV value of $4 \cdot 10^5$ W (400KW) a significant amount of annual energy can be converted, this value was chosen to be the device's nominal power value. Higher RPV analysed would only permit extract only little more energy.

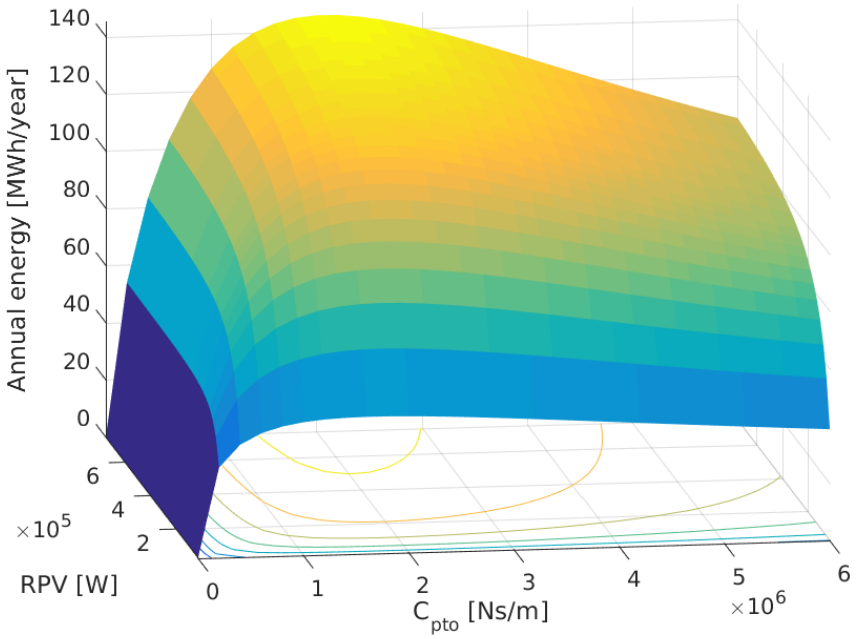

Figure 6.14: .

Considering a 400 KW rated device, as is clearly shown in Figure 6.15, for $2 \cdot 10^6$ Ns/m the most annual energy can be obtained. This appear to be also the optimal C_{pto} for all others RPV values considered (Figure 6.14). For this device, having estimated the effect of tide (12.2 % losses) and for only one optimal C_{pto} damping coefficient value is used, the annual energy extracted is equal to 119.54 MWh/year.

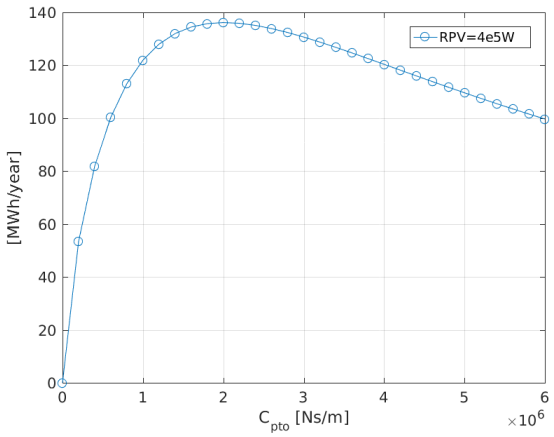

Figure 6.15: .

Two more steps were performed to optimise the device. The first, concerned to find best C_{pto} damping coefficients for each of the sea states. The second step concerned a further optimisation of C_{pto} coefficients for those sea states in which high mooring loads occurred. Results are reported in Figure 6.16. In the first table of this figure are reported the optimal coefficients for maximising annual energy extraction (Step 1). For those sea states for which high mooring load occurred, these damping coefficients were further optimised aiming at obtaining a good compromise between energy extraction performance and the number of mooring load peaks (Step 2). In both tables of Figure 6.16 the blue colour indicates lower values of C_{pto} increasing up to orange values which are the highest. During Step 2 only C_{pto} coefficients of Sea States from 30 to 47 were further optimised for reducing mooring load peaks. The device simulated in the other sea states (1-29) did not present mooring loads peaks above the chosen threshold value ($2 \cdot 10^6$ N); thus C_{pto} coefficients obtained with the first optimisation step were kept the same.

Results of first step of the optimization:

T _10 (s)	H_m0 (m) [Ns/m]	0.75	1.25	1.75	2.25	2.75	3.25	3.75	4.25	4.75	5.25
6		8.00E+5	8.00E+5	8.00E+5	0.00E+0	0.00E+0	0.00E+0	0.00E+0	0.00E+0	0.00E+0	0.00E+0
8		1.40E+6	1.60E+6	1.40E+6	1.40E+6	1.40E+6	1.40E+6	0.00E+0	0.00E+0	0.00E+0	0.00E+0
10		2.00E+6	2.00E+6	2.00E+6	2.20E+6	2.00E+6	2.20E+6	2.00E+6	2.00E+6	0.00E+0	0.00E+0
12		2.20E+6	2.40E+6	2.40E+6	2.40E+6	2.20E+6	2.40E+6	2.40E+6	2.60E+6	2.40E+6	2.60E+6
14		2.40E+6	2.00E+6	2.40E+6	2.40E+6	2.60E+6	2.20E+6	2.80E+6	2.80E+6	3.00E+6	3.00E+6
16		2.20E+6	2.00E+6	2.40E+6	2.40E+6	2.40E+6	2.40E+6	2.80E+6	3.20E+6	3.00E+6	2.80E+6

Results of second step of the optimization:

T _10 (s)	H_m0 (m) [Ns/m]	0.75	1.25	1.75	2.25	2.75	3.25	3.75	4.25	4.75	5.25
6		8.00E+5	8.00E+5	8.00E+5	0.00E+0	0.00E+0	0.00E+0	0.00E+0	0.00E+0	0.00E+0	0.00E+0
8		1.40E+6	1.60E+6	1.40E+6	1.40E+6	1.40E+6	1.40E+6	0.00E+0	0.00E+0	0.00E+0	0.00E+0
10		2.00E+6	2.00E+6	2.00E+6	2.20E+6	2.00E+6	2.00E+6	2.00E+6	1.60E+6	0.00E+0	0.00E+0
12		2.20E+6	2.40E+6	2.40E+6	2.40E+6	2.20E+6	2.00E+6	1.60E+6	1.80E+6	1.40E+6	1.80E+6
14		2.40E+6	2.00E+6	2.40E+6	2.40E+6	2.60E+6	2.00E+6	2.00E+6	1.60E+6	1.00E+6	1.40E+6
16		2.20E+6	2.00E+6	2.40E+6	2.40E+6	2.40E+6	2.00E+6	2.00E+6	1.40E+6	1.80E+6	8.00E+5

Figure 6.16: Optimized C_{pto} coefficients.

Results of the optimization are reported in Table 6.4. By implementing the optimal C_{pto} damping coefficients for each sea state, an increase of up to 2.23 MWh/year of absorbed energy can be obtained (Step 1). The times of low mooring loads ($F_m < 1.5E4$N) for the three optimal configurations considered are similar, these ranged between $1.24 \cdot 10^5$ to $1.66 \cdot 10^5$, for the sea states analysed. In contrast, the mooring load peaks ($F_m > 2E6$ N) are substantially reduced for what concern the optimal configuration obtained after Step 2. For this last configuration a reduction of 1320 mooring load peaks with respect to results concerning single damping configuration (Step 0) and 3950 mooring load peaks less with respect of results after Step 1.

	Annual energy [MWh/year]	Times low mooring load ($F_m < 1.5E4$N)	Mooring load peaks ($F_m > 2E6$N)
Single C_{pto} (Step 0)	119.54	1.24E+05	2.04E+03
Multiple C_{pto} (Step 1)	121.77	1.66E+05	4.67E+03
Multiple C_{pto} (Step 2)	120.72	1.40E+05	7.20E+02

Table 6.4: Annual extracted energy, mooring load peaks and minimums for the optimal configurations found.

Chapter 7

Summary and conclusions

At first in the introduction of this thesis, the primary motivations of this study were discussed. These mainly concern the need of identifying main differences between characteristics of traditional moored structures and moored WECs, to review literature, to understand new requirements, and to search of new solutions.

In chapter 2, the problem of station keeping related to wave energy converters is introduced. Major mooring system requirements, which also depend on the type of wave energy converters (WEC) technology, are discussed. Distinctions with mooring requirements of conventional floating structures are identified and possible mooring solutions, in general terms, are reviewed and discussed.

The revision on the existing literature on mooring system analysis techniques and methodologies indicated that current works found are very variegated and design specific. Often, where the mooring component was considered into mathematical and numerical models, the effects of this were included in conventional ways such as static, quasi-static or frequency-domain types of methods. On the other hand, through the most recent research, there is a trend about the use of more advanced and complex methodologies, by which the mooring system design and the power-take-off mechanism can be in some ways be included into a nonlinear time-domain formulation of

the problem. Most of techniques and methods were developed for conventional floating structures, which have different mooring system requirements. These are complex methods not suitable to be applied in the case of WECs. Besides, most of the times published results obtained with the mentioned methods were often not validated with experimental data.

Given these motivational aspects stated in the introduction and findings of the literature review a generic new methodology to be used for designing and analysing the entire system of a WEC, including the mooring component as an integral part, was proposed. To justify and put in practice such methodology a set of main project objectives were defined. These concerned: to review the literature; the development of a numerical tool; to obtain empirical data for an Earth-reacting device; to validate the numerical code developed; and to show possible applications of the numerical code and the generic methodology, as for investigating best system design. Details concerning defined objectives and where these are addressed are recapitulated in Section 7.0.5.

With the aim of including the mooring component in the analysis of the entire WEC-mooring system, a simplified Earth-reacting WEC simulation method was defined. The method was applied to generic point absorber (PA) single tethered devices, and a numerical code was developed (Chapter 3). This method overcomes limitations of static, quasi-static and frequency-domain only, mooring analysis approaches. The proposed method consent to analyse the dynamics of the entire mooring system-WEC's performance so that the effects of power-take-off and the mooring line component are included in the complete analysis. In this way, the whole structure response and its loads are predicted more realistically. The defined numerical code is based on the frequency-domain and on time-domain methods, where this last is formulated with the Cumin's equation. The equation of motion is solved for surge and heave. The time-domain solution permits the inclusion into the analysis of transient hydrodynamic effects, thus allowing overcoming limitations of the frequency-domain only approach. Furthermore, the proposed method enables the option of implementing, into the model, a defined free surface elevation signal as a wave loading input function. The latter is also needed for

real-time applications, where the incoming wave can be measured at a certain distance upwind. When designing the mooring system, these extra capabilities are advantages to conventional methods where only resonance conditions can be predicted, and nonlinear forces cannot be included.

Compared to commercially available codes, the proposed code is tailored to the specific case of Earth-reacting WECs. The developed code is advantageous as this focuses on the peculiar requirements of WECs mooring analysis and design. To the best Author's knowledge, no existing code which focuses on two-dimensional Earth-reacting WEC exist. All available similar numerical tools concern the unidimensional case only or are made for analysing slack mooring configurations. The proposed code is developed by taking into account the main mooring analysis and design requirement for WECs, which concern chasing the optimal system design for optimal power performance. This advantage is a unique to existing commercial codes as these other codes do not consider this significant aspect.

The numerical tool was firstly validated and then, through two case studies, was used to investigate the influence of specific system parameters on the power performance and mooring load statistics, so to identify the best design.

Experimental work on basic moored spherical PA physical models, for gathering reliable empirical data, was carried out. The empirical work is described in Chapter 4. The primary objective of this was to gather valuable empirical data to be used for validating the numerical code. Thus, three sessions of experiments, with three small-scale WEC models, were conducted. Of these models, one was manufactured at 1:86 scale and two more at 1:33 scale. The models in question represented point absorber (PA) WECs devices which comprehended a spherical floater (half-immersed or wholly submerged spheres), a damping mechanism and spring. The half-immersed and submerged spherical PA WECs were tested in regular and irregular simulated seas. All details of experiments including scaled models, the calibration process, methods and estimation of uncertainties are described. For illustration the primary results are also reported in

Chapter 4 and all other empirical relevant data only of the third session of experimental tests is reported in tabular form in the Appendix A.1.3 (in the form of motion RAOs, system loads, and other empirical measurements).

In Chapter 5 the numerical code developed was firstly verified and then validated with the most reliable experimental data. For initially verify numerical results, at first some results were compared with analytical results given by others. Besides, outputs obtained by two calculation methods implemented for calculating the wave forces were compared between them. Subsequently, numerical results obtained by the tool were compared to experimental data. This step was done for free decay, regular and irregular sea tests. In general, the numerical tool showed to predict within reasonable accuracy the moored WEC's performance and dynamic behaviour. For most cases, taking into account experiments uncertainties, numerical predictions were of values falling on valid ranges.

After having assessed the validity of numerical results, two case studies showing possible applications of the proposed generic methodology were developed. For practically perform this task the numerical code developed was used. In Chapter 6, in Case Study 1, firstly a simplified method for assessing the device's mooring loads and power performance was defined and applied to the specific PA considered in this project. The system was investigated in a parametric way. This task was possible by further extending the code so that it became runnable within multiple loops. The mooring length, along with the values of the dynamic mooring load, and the one of the power performance were analysed systemically, and best configurations of the system were discussed. In general, by increasing the immersion depth, intense cycles of mooring load are not much reduced. A better configuration regarding a reduction of mooring load fatigue can be found by decreasing the damping value. However, in most cases, this negatively affects the device's energy extraction performance. In Case Study 2 a realistic device was defined. By looking at both, obtaining optimal power absorption and mitigating mooring load peaks, PTO damping coefficients were optimized for obtaining best system performance. For the optimised device annual energy extraction was also estimated.

Given the project motivations and objectives, a general methodology was defined and proved, and this is at the base of the entire PhD project. To justify the application of the proposed general methodology at first the numerical tool was developed. This tool was needed for solving the entire system dynamics of a moored WEC. By using the tool is possible to obtain predictions of motion and loads of the system under study. The numerical tool had to be validated, so extensive empirical data was acquired. The most feasible data was then used to validate the tool. Once the validity of the tool was confirmed this was used to show that this can be used to analyse and optimise moored WECs. While an example of analysis was illustrated in Case Study 1, in Case Study 2 an instance of possible optimisation processes for a realistic device was shown. The PhD study mainly focused on the case of Earth-reacting WECs but the methodology may be relevant to be applied to other types of moored WECs.

Regarding Chapters no. 2, no. 4, no. 5 and no. 6 a series of remarks were outlined. These are the main findings of this project and are listed here next.

- When simulating the PTO mechanism at the laboratory, uncertainties related to all system damping are difficult to reduce and to differentiate. This aspect is a significant problem to be addressed. Often it happens that very wrong power prediction is obtained. This mistake is often also happening in experiments on commercial devices models. Extreme care in system design and component selection is essential to allow acceptable results to be obtained.

- The system damping uncertainties can be caused by many system components and can largely affect model tests results. During this project, it was found that together with the PTO mechanism, the thickness and material of the mooring rope, and the type of pulley, are also significant factors that introduce consistent uncertainties. Improvements of system components and details are indispensable solutions. For example, the use of dyneema thin mooring ropes during experimental tests was found to be a valuable alternative to thin steel cables.

- Empirical tests indicated that for the considered point absorber the amount of

energy extracted is little influenced by the floater's surge motion. This statement is supported by empirical tests data where surge motion was significant (in particular for the submerged spherical floater tests). In most cases, the mooring displacement amplitude was almost coinciding with the heave amplitude. Thus, even if it may happen that the surge amplitude was large; by the only surge motion, the PTO mechanism is very little activated.

- The quantitative analysis showed that margins between experimentally measured quantities to numerical predictions exist. For irregular sea simulations, when drift forces are included, the relative errors for the half-immersed sphere in predicting surge, heave, mooring load and power are respectively $\pm 14\%$, $\pm 11\%$, $\pm 5\%$ and $\pm 7\%$.

- Decreasing the damping and tuning the mooring length can be a way of optimising the whole WEC system so that intense mooring load cycles are considerably reduced. The results of Case Study 1 support this statement.

- Findings of Case Study 1 indicated that even if the use of a latching strategy method would increase energy extraction to a great extent, the high mooring loads cycles and maximum values would drastically increase. Thus, if such an option may be chosen, considerable extra structural costs may exist.

- Through both case studies the methodology proposed in this thesis was implemented for analysing and design taut moored Earth-reacting WECs. For this task, the numerical tool was used. This methodology firstly was needed to assess the system performance and assess mooring load basic statistics, when the mooring length and PTO damping were varied. Successively this was applied for optimising a realistic moored Earth-reacting WEC and for calculating its annual energy extraction. In both cases by following the proposed generic methodology is showed that this is a valid approach. These may also be applied to any type of Earth-reacting WECs. Also, the effect of the other system parameters may be investigated with this methodology.

To the best author's knowledge major original contributions of this thesis concern:

- The definition of a new methodology for analysis and design moored WECs.
- The development of a practical numerical method capable of analysing simplified Earth-reacting axisymmetric PA taking both surge and heave motions into account. Compared to commercial software available, it was found that the proposed numerical method robustly allows of taking into account the mooring pretension, when a fully dynamic approach is implemented.
- Having provided extensive empirical results along with information on results uncertainties for a PA generic model. These results hopeful may be beneficial for others to be used for other numerical models validation.
- Having provided unique solutions for practical model making and experimental set-up related to the generic taut moored PA assessed at laboratories.

7.0.5 Verification of project objectives

Next is explained in which part of this thesis each of the objectives stated at the beginning of this thesis is fulfilled. Experimental study Chapter:

1. To explore the existing literature on the topic of interest both, from a wider perspective and with a specific focus on a particular type of WECs. This objective is addressed in Sections 2.2 and 2.3 of Chapter 2.
2. To develop a numerical tool for practical simulating Earth-reacting wave energy converters of generic geometry. This objective is addressed in all Chapter 3.
3. To develop different experimental set-ups and methods and to accurately simulate the considered generic Earth-reacting device at hydrodynamics laboratories. This objective is mainly addressed in Sections 4.4 and 4.5 of Chapter 4.

4. To obtain reliable and repeatable empirical results. This objective is addressed in Sections 4.5 and 4.7 of Chapter 4 were the calibration work, the selection of equipment task was explained, and uncertainty analysis for each experimental set-up identified was reported.

5. To verify and validate the numerical methods proposed with the results of the experimental work. This objective is addressed in Chapter 5.

6. To show how the numerical tool developed could be used to investigate the best parameters for optimum system design. This objective is addressed in Chapter 6.

7. To investigate in an empirical way: the motion response, the axial mooring line displacement, the mooring loads and the power absorption, for the considered device. This objective was mainly addressed in Section 4.8 of Chapter 4.

8. To quantify the uncertainties of the experimental results of the different conducted experiments. This objective was addressed in Section 4.7 of Chapter 4.

7.0.6 Future work recommendations

The numerical tool created in this projects could be improved by considering the following comments.

- The proposed method can be extended to more degrees of freedom and multi-directional sea. For simplicity, in this project, the floater was assumed to be only moving vertically and horizontally. In contrast, depending on the geometry of the floater, the hydrodynamic coupling (neglected here because of the use of spherical floaters) may be significant. Thus the methodology can be extended to all 6 degrees of freedom so that can be applied effectively to floaters of any particular geometry and with any mass distribution having considerable hydrodynamic coupling between the different modes of motion.

- At the actual stage, the numerical code developed is tested and verified for deep water waves. With a little effort, the code may be upgraded to intermediate and shallow water cases. Further validation will be required.

- It was found that for point absorbers with submerged floaters having a limited mooring pretension, the system natural frequency may be considerably lower. Thus, in certain cases, the oscillation amplitude of the laboratory model, at resonance condition, together with the value of instant extracted power were found to be considerably large. For what concern multiple devices to be deployed in arrays of defined fixed area, it would be of interest to investigate the influence between floaters' radius or mass to the annual mooring load cycles and energy production. Similar methods to the one used in this project could be developed for this purpose.

Appendix A

Appendix

A.1 Experimental work

All details of the experimental work are explained in Chapter 4. In this section extra information on experiments and detailed results are provided.

A.1.1 Session 1

In Tables A.1 and A.2 are reported details of most reliable tests performed during Session 1 with Model 1.

Test no.	Omega	Ampl.(mm)	PTO	Fp(N)	Description
13bis	6.28	13.69	na	1.605	Regular waves
14bis	6.28	13.64	no	1.6	Regular waves
15bis	free osc.	free osc.	na	1.6	H. f.o. Z(0)=1, Z(0)=3 cm
16bis	free osc.	free osc.	na	1.56	H. f.o. Z(0)=1, Z(0)=3 cm
17bis	free osc.	free osc.	no	1.56	H. f.o. Z(0)=1, Z(0)=3 cm
18bis	free osc.	free osc.	no	1.52	H. f.o. Z(0)=1, Z(0)=3 cm
19bis	free osc.	free osc.	na	1.52	Surge f.o. X(0)=5, X(0)=10 cm
20bis	free osc.	free osc.	no	1.52	Surge f.o. X(0)=5, X(0)=10 cm
21bis	2.52	13.07	yes	1.56	Regular waves
22bis	5.66	12.54	yes	1.63	Regular waves
23bis	7.54	12.18	yes	1.57	Regular waves
24bis	8.79	12.58	yes	1.57	Regular waves
25bis	9.41	12.58	yes	1.57	Regular waves
26bis	10.03	12.59	yes	1.57	Regular waves
27bis	10.74	12.79	yes	1.56	Regular waves
28bis	11.32	12.60	yes	1.56	Regular waves
29bis	11.94	12.61	yes	1.56	Regular waves
30bis	free osc.	free osc.	yes	1.56	H. f.o. Z(0)=1, Z(0)=3 cm
31bis	free osc.	free osc.	no	1.56	H. f.o. Z(0)=1, Z(0)=3 cm
32bis	free osc.	free osc.	no	1.56	Surge f.o. X(0)=5, X(0)=10 cm
33bis	free osc.	free osc.	yes	1.56	Surge f.o. X(0)=5, X(0)=10 cm
34bis	free osc.	free osc.	yes	1.56	Surge f.o. X(0)=15 cm
35bis	free osc.	free osc.	no	1.56	Surge f.o. X(0)=15 cm
36bis	2.45	10.04	yes	1.6	Regular waves
37bis	5.66	12.57	yes	1.55	Wrong test
38bis	8.84	12.50	no	1.57	Regular waves
39bis	8.83	12.49	yes	1.57	Regular waves
40bis	7.54	12.31	yes	1.57	Regular waves
41bis	8.80	12.63	yes	1.57	Regular waves
42bis	9.40	12.59	yes	1.57	Regular waves
43bis	9.98	12.63	yes	1.57	Regular waves

Table A.1: Description of tests (1/2)

Test no.	Omega	Ampl.(mm)	PTO	Fp(N)	Description
44bis	na	na	yes	1.57	Wrong test
45bis	10.51	12.69	yes	1.57	Regular waves
46bis	na	na	yes	1.57	Wrong test
47bis	1.89	12.59	yes	1.6	Regular waves
48bis	2.50	10.98	yes	1.6	Regular waves
49bis	3.77	12.59	yes	1.6	Regular waves
50bis	5.66	12.61	yes	1.6	Regular waves
51bis	7.54	12.45	yes	1.6	Regular waves
52bis	8.78	12.62	yes	1.6	Regular waves
53bis	9.41	12.59	yes	1.6	Regular waves
54bis	10.02	12.74	yes	1.6	Regular waves
55bis	10.45	12.72	yes	1.6	Regular waves
56bis	11.35	12.58	yes	1.6	R.w., experienced high pitch
57bis	11.92	12.55	yes	1.6	R.w., experienced high pitch
58bis	2.51	11.33	yes	1.6	Regular waves
59bis	4.64	11.61	yes	1.6	Regular waves
60bis	5.84	12.98	yes	1.59	R.w.;different PTO force
61bis	7.79	12.26	yes	1.58	Regular waves
62bis	4.64	11.82	yes	1.58	Regular waves
63bis	5.84	12.73	yes	1.58	Regular waves
64bis	7.79	12.62	yes	1.57	Regular waves
65bis	4.65	12.24	yes	1.57	Regular waves
66bis	4.65	12.22	yes	1.55	Regular waves
67bis	5.84	12.65	yes	1.5	Regular waves
68bis	8.80	12.61	yes	1.5	Regular waves
69bis	4.64	12.24	yes	1.5	Regular waves
70bis	5.84	12.67	yes	1.5	Regular waves
71bis	7.79	12.59	yes	1.5	Regular waves
72bis	4.65	12.24	yes	1.5	R.w.; same par. as Test no.69bis
73bis	4.65	12.23	yes	1.5	Regular waves
74bis	5.85	12.66	yes	1.53	Regular waves
75bis	7.80	12.59	yes	1.55	Regular waves
76bis	irr.sea	irr.sea	yes	1.58	Hs=2 Tp=10 γ=2.6 gain=1.9
77bis	irr.sea	irr.sea	yes	1.58	Hs=2 Tp=10 γ=2.6 gain=1.9
78bis	irr.sea	irr.sea	yes	1.58	Hs=2 Tp=10 γ=2.6 gain=1
79bis	irr.sea	irr.sea	yes	1.58	Hs=2 Tp=7.5 γ=2.6 gain=1
80bis	irr.sea	irr.sea	yes	1.58	Hs=2 Tp=12.5 γ=2.6 gain=1
81bis	irr.sea	irr.sea	yes	1.58	Hs=2 Tp=10 γ=2.6 gain=1

Table A.2: Description of tests (2/2)

A.1.2 Session 2

In Table A.3 are reported details of tests run with Model 2 during Session 2.

Test no.	Cpto	Input in wavemaker		Test no.	Cpto	Input in wavemaker	
		Frequency(Hz)	Amplitude(m)			Frequency(Hz)	Amplitude(m)
1	off	0.3	0.02	38	on	1.4	0.04
2	off	0.4	0.02	39	on	0.7	0.04
3	off	0.5	0.02	40	on	0.7	0.08
4	off	0.6	0.02	41	on	0.3	0.08
5	off	0.7	0.02	42	on	0.4	0.08
6	off	0.2	0.02	43	on	0.5	0.08
7	off	0.8	0.02	44	on	0.6	0.08
8	off	0.9	0.02	45	on	0.8	0.08
9	off	1	0.02	46	on	0.9	0.08
10	off	1.1	0.02	47	on	1	0.08
11	off	1.2	0.02	48	on	1.1	0.08
12	on	0.3	0.02	49	on	1.2	0.08
13	on	0.4	0.02	50	on	1.3	0.08
14	on	0.5	0.02	51	on	1.4	0.08
15	on	0.6	0.02	52	on		0.08
16	on	0.7	0.02	53	on	0.8	0.03
17	on	0.8	0.02	54	on	1	0.03
18	on	0.9	0.02	55	on	1.2	0.03
19	on	1	0.02	56	on	1.4	0.03
20	on	1.1	0.02	57	on	1.5	0.03
21	on	1.2	0.02	58	on	0.5	0.04
22	on	1.3	0.02	59	on	0.7	0.04
23	on	1.4	0.02	60	on	0.9	0.04
24	on	NA		61	on	1.1	0.04
25	on	0.9	0.03	62	on	NA	
26	off	0.9	0.03	63	on	0.5	0.08
27	on	0.3	0.04	64	on	0.7	0.08
28	on	0.4	0.04	65	on	0.9	0.08
29	on	0.5	0.04	66	on	NA	
30	on	0.6	0.04	67	on	0.3	0.16
31	on	0.6	0.04	68	on	0.5	0.11
32	on	0.8	0.04	69	on	0.7	0.11
33	on	0.9	0.04	70	on	0.9	0.11
34	on	1	0.04	71	on	0.5	0.11
35	on	1.1	0.04	72	on	Hs=0.091	Tp=1.206
36	on	1.2	0.04	73	on	Free osc.	
37	on	1.3	0.04				

Table A.3: Session 2 (Model 2) tests overview.

A.1.3 Session 3

Compared to the other sessions, during Session 3, the most accurate empirical data was acquired. Over 400 regular waves tests were carried out. Further 35 tests related irregular sea states and free oscillations tests. Here in this section. All relevant results of regular waves tests not reported in Chapter 4 are reported. All results are also reported

in tabular form. In Tables A.4 to A.20 are reported results for all configurations tested during Session 3. These results concern heave, surge, wave probe, load cell, mooring displacement and RAOs amplitudes and frequencies related to the physical models in resonance with waves. Also, input parameters and their real scale corresponding values are reported.

Half-immersed spherical PA model tests results

In Figures A.1, 4.49 and Figure A.2 are shown the results of 3 different level of PTO force simulated. This force varied according to the 3 levels of damping chosen. The *low damping* value is 25 % lower than the *normal damping* value and the *high damping* is 25% more than the *normal damping* value. The *normal damping* value was equal to 40 kg/s ($2.5 \cdot 10^5$ kg/s) at real-scale) which in dimensionless form (C^*) corresponds to the value of 0.5. These and results of all other configurations tested are also reported in tabular form, in the following tables.

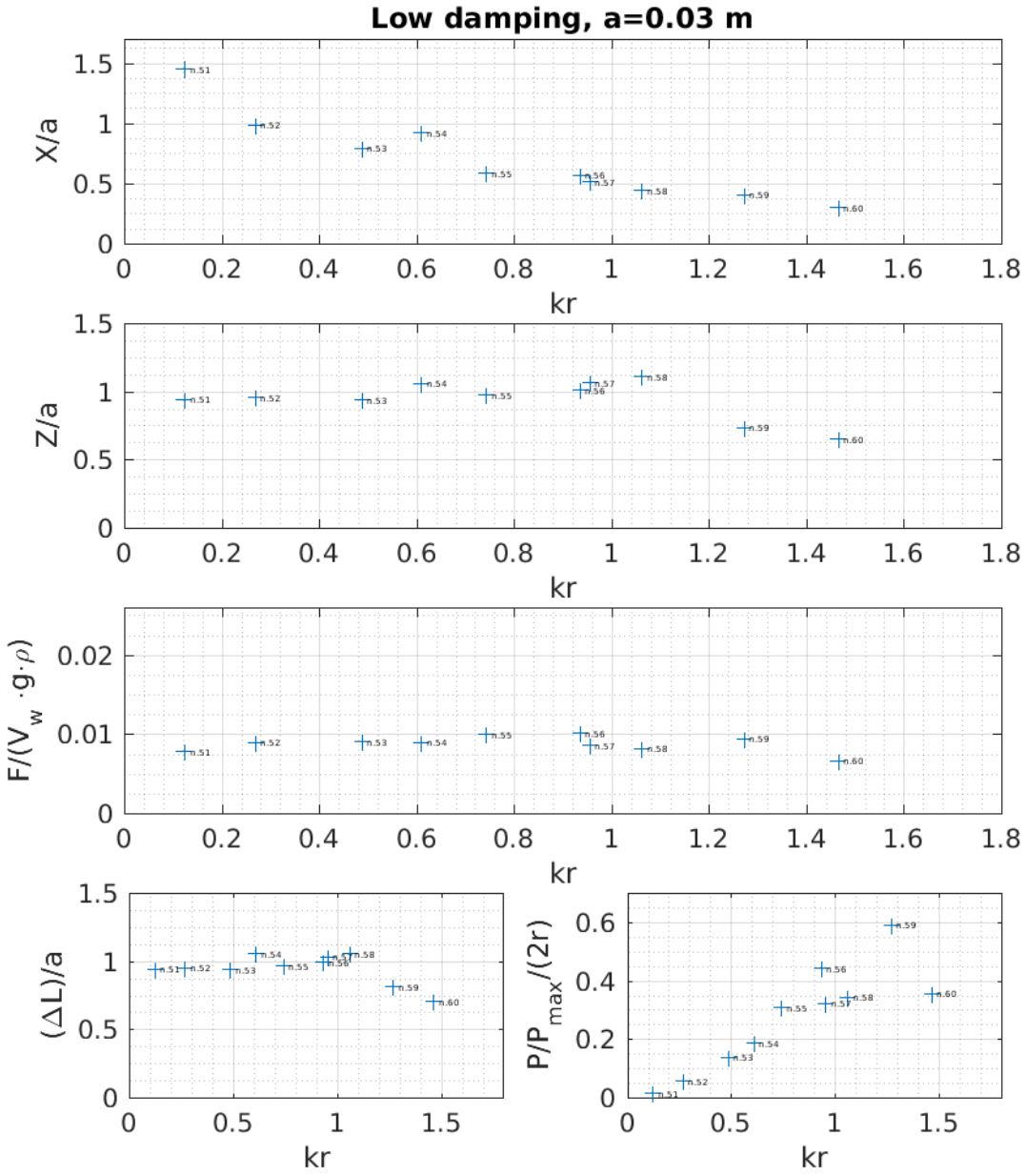

Figure A.1: Experiments results related to the *low damping* configuration of half-immersed PA in regular waves of amplitude a=0.03 m.

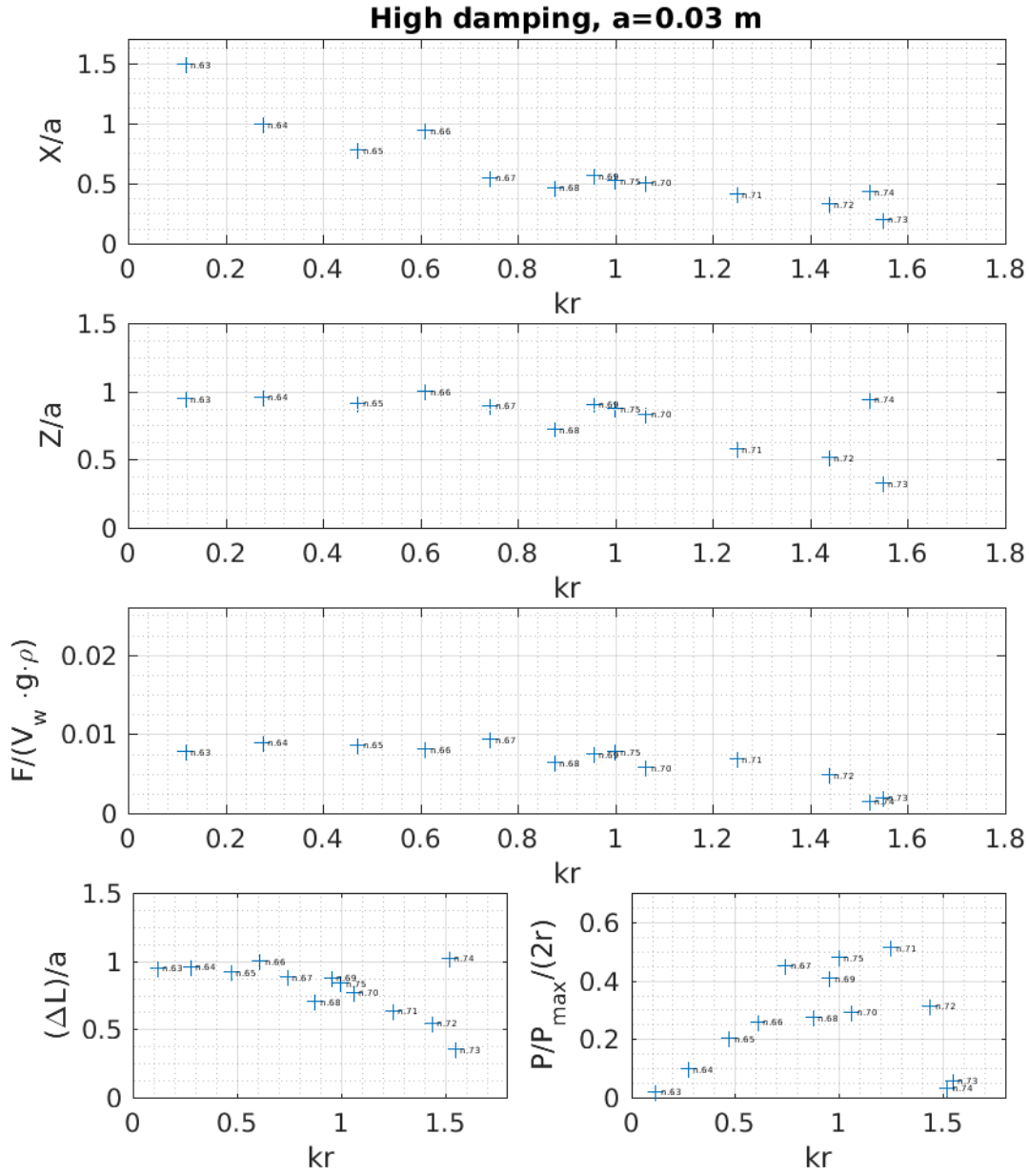

Figure A.2: Experiments results related to the *high damping* configuration of half-immersed PA in regular waves of amplitude a=0.03 m.

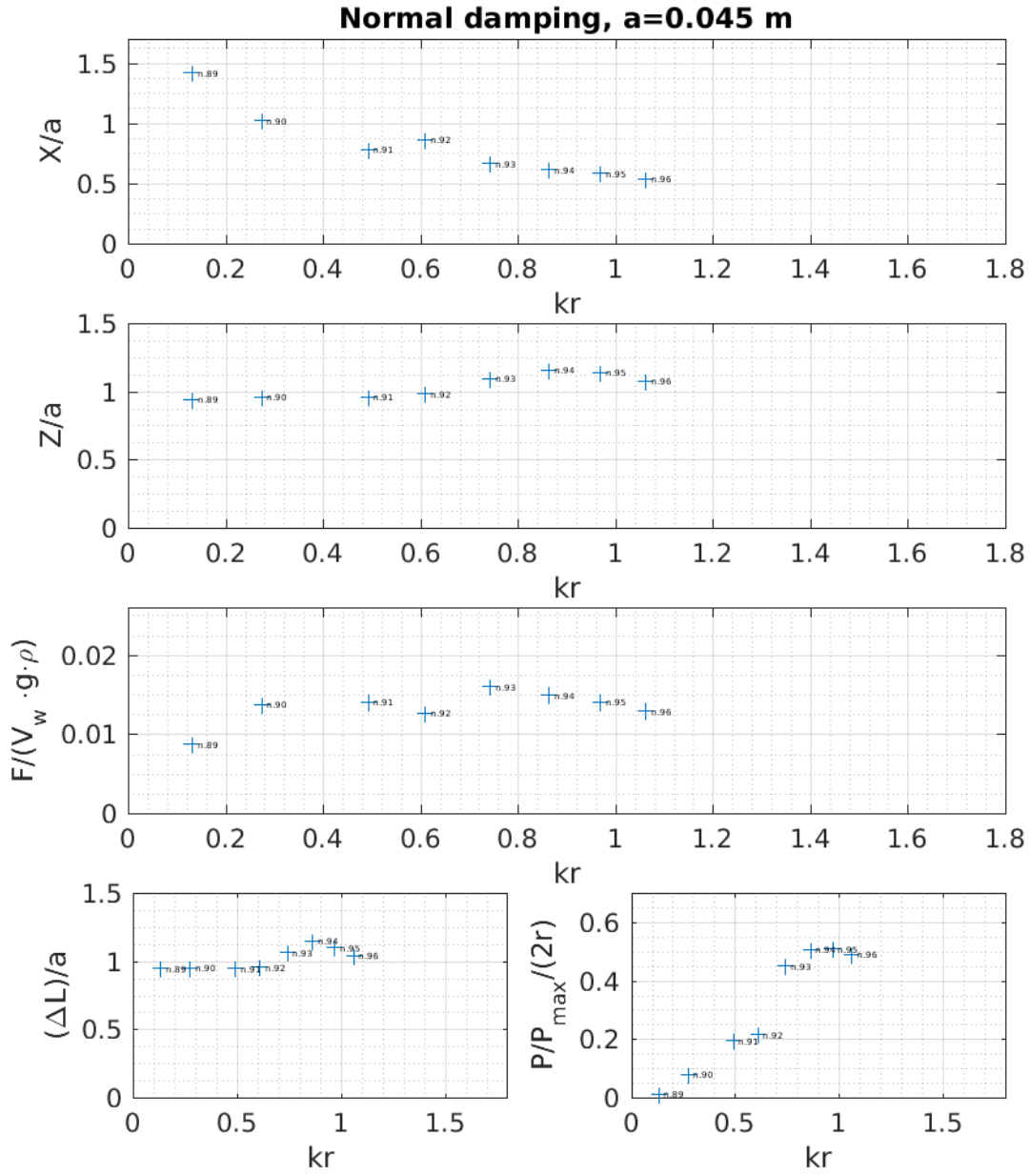

Figure A.3: Experiments results related to the *normal damping* configuration of half-immersed PA in regular waves of amplitude a=0.045 m.

Test no.		39	40	41	42	43	44	45	46	47	48	49	50
Descr.		CptoN=s	CptoN=s	CptoN=s	CptoN=s	CptoN=s	CptoN=s	CptoN=s	CptoN=s	CptoN=s	CptoN=s	CptoN=s	CptoN=s
Waves ampl. real sc.	(m)	1.000	1.000	1.000	1.000	1.000	1.000	1.000	1.000	1.000	1.000	1.000	1.000
Waves ang. freq. r.s.	(rad/s)	0.900	1.000	1.100	1.150	1.200	1.300	1.400	1.500	1.600	0.400	0.600	0.800
Freq.	(Hz)	0.143	0.159	0.175	0.183	0.191	0.207	0.223	0.239	0.255	0.064	0.095	0.127
Digital gain	n.d.	0.900	1.100	1.500	1.700	2.100	2.100	2.100	2.100	2.100	-0.300	0.100	0.800
Heave	ampl.(mm)	29.077	33.154	30.143	30.457	25.852	26.916	18.090	10.904	8.847	27.582	31.408	30.045
	ang.freq.(rad/s)	5.156	5.748	6.320	6.620	6.866	7.455	8.038	8.306	7.944	2.307	3.449	4.581
	phase(rad)	4.160	2.034	0.733	1.428	2.200	2.495	1.277	4.541	0.812	0.924	2.598	0.864
	offset	-0.062	-0.175	-0.396	-0.708	-0.937	-1.260	-1.446	-1.521	-1.807	-0.956	-0.685	-0.339
	freq.(Hz)	0.821	0.915	1.006	1.054	1.093	1.186	1.279	1.322	1.264	0.367	0.549	0.729
Surge	ampl.(mm)	26.538	23.119	18.527	17.521	13.383	14.800	10.583	9.791	6.097	40.456	32.375	26.778
	ang.freq.(rad/s)	5.154	5.792	6.293	6.586	6.882	7.469	8.010	8.380	8.650	2.293	3.453	4.614
	phase(rad)	-0.393	3.781	2.844	3.433	4.283	4.866	4.382	1.405	3.137	2.483	4.248	-0.165
	offset	1121.780	1121.780	1106.180	1092.150	1100.920	1028.510	1051.010	1055.910	1053.060	1123.550	1129.490	1125.130
	freq.(Hz)	0.820	0.922	1.002	1.048	1.095	1.189	1.275	1.334	1.377	0.365	0.550	0.734
Inline sonic probe	ampl.(mm)	29.421	35.189	33.778	30.245	26.224	37.947	30.826	28.950	32.138	29.694	32.928	33.296
	ang.freq.(rad/s)	5.160	5.748	6.327	6.606	6.872	7.459	8.019	8.464	8.277	2.307	3.444	4.582
	phase(rad)	3.979	2.088	0.961	1.664	2.303	3.427	2.319	-0.069	1.634	0.891	2.552	4.536
	offset	-208.636	-208.298	-207.677	-207.580	-207.902	-205.835	-206.233	-205.389	-204.549	-209.591	-209.659	-209.409
	freq.(Hz)	0.821	0.915	1.007	1.051	1.094	1.187	1.276	1.347	1.317	0.367	0.548	0.729
Load cell	ampl.(N)	2.122	2.420	2.167	2.206	1.817	2.221	1.509	0.887	0.740	1.988	2.274	2.181
	ang.freq.(rad/s)	5.155	5.749	6.317	6.619	6.862	7.455	8.034	8.373	7.950	2.308	3.449	4.583
	phase(rad)	5.055	3.526	4.997	5.194	4.335	3.923	-0.020	0.569	3.540	1.976	3.542	3.686
	offset	26.460	26.475	26.490	26.508	26.511	26.755	26.550	26.528	26.516	26.440	26.454	26.456
	freq.(Hz)	0.820	0.915	1.005	1.054	1.092	1.187	1.279	1.333	1.265	0.367	0.549	0.729
Mooring displ.	ampl.(mm)	28.957	32.999	29.199	29.544	24.452	29.590	19.890	11.333	9.760	27.695	31.316	29.828
	ang.freq.(rad/s)	5.154	5.747	6.316	6.619	6.864	7.456	8.034	8.363	7.945	2.308	3.449	4.582
	phase(rad)	4.035	1.887	0.565	1.248	2.033	2.299	1.075	4.231	0.696	0.855	2.513	4.415
	offset	101.207	101.388	101.221	101.296	101.198	104.675	101.962	101.626	101.351	100.603	100.780	100.755
	freq.(Hz)	0.820	0.915	1.005	1.053	1.093	1.187	1.279	1.331	1.264	0.367	0.549	0.729
Heave RAO	n.d	0.988	0.942	0.892	1.007	0.986	0.709	0.587	0.377	0.275	0.929	0.954	0.902
Surge RAO	n.d.	0.902	0.657	0.548	0.579	0.510	0.390	0.343	0.338	0.190	1.362	0.983	0.804

Table A.4: Tests of half-immersed floater Session 3 (1:33 scale model), where PTO damping of c.a. 40 kg/s was simulated. This corresponds to the standard damping value used, i.e. ca. $2.5 \cdot 10^5$ kg/s, at real-scale.

Test no.		12	13	14	15	16	17	18	19	20	21	22	23	24
Descr.		No Cpto	No Cpto	No Cpto	No Cpto	No Cpto	No Cpto	No Cpto	No Cpto	No Cpto	No Cpto	No Cpto	No Cpto	No Cpto
Waves ampl. real sc.	(m)	1.000	1.000	1.000	1.000	1.000	1.000	1.000	1.000	1.000	1.000	1.000	1.000	1.000
Waves ang. freq. r.s.	(rad/s)	0.400	0.600	0.800	0.900	1.000	1.100	1.200	1.300	1.400	1.500	1.600	1.700	1.150
Freq.	(Hz)	0.064	0.095	0.127	0.143	0.159	0.175	0.191	0.207	0.223	0.239	0.255	0.271	0.183
Digital gain	n.d.	off	off	off	off	off	off	off	off	off	off	off	off	off
Heave	ampl.(mm)	27.596	30.597	29.527	29.896	36.239	39.557	31.784	39.298	27.374	16.955	10.840	20.720	38.208
	ang.freq.(rad/s)	2.306	3.446	4.585	5.140	5.770	6.330	6.900	7.438	7.970	8.358	8.070	7.396	6.565
	phase(rad)	5.311	2.597	3.193	0.637	3.884	-0.493	4.762	4.232	-0.149	-0.735	3.885	1.400	4.935
	offset	1.043	1.195	1.398	1.506	1.421	1.250	0.503	0.042	-0.395	-0.847	-0.238	-0.806	0.039
	freq.(Hz)	0.367	0.549	0.730	0.818	0.918	1.007	1.098	1.184	1.269	1.330	1.284	1.177	1.045
Surge	ampl.(mm)	40.234	32.128	26.168	26.630	20.743	18.198	12.240	15.633	9.975	8.600	7.414	9.722	16.620
	ang.freq.(rad/s)	2.284	3.449	4.643	5.077	5.773	6.337	6.876	7.445	8.006	8.358	8.459	7.875	6.335
	phase(rad)	0.742	4.187	-0.330	2.306	5.579	1.316	0.580	0.420	2.297	2.675	2.023	3.094	0.764
	offset	1123.860	1123.720	1134.420	1133.300	1138.140	1119.030	1105.220	1006.920	1015.940	1014.840	1091.450	1049.930	1089.630
	freq.(Hz)	0.364	0.549	0.739	0.808	0.919	1.009	1.094	1.185	1.274	1.330	1.346	1.253	1.008
Inline sonic probe	ampl.(mm)	29.517	32.470	33.027	28.781	34.702	34.628	26.542	39.772	33.209	26.751	38.583	31.215	30.660
	ang.freq.(rad/s)	2.305	3.447	4.596	5.166	5.755	6.313	6.910	7.473	8.017	8.489	9.512	10.992	6.622
	phase(rad)	5.278	2.544	4.323	0.299	3.796	-0.459	4.804	5.452	0.642	1.441	5.528	4.355	5.039
	offset	-208.964	-208.954	-208.770	-208.514	-208.278	-207.566	-207.741	-205.137	-205.692	-205.796	-205.554	-202.165	-208.338
	freq.(Hz)	0.367	0.549	0.731	0.822	0.916	1.005	1.100	1.189	1.276	1.351	1.514	1.749	1.054
Load cell	ampl.(N)	1.982	2.211	2.156	2.180	2.632	2.890	2.278	3.230	2.254	1.406	0.726	1.676	2.735
	ang.freq.(rad/s)	2.306	3.446	4.588	5.137	5.764	6.336	6.899	7.442	7.981	8.362	7.891	7.325	6.558
	phase(rad)	-0.378	2.356	2.151	-0.189	1.080	0.981	4.229	5.412	0.609	4.085	1.772	1.230	2.325
	offset	25.514	25.508	25.528	25.541	25.537	25.547	25.648	25.890	25.704	25.718	25.490	25.630	25.619
	freq.(Hz)	0.367	0.549	0.730	0.818	0.917	1.008	1.098	1.184	1.270	1.331	1.256	1.166	1.044
Mooring displ.	ampl.(mm)	27.747	30.710	29.732	29.798	35.768	39.054	30.642	43.293	29.937	18.639	9.621	22.149	36.935
	ang.freq.(rad/s)	2.306	3.446	4.587	5.137	5.763	6.335	6.899	7.443	7.987	8.359	7.807	7.318	6.560
	phase(rad)	5.242	2.507	4.326	0.530	3.774	-0.643	4.706	4.050	5.167	5.365	-0.309	1.275	4.804
	offset	105.201	105.205	105.027	105.182	104.952	105.215	106.423	110.025	107.154	106.213	103.030	104.622	104.909
	freq.(Hz)	0.367	0.548	0.730	0.818	0.917	1.008	1.098	1.185	1.271	1.330	1.242	1.165	1.044
Heave RAO	n.d	0.935	0.942	0.894	1.039	1.044	1.142	1.198	0.988	0.824	0.634	0.281	0.664	1.246
Surge RAO	n.d.	0.686	0.952	1.128	1.123	1.747	2.174	2.597	2.514	2.744	1.972	1.462	2.131	2.299

Table A.5: Tests of half-immersed floater Session 3 (1:33 scale model) when the servomotor was set to off (no induced damping).

Test no.		51	52	53	54	55	56	57	58	59	60	61	62
Descr.		CptoN=L	CptoN=L	CptoN=L	CptoN=L	CptoN=L	CptoN=L	CptoN=L	CptoN=L	CptoN=L	CptoN=L	CptoN=L	CptoN=L
Waves ampl. real sc.	(m)	1.000	1.000	1.000	1.000	1.000	1.000	1.000	1.000	1.000	1.000	1.000	1.000
Waves ang. freq. r.s.	(rad/s)	0.400	0.600	0.800	0.900	1.000	1.100	1.150	1.200	1.300	1.400	1.500	1.600
Freq.	(Hz)	0.064	0.095	0.127	0.143	0.159	0.175	0.183	0.191	0.207	0.223	0.239	0.255
Digital gain	n.d.	-0.300	-0.300	0.000	0.200	0.500	0.700	0.900	1.000	1.200	1.200	1.200	1.200
Heave	ampl.(mm)	25.322	31.193	31.258	31.156	33.410	36.133	33.400	27.454	31.231	20.641	15.566	7.977
	ang.freq.(rad/s)	2.300	3.444	4.594	5.176	5.761	6.318	6.619	6.898	7.462	8.035	8.351	8.280
	phase(rad)	0.788	2.148	5.515	2.905	3.215	4.842	4.389	4.560	4.477	1.999	0.601	1.992
	offset	-0.990	-0.670	-0.488	-0.516	-0.403	-0.633	-0.717	-1.255	-1.509	-1.463	-1.579	-1.359
	freq.(Hz)	0.366	0.548	0.731	0.824	0.917	1.006	1.053	1.098	1.188	1.279	1.329	1.318
Surge	ampl.(mm)	41.449	32.407	25.295	26.913	22.926	18.988	16.907	12.700	14.989	20.641	8.685	-6.704
	ang.freq.(rad/s)	2.296	3.453	4.592	5.127	5.800	6.317	6.599	6.910	7.479	8.035	8.741	8.280
	phase(rad)	2.187	3.803	0.879	1.164	4.937	0.523	0.029	0.404	0.680	1.999	3.636	1.822
	offset	1123.970	1129.640	1130.450	1139.020	1128.280	1105.900	1099.640	1093.410	1017.730	-1.463	1033.330	1061.380
	freq.(Hz)	0.365	0.550	0.731	0.816	0.923	1.005	1.050	1.100	1.190	1.279	1.391	1.318
Inline sonic probe	ampl.(mm)	27.031	33.320	33.884	29.504	35.893	34.641	30.777	27.021	40.495	32.539	33.950	30.078
	ang.freq.(rad/s)	2.299	3.448	4.594	5.166	5.760	6.315	6.601	6.891	7.472	8.030	8.763	9.384
	phase(rad)	0.753	2.057	5.491	5.395	3.204	5.073	4.522	4.860	-0.557	3.184	2.536	2.177
	offset	-209.583	-209.484	-209.205	-209.076	-208.398	-207.940	-208.113	-208.122	-205.688	-206.199	-205.035	-206.213
	freq.(Hz)	0.366	0.549	0.731	0.822	0.917	1.005	1.051	1.097	1.189	1.278	1.395	1.494
Load cell	ampl.(N)	1.822	2.256	2.278	2.281	2.442	2.629	2.421	1.920	2.558	1.703	1.282	0.640
	ang.freq.(rad/s)	2.299	3.444	4.594	5.175	5.759	6.318	6.618	6.899	7.464	8.038	8.367	8.401
	phase(rad)	2.324	5.377	2.147	4.393	3.984	4.290	4.707	-0.713	-0.470	2.137	4.664	5.337
	offset	26.447	26.457	26.470	26.482	26.469	26.496	26.508	26.525	26.816	26.563	26.621	26.536
	freq.(Hz)	0.366	0.548	0.731	0.824	0.917	1.006	1.053	1.098	1.188	1.279	1.332	1.337
Mooring displ.	ampl.(mm)	25.264	31.121	31.253	31.180	33.180	35.387	32.418	25.701	34.031	22.634	17.088	8.338
	ang.freq.(rad/s)	2.299	3.444	4.594	5.176	5.760	6.318	6.617	6.899	7.463	8.038	8.358	8.348
	phase(rad)	0.723	2.064	5.407	5.559	3.079	4.684	4.239	4.431	4.305	1.802	0.451	1.661
	offset	100.671	100.732	100.832	100.867	100.741	101.064	101.071	101.146	105.220	101.720	102.349	101.129
	freq.(Hz)	0.366	0.548	0.731	0.824	0.917	1.006	1.053	1.098	1.188	1.279	1.330	1.329
Heave RAO	n.d	0.937	0.936	0.922	1.056	0.931	1.043	1.085	1.016	0.771	0.634	0.458	0.265
Surge RAO	n.d.	1.533	0.973	0.747	0.912	0.639	0.548	0.549	0.470	0.370	0.634	0.256	-0.223

Table A.6: Tests of half imm. floater Session 3 (1:33 scale model), where PTO damping of c.a. 30 kg/s was simulated. This correspond to the *low damping* value used.

Test no.		63	64	65	66	67	68	69	70	71	72	73	75
Descr.		CptoN=H	CptoN=H	CptoN=H	CptoN=H	CptoN=H	CptoN=H	CptoN=H	CptoN=H	CptoN=H	CptoN=H	CptoN=H	CptoN=H
Waves ampl. real sc.	(m)	1	1	1	1	1	1	1	1	1	1	1	1
Waves ang. freq. r.s.	(rad/s)	0.400	0.600	0.800	0.900	1.000	1.100	1.150	1.200	1.300	1.400	1.500	1.150
Freq.	(Hz)	0.064	0.095	0.127	0.143	0.159	0.175	0.183	0.191	0.207	0.223	0.239	0.183
Digital gain	n.d.	0.400	0.900	1.400	1.700	2.100	2.400	2.600	3.000	3.000	3.000	3.000	2.600
Heave	ampl.(mm)	28.084	31.404	31.162	27.686	32.669	25.197	27.822	20.624	21.918	17.796	10.456	27.783
	ang.freq.(rad/s)	2.308	3.448	4.584	5.164	5.720	6.318	6.634	6.872	7.445	7.988	8.781	6.610
	phase(rad)	1.139	1.071	3.233	5.007	2.491	2.949	5.383	3.165	4.082	0.658	-0.214	-0.388
	offset	-0.789	-0.883	-0.264	-0.352	-0.578	-1.131	-0.924	-1.308	-1.390	-1.418	-1.607	-0.699
	freq.(Hz)	0.367	0.549	0.730	0.822	0.910	1.006	1.056	1.094	1.185	1.271	1.398	1.052
Surge	ampl.(mm)	39.483	32.423	27.340	26.563	21.672	17.516	16.204	11.587	14.212	10.549	8.966	17.259
	ang.freq.(rad/s)	2.296	3.451	4.626	5.174	5.720	6.346	6.558	6.978	7.440	7.977	8.720	6.583
	phase(rad)	2.759	2.754	4.818	1.686	-0.336	6.365	1.152	5.052	-0.740	3.641	2.865	1.679
	offset	1123.440	1123.470	1124.130	1119.250	1091.450	1105.970	1092.390	1100.340	1040.600	1048.710	1035.180	1089.700
	freq.(Hz)	0.365	0.549	0.736	0.824	0.910	1.010	1.044	1.111	1.184	1.270	1.388	1.048
Inline sonic probe	ampl.(mm)	30.016	32.892	33.502	28.910	37.358	34.785	31.266	26.374	40.151	31.399	32.235	31.045
	ang.freq.(rad/s)	2.307	3.444	4.597	5.175	5.733	6.321	6.620	6.892	7.439	8.025	8.773	6.606
	phase(rad)	1.125	1.039	3.245	-0.246	4.181	4.603	-0.706	3.546	4.124	1.627	1.752	-0.085
	offset	-209.667	-210.142	-209.504	-209.468	-208.436	-208.092	-208.344	-208.709	-206.084	-207.054	-205.144	-208.599
	freq.(Hz)	0.367	0.548	0.732	0.824	0.913	1.006	1.054	1.097	1.184	1.277	1.396	1.051
Load cell	ampl.(N)	2.022	2.269	2.264	2.011	2.446	1.814	2.008	1.371	1.809	1.487	0.868	2.000
	ang.freq.(rad/s)	2.309	3.449	4.583	5.162	5.739	6.311	6.636	6.898	7.443	7.977	8.777	6.622
	phase(rad)	1.383	2.506	3.722	3.214	5.398	2.684	1.052	2.826	4.458	1.360	-0.226	3.344
	offset	26.440	26.434	26.451	26.445	26.484	26.419	26.439	26.434	26.624	26.502	26.521	26.391
	freq.(Hz)	0.367	0.549	0.729	0.822	0.913	1.004	1.056	1.098	1.185	1.270	1.397	1.054
Mooring displ.	ampl.(mm)	28.230	31.503	31.216	27.593	33.339	24.604	26.960	18.375	24.137	19.658	11.425	26.861
	ang.freq.(rad/s)	2.308	3.448	4.582	5.164	5.738	6.312	6.633	6.903	7.443	7.976	8.785	6.621
	phase(rad)	1.076	0.979	3.108	-0.302	3.789	4.060	5.181	2.817	2.874	0.462	-0.489	5.665
	offset	100.320	100.380	100.577	100.438	101.094	100.138	100.619	100.599	103.669	101.936	102.044	100.643
	freq.(Hz)	0.367	0.549	0.729	0.822	0.913	1.005	1.056	1.099	1.185	1.269	1.398	1.054
Heave RAO	n.d	0.936	0.955	0.930	0.958	0.874	0.724	0.890	0.782	0.546	0.567	0.324	0.895
Surge RAO	n.d.	0.936	0.955	0.930	0.958	0.874	0.724	0.890	0.782	0.546	0.567	0.324	0.895

Table A.7: Tests of half imm. floater Session 3 (1:33 scale model), where PTO damping of c.a. 50 kg/s was simulated. This correspond to the *high damping* value used.

Test no.		99	100	101	102	103	104	105	106	107	108
Descr.		a=2a	a=2a	a=2a	a=2a	a=2a	a=2a	a=2a	a=2a	a=2a	a=2a
Waves ampl. real sc.	(m)	2	2	2	2	2	2	2	2	2	2
Waves ang. freq. r.s.	(rad/s)	0.4	0.6	0.8	0.9	1	1.1	1.15	1.2	1.3	1.15
Freq.	(Hz)	0.064	0.095	0.127	0.143	0.159	0.175	0.183	0.191	0.207	0.183
Digital gain	n.d.	-0.300	0.100	0.800	0.900	1.100	1.500	1.700	2.100	2.100	1.700
Heave	ampl.(mm)	56.916	64.681	67.609	57.203	73.794	87.081	62.724	65.545	46.044	67.504
	ang.freq.(rad/s)	2.307	3.444	4.597	5.163	5.734	6.319	6.605	6.879	7.442	6.596
	phase(rad)	1.291	0.221	4.329	3.216	1.793	4.638	4.776	0.507	1.691	0.223
	offset	-1.766	-1.313	-0.783	-0.727	0.287	-0.091	-1.874	-2.569	-4.035	-1.511
	freq.(Hz)	0.367	0.548	0.732	0.822	0.913	1.006	1.051	1.095	1.184	1.050
Surge	ampl.(mm)	83.161	68.919	54.989	51.275	45.208	41.649	35.386	30.923	23.442	34.765
	ang.freq.(rad/s)	2.291	2.779	4.597	5.163	5.740	6.319	6.590	6.870	7.442	6.596
	phase(rad)	2.937	2.702	3.486	4.946	3.699	0.497	4.206	2.816	4.340	2.221
	offset	1123.060	1127.460	1101.740	1095.280	1042.420	922.744	952.655	888.926	856.098	938.597
	freq.(Hz)	0.365	0.442	0.732	0.822	0.914	1.006	1.049	1.093	1.184	1.050
Inline sonic probe	ampl.(mm)	60.283	66.959	67.039	62.573	67.484	63.996	64.269	53.824	43.478	60.071
	ang.freq.(rad/s)	2.306	3.443	4.593	5.171	5.739	6.319	6.590	6.893	7.442	6.596
	phase(rad)	1.251	4.088	1.956	3.041	1.974	-0.442	12.437	2.219	3.486	1.748
	offset	-212.232	-211.934	-210.170	-209.595	-207.974	-211.229	-216.696	-207.121	-209.414	-207.074
	freq.(Hz)	0.367	0.548	0.731	0.823	0.913	1.006	1.049	1.097	1.184	1.050
Load cell	ampl.(N)	4.086	4.640	4.906	4.179	5.444	6.555	4.691	5.014	3.702	4.966
	ang.freq.(rad/s)	2.308	3.444	4.594	5.161	5.734	6.319	6.604	6.879	7.444	6.597
	phase(rad)	2.296	0.700	0.772	4.028	2.938	1.715	3.588	5.003	3.095	4.172
	offset	26.734	26.757	26.870	26.798	27.003	27.685	27.345	27.840	28.281	27.421
	freq.(Hz)	0.367	0.548	0.731	0.821	0.913	1.006	1.051	1.095	1.185	1.050
Mooring displ.	ampl.(mm)	56.242	63.207	66.852	56.674	74.598	91.405	63.428	71.395	49.409	67.780
	ang.freq.(rad/s)	2.307	3.444	4.593	5.164	5.733	6.324	6.609	6.876	7.448	6.604
	phase(rad)	1.205	4.033	1.712	3.001	1.579	4.316	4.477	0.199	1.320	0.236
	offset	106.610	106.982	108.310	107.142	110.059	121.968	114.791	122.245	128.103	116.472
	freq.(Hz)	0.367	0.548	0.731	0.822	0.912	1.007	1.052	1.094	1.185	1.051
Heave RAO	n.d	0.944	0.966	1.008	0.914	1.094	1.361	0.976	1.218	1.059	1.124
Surge RAO	n.d.	1.380	1.029	0.820	0.819	0.670	0.651	0.551	0.575	0.539	0.579

Table A.8: Tests of half imm. floater Session 3 (1:33 scale model), *standard damping* was simulated and waves amplitude was doubled (a=2m at real-scale).

Submerged spherical PA model tests results

In Figure A.4 are reported results in graphical form relative to the no motor configuration (submerged model) at Depth 2 with the second spring used.

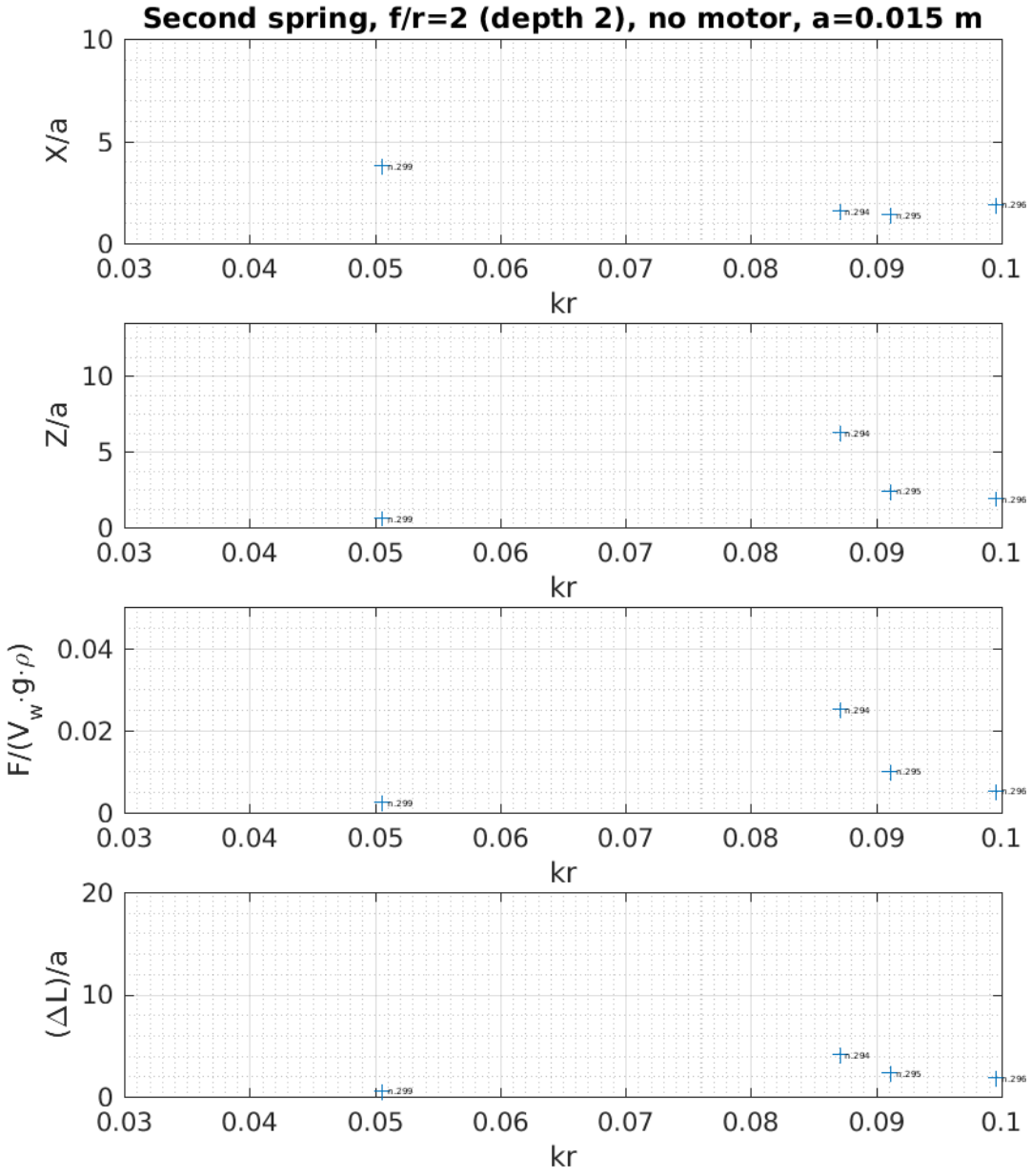

Figure A.4: Experiments results related to submerged spherical PA in regular waves of amplitude a=0.015 m when the servomotor was removed and the spring n.2 was used. For this configuration some tests were not done or not included in here because the floater was coming afloat and thus in those occasions the mooring line became slack giving misleading results.

Test no.		316	317	318	319	320	321	322	323	324	325	326
Descr.		Spring n.1	Spring n.1	Spring n.1	Spring n.1	Spring n.1	Spring n.1	Spring n.1	Spring n.1	Spring n.1	Spring n.1	Spring n.1
		Imm.1	Imm.1	Imm.1	Imm.1	Imm.1	Imm.1	Imm.1	Imm.1	Imm.1	Imm.1	Imm.1
Waves ampl. real sc.	(m)	0.990	0.990	0.990	0.990	0.990	0.495	0.495	0.495	0.495	0.495	0.000
Waves ang. freq. r.s.	(rad/s)	0.405	0.798	0.995	1.203	1.400	0.405	0.798	0.995	1.203	1.400	1.597
R.s. freq.	(Hz)	0.064	0.127	0.158	0.191	0.223	0.064	0.127	0.158	0.191	0.223	0.254
Floater imm.	(m)	-0.350	-0.350	-0.350	-0.350	-0.350	-0.350	-0.350	-0.350	-0.350	-0.350	-0.350
Digital gain	n.d.	no mot.	no mot.	no mot.	no mot.	no mot.	no mot.	no mot.	no mot.	no mot.	no mot.	no mot.
Input in wave gen.	freq.(Hz)	0.370	0.730	0.910	1.100	1.280	0.370	0.730	0.910	1.100	1.280	1.460
	ampl.(m)	0.030	0.030	0.030	0.030	0.030	0.015	0.015	0.015	0.015	0.015	
	ang.freq.(rad/s)	2.325	4.587	5.718	6.912	8.042	2.325	4.587	5.718	6.912	8.042	9.173
Heave	ampl.(mm)	27.478	18.451	12.072	3.771	3.964	13.666	8.463	5.925	2.114	2.004	0.889
	ang.freq.(rad/s)	2.329	4.586	5.718	6.906	8.022	2.330	4.588	5.715	6.915	8.055	9.160
	phase(rad)	2.001	1.020	6.103	4.860	1.474	2.196	0.052	1.673	3.105	1.027	0.617
	offset	-349.025	-349.250	-345.156	-343.362	-340.626	-347.481	-347.711	-346.735	-346.469	-346.027	-346.213
	freq.(Hz)	0.371	0.730	0.910	1.099	1.277	0.371	0.730	0.909	1.101	1.282	1.458
Surge	ampl.(mm)	31.353	16.031	12.822	5.360	3.140	16.511	7.651	5.597	2.827	1.809	0.670
	ang.freq.(rad/s)	2.325	4.586	5.718	6.906	8.022	2.329	4.588	5.715	6.911	8.055	9.160
	phase(rad)	0.622	5.704	4.691	3.443	-0.124	0.833	4.729	0.185	1.494	59.052	5.490
	offset	293.436	282.800	296.312	284.543	281.906	280.855	282.421	280.997	279.670	279.703	279.417
	freq.(Hz)	0.370	0.730	0.910	1.099	1.277	0.371	0.730	0.909	1.100	1.282	1.458
Sonic probe(inline)	ampl.(mm)	28.203	31.206	33.556	29.366	28.293	13.776	15.126	16.697	12.659	12.442	13.681
	ang.freq.(rad/s)	2.325	4.585	5.718	6.906	8.025	2.330	4.586	5.717	6.911	8.046	9.160
	phase(rad)	1.923	0.933	-0.126	4.715	0.998	2.103	-0.035	1.592	2.523	0.210	-0.004
	offset	-377.631	-377.007	-376.179	-375.084	-372.348	-377.519	-377.276	-377.140	-377.282	-376.796	-376.199
	freq.(Hz)	0.370	0.730	0.910	1.099	1.277	0.371	0.730	0.910	1.100	1.281	1.458
Load cell	ampl.(N)	1.908	1.288	0.907	0.393	0.264	0.944	0.622	0.422	0.210	0.128	0.058
	ang.freq.(rad/s)	2.328	4.584	5.718	6.906	8.022	2.331	4.587	5.713	6.915	8.056	9.183
	phase(rad)	2.038	-0.252	4.350	6.106	5.026	2.511	5.127	2.841	-0.402	1.361	-0.132
	offset	37.872	37.941	38.167	38.240	38.435	37.951	37.984	38.025	38.036	38.096	38.074
	freq.(Hz)	0.371	0.730	0.910	1.099	1.277	0.371	0.730	0.909	1.101	1.282	1.462
Mooring displ.(mm)	ampl.(mm)	20.835	13.868	9.415	4.089	2.485	10.301	6.976	4.512	2.266	1.412	0.593
	ang.freq.(rad/s)	2.328	4.584	5.718	6.906	8.008	2.331	4.588	5.712	6.924	8.046	9.160
	phase(rad)	1.956	0.968	12.468	4.844	1.231	2.177	-0.012	1.659	2.894	0.865	0.924
	offset	372.726	373.715	376.143	373.540	375.498	369.726	370.197	370.423	370.446	371.175	371.041
	freq.(Hz)	0.370	0.730	0.910	1.099	1.275	0.371	0.730	0.909	1.102	1.281	1.458
Wave p. (upstream)	ampl.(mm)	25.344	30.657	28.009	30.290	25.406	12.411	14.885	13.225	15.015	16.242	13.228
	ang.freq.(rad/s)	2.324	4.586	5.716	6.915	8.050	2.331	4.587	5.721	6.915	8.049	9.182
	phase(rad)	-0.681	0.443	-0.448	0.614	-0.271	-0.445	-0.427	1.536	4.999	-0.165	4.339
	offset	-323.105	-322.532	-321.885	-320.149	-318.331	-323.316	-323.090	-322.890	-322.495	-321.822	-321.661
	freq.(Hz)	0.370	0.730	0.910	1.101	1.281	0.371	0.730	0.911	1.101	1.281	1.461
Heave RAO	n.d	0.974	0.591	0.360	0.128	0.140	0.992	0.560	0.355	0.167	0.161	0.065
Surge RAO	n.d	13.486	3.496	2.242	0.776	0.391	7.086	1.668	0.979	0.409	0.225	0.073

Table A.9: Tests of submerged floater Session 3 (1:33 scale model). Here results of tests where the immersion of floater was -0.345 m (Imm. value n.1) are shown. For these tests the servomotor was unplugged and regular waves of relatively high frequency were used. Heave resonance in this range of frequencies was not ocurring.

Test no.		22	18	16	17	19	20	21
Descr.		Imm.1	Imm.1	Imm.1	Imm.1	Imm.1	Imm.1	Imm.1
		floater went out of water	float. w. o. of w.				float. w. o. of w.	float. w. o. of w.
Waves ampl. real sc.	(m)	0.495	0.495	0.495	0.495	0.495	0.495	0.495
Waves ang. freq. r.s.	(rad/s)	0.175	0.197	0.219	0.241	0.208	0.186	0.153
Freq.	(Hz)	0.028	0.031	0.035	0.038	0.033	0.030	0.024
Floater imm.	(m)	-0.345	-0.345	-0.345	-0.345	-0.345	-0.345	-0.345
digital gain	n.d.	no motor	no motor	no motor	no motor	no motor	no motor	no motor
Input in wave gen	freq.(Hz)	0.160	0.180	0.200	0.220	0.190	0.170	0.140
	ampl.(m)	0.015	0.015	0.015	0.015	0.015	0.015	0.015
	ang.freq.(rad/s)	1.005	1.131	1.257	1.382	1.194	1.068	0.880
Heave	ampl.(mm)	151.897	67.932	36.957	27.125	38.382	76.353	62.673
	ang.freq.(rad/s)	1.039	1.142	1.255	1.381	1.214	1.061	0.879
	phase(rad)	3.573	0.134	4.890	4.541	3.469	5.349	0.796
	offset	-353.933	-343.941	-344.403	-344.613	-344.718	-344.520	-343.415
	freq.(Hz)	0.165	0.182	0.200	0.220	0.193	0.169	0.140
Surge	ampl.(mm)	54.883	39.475	51.219	26.501	30.188	40.528	68.247
	ang.freq.(rad/s)	1.000	1.142	1.255	1.381	1.189	1.061	0.865
	phase(rad)	0.913	1.541	0.187	2.546	2.451	2.946	2.959
	offset	314.347	306.250	307.248	306.232	304.486	312.008	307.715
	freq.(Hz)	0.159	0.182	0.200	0.220	0.189	0.169	0.138
Sonic probe(inline)	ampl.(mm)	14.177	23.106	15.855	14.419	14.146	16.986	16.135
	ang.freq.(rad/s)	1.006	1.129	1.257	1.383	1.193	1.068	0.881
	phase(rad)	2.490	0.059	4.625	4.305	3.445	4.812	4.389
	offset	-373.551	-373.008	-373.125	-373.145	-373.105	-373.531	-373.506
	freq.(Hz)	0.160	0.180	0.200	0.220	0.190	0.170	0.140
Load cell	ampl.(N)	10.860	4.867	2.639	1.935	2.739	5.458	4.472
	ang.freq.(rad/s)	1.039	1.142	1.255	1.381	1.214	1.061	0.879
	phase(rad)	1.946	-0.705	-0.542	5.015	-0.393	3.695	3.370
	offset	37.169	37.875	37.855	37.811	37.796	37.844	37.937
	freq.(Hz)	0.165	0.182	0.200	0.220	0.193	0.169	0.140
Mooring displ.(mm)	ampl.(mm)	156.301	68.846	36.610	26.734	38.005	82.224	63.160
	ang.freq.(rad/s)	1.039	1.142	1.255	1.381	1.214	1.059	0.879
	phase(rad)	3.548	0.106	4.864	4.512	3.447	-0.113	0.776
	offset	309.064	319.896	319.692	318.959	318.867	319.448	321.317
	freq.(Hz)	0.165	0.182	0.200	0.220	0.193	0.169	0.140
Wave p. (upstream)	ampl.(mm)	17.090	14.673	22.667	12.089	12.147	15.763	17.236
	ang.freq.(rad/s)	1.004	1.129	1.258	1.381	1.196	1.066	0.880
	phase(rad)	0.613	4.679	3.344	5.069	2.424	3.664	2.420
	offset	319.214	319.243	319.249	319.236	318.997	319.206	319.261
	freq.(Hz)	0.160	0.180	0.200	0.220	0.190	0.170	0.140
Heave RAO	n.d	10.715	2.940	2.331	1.881	2.713	4.495	3.884
Surge RAO	n.d	3.871	1.708	3.231	1.838	2.134	2.386	4.230

Table A.10: Tests of submerged floater Session 3 (1:33 scale model). Here results of tests where the immersion of floater was -0.345 m (Imm. value n.1) are shown. For these tests the servomotor was unplugged.

Test no.		1	2	3	4	5	6	7	8	9	10
Descr.		Imm. 2	Imm. 2	Imm. 2	Imm. 2	Imm. 2	Imm. 2	Imm. 2	Imm. 2	Imm. 2	Imm. 2
Waves ampl. real sc.	(m)	0.495	0.495	0.495	0.495	0.495	0.495	0.495	0.495	0.495	0.495
Waves ang. freq. r.s.	(rad/s)	0.164	0.175	0.197	0.219	0.241	0.263	0.284	0.170	0.180	0.153
Freq.	(Hz)	0.026	0.028	0.031	0.035	0.038	0.042	0.045	0.027	0.029	0.024
Floater imm.	(m)	-0.500	-0.500	-0.500	-0.500	-0.500	-0.500	-0.500	-0.500	-0.500	-0.500
digital gain	n.d.	no motor	no motor	no motor	no motor	no motor	no motor	no motor	no motor	no motor	no motor
Input in wave gen	freq.(Hz)	0.150	0.160	0.180	0.200	0.220	0.240	0.260	0.155	0.165	0.140
	ampl.(m)	0.015	0.015	0.015	0.015	0.015	0.015	0.015	0.015	0.015	0.015
	ang.freq.(rad/s)	0.942	1.005	1.131	1.257	1.382	1.508	1.634	0.974	0.974	1.037
Heave	ampl.(mm)	99.225	157.353	73.674	31.634	23.058	20.407	20.241	168.501	126.140	35.641
	ang.freq.(rad/s)	0.948	0.998	1.129	1.257	1.389	1.514	1.635	0.974	1.023	0.877
	phase(rad)	1.145	0.227	2.115	2.661	-0.067	1.706	3.412	5.167	3.913	5.335
	offset	-496.924	-496.327	-495.862	-496.414	-496.907	-497.452	-497.153	-495.172	-495.336	-495.919
	freq.(Hz)	0.151	0.159	0.180	0.200	0.221	0.241	0.260	0.155	0.163	0.140
Surge	ampl.(mm)	69.884	56.776	41.353	52.005	25.728	26.296	22.797	67.877	49.875	84.686
	ang.freq.(rad/s)	0.942	1.006	1.129	1.257	1.387	1.509	1.634	0.974	1.033	0.879
	phase(rad)	3.674	3.445	3.423	1.078	4.216	0.045	1.908	1.686	1.211	1.064
	offset	312.769	294.279	304.703	305.379	302.981	305.451	303.357	314.947	310.853	276.309
	freq.(Hz)	0.150	0.160	0.180	0.200	0.221	0.240	0.260	0.155	0.164	0.140
Sonic probe(inline)	ampl.(mm)	16.272	14.298	22.752	15.537	14.259	14.839	16.600	15.725	14.239	16.195
	ang.freq.(rad/s)	0.942	1.007	1.130	1.257	1.387	1.509	1.637	0.973	1.033	0.880
	phase(rad)	5.170	5.143	1.776	2.403	-0.271	1.604	3.243	3.315	3.119	2.627
	offset	-373.836	-373.333	-373.246	-373.213	-373.336	-373.268	-373.095	-373.331	-373.163	-373.347
	freq.(Hz)	0.150	0.160	0.180	0.200	0.221	0.240	0.260	0.155	0.164	0.140
Load cell	ampl.(N)	7.075	11.270	5.248	2.260	1.657	1.454	1.437	11.990	8.990	2.617
	ang.freq.(rad/s)	0.949	0.998	1.128	1.256	1.389	1.514	1.635	0.974	1.022	0.877
	phase(rad)	1.957	2.399	2.812	4.148	1.484	1.791	4.508	3.791	0.605	4.908
	offset	37.701	37.729	37.731	37.707	37.654	37.607	37.634	37.828	37.778	37.785
	freq.(Hz)	0.151	0.159	0.180	0.200	0.221	0.241	0.260	0.155	0.163	0.140
Mooring displ.(mm)	ampl.(mm)	125.481	199.564	92.889	39.378	28.818	25.260	24.909	205.612	160.855	45.718
	ang.freq.(rad/s)	0.949	0.998	1.129	1.256	1.389	1.514	1.635	0.974	1.022	0.877
	phase(rad)	1.119	0.206	2.097	2.659	-0.082	1.692	3.398	5.145	3.894	5.258
	offset	199.649	199.783	200.821	200.752	199.944	199.087	199.449	202.249	201.879	202.755
	freq.(Hz)	0.151	0.159	0.180	0.200	0.221	0.241	0.260	0.155	0.163	0.140
Wave p. (upstream)	ampl.(mm)	17.477	17.118	15.063	22.136	12.038	14.732	16.413	18.267	16.163	17.242
	ang.freq.(rad/s)	0.942	1.005	1.132	1.258	1.389	1.511	1.637	0.974	1.033	0.879
	phase(rad)	3.313	3.275	0.071	1.113	4.532	0.515	2.544	1.468	1.050	0.644
	offset	318.686	318.602	318.522	318.568	318.569	318.504	318.446	318.716	318.784	318.868
	freq.(Hz)	0.150	0.160	0.180	0.200	0.221	0.240	0.261	0.155	0.164	0.140
Heave RAO	n.d	6.098	11.005	3.238	2.036	1.617	1.375	1.219	10.716	8.859	2.201
Surge RAO	n.d	4.295	3.971	1.818	3.347	1.804	1.772	1.373	4.317	3.503	5.229

Table A.11: Tests of submerged floater Session 3 (1:33 scale model). Here results of tests where the immersion of floater was -0.50 m (c.a. value n.2) are shown. For these tests the servomotor was unplugged.

Test no.		25	26	27	28	29	30	31	32	33	34	35	36	37	38	39	40	41	42	43
Descr.		Imm. 3	Imm. 3	Imm. 3	Imm. 3	Imm. 3	Imm. 3	Imm. 3	Imm. 3	Imm. 3	Imm. 3	Imm. 3	Imm. 3	Imm. 3	Imm. 3	Imm. 3	Imm. 3	Imm. 3	Imm. 3	Imm. 3
Waves ampl. real sc.	(m)	0.495	0.495	0.495	0.495	0.495	0.495	0.495	0.495	0.495	0.495	0.990	0.990	0.990	0.990	0.990	0.990	0.990	0.990	0.990
Waves ang. freq. r.s.	(rad/s)	0.131	0.153	0.164	0.170	0.175	0.180	0.186	0.197	0.219	0.263	0.131	0.153	0.164	0.170	0.180	0.186	0.197	0.219	0.263
Freq.	(Hz)	0.021	0.024	0.026	0.027	0.028	0.029	0.030	0.031	0.035	0.042	0.021	0.024	0.026	0.027	0.029	0.030	0.031	0.035	0.042
Floater imm.	(m)	-0.580	-0.580	-0.580	-0.580	-0.580	-0.580	-0.580	-0.580	-0.580	-0.580	-0.580	-0.580	-0.580	-0.580	-0.580	-0.580	-0.580	-0.580	-0.580
digital gain	n.d.	no motor	no mot.	no mot.	no mot.	no mot.	no mot.	no mot.	no mot.	no mot.	no mot.	no mot.	no mot.	no mot.	no mot.	no mot.	no mot.	no mot.	no mot.	no mot.
Input in wave gen	freq.(Hz)	0.120	0.140	0.150	0.155	0.160	0.165	0.170	0.180	0.200	0.240	0.120	0.140	0.150	0.155	0.165	0.170	0.180	0.200	0.240
	ampl.(m)	0.015	0.015	0.015	0.015	0.015	0.015	0.015	0.015	0.015	0.015	0.030	0.030	0.030	0.030	0.030	0.030	0.030	0.030	0.030
	ang.freq.(rad/s)	0.754	0.880	0.942	0.974	1.005	1.037	1.068	1.131	1.131	1.257	1.508	0.754	0.880	0.942	0.974	1.037	1.068	1.131	1.257
Heave	ampl.(mm)	8.562	33.305	83.633	178.907	167.498	113.168	75.091	67.869	24.191	19.204	29.104	75.596	243.950	255.856	235.158	151.727	150.601	61.514	39.218
	ang.freq.(rad/s)	0.735	0.873	0.945	0.974	1.001	1.026	1.081	1.137	1.242	1.509	0.751	0.872	0.938	0.966	1.028	1.085	1.108	1.259	1.501
	phase(rad)	5.701	4.855	5.160	2.070	1.837	-0.465	5.177	5.037	4.839	1.231	0.186	4.962	1.127	0.919	1.785	0.269	1.047	0.325	2.732
	offset	-581.743	-577.013	-575.866	-574.612	-573.891	-572.994	-573.314	-573.076	-574.081	-574.250	-583.681	-578.230	-571.926	-581.841	-576.493	-574.606	-574.574	-574.005	-572.795
	freq.(Hz)	0.117	0.139	0.150	0.155	0.159	0.163	0.172	0.181	0.198	0.240	0.119	0.139	0.149	0.154	0.164	0.173	0.176	0.200	0.239
Surge	ampl.(mm)	113.551	86.990	73.466	69.905	58.529	50.075	46.822	43.241	44.663	25.900	262.229	155.223	160.340	140.489	101.784	95.143	84.388	101.155	52.741
	ang.freq.(rad/s)	0.781	0.886	0.935	0.975	1.007	1.039	1.070	1.129	1.262	1.507	0.761	0.881	0.938	0.909	1.032	1.065	1.131	1.256	1.499
	phase(rad)	1.398	0.496	1.402	4.822	5.245	3.221	3.052	3.288	-6.516	-0.518	2.356	0.599	3.657	4.145	-0.353	4.833	5.282	5.157	1.079
	offset	282.017	270.884	315.898	321.497	317.195	313.483	314.634	313.531	276.255	310.174	317.726	313.605	336.338	350.057	319.173	314.806	314.095	312.233	301.608
	freq.(Hz)	0.124	0.141	0.149	0.155	0.160	0.165	0.170	0.180	0.201	0.240	0.121	0.140	0.149	0.145	0.164	0.169	0.180	0.200	0.239
Sonic probe(inline)	ampl.(mm)	15.819	16.049	16.169	15.707	14.171	13.549	17.314	21.956	14.077	14.766	30.671	32.136	32.998	28.430	26.786	35.655	45.047	31.645	30.879
	ang.freq.(rad/s)	0.756	0.883	0.942	0.974	1.005	1.035	1.068	1.129	1.262	1.509	0.755	0.879	0.941	0.974	1.033	1.070	1.130	1.258	1.501
	phase(rad)	2.923	2.112	2.769	0.138	0.677	5.145	4.982	4.834	4.275	0.993	3.774	2.135	5.139	5.425	1.445	0.361	0.560	0.184	2.608
	offset	-374.011	-373.918	-373.930	-374.219	-374.189	-374.286	-374.608	-374.563	-374.591	-374.424	-374.789	-374.723	-374.754	-374.554	-374.279	-374.206	-374.509	-374.631	-374.502
	freq.(Hz)	0.120	0.141	0.150	0.155	0.160	0.165	0.170	0.180	0.201	0.240	0.120	0.140	0.150	0.155	0.164	0.170	0.180	0.200	0.239
Load cell	ampl.(N)	0.737	2.455	5.891	12.610	11.827	7.988	5.311	4.784	1.724	1.349	1.880	5.289	16.657	18.129	16.584	10.679	10.515	4.338	2.755
	ang.freq.(rad/s)	0.743	0.875	0.945	0.974	1.001	1.026	1.081	1.137	1.244	1.509	0.759	0.869	0.948	0.967	1.028	1.085	1.115	1.259	1.501
	phase(rad)	0.121	-0.702	1.428	-0.081	2.446	2.008	3.181	4.935	-0.017	4.806	1.941	4.566	3.880	4.814	1.721	5.441	3.029	4.199	3.620
	offset	37.483	37.669	37.663	37.699	37.678	37.677	37.686	37.691	37.653	37.588	37.935	37.764	37.941	37.701	37.594	37.684	37.549	37.728	37.748
	freq.(Hz)	0.118	0.139	0.150	0.155	0.159	0.163	0.172	0.181	0.198	0.240	0.121	0.138	0.151	0.154	0.164	0.173	0.177	0.200	0.239
Mooring displ.(mm)	ampl.(mm)	9.672	27.565	62.404	143	137	92	72.000	56.4	23.590	14.067	35.000	70		260.000		155.835	152.841	61.756	39.081
	ang.freq.(rad/s)	0.739	0.875	0.945	0.973	1.002	1.026	1.081	1.137	1.260	1.509	0.759	0.879		0.972		1.085	1.115	1.259	1.502
	phase(rad)	5.468	4.732	5.129	2.033	1.787	-0.495	5.137	5.003	4.655	1.172	0.069	4.846		0.876		0.251	0.950	0.296	2.711
	offset	349.207	343.888	341.083	321.244	324.647	337.269	337.312	338.404	339.118	338.108	337.952	335.890	0.000	319.436	0.000	442.827	440.046	445.236	446.048
	freq.(Hz)	0.118	0.139	0.150	0.155	0.159	0.163	0.172	0.181	0.201	0.240	0.121	0.140		0.155		0.173	0.177	0.200	0.239
Wave p. (upstream)	ampl.(mm)	13.018	17.329	17.407	18.281	17.094	15.602	15.961	14.832	20.212	14.776	28.743	31.213	36.599	35.294	31.289	32.056	30.096	43.983	29.675
	ang.freq.(rad/s)	0.760	0.880	0.943	0.974	1.005	1.036	1.069	1.131	1.263	1.508	0.757	0.879	0.942	0.975	1.037	1.068	1.132	1.257	1.500
	phase(rad)	0.917	0.161	0.898	4.595	5.041	3.088	2.901	3.126	3.000	-0.054	1.719	0.177	4.696	3.638	-0.674	4.584	5.174	5.214	1.566
	offset	319.788	319.843	319.788	320.015	320.026	319.878	320.044	320.272	320.366	320.100	320.396	320.467	320.473	320.406	320.126	320.301	320.349	320.152	320.369
	freq.(Hz)	0.121	0.140	0.150	0.155	0.160	0.165	0.170	0.180	0.201	0.240	0.120	0.140	0.150	0.155	0.165	0.170	0.180	0.200	0.239
Heave RAO	n.d	0.541	2.075	5.173	11.390	11.820	8.352	4.337	3.091	1.718	1.301	0.949	2.352	7.393	8.999	8.779	4.255	3.343	1.944	1.270
Surge RAO	n.d	7.178	5.420	4.544	4.451	4.130	3.696	2.704	1.969	3.173	1.754	8.550	4.830	4.859	4.942	3.800	2.668	1.873	3.197	1.708

Table A.12: Tests of submerged floater Session 3 (1:33 scale model). Here results of tests where the immersion of floater was -0.58 m (c.a. value n.3) are shown. For these tests the servomotor was unplugged.

Test no.		117	118	119	120	121	122	123
Descr.		Cpto n. 1	Cpto n. 1	Cpto n. 1	Cpto n. 1	Cpto n. 1	Cpto n. 1	Cpto n. 1
		Imm.1	Imm.1	Imm.1	Imm.1	Imm.1	Imm.1	Imm.1
Waves ampl. real sc.	(m)	0.990	0.990	0.990	0.990	0.990	0.990	0.990
Waves ang. freq. r.s.	(rad/s)	0.131	0.153	0.164	0.197	0.219	0.263	0.197
Freq.	(Hz)	0.021	0.024	0.026	0.031	0.035	0.042	0.031
Floater imm.	(m)	-0.345	-0.345	-0.345	-0.345	-0.345	-0.345	-0.345
digital gain	n.d.	0.400	0.400	0.400	0.400	0.400	0.400	0.400
Input in wave gen	freq.(Hz)	0.120	0.140	0.150	0.180	0.200	0.240	0.180
	ampl.(m)	0.030	0.030	0.030	0.030	0.030	0.030	0.030
	ang.freq.(rad/s)	0.754	0.880	0.942	1.131	1.257	1.508	1.131
Heave	ampl.(mm)	21.579	76.582	119.739	125.116	66.323	44.186	126.544
	ang.freq.(rad/s)	0.754	0.877	0.943	1.129	1.257	1.509	1.131
	phase(rad)	1.816	0.153	4.647	0.357	4.686	1.628	0.796
	offset	-353.259	-348.324	-349.921	-345.895	-348.167	-347.215	-346.171
	freq.(Hz)	0.120	0.140	0.150	0.180	0.200	0.240	0.180
Surge	ampl.(mm)	210.902	138.359	142.262	79.781	96.223	53.583	80.923
	ang.freq.(rad/s)	0.762	0.881	0.943	1.129	1.257	1.508	1.126
	phase(rad)	4.273	2.577	1.131	4.493	84.699	-0.149	5.105
	offset	302.482	303.692	308.491	304.068	299.981	298.907	303.984
	freq.(Hz)	0.121	0.140	0.150	0.180	0.200	0.240	0.179
Sonic probe(inline)	ampl.(mm)	29.475	32.019	32.745	45.332	31.465	30.420	45.374
	ang.freq.(rad/s)	0.754	0.880	0.942	1.130	1.258	1.508	1.130
	phase(rad)	-0.502	4.081	2.643	-0.222	4.320	1.396	0.263
	offset	-375.880	-375.957	-375.879	-375.685	-375.776	-375.614	-376.004
	freq.(Hz)	0.120	0.140	0.150	0.180	0.200	0.240	0.180
Load cell	ampl.(N)	1.647	5.506	8.551	8.972	4.747	3.139	9.061
	ang.freq.(rad/s)	0.743	0.877	0.943	1.129	1.257	1.509	1.131
	phase(rad)	1.521	3.643	1.842	1.900	-0.254	3.760	1.972
	offset	38.743	38.753	38.669	38.780	38.622	38.602	38.741
	freq.(Hz)	0.118	0.140	0.150	0.180	0.200	0.240	0.180
Mooring displ.(mm)	ampl.(mm)	23.248	77.812	119.429	124.632	66.028	44.364	127.269
	ang.freq.(rad/s)	0.743	0.878	0.943	1.128	1.257	1.508	1.131
	phase(rad)	1.906	0.096	4.615	0.345	4.663	1.608	0.760
	offset	148.384	148.836	147.276	149.633	147.126	147.026	149.489
	freq.(Hz)	0.118	0.140	0.150	0.180	0.200	0.240	0.180
Wave p. (upstream)	ampl.(mm)	28.148	31.271	36.492	29.849	44.107	30.014	29.896
	ang.freq.(rad/s)	0.752	0.879	0.943	1.131	1.258	1.508	1.131
	phase(rad)	0.639	5.274	3.987	1.255	-0.077	3.481	1.745
	offset	-321.756	-321.810	-321.703	-321.800	-321.556	-321.427	-322.064
	freq.(Hz)	0.120	0.140	0.150	0.180	0.200	0.240	0.180
Heave RAO	n.d	0.732	2.392	3.657	2.760	2.108	1.453	2.789
Surge RAO	n.d	7.155	4.321	4.345	1.760	3.058	1.761	1.783

Table A.13: Tests of submerged floater Session 3 (1:33 scale model). Here tests results, where the immersion of floater was -0.345 m (value n.1), are shown. For these tests the servomotor was set to Damping n.1 (c.a. 18.5 kg/s).

Test no.		95	96	97	98	99	101	102	103	104	105	106
Descr.		Cpto n. 4	Cpto n. 4	Cpto n. 4	Cpto n. 4	Cpto n. 4	Cpto n. 4	Cpto n. 4	Cpto n. 4	Cpto n. 4	Cpto n. 4	Cpto n. 4
		Imm.1	Imm.1	Imm.1	Imm.1	Imm.1	Imm.1	Imm.1	Imm.1	Imm.1	Imm.1	Imm.1
Waves ampl. real sc.	(m)	0.990	0.990	0.990	0.990	0.990	0.990	0.990	0.990	0.990	0.990	0.990
Waves ang. freq. r.s.	(rad/s)	0.131	0.153	0.164	0.170	0.175	0.186	0.197	0.164	0.186	0.219	0.263
Freq.	(Hz)	0.021	0.024	0.026	0.027	0.028	0.030	0.031	0.026	0.030	0.035	0.042
Floater imm.	(m)	-0.345	-0.345	-0.345	-0.345	-0.345	-0.345	-0.345	-0.345	-0.345	-0.345	-0.345
digital gain	n.d.	1.200	1.200	1.200	1.200	1.200	1.200	1.200	1.200	1.200	1.200	1.200
Input in wave gen	freq.(Hz)	0.120	0.140	0.150	0.155	0.160	0.170	0.180	0.150	0.170	0.200	0.240
	ampl.(m)	0.030	0.030	0.030	0.030	0.030	0.030	0.030	0.030	0.030	0.030	0.030
	ang.freq.(rad/s)	0.754	0.880	0.942	0.974	1.005	1.068	1.131	0.942	1.068	1.257	1.508
Heave	ampl.(mm)	21.168	48.884	67.084	67.798	59.441	93.096	102.574	60.144	98.407	57.413	42.399
	ang.freq.(rad/s)	0.762	0.880	0.943	0.974	1.006	1.069	1.130	0.945	1.073	1.254	1.509
	phase(rad)	1.528	1.458	3.308	4.026	-0.443	0.611	1.411	1.401	0.865	1.036	2.129
	offset	-354.417	-350.071	-349.295	-348.921	-349.332	-347.544	-346.504	-347.535	-345.089	-346.741	-347.007
	freq.(Hz)	0.121	0.140	0.150	0.155	0.160	0.170	0.180	0.150	0.171	0.200	0.240
Surge	ampl.(mm)	206.283	146.279	144.423	136.068	113.128	90.410	78.918	140.038	90.213	97.063	54.480
	ang.freq.(rad/s)	0.742	0.880	0.940	0.974	1.006	1.060	1.131	0.945	1.070	1.254	1.509
	phase(rad)	4.537	4.147	0.106	0.807	2.591	4.051	5.257	4.479	4.249	-0.927	0.172
	offset	290.888	304.677	302.534	303.173	301.473	306.367	307.659	299.013	306.001	303.176	297.618
	freq.(Hz)	0.118	0.140	0.150	0.155	0.160	0.169	0.180	0.150	0.170	0.200	0.240
Sonic probe(inline)	ampl.(mm)	29.692	32.074	32.876	30.690	27.444	35.384	44.917	32.735	35.977	30.872	30.577
	ang.freq.(rad/s)	0.754	0.879	0.942	0.973	1.007	1.069	1.129	0.943	1.071	1.258	1.508
	phase(rad)	-0.590	-0.587	1.538	2.391	4.329	-0.420	0.582	-0.331	-0.090	0.349	1.749
	offset	-375.390	-375.140	-375.422	-375.407	-375.164	-375.516	-375.347	-375.569	-375.258	-375.562	-375.270
	freq.(Hz)	0.120	0.140	0.150	0.155	0.160	0.170	0.180	0.150	0.170	0.200	0.240
Load cell	ampl.(N)	1.655	3.538	4.851	4.908	4.297	6.661	7.346	4.362	7.063	4.107	3.014
	ang.freq.(rad/s)	0.758	0.879	0.943	0.974	1.007	1.069	1.130	0.944	1.071	1.254	1.509
	phase(rad)	10.044	1.354	1.830	2.651	3.906	4.689	3.016	2.866	4.582	-0.063	4.497
	offset	38.622	38.624	38.672	38.651	38.553	38.684	38.686	38.798	38.719	38.677	38.589
	freq.(Hz)	0.121	0.140	0.150	0.155	0.160	0.170	0.180	0.150	0.171	0.200	0.240
Mooring displ.(mm)	ampl.(mm)	23.771	50.357	68.452	69.257	60.807	93.367	102.871	61.443	97.181	57.925	42.487
	ang.freq.(rad/s)	0.758	0.879	0.943	0.974	1.007	1.069	1.130	0.944	1.070	1.254	1.509
	phase(rad)	1.535	1.431	3.280	3.996	-0.477	0.590	1.389	1.379	0.919	0.996	2.097
	offset	145.491	145.414	146.254	145.976	144.715	145.395	145.563	146.296	148.831	147.476	146.015
	freq.(Hz)	0.121	0.140	0.150	0.155	0.160	0.170	0.180	0.150	0.170	0.200	0.240
Wave p. (upstream)	ampl.(mm)	28.494	31.193	36.662	38.313	35.002	32.071	30.013	36.544	32.213	43.060	29.980
	ang.freq.(rad/s)	0.752	0.878	0.943	0.974	1.005	1.068	1.130	0.943	1.069	1.258	1.509
	phase(rad)	0.563	0.600	2.894	3.703	-0.711	0.658	2.062	1.033	1.026	2.200	3.834
	offset	-321.376	-321.463	-321.634	-321.456	-321.390	-321.311	-321.424	-321.200	-321.461	-321.378	-321.206
	freq.(Hz)	0.120	0.140	0.150	0.155	0.160	0.170	0.180	0.150	0.170	0.200	0.240
Heave RAO	n.d	0.713	1.524	2.040	2.209	2.166	2.631	2.284	1.837	2.735	1.860	1.387
Surge RAO	n.d	6.947	4.561	4.393	4.434	4.122	2.555	1.757	4.278	2.508	3.144	1.782

Table A.14: Tests of submerged floater Session 3 (1:33 scale model). Here tests results, where the immersion of floater was -0.345 m (value n.1), are shown. For these tests the servomotor was set to Damping n.4 (c.a. 31.5 kg/s).

Test no.		175	176	177	178	179	180	181	182	183
Descr.		Cpto n.1	Cpto n.1	Cpto n.1	Cpto n.1	Cpto n.1	Cpto n.1	Cpto n.1	Cpto n.1	Cpto n.1
		Imm.2	Imm.2	Imm.2	Imm.2	Imm.2	Imm.2	Imm.2	Imm.2	Imm.2
Waves ampl. real sc.	(m)	0.990	0.990	0.990	0.990	0.990	0.990	0.990	0.990	0.990
Waves ang. freq. r.s.	(rad/s)	0.131	0.153	0.164	0.170	0.175	0.186	0.197	0.219	0.263
Freq.	(Hz)	0.021	0.024	0.026	0.027	0.028	0.030	0.031	0.035	0.042
Floater imm.	(m)	-0.460	-0.460	-0.460	-0.460	-0.460	-0.460	-0.460	-0.460	-0.460
Digital gain	n.d.	0.400	0.400	0.400	0.400	0.400	0.400	0.400	0.400	0.400
Input in wave gen	freq.(Hz)	0.120	0.140	0.150	0.155	0.160	0.170	0.180	0.200	0.240
	ampl.(m)	0.030	0.030	0.030	0.030	0.030	0.030	0.030	0.030	0.030
	ang.freq.(rad/s)	0.754	0.880	0.942	0.974	1.005	1.068	1.131	1.257	1.508
Heave	ampl.(mm)	22.050	50.342	121.453	126.237	118.693	121.382	127.531	61.786	41.017
	ang.freq.(rad/s)	0.749	0.878	0.944	0.972	1.002	1.071	1.130	1.255	1.509
	phase(rad)	5.681	0.426	1.391	5.110	2.398	2.910	1.898	0.124	3.642
	offset	-466.630	-459.554	-456.909	-457.111	-456.344	-456.445	-456.826	-457.701	-457.436
	freq.(Hz)	0.119	0.140	0.150	0.155	0.159	0.170	0.180	0.200	0.240
Surge	ampl.(mm)	233.279	151.157	149.998	139.187	121.014	86.332	81.944	100.236	52.699
	ang.freq.(rad/s)	0.750	0.880	0.943	0.970	1.002	1.071	1.130	1.258	1.510
	phase(rad)	2.063	2.986	4.263	1.918	55.849	3.321	-0.271	4.627	1.775
	offset	301.565	304.937	316.270	317.277	314.734	305.903	313.343	303.408	304.380
	freq.(Hz)	0.119	0.140	0.150	0.154	0.159	0.170	0.180	0.200	0.240
Sonic probe(inline)	ampl.(mm)	29.624	32.029	33.145	30.831	27.341	35.616	45.420	31.696	30.507
	ang.freq.(rad/s)	0.754	0.879	0.943	0.973	1.005	1.069	1.130	1.256	1.507
	phase(rad)	3.362	4.513	-0.558	3.459	0.997	2.090	1.301	-0.283	3.377
	offset	-376.475	-376.705	-377.173	-377.224	-377.141	-376.594	-376.780	-376.605	-376.904
	freq.(Hz)	0.120	0.140	0.150	0.155	0.160	0.170	0.180	0.200	0.240
Load cell	ampl.(N)	1.755	3.694	8.680	9.017	8.464	8.676	9.120	4.431	2.944
	ang.freq.(rad/s)	0.750	0.879	0.944	0.973	1.001	1.070	1.130	1.255	1.509
	phase(rad)	1.661	0.434	2.510	4.807	0.568	-0.425	1.994	3.846	2.746
	offset	38.640	38.732	38.950	38.887	38.876	38.813	38.737	38.713	38.648
	freq.(Hz)	0.119	0.140	0.150	0.155	0.159	0.170	0.180	0.200	0.240
Mooring displ.(mm)	ampl.(mm)	19.995	41.639	96.746	100.495	94.158	96.620	101.750	49.646	33.102
	ang.freq.(rad/s)	0.750	0.879	0.944	0.973	1.001	1.070	1.130	1.255	1.509
	phase(rad)	5.539	0.367	1.374	5.079	2.377	2.892	1.875	0.119	3.627
	offset	142.740	144.051	147.791	146.898	146.671	145.874	144.824	143.839	142.859
	freq.(Hz)	0.119	0.140	0.150	0.155	0.159	0.170	0.180	0.200	0.240
Wave p. (upstream)	ampl.(mm)	28.222	31.269	36.753	38.161	34.877	32.126	29.980	43.820	30.288
	ang.freq.(rad/s)	0.753	0.880	0.942	0.974	1.004	1.069	1.132	1.258	1.508
	phase(rad)	4.486	-0.598	0.828	4.763	2.239	3.139	2.775	1.565	5.464
	offset	-322.485	-322.593	-322.526	-322.521	-322.591	-322.317	-322.661	-322.297	-322.263
	freq.(Hz)	0.120	0.140	0.150	0.155	0.160	0.170	0.180	0.200	0.240
Heave RAO	n.d	0.744	1.572	3.664	4.095	4.341	3.408	2.808	1.949	1.344
Surge RAO	n.d	309.368	171.885	159.145	143.081	120.414	80.773	72.486	79.775	34.960

Table A.15: Tests of submerged floater Session 3 (1:33 scale model). Here tests results, where the immersion of floater was -0.46 m (value n.2), are shown. For these tests the servomotor was set to Damping n.1(c.a. 18.5 kg/s).

Test no.		157	158	159	160	161	162	163	164	165
Descr.		Cpto n.4	Cpto n.4	Cpto n.4	Cpto n.4	Cpto n.4	Cpto n.4	Cpto n.4	Cpto n.4	Cpto n.4
		Imm.2	Imm.2	Imm.2	Imm.2	Imm.2	Imm.2	Imm.2	Imm.2	Imm.2
Waves ampl. real sc.	(m)	0.990	0.990	0.990	0.990	0.990	0.990	0.990	0.990	0.990
Waves ang. freq. r.s.	(rad/s)	0.131	0.153	0.164	0.170	0.175	0.186	0.197	0.219	0.263
Freq.	(Hz)	0.021	0.024	0.026	0.027	0.028	0.030	0.031	0.035	0.042
Floater imm.	(m)	-0.460	-0.460	-0.460	-0.460	-0.460	-0.460	-0.460	-0.460	-0.460
digital gain	n.d.	1.200	1.200	1.200	1.200	1.200	1.200	1.200	1.200	1.200
Input in wave gen	freq.(Hz)	0.120	0.140	0.150	0.155	0.160	0.170	0.180	0.200	0.240
	ampl.(m)	0.030	0.030	0.030	0.030	0.030	0.030	0.030	0.030	0.030
	ang.freq.(rad/s)	0.754	0.880	0.942	0.974	1.005	1.068	1.131	1.257	1.508
Heave	ampl.(mm)	16.125	41.282	53.030	56.296	49.429	91.296	102.122	51.677	37.843
	ang.freq.(rad/s)	0.759	0.880	0.942	0.974	1.006	1.069	1.130	1.256	1.508
	phase(rad)	4.432	0.958	4.937	4.991	2.665	3.597	1.838	5.511	-0.518
	offset	-466.314	-459.537	-459.135	-458.580	-458.146	-458.046	-457.357	-456.529	-457.360
	freq.(Hz)	0.121	0.140	0.150	0.155	0.160	0.170	0.180	0.200	0.240
Surge	ampl.(mm)	224.412	145.441	149.151	142.753	112.602	93.605	80.666	99.664	53.557
	ang.freq.(rad/s)	0.754	0.879	0.942	0.976	1.005	1.069	1.130	1.259	1.508
	phase(rad)	0.802	3.767	1.683	1.684	0.633	3.788	-0.550	3.417	3.777
	offset	283.643	307.176	308.187	307.999	306.918	308.915	309.639	307.065	297.172
	freq.(Hz)	0.120	0.140	0.150	0.155	0.160	0.170	0.180	0.200	0.240
Sonic probe(inline)	ampl.(mm)	29.456	32.220	32.919	30.800	27.341	35.030	45.143	31.588	30.469
	ang.freq.(rad/s)	0.754	0.880	0.943	0.973	1.006	1.068	1.130	1.256	1.508
	phase(rad)	2.141	5.247	3.121	3.318	2.318	2.551	0.984	4.808	5.317
	offset	-376.649	-376.630	-376.689	-376.632	-376.470	-376.496	-376.346	-376.457	-376.150
	freq.(Hz)	0.120	0.140	0.150	0.155	0.160	0.170	0.180	0.200	0.240
Load cell	ampl.(N)	1.516	3.052	3.878	4.117	3.611	6.527	7.309	3.734	2.740
	ang.freq.(rad/s)	0.762	0.880	0.943	0.974	1.006	1.069	1.130	1.256	1.508
	phase(rad)	4.899	3.818	4.626	2.383	4.376	2.822	0.306	0.807	-0.826
	offset	38.619	38.677	38.709	38.738	38.687	38.659	38.666	38.761	38.640
	freq.(Hz)	0.121	0.140	0.150	0.155	0.160	0.170	0.180	0.200	0.240
Mooring displ.(mm)	ampl.(mm)	20.528	54.877	89.505	93.877	85.239	109.591	122.028	60.966	42.159
	ang.freq.(rad/s)	0.762	0.880	0.943	0.974	1.006	1.069	1.130	1.256	1.508
	phase(rad)	4.183	0.922	4.898	4.958	3.817	3.574	1.810	5.499	-0.518
	offset	143.400	144.205	144.639	144.981	144.140	143.733	143.881	144.889	143.141
	freq.(Hz)	0.121	0.140	0.150	0.155	0.160	0.170	0.180	0.200	0.240
Wave p. (upstream)	ampl.(mm)	28.294	31.291	36.546	38.111	34.840	31.976	30.059	44.137	30.135
	ang.freq.(rad/s)	0.756	0.880	0.943	0.974	1.005	1.069	1.130	1.258	1.508
	phase(rad)	3.238	0.151	4.482	4.635	3.540	3.594	2.470	0.374	1.140
	offset	-321.925	-321.923	-322.336	-322.240	-322.216	-322.219	-322.337	-322.088	-321.969
	freq.(Hz)	0.120	0.140	0.150	0.155	0.160	0.170	0.180	0.200	0.240
Heave RAO	n.d	0.547	1.281	1.611	1.828	1.808	2.606	2.262	1.636	1.242
Surge RAO	n.d	297.498	165.329	158.186	146.685	111.914	87.643	71.376	79.343	35.510

Table A.16: Tests of submerged floater Session 3 (1:33 scale model). Here tests results, where the immersion of floater was -0.46 m (value n.2), are shown. For these tests the servomotor was set to Damping n.4 (c.a. 31.5 kg/s).

Test no.		75	76	77	78	79	80	81	82	83
Descr.		Cpto n.1	Cpto n.1	Cpto n.1	Cpto n.1	Cpto n.1	Cpto n.1	Cpto n.1	Cpto n.1	Cpto n.1
		Imm.3	Imm.3	Imm.3	Imm.3	Imm.3	Imm.3	Imm.3	Imm.3	Imm.3
Waves ampl. real sc.	(m)	0.990	0.990	0.990	0.990	0.990	0.990	0.990	0.990	0.990
Waves ang. freq. r.s.	(rad/s)	0.131	0.153	0.164	0.170	0.175	0.186	0.197	0.219	0.263
Freq.	(Hz)	0.021	0.024	0.026	0.027	0.028	0.030	0.031	0.035	0.042
Floater imm.	(m)	-0.580	-0.580	-0.580	-0.580	-0.580	-0.580	-0.580	-0.580	-0.580
Digital gain	n.d.	0.400	0.400	0.400	0.400	0.400	0.400	0.400	0.400	0.400
Input in wave gen	freq.(Hz)	0.120	0.140	0.150	0.155	0.160	0.170	0.180	0.200	0.240
	ampl.(m)	0.030	0.030	0.030	0.030	0.030	0.030	0.030	0.030	0.030
	ang.freq.(rad/s)	0.754	0.880	0.942	0.974	1.005	1.068	1.131	1.257	1.508
Heave	ampl.(mm)	25.575	37.962	107.656	115.696	114.076	116.499	118.890	58.127	39.659
	ang.freq.(rad/s)	1.068	0.884	0.943	0.972	1.003	1.072	1.129	1.257	1.510
	phase(rad)	-0.374	4.589	1.123	0.518	3.728	4.274	2.979	4.653	3.065
	offset	-579.346	-579.223	-577.720	-577.026	-575.753	-575.234	-575.755	-576.325	-575.412
	freq.(Hz)	0.170	0.141	0.150	0.155	0.160	0.171	0.180	0.200	0.240
Surge	ampl.(mm)	269.335	154.552	156.687	141.071	121.566	93.295	84.507	101.299	52.856
	ang.freq.(rad/s)	0.752	0.890	0.943	0.975	1.006	1.073	1.134	1.258	1.510
	phase(rad)	0.509	0.800	3.911	3.440	0.529	1.439	0.708	2.896	1.227
	offset	302.953	306.544	312.321	312.225	310.164	308.347	307.218	303.822	300.999
	freq.(Hz)	0.120	0.142	0.150	0.155	0.160	0.171	0.180	0.200	0.240
Sonic probe(inline)	ampl.(mm)	29.701	32.058	33.304	30.821	27.484	35.672	45.235	31.671	30.477
	ang.freq.(rad/s)	0.755	0.881	0.943	0.973	1.006	1.069	1.130	1.259	1.510
	phase(rad)	1.773	2.442	5.362	5.041	2.243	3.425	2.292	4.192	2.763
	offset	-375.402	-375.308	-375.628	-375.829	-375.717	-375.728	-375.666	-375.715	-375.859
	freq.(Hz)	0.120	0.140	0.150	0.155	0.160	0.170	0.180	0.200	0.240
Load cell	ampl.(N)	2.588	2.745	7.668	8.408	8.122	8.314	8.493	4.143	2.804
	ang.freq.(rad/s)	1.114	0.882	0.943	0.972	1.003	1.072	1.130	1.257	1.510
	phase(rad)	4.828	1.852	4.947	1.535	0.503	1.561	3.472	3.433	1.884
	offset	38.992	38.544	38.631	38.673	38.637	38.585	38.520	38.523	38.478
	freq.(Hz)	0.177	0.140	0.150	0.155	0.160	0.171	0.180	0.200	0.240
Mooring displ.(mm)	ampl.(mm)	36.704	38.956	107.130	117.396	113.357	115.923	118.504	58.349	39.744
	ang.freq.(rad/s)	1.102	0.882	0.943	0.972	1.003	1.072	1.130	1.257	1.510
	phase(rad)	5.446	4.567	1.102	0.497	3.700	4.248	2.949	4.634	3.048
	offset	118.457	113.512	114.753	115.377	114.920	114.253	113.541	113.296	112.791
	freq.(Hz)	0.175	0.140	0.150	0.155	0.160	0.171	0.180	0.200	0.240
Wave p. (upstream)	ampl.(mm)	28.255	31.235	36.747	38.211	34.980	32.169	29.914	43.975	30.381
	ang.freq.(rad/s)	0.754	0.880	0.943	0.973	1.005	1.069	1.131	1.259	1.512
	phase(rad)	2.910	3.636	0.458	0.080	3.481	4.486	3.775	-0.197	4.844
	offset	-321.181	-321.100	-321.309	-321.323	-321.111	-321.318	-321.407	-321.260	-321.538
	freq.(Hz)	0.120	0.140	0.150	0.155	0.160	0.170	0.180	0.200	0.241
Heave RAO	n.d	0.861	1.184	3.233	3.754	4.151	3.266	2.628	1.835	1.301
Surge RAO	n.d	356.594	175.524	166.153	144.950	120.805	87.303	74.779	80.447	34.995

Table A.17: Tests of submerged floater Session 3 (1:33 scale model). Here tests results, where the immersion of floater was -0.58 m (c.a. value n.2), are shown. For these tests the servomotor was set to Damping n.1 (c.a. 18.5 kg/s).

Test no.		57	58	59	60	61	62	63	64	65
Descr.		Cpto n.4	Cpto n.4	Cpto n.4	Cpto n.4	Cpto n.4	Cpto n.4	Cpto n.4	Cpto n.4	Cpto n.4
		Imm.3	Imm.3	Imm.3	Imm.3	Imm.3	Imm.3	Imm.3	Imm.3	Imm.3
Waves ampl. real sc.	(m)	0.990	0.990	0.990	0.990	0.990	0.990	0.990	0.990	0.990
Waves ang. freq. r.s.	(rad/s)	0.131	0.153	0.164	0.170	0.175	0.186	0.197	0.219	0.263
Freq.	(Hz)	0.021	0.024	0.026	0.027	0.028	0.030	0.031	0.035	0.042
Floater imm.	(m)	-0.580	-0.580	-0.580	-0.580	-0.580	-0.580	-0.580	-0.580	-0.580
Digital gain	n.d.	1.200	1.200	1.200	1.200	1.200	1.200	1.200	1.200	1.200
Input in wave gen	freq.(Hz)	0.120	0.140	0.150	0.155	0.160	0.170	0.180	0.200	0.240
	ampl.(m)	0.030	0.030	0.030	0.030	0.030	0.030	0.030	0.030	0.030
	ang.freq.(rad/s)	0.754	0.880	0.942	0.974	1.005	1.068	1.131	1.257	1.508
Heave	ampl.(mm)	18.121	29.229	51.598	54.384	45.110	83.597	92.375	49.016	38.086
	ang.freq.(rad/s)	0.764	0.882	0.944	0.972	1.005	1.072	1.127	1.253	1.507
	phase(rad)	3.926	0.275	3.999	0.128	4.855	0.100	3.723	3.722	-0.390
	offset	-582.162	-579.304	-577.594	-577.025	-576.320	-575.764	-573.811	-574.801	-574.751
	freq.(Hz)	0.122	0.140	0.150	0.155	0.160	0.171	0.179	0.199	0.240
Surge	ampl.(mm)	254.068	156.857	152.307	147.245	121.773	95.460	83.408	98.622	53.702
	ang.freq.(rad/s)	0.754	0.880	0.947	0.974	1.005	1.064	1.128	1.259	1.509
	phase(rad)	0.330	2.945	0.583	3.057	1.471	3.467	-1.810	1.562	3.841
	offset	305.168	304.421	306.474	305.402	300.551	306.909	306.837	304.624	302.155
	freq.(Hz)	0.120	0.140	0.151	0.155	0.160	0.169	0.179	0.200	0.240
Sonic probe(inline)	ampl.(mm)	29.556	32.046	32.733	30.918	27.466	35.699	43.456	31.608	30.547
	ang.freq.(rad/s)	0.754	0.881	0.941	0.973	1.007	1.070	1.130	1.256	1.508
	phase(rad)	1.648	4.398	2.143	4.637	3.145	5.290	2.795	2.931	5.406
	offset	-374.743	-374.646	-374.853	-375.083	-375.081	-374.968	-375.359	-375.388	-375.062
	freq.(Hz)	0.120	0.140	0.150	0.155	0.160	0.170	0.180	0.200	0.240
Load cell	ampl.(N)	2.401	2.161	3.701	3.938	3.295	5.998	6.622	3.517	2.711
	ang.freq.(rad/s)	1.162	0.881	0.944	0.972	1.006	1.072	1.128	1.254	1.508
	phase(rad)	0.226	1.243	4.427	4.001	-0.433	-0.380	1.759	2.920	2.517
	offset	39.130	38.497	38.598	38.615	38.592	38.563	38.724	38.672	38.592
	freq.(Hz)	0.185	0.140	0.150	0.155	0.160	0.171	0.179	0.200	0.240
Mooring displ.(mm)	ampl.(mm)	34.123	30.834	52.325	55.529	46.614	83.995	92.621	49.627	38.417
	ang.freq.(rad/s)	1.162	0.881	0.944	0.972	1.006	1.072	1.128	1.254	1.508
	phase(rad)	1.295	0.245	3.965	0.089	4.804	0.073	3.691	3.697	-0.415
	offset	121.062	113.698	114.400	114.445	114.109	113.810	115.433	114.856	113.577
	freq.(Hz)	0.185	0.140	0.150	0.155	0.160	0.171	0.179	0.200	0.240
Wave p. (upstream)	ampl.(mm)	28.266	31.305	36.375	38.327	34.976	32.223	29.580	43.703	30.294
	ang.freq.(rad/s)	0.754	0.880	0.944	0.975	1.005	1.069	1.131	1.259	1.509
	phase(rad)	2.766	-0.684	3.461	-0.335	4.395	0.086	4.245	4.762	1.202
	offset	-320.695	-320.843	-321.121	-321.166	-320.970	-320.944	-321.240	-321.176	-320.940
	freq.(Hz)	0.120	0.140	0.150	0.155	0.160	0.170	0.180	0.200	0.240
Heave RAO	n.d	0.613	0.912	1.576	1.759	1.642	2.342	2.126	1.551	1.247
Surge RAO	n.d	336.990	177.990	161.820	151.297	120.919	89.178	73.835	78.513	35.600

Table A.18: Tests of submerged floater Session 3 (1:33 scale model). Here tests results, where the immersion of floater was -0.58 m (c.a. value n.3), are shown. For these tests the servomotor was set to Damping n.4 (c.a. 31.5 kg/s).

Test no.		270	271	272	273	274	275	276
Descr.		Cpto n.4	Cpto n.4	Cpto n.4	Cpto n.4	Cpto n.4	Cpto n.4	Cpto n.4
		Imm.2, spring n.2	Imm.2,spr.2	Imm.2,spr.2	Imm.2,spr.2	Imm.2,spr.2	Imm.2,spr.2	Imm.2,spr.2
Waves ampl. real sc.	(m)	0.495	0.495	0.495	0.495	0.495	0.495	0.495
Waves ang. freq. r.s.	(rad/s)	0.219	0.230	0.241	0.252	0.263	0.284	0.306
Freq.	(Hz)	0.035	0.037	0.038	0.040	0.042	0.045	0.049
Floater imm.	(m)	-0.460	-0.460	-0.460	-0.460	-0.460	-0.460	-0.460
Digital gain	n.d.	1.200	1.200	1.200	1.200	1.200	1.200	1.200
Input in wave gen	freq.(Hz)	0.200	0.210	0.220	0.230	0.240	0.260	0.280
	ampl.(m)	0.015	0.015	0.015	0.015	0.015	0.015	0.015
	ang.freq.(rad/s)	1.257	1.319	1.382	1.445	1.508	1.634	1.759
Heave	ampl.(mm)	31.965	28.467	38.426	44.780	35.433	33.853	18.323
	ang.freq.(rad/s)	1.259	1.319	1.387	1.443	1.510	1.633	1.759
	phase(rad)	0.091	0.559	1.676	4.040	0.527	4.357	0.478
	offset	-460.943	-460.637	-461.288	-461.291	-460.713	-460.548	-460.438
	freq.(Hz)	0.200	0.210	0.221	0.230	0.240	0.260	0.280
Surge	ampl.(mm)	50.615	36.927	25.178	25.724	26.021	22.855	20.809
	ang.freq.(rad/s)	1.258	1.317	1.395	1.448	1.510	1.635	1.760
	phase(rad)	2.927	3.187	4.588	1.289	4.271	2.234	4.473
	offset	303.406	301.516	301.569	302.526	302.386	301.753	300.479
	freq.(Hz)	0.200	0.210	0.222	0.230	0.240	0.260	0.280
Sonic probe(inline)	ampl.(mm)	15.781	12.293	14.157	15.459	14.674	16.505	10.978
	ang.freq.(rad/s)	1.257	1.320	1.386	1.445	1.509	1.634	1.759
	phase(rad)	4.279	4.927	0.195	2.856	-0.450	3.641	-0.139
	offset	-376.554	-376.801	-376.646	-376.667	-376.582	-376.933	-376.988
	freq.(Hz)	0.200	0.210	0.221	0.230	0.240	0.260	0.280
Load cell	ampl.(N)	4.302	3.812	5.118	5.949	4.704	4.455	2.427
	ang.freq.(rad/s)	1.259	1.319	1.387	1.443	1.510	1.633	1.759
	phase(rad)	-0.641	1.279	4.074	1.525	-0.351	0.202	-0.598
	offset	40.157	40.194	40.130	40.121	40.202	40.237	40.271
	freq.(Hz)	0.200	0.210	0.221	0.230	0.240	0.260	0.280
Mooring displ.(mm)	ampl.(mm)	25.845	3.073	30.648	35.450	28.202	26.585	14.806
	ang.freq.(rad/s)	1.259	1.911	1.387	1.443	1.510	1.633	1.759
	phase(rad)	0.042	-0.488	1.632	3.998	0.491	4.322	0.447
	offset	120.730	121.763	120.543	120.354	120.662	120.812	120.823
	freq.(Hz)	0.200	0.304	0.221	0.230	0.240	0.260	0.280
Wave p. (upstream)	ampl.(mm)	22.536	16.229	11.584	13.750	14.636	16.469	11.442
	ang.freq.(rad/s)	1.259	1.318	1.389	1.446	1.507	1.634	1.759
	phase(rad)	-0.150	0.165	1.861	4.876	1.661	-0.205	2.173
	offset	-322.626	-322.428	-322.422	-322.416	-322.516	-322.746	-322.776
	freq.(Hz)	0.200	0.210	0.221	0.230	0.240	0.260	0.280
Heave RAO	n.d	2.026	2.316	2.714	2.897	2.415	2.051	1.669
Surge RAO	n.d	40.272	27.974	18.161	17.804	17.244	13.988	11.827

Table A.19: Tests of submerged floater Session 3 (1:33 scale model). Here tests results, where the second spring was used and the immersion of floater was set to -0.46 m (c.a. value n.2), are shown. For these tests the servomotor was set to Damping n.4 (c.a. 31.5 kg/s).

Test no.		236	237	238	239	240	241	242	243	244
Descr.		Cpto n.4, spring n.2	Spr. n.2	Spr. n.2	Spr. n.2	Spr. n.2	Spr. n.2	Spr. n.2	Spr. n.2	Spr. n.2
		a=0.015	a=0.015	a=0.015	a=0.015	a=0.015	a=0.015	a=0.015	a=0.015	a=0.015
Waves ampl. real sc.	(m)	0.495	0.495	0.495	0.495	0.495	0.495	0.495	0.495	0.495
Waves ang. freq. r.s.	(rad/s)	0.197	0.208	0.219	0.230	0.241	0.252	0.263	0.284	0.306
R.s.freq.	(Hz)	0.031	0.033	0.035	0.037	0.038	0.040	0.042	0.045	0.049
Floater imm.	(m)	-0.572	-0.572	-0.572	-0.572	-0.572	-0.572	-0.572	-0.572	-0.572
Digital gain	n.d.	1.200	1.200	1.200	1.200	1.200	1.200	1.200	1.200	1.200
Input in wave gen	freq.(Hz)	0.180	0.190	0.200	0.210	0.220	0.230	0.240	0.260	0.280
	ampl.(m)	0.015	0.015	0.015	0.015	0.015	0.015	0.015	0.015	0.015
	ang.freq.(rad/s)	1.131	1.194	1.257	1.319	1.382	1.445	1.508	1.634	1.759
Heave	ampl.(mm)	22.190	9.529	26.796	20.883	31.149	35.034	30.570	29.420	16.401
	ang.freq.(rad/s)	1.132	1.196	1.257	1.320	1.383	1.444	1.509	1.634	1.765
	phase(rad)	3.393	2.300	0.949	5.571	2.594	5.029	-0.721	5.489	3.755
	offset	-573.108	-571.924	-573.178	-572.730	-572.467	-572.804	-572.574	-572.616	-572.616
	freq.(Hz)	0.180	0.190	0.200	0.210	0.220	0.230	0.240	0.260	0.281
Surge	ampl.(mm)	43.199	33.007	52.767	36.979	26.184	25.508	26.035	22.585	20.893
	ang.freq.(rad/s)	1.125	1.196	1.258	1.318	1.384	1.446	1.507	1.633	1.763
	phase(rad)	-0.423	2.405	3.878	2.002	5.549	2.165	2.970	3.348	1.478
	offset	301.932	301.593	305.532	304.057	302.741	304.002	303.270	302.490	301.598
	freq.(Hz)	0.179	0.190	0.200	0.210	0.220	0.230	0.240	0.260	0.281
Sonic probe(inline)	ampl.(mm)	22.503	14.092	15.682	12.353	14.480	15.466	14.680	16.503	11.156
	ang.freq.(rad/s)	1.130	1.194	1.258	1.320	1.383	1.445	1.508	1.634	1.764
	phase(rad)	1.086	0.368	5.180	3.739	1.036	3.720	4.500	4.733	3.142
	offset	-376.460	-376.520	-376.574	-376.450	-376.485	-376.580	-376.444	-376.449	-376.636
	freq.(Hz)	0.180	0.190	0.200	0.210	0.220	0.230	0.240	0.260	0.281
Load cell	ampl.(N)	2.981	1.315	3.641	2.819	4.162	4.663	4.070	3.886	2.180
	ang.freq.(rad/s)	1.132	1.195	1.257	1.320	1.383	1.444	1.509	1.634	1.765
	phase(rad)	-0.109	0.547	4.713	0.029	-0.396	2.537	4.663	1.542	1.730
	offset	40.264	40.404	40.249	40.273	40.269	40.237	40.251	40.231	40.256
	freq.(Hz)	0.180	0.190	0.200	0.210	0.220	0.230	0.240	0.260	0.281
Mooring displ.(mm)	ampl.(mm)		10.069	27.536	21.202	31.203	35.107	30.694	29.264	16.421
	ang.freq.(rad/s)	1.618	1.196	1.257	1.310	1.383	1.444	1.509	1.630	1.765
	phase(rad)	1.707	2.315	0.899	5.618	2.552	4.988	5.526	5.525	3.730
	offset	47.779	34.547	52.436	35.006	23.660	22.072	21.578	17.281	14.809
	freq.(Hz)	0.257	0.190	0.200	0.208	0.220	0.230	0.240	0.259	0.281
Wave p. (upstream)	ampl.(mm)	15.013	12.502	22.846	16.272	12.035	13.771	14.646	16.429	11.644
	ang.freq.(rad/s)	1.132	1.192	1.258	1.319	1.381	1.447	1.507	1.634	1.763
	phase(rad)	2.555	2.456	0.799	5.263	2.759	-0.554	0.316	0.884	5.463
	offset	-322.238	-322.405	-322.400	-322.482	-322.392	-322.281	-322.261	-322.311	-322.327
	freq.(Hz)	0.180	0.190	0.200	0.210	0.220	0.230	0.240	0.260	0.281
Heave RAO	n.d	0.986	0.676	1.709	1.690	2.151	2.265	2.082	1.783	1.470
Surge RAO	n.d	38.224	27.638	41.949	28.005	18.928	17.658	17.262	13.825	11.847

Table A.20: Tests of submerged floater Session 3 (1:33 scale model). Here tests results, where the second spring was used and the immersion of floater was set to -0.58 m (c.a. value n.3), are shown. For these tests the servomotor was set to Damping n.4 (c.a. 31.5 kg/s).

A.2 Verification and validation of numerical tool with experiments

Validation of Nemoh code results

Also, hydrodynamic coefficients for the DNV caisson have been calculated with the Nemoh code. These coefficients are reported and compared to the results given by others. This task was done to verify the Nemoh code itself and verify how this code was integrated into the numerical tool developed in this project. Results for the caisson are illustrated next.

Results for caisson

The D.N.V. Caisson was analysed with a range of wave periods and compared to existing results obtained by (T = 1 to 40 seconds) Faltinsen and Michelsen (1974) and those obtained by Delhommeau (1987). The geometry analysed is shown in Figure A.5.

In Figures A.6 to A.9 are shown respectively the added mass, radiation damping, RAOs, wave excitation forces (modules and moment) of the DNV caisson. This last is measuring 90 m width, 90 m long and has a draught of 40 m. The mesh created was made of 300 panels. In Figure A.5 half of the caisson is displayed.

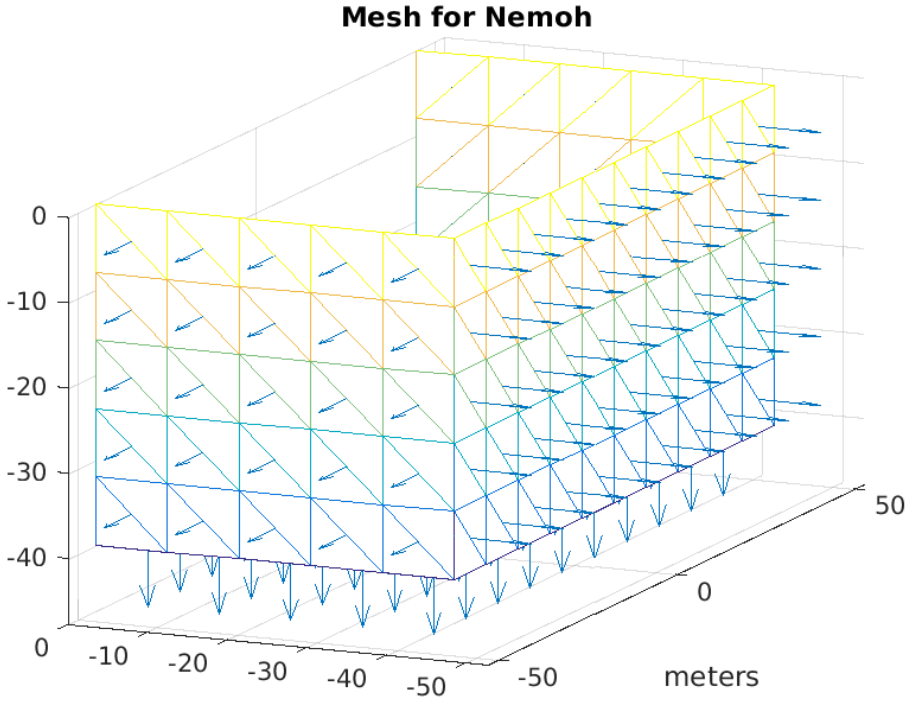

Figure A.5: Mesh of DNV caisson (150 panels)

.

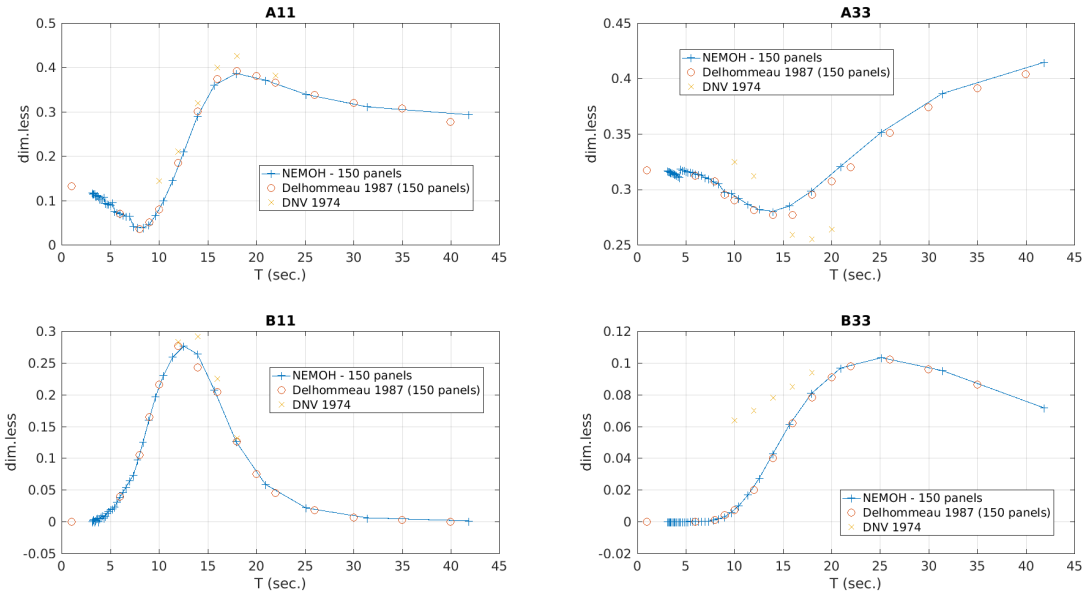

Figure A.6: Added mass and radiation damping of DNV caisson

.

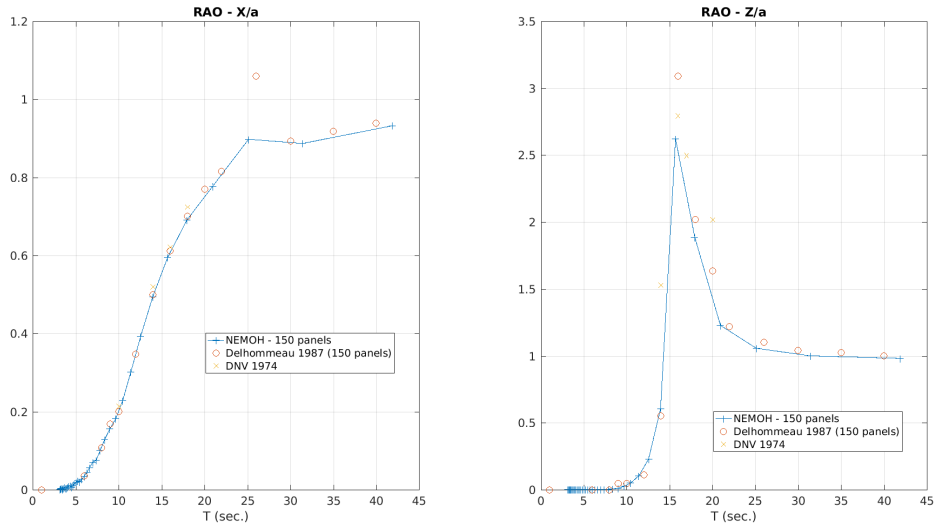

Figure A.7: Response amplitude operators (RAOs) for DNV caisson

.

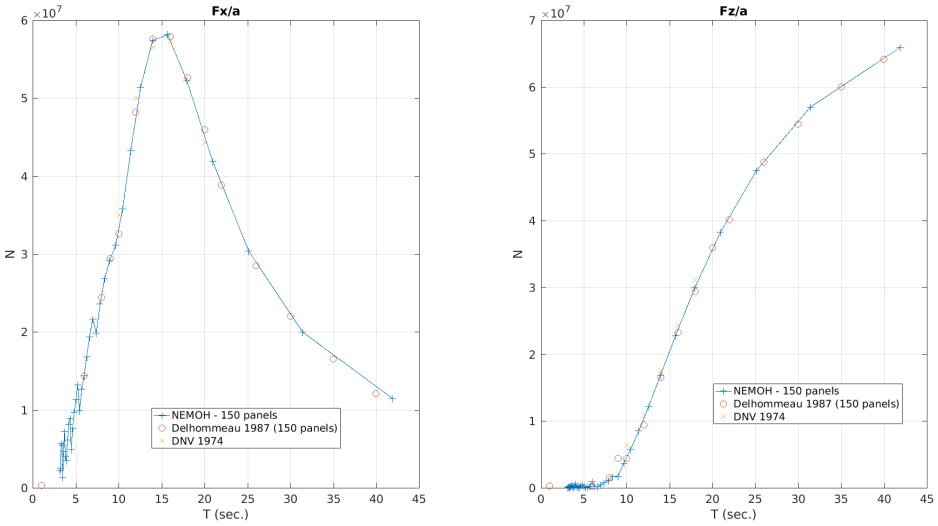

Figure A.8: Wave excitation loads for DNV caisson

.

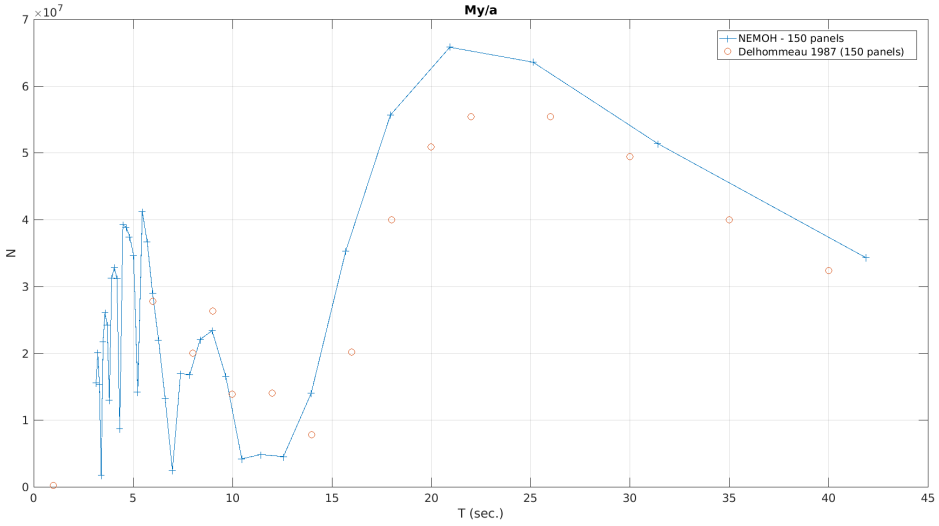

Figure A.9: Wave excitation moment for DNV caisson

.

A.2.1 Extra regular waves validation figures

In the following figures is shown the comparison of numerical results with empirical results relative to the immersed floater at Depth 3. Results confirm of what was found for Depth 1.

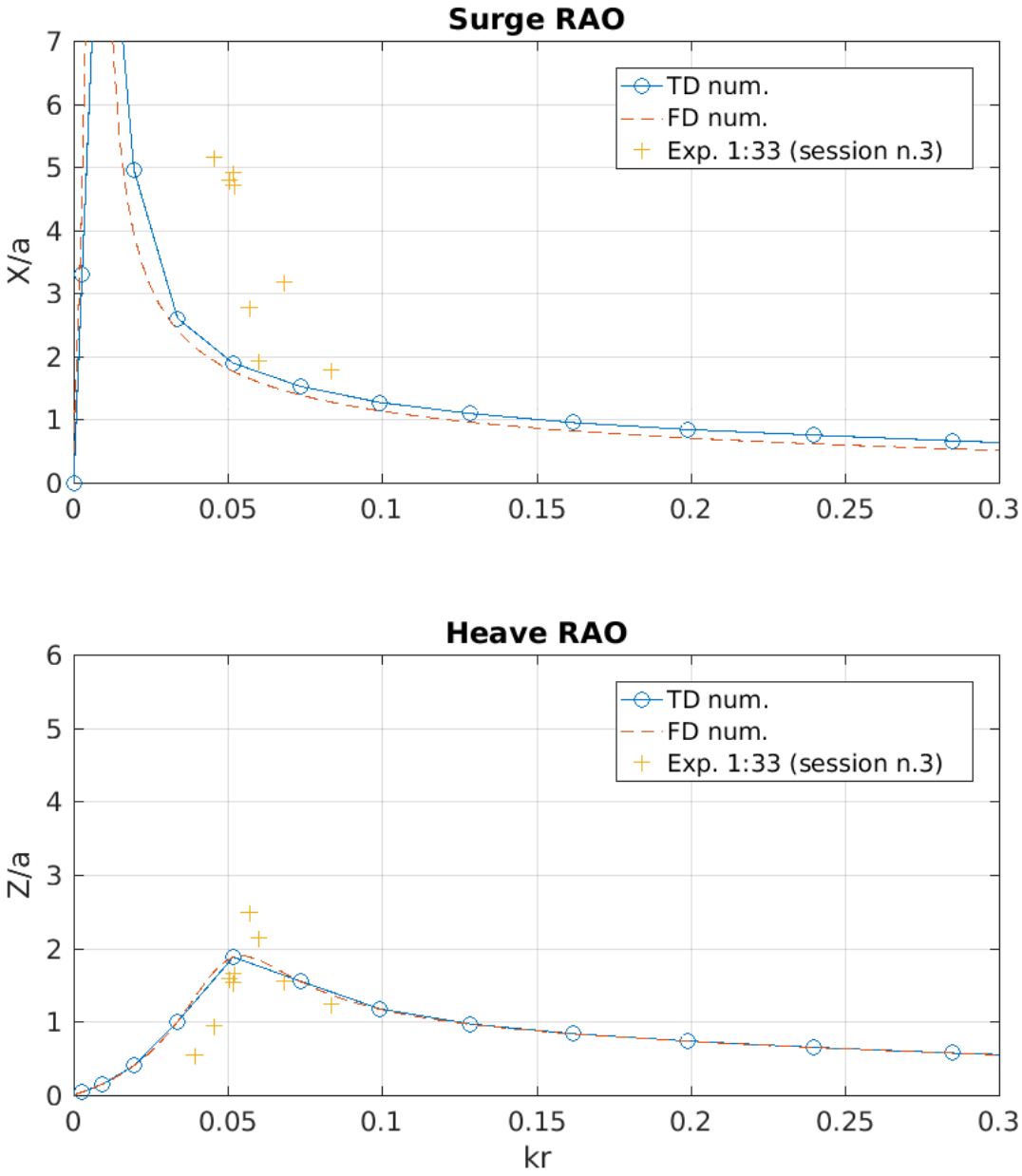

Figure A.10: RAOs obtained with different methods: TD and FD calculations; experimental results. The depth for this set of tests was set to *f/r=2.5* (Depth n.4) and the damping value corresponded to the value referred as *Damping n.4* (refer to Section 4.8.3).

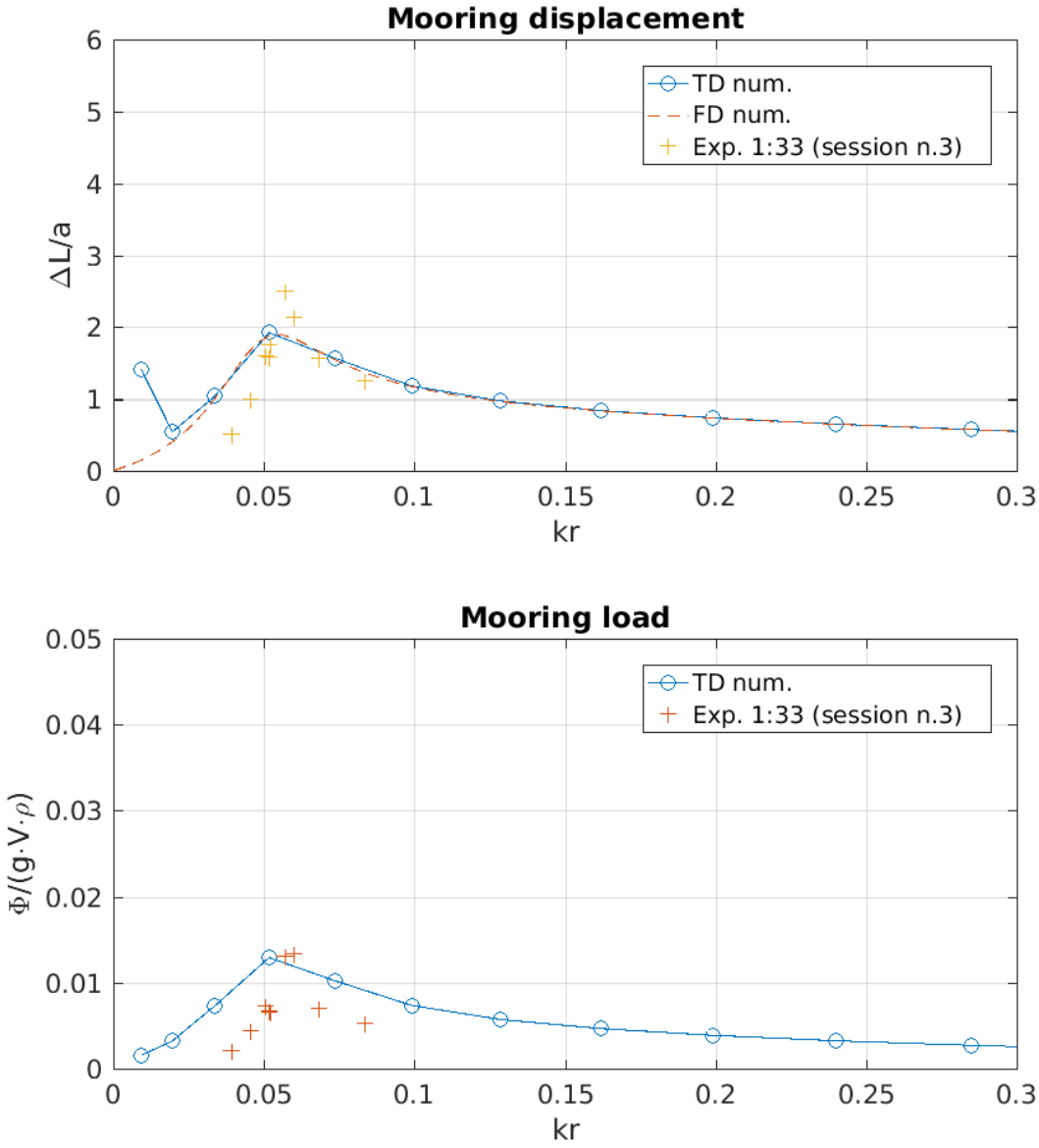

Figure A.11: Comparison of mooring displacement and mooring force (at load cell). The depth for these tests was set to *f/r=2.5* (Depth n.4) and the damping value corresponded to the value referred as *Damping n.4* (refer to Section 4.8.3).

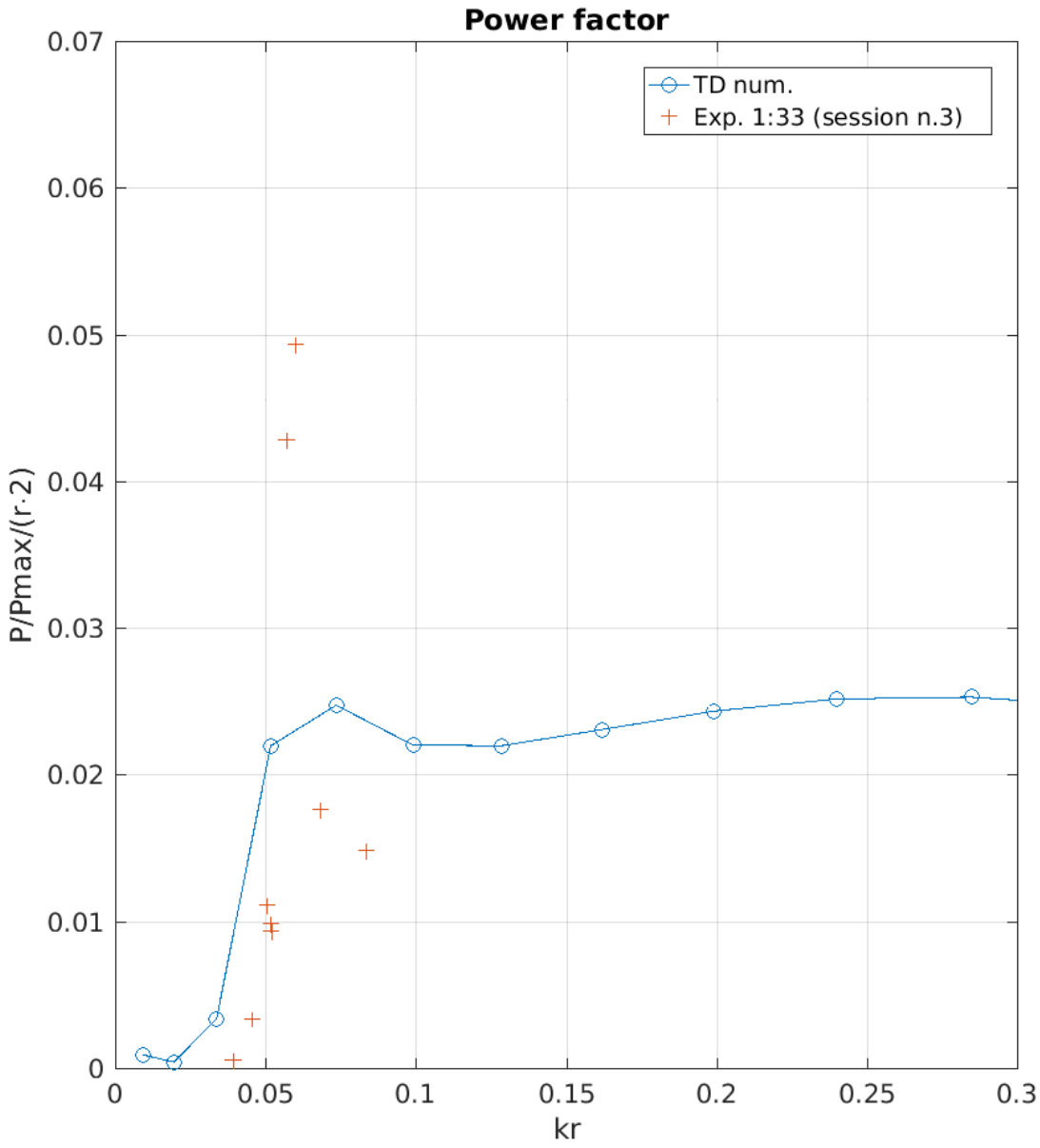

Figure A.12: Estimated power factor values from experimental data and from the numerical code. The depth for these tests was set to *f/r=2.5* (Depth n.4) and the damping value corresponded to the value referred as *Damping n.4* (refer to Section 4.8.3).

A.2.2 Extra comparisons of time-domain calculations with experimental results

In Figure A.13 is shown further comparison of floater and mooring load trajectories plotted against surge for a regular waves test. TD results in this case were obtained without considering drift forces.

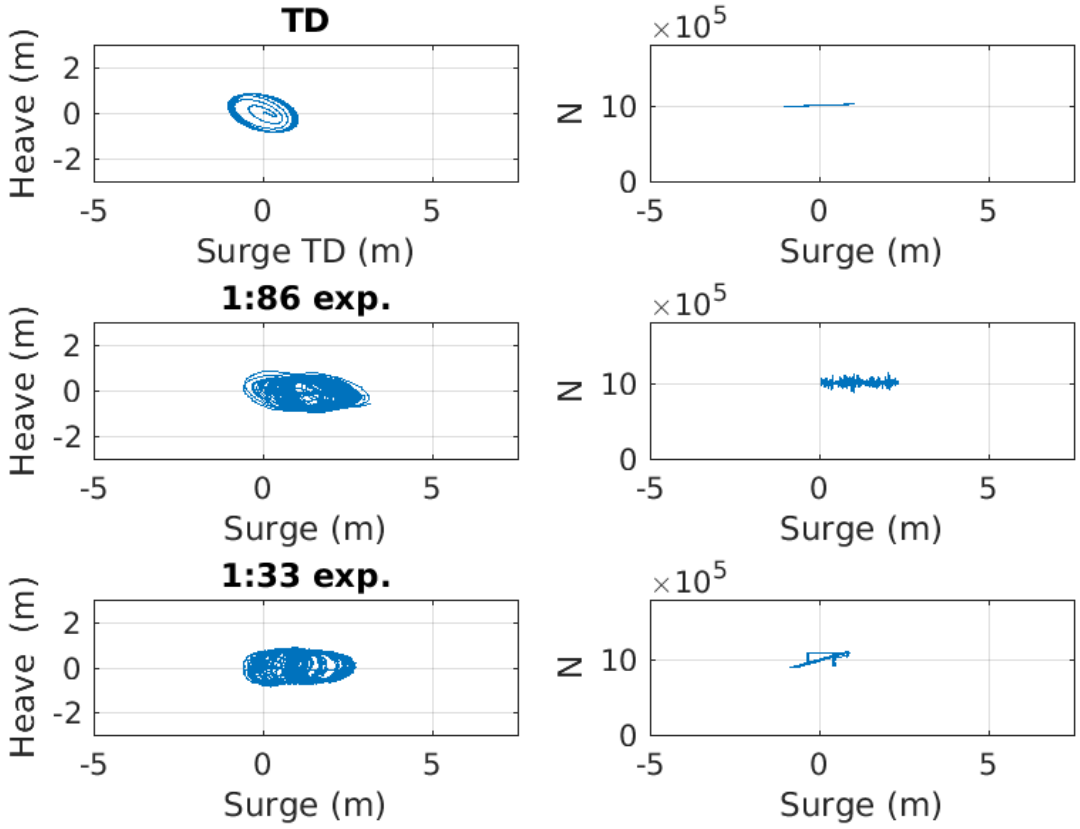

Figure A.13: Comparison of time-domain calculations with experimental results at 1:33 and 1:86 scale (where horizontal drift forces are not included in the TD calculations). On left hand figures the floater trajectory is shown. On right hand figures the mooring load after damping mechanism is plotted against the surge position.

References

Aamo, O.M. and T. I. Fossen (2000). "Finite element modelling of mooring lines". In: *Mathematics and Computers in Simulation*.

Babarit, A. (2014). "Nemoh - Website". http://lheea.ec-nantes.fr/doku.php/emo/nemoh/start.

Babarit, A. et al. (2011). *Numerical estimation of energy delivery from a selection of wave energy converters*. Tech. rep. Ecole Central de Nantes.

Bachynscki, E.E., Y.L. Young, and R.Y. Yeung (2012). "Analysis and optimization of a tethered wave energy converter in irregular waves". In: *Renewable Energy*, pp. 133–145.

Barltrop, N.D.P. (1998). *Floating structures: a guide for design and analysis*. Vol. 1 & 2. Energy Institute.

Budal, K. and J. Falnes (1980). "Interacting point absorber with control motion". In: *Power from Sea Waves*. Count, B.

Chakrabarti, S. K. (2005). *Handbook of Offshore Engineering*. Vol. II. Elsevier.

Cruz, J. (2008). *Ocean Wave Energy Current Status and Future Prepectives*. Ed. by Springer. Cambridge University Press.

Cruz, J.M.B.P. and A.J.N.A. Sarmento (2005). "Time domain simulations on a single point moored submerged sphere of variable radius". In: *24th International Conference on Offshore Mechanics and Arctic Engineering. Halkidiki*.

Cummins, W.E. (1962). "The impulse response function and ship motions". In: *Schiffstechnic*, 101109.

Delhommeau, G. (1987). “Les Problemes de Diffraction-Radiation et de Resistance de Vagues: Etude Theorique et Resolution Numerique par la Methode des Singularites”. PhD thesis. Ecole Nationale Superieure de Mecanique de Nantes.

— (1993). *Numerical Simulation of Hydrodynams: Ships and Offshore Structure - Seakeeping codes AQUADYN and AQUAPLUS*. Tech. rep. Ecole Central de Nantes.

Ding, B. et al. (2017). “Study of fully submerged point absorber wave energy converter - modelling, simulation and scaled experiment”. In: *The 32nd International Workshop on Water Waves and Floating Bodies, Dalian, China, 23-26 April*.

EMEC (2009). *Tank Testing on Wave Energy Conversion Systems*. Tech. rep. The European Marine Energy Center Ltd.

EWPP (1984). *Bending Moments in Long Spines*. Tech. rep. Report of Edinburgh Wave Power Project. University of Edinburg.

— (1986). *Long Spine Mooring*. Tech. rep. Report of Edinburgh Wave Power Project. University of Edinburgh.

— (1987). *Solo Duck Linear Analysis*. Tech. rep. Report of Edinburgh Wave Power Project. University of Edinburgh.

Elwood, D. et al. (2011). “Estimating the energy production capacity of a taut-moored dual-body wave energy conversion system using numerical modelling and physical testing”. In: *Journal of Offshore Mechanics and Arctic Engineering*.

Evans, D.V. (1980). “Power from Sea Waves”. In: ed. by B. Count. Academic Press. Chap. Hydrodynamic theory and its applications to wave energy, p. 213.

Falcão, A.F.de O. (2010). “Wave energy utilization: A review of the technologies”. In: *Renewable and Sustainable Energy Reviews*.

Falnes, J. (2002). *Ocean Waves and Oscillating Systems*. Cambridge University Press.

Falnes, J. and K. Budal (1978). “Norwegian Maritime Research”. In: chap. 6, pp. 2–11.

Faltinsen, L.M. and F.C. Michelsen (1974). “Motions of Large Structures in Waves at Zero Froude Number”. In: *Proc. Intern. Symp. Dyn. Mar. Vehicles Struct. Waves*. Ed. by Norske Veritas.

FitzGerald, J. (2009). “Position Mooring of Wave Energy Converters”. PhD thesis. Chalmers University of Technology.

Fitzgerald, J. and L. Bergdahl (2008). “Including moorings in the assessment of a generic offshore wave energy converter: A frequency domain approach”. In: *Marine Structures*, pp. 23–46.

— (2009). “Rigid moorings in shallow water: A wave power application. Part I: Experimental verification of methods”. In: *Marine Structures*, pp. 809–835.

Fonseca, N. et al. (2009). “Design of a mooring system with synthetic ropes for the FLOW wave energy converter”. In: *28th International Conference on Ocean, Offshore and Arctic Engineering. Honolulu.*

Fossen, T. I. (2011). *Handbook of Marine Craft Hydrodynamics and Motion Control.* Ed. by John Wiley & Sons. ILE.

Gao, Z. and T. Moan (2009). “Mooring system analysis of multiple wave energy converters in a farm configuration”. In: *8th European Wave and Tidal Energy Conference. Uppsala*, pp. 509–518.

Gilloteaux, J-C. and J. Ringwood (2009). “Influences of wave directionality on a generic point absorber”. In: *Proceedings of the 8th European Wave and Tidal Energy Conference, Uppsala, Sweden.*

Gordelier, T. et al. (2015). “A Novel Mooring Tether for Highly-Dynamic Offshore Applications; Mitigating Peak and Fatigue Loads via Selectable Axial Stiffness”. In: *Marine Science and Engineering.*

Gunn, D. F., M. Rudman, and R. C. Z. Cohen (2018). “Wave interaction with a tethered buoy: SPH simulation and experimental validation”. In: *Ocean Engineering.*

Gutirrez-Romeo, J. E. et al. (2016). “Non-linear dynamic analysis of the response of moored floating structures”. In: *Marine Structures.*

Hall, M. and A. Goupe (2015). “Validation of a lumped-mass mooring model with DeepCDeep semisubmersible model test data”. In: *Ocean Engineering.*

Hann, M., D. Greaves, and A. Raby (2015). “Snatch loading of a single taut moored floating wave energy converter due to focused wave groups”. In: *Ocean Engineering.*

Harnois, V. et al. (2015). “Numerical model validation for mooring systems: Method and application for wave energy converters”. In: *Renewable Energy.*

Harris, R.E., L. Johanning, and J. Wolfram (2004). "Mooring system for wave energy converters: A review of design issues and choices". In: *Paper presented at 3rd International Conference on Marine Renewable Energy*. [pdf], Available online [Accessed 10 Jan. 2016]. URL: `http://www.energiatalgud.ee/`.

Henriques, J.C.C. et al. (2013). "Wave energy resource assessment for a breakwater-integrated oscillating water column plant at Porto, Portugal". In: *Energy*.

Herbich, J.B. (2000). *Handbook of coastal engineering*. McGraw-Hill Professional.

Hsu, F.H. and K.A. Blenkarn (1970). "Analysis of peak mooring force caused by slow vessel drift oscillation in random seas". In: *Offshore Technology Conference*. paper n. 1159.

Hulme, A. (1982). "The wave forces acting on a floating hemisphere undergoing forced periodic oscillations". In: *Journal of Fluids Mechanics*, pp. 443–463.

IDEMAT (2003). *Industrial Design & Engineering MATerials database*. URL: `https://www.matbase.com`.

ITTC (2017a). "Uncertainty Analysis, Instrument Calibration". In: *ITTC Quality System Manual Recommended Procedures and Guidelines*. Ed. by Qualuty System Group of 28th ITTC. Vol. 7.5-01-03-01. International Towing Tank Conference.

— (2017b). "Uncertainty Analysis for a Wave Energy Converter". In: *ITTC Quality System Manual - Recommended Procedures and Guidelines*. Ed. by Specialist Committee on Testing of Marine Renewable Devices of the 28th ITTC. 7.5-02-07-03.12. International Towing Tank Conference.

Idris, K., J. W. Leonard, and C.S. Yim (1997). "Coupled Dynamics of Tethered Buoy Systems". In: *Ocean Engineering*.

Johanning, L., G.H. Smith, and C. Bullen (2007). "Large scale mooring line experiments and comparison with a fully dynamic simulation program with importance to WEC installation". In: *Proceedings of the Seventeenth (2007) International Offshore and Polar Engineering Conference. Lisbon*.

Johanning, L., G.H. Smith, and J. Wolfram (2006). "Mooring design approach for wave energy converters". In: *Proceeding of the Institution of Mechanical Engineers, Part M: Journal of Engineering for the Maritime Environment*, pp. 159–174.

Journee, J.M.J. and W.W. Massie (2001). *Offshore Hydromechanics*. Delf University of Technology, available for free online.

Krivtsov, V., B. Linfoot, and R.E. Harris (2012). "Effects of the shape and size of a mooring line surface buoy on the mooring load of wave energy converters". In: *Journal of Chongqing University (Eng.Ed.)*

Lau, L. S., Z. Ji, and C. O. Ng (1990). "Dynamics of an Elastically Moored Floating Body by the Three-Dimensional Infinite Element Method". In: *Ocean Engineering*.

Luxmoore, F. J. et al. (2016). "Analytical performance assessment of a novel active mooring system for load reduction in marine energy converters". In: *Ocean Engineering*.

MARINET (2013). *UoStrath - Kelvin Hydrodynamics Laboratory (Formerly Acre Road Wave and Tow Tank)*. Tech. rep. [pdf format, Accessed: 10th Jan. 2015]. URL: `www.fp7-marinet.eu/Uni_Strath-acre-road-wave-tow-tank.html`.

Ma, C. et al. (2016). "Theoretical, experimental and numerical investigations into nonlinear motion of a tethered-buoy system". In: *Journal of Marine Science and Technology*.

Martinelli, L., P. Roul, and G. Cortellazzo (2012). "On mooring design of wave energy converters: The Seabreath application". In: *Coastal Engineering*.

Masuda, Y., L. Xianguang, and G. Xiangf (1993). "High performance of cylinder float backward bent duct buoy (BBDB) and its use in European seas". In: *Proceedings of (First) European Wave Energy Symposium p. 32337*. Ed. by European Wave Energy Symposium.

Mavrakos, S. A. and G. M. Katsaounis (2005). "Parametric evaluation of the performance characteristics of a tight moored wave energy converter". In: *Proceedings of OMAE2005*.

Mavrakos, S. A., G. M. Katsaounis, and M. S. Apostolidis (2009). "Effects of floaters' geometry on the performance characteristics of a tighly moored wave energy converters". In: *Proceedings of the ASME 2009 28th International Conference on Ocean, Offshore and Arctic Engineering*.

Mavrakos, S. A. et al. (1996). "Deep Water Mooring Dynamics". In: *Marine Structures*.

Mei, C.C. (1976). "Power extraction from water waves". In: *Journal of Ship Rearch*, pp. 63–66.

Mørk, G. et al. (2010). "Assessing the global wave energy potential". In: *29th International Conference on Ocean, Offshore Mechanics and Arctic Engineering*.

Muliawan, M.J. et al. (2011). "Analysis of a two-body floating wave energy converter with particular focus on the effects of power take off and mooring systems on energy capture". In: *30th International Conference on Ocean, Offshore and Arctic Engineering. Rotterdam*.

Newman, J. N. (1963). *The exciting forces on fixed bodies in waves*. Tech. rep. Department of the Navy - David Taylor Model Basin.

Ogilvie, T. F. (1964). *Recent progress toward the understanding and prediction of ship motions*. Tech. rep. David Taylor Model Basin.

Orszaghova, J. et al. (2016). "Experimental Study of Extreme Responses of a Point Absorber Wave Energy Converter". In: *20th Australasian Fluid Mechanics Conference*.

Parmeggiani, S., J.P. Kofoed, and E. Friis-Madsen (2011). "Extreme loads on the mooring lines and survivability mode for the wave dragon wave energy converter". In: *World Renewable Energy Congress. Linkoping*, pp. 2159–2166.

Pascoal, R. et al. (2005). "Equivalent force model for the effect of mooring systems on the horizonatal motions". In: *Applied Ocean Research*.

Payne, G. (2008). *Guidance for the experimental tank testing of wave energy converters*. Tech. rep. The University of Edinburgh.

Pizer, D. (1994). *Numerical Modelling of Wave Energy Absorbers*. Tech. rep. University of Edinburgh.

Qualysis (2016). Qualysis QTM Manual. [Accessed 15 Nov. 2016]. URL: `http://fy.chalmers.se/~f7xiz/TIF081C/QTM-usermanual.pdf`.

Radhakrishnan, S., R Datla, and R. I. Hires (2007). "Theoretical and experimental analysis of tethered buoy instability in gravity waves". In: *Ocean Engineering*.

Raman-Nair, W. and R. E. Baddour (2002). "Three-Dimensional Coupled Dynamics of a Buoy and Multiple Mooring Lines: Formulation and Algoritm". In: *Journal of Mechanics and Applied Mathematics*.

Ran, Z., M. H. Kim, and W. Zheng (1999). "Coupled Dynamic Analysis of a Moored Spar in Random Waves and CCurrent -Time-Domain Versus Frequency-Domain Analysis-". In: *Offshore Mechanics and Artic Engineering*.

Remery, G. F. M. and A. J. Hermans (1971). "The slow drift oscillations of a moored object in random seas". In: *Offshore Technology Conference*. preprint, paper number OCT 1500.

Ridge, I.M.L., S.J. Banfield, and J. Mackay (2010). "Nylon fibre rope moorings for wave energy converters". In: *IEEE Conference Publications*.

Ross, D. (1995). *Power from sea waves*. Oxford University Press.

Salter, S.H. (1974). "Wave power". In: *Nature*, pp. 720–724.

Spanos, P. D. et al. (2016). "Efficient Dynamic Analysis of a Nonlinear Wave Energy Harvester Model". In: *Journal of Offshore Mechanics and Arctic Engineering*.

Sumer, B. M. and J. Fredsœ (2006). *Hydrodynamics Around Cylindrical Structures*. Ed. by P. L-F Liu. World Scientific.

Swaroop, N. B. (2004). "Hydrodynamic coefficients for water-wave diffraction by spherical structures". In: *Sādhāna*.

Thies, P. R., L. Johanning, and P. McEvoy (2014). "A novel mooring tether for peak load mitigation: Initial performance and service simulation testing." In: *International Journal of Marine Energy*.

Thies, P. R., G. Smith, and L. P. Johanning (2012). "Addressing failure rate uncertainties of marine energy converters". In: *Renewable Energy*.

Thies, P. R. et al. (2014). "Mooring line fatigue damage evaluation for floating marine energy converters: Field Measurements and prediction". In: *Renewable Energy*.

Tide-forcast (2018). *Tide Times for Porto*. URL: `https://www.tide-forecast.com/locations/Porto/tides/latest`.

Torsethaugen, K. (2004). "Simplified double peak spectral model for ocean waves". In: *Paper No. 2004JSC-193, ISOPE Touson France*.

Van Den Boom, H. J. J. (1985). "Dynamic Behauviour of Mooring Lines". In: *Behavior of Offshore Structures*.

Vicente, P.C. et al. (2009). "Dynamics of arrays of floating point-absorber wave energy converters with inter-body and bottom slack-mooring connections". In: *Applied Ocean Research*, pp. 267–281.

Vicente, P.V., A.F.O. Falcão, and P.A.P. Justino (2013). "Nonlinear dynamics of a tighly moored point-absorber wave energy converter". In: *Ocean Engineering*.

Vickers, A.W. and L. Johanning (2009). "Comparison of damping properties for three different mooring arrangements". In: *Proceedings of the 8th European Wave and Tidal Energy Conference. Uppsala*, pp. 637–645.

Virgala, I., P. Frankovsky, and M. Kenderov (2013). "Friction Effect Analysis of a DC Motor". In: *American Journal of Mechanical Engineering*.

Wang, S. (1986). "Motions of spherical submarine in waves". In: *Ocean Engineering*.

Wang, W. et al. (2018). "Estimation of numerical uncertainty in CFD simulations of a passively controlled wave energy converter". In: *Journal of Engineering for the Maritime Environment*.

Weller, S. D. et al. (2015). "Synthetic mooring ropes for marine renewable Energy applications". In: *Renewable Energy*.

Weller, S. et al. (2013). *Guidance on the use of synthetic fibre ropes for marine energy devices*. Tech. rep. MERiFiC.

Wilson, J. F. et al. (2003). *Dynamics of Offshore Structures*. Ed. by J. F. Wilson. John W. and Sons, Inc.

Yang, M. et al. (2012). "Coupled dynamic Analysis for wave interaction with a truss spar and its mooring line/riser system in time domain". In: *Ocean Engineering*.

Young, H. E. and J. Pollok (1985). *Variable Coefficents Control of a Wave-Energy Device - Report of Edinburgh Wave Power Project*. Tech. rep. University of Edinburgh.